COHERENT PHOTON SCATTERING ON NUCLEI IN THE Δ(1232) RESONANCE REGION

A Thesis

Submitted to the

College of Graduate Studies and Research

in Partial Fulfillment of the Requirements

for the

Degree of

Doctor of Philosophy

in the

Department of Physics

University of Saskatchewan

Saskatoon

Canada

by

Ryuichi Igarashi

Fall 1993

PERMISSION TO USE

In presenting this thesis in partial fulfillment of the requirements for a Postgraduate degree from the University of Saskatchewan, I agree that the Libraries of this University may make it freely available for inspection. I further agree that permission for copying of this thesis in any manner, in whole or in part, for scholarly purposes may be granted by the professor or professors who supervised my thesis work or, in their absence, by the Head of the Department or the Dean of the College in which my thesis work was done. It is understood that any copying or publication or use of this thesis or parts thereof for financial gain shall not be allowed without my written permission. It is also understood that due recognition shall be given to me and to the University of Saskatchewan in any scholarly use which may be made of any material in my thesis.

Requests for permission to copy of make other use of material in this thesis in whole or part should be addressed to:

Head of the Department of Physics
University of Saskatchewan
Saskatoon, Saskatchewan
Canada
S7N 0W0

ABSTRACT

Angular distributions for photon scattering from ^{12}C have been measured at the Saskatchewan Accelerator Laboratory (SAL) high duty factor bremsstrahlung facility. Data were taken at 160, 200, 250 and 290 MeV endpoint energies and at angles ranging from 20 degrees to 150 degrees with the 53cm diameter x 56cm long Boston University Sodium Iodide (BUNI) detector. Coherently scattered photons were easily distinguished from neutral pion decay photons in detected energy spectra. The excellent resolution of the detector and the high duty cycle at SAL have made it possible to obtain new data on the angular distributions for elastic and, in some cases, for inelastic scattering as well.

It was essential to distinguish between elastic scattering and inelastic scattering to the 4.44 MeV state in ^{12}C. This was further complicated by the continuous nature of bremsstrahlung such that only a region within about 4 MeV of the endpoint could be used. Hence, precise energy calibration and stability of the calibration were required. Since elastic cross sections can be small, pileup transferring inelastic events into the elastic region was a concern and required careful attention.

The angular distributions for elastic scattering were compared with a simple calculation of a dipole distribution weighted by the charge form factor and scaled by forward cross sections derived from total absorption cross sections with dispersion relations. This calculation badly underestimates cross sections at back angles. The more serious calculation with the Δ-hole model at 200 MeV overestimates the measurements at all angles.

Some cross sections for inelastic scattering leading to the 4.44 MeV first excited state in carbon have been extracted. These cross sections are small compared to the elastic channel at forward angles, but are dominant at backward angles. Since this experiment was the first to separate elastic from inelastic photon scattering at these energies, these new data should stimulate further theoretical study.

ACKNOWLEDGEMENTS

This was a large project that consumed the resources of many people. To these people I would like to express my thanks:

Dr. Henry Caplan, my supervisor, whose extensive experience in Physics has saved me from some pretty ugly situations, and for his patient guidance in the preparation of this thesis. Dr. Ed Booth, the instigator of this affair, who tackled this experiment with a verve that was simply inspirational and a lot of fun to be a part of. Dr. Evans Hayward, Dr. Al Nathan, Dr. Jim Miller, Dr. Jack Bergstrom, Dr. J. Arends, Frank Wissman, Dr. Ed Tomusiak, Dr. Juhachi Asai, and Dr. Jim Friar for enlightening discussions on theoretical and experimental aspects of this experiment. Emil Hallin for his discussions, recommendations and collaboration in analysing the massive volume of data from this experiment. Dr. Doug Wells whose instruction on the maintenance and repair of the helium cryostat was indispensable. Dave Amendt, Mark Lucas, Bruce MacGibbon, and Dom Delli Carpini, my grad student cohorts in this experiment.

Dr. Dennis Skopik, Dr. Rob Pywell, and Dr. Les Dallin for setting up the accelerator and ring and keeping both tuned up, especially during late/early hours.

Noel Craddock, Mark "Duke" Besse and Peter Fremanis for putting up with a bunch of physicists who wanted to move BUNI in the middle of the night, and, with Don Gulak and John Grefkes and his shop, for doing some great mechanical and engineering work for us. Tom West and Rino Verhulst for putting up with a greenhorn machine operator who had a tendency to call for help at 4 AM, and, with the operations crew, for getting breakdowns repaired so promptly, thus allowing us to run for so long. Curtis Figley for keeping the Kickers going despite the hammering they took from us.

Ervin Neudorf and Jim Bergstrom for arranging deliveries so efficiently, for contending with customs, and procuring specialty items so quickly.

Doug Murray, Glen Wright, Tony Wilson, Eric Norum, and Skeeter Abell-Smith, for teaching me the C programming language, for showing me what good programming looks like (though, I still don't program well), and for your friendship.

Joyce Gayle, Arlene Figley, and Lavina Carter for putting up with last minute submissions to Annual Reports, putting up with confused airline tickets, and making sure the paperwork got done right. Irene Sigstad for putting up with a student that never had a clue about registration and for setting me straight on the formalities required of a grad student.

Greg Retzlaff for putting a roof over my head when I arrived in Saskatoon.

Dr. Johannes Vogt for the finer points of particle detection and electronics, and he and his wife, Iris, for cheerful jibes and outrageous attempts of persuasion.

Jeanne Kelly and my family: Yuriko Kitamura, Sak Igarashi, Kathy Horwood, Sho Igarashi, for providing moral support, some fun, and some sanity. To the Fiasco Brigade: "FIASCO!!!".

The lab rats, Mark Silzer, Don Tiller, Dwain Stensrud, Kevin Fissum, Ken "LGP" Garrow, Dave Hornidge, Jim Sigurdson, Jaret Heise, Keith Helgason, Evan "Foz" Hackett, Grant O'Rielly, Benno van den Brink, Hyunjung Choi, Hyntai Chung, Mohamed Benmerrouche, Kara J. Keeter, Jerry Feldman, Dan Simon, Richard Florizone, and Adam Sarty for their, sometimes enlightening, but more often plain B.S., conversations and your friendship.

TABLE OF CONTENTS

LIST OF FIGURES

LIST OF TABLES

Chapter 1. INTRODUCTION

There are many ways of probing the structure and dynamics of matter. The study of matter at the nuclear scale requires probes of effective wavelengths ($\lambda = h / p$) of the order of the size of nuclei, about 1 fm. Unfortunately, at this scale no technology exists to produce images of nuclei. Instead, only the intensity of scattered particles can be measured from which structure must be inferred. This may be complicated by the nature of the probe being used in the measurement, especially if the interaction with the nucleus is not well known. However, the electromagnetic interaction is the best understood interaction in nature and this makes photons and electrons good probes of nuclei through their electric and magnetic properties. Photons have the added advantage that they do not suffer from distortions due to Coulomb effects as electrons do. In this thesis, the information that may be learned by nuclear scattering of intermediate energy photons is discussed.

1.1 Photon Scattering From a Free Charged Point Particle

One of the most important concepts of electromagnetic theory is that an oscillating charge (or more generally, an oscillating electric or magnetic multipole) radiates. The oscillating fields of a photon can drive a free charged point particle thereby inducing it to radiate. This process, for long wavelengths or low energy, is known as Thomson scattering and has an angular distribution, or differential cross section $\frac{d\sigma}{d\Omega}$, for unpolarized photons, given by Eqn. 1.1.

$$\frac{d\sigma}{d\Omega} = \left(\frac{e^2}{m}\right)^2 \frac{(1 + \cos^2\theta)}{2} \tag{1.1}$$

where e and m are the charge and the mass of the particle, and θ is the angle of the emitted radiation with respect to the incident photon. This classical expression which applies to

electrons and protons in the long wavelength limit is derived in the well known textbook by Jackson [Jackson 75a].

As the momentum of the photon (= hk/2π) becomes large enough to cause the charged particle to recoil, the cross section expression becomes more complicated:

$$\frac{d\sigma}{d\Omega} = \left(\frac{e^2}{m}\right)^2 \left(\frac{k'}{k}\right)^2 \frac{(1+\cos^2\theta)}{2} \tag{1.2}$$

for spinless point particles, and

$$\frac{d\sigma}{d\Omega} = \left(\frac{e^2}{m}\right)^2 \left(\frac{k'}{k}\right)^2 \left(\frac{(1+\cos^2\theta)}{2} + \frac{(k-k')^2}{4kk'}\right) \tag{1.3}$$

for spin 1/2 point particles, where k and k' are the wave numbers ($k = 2\pi/\lambda$)for the incident and scattered photon. This is Compton scattering and Eqn. 1.3 is called the Klein-Nishina formula for Compton scattering. It was calculated using quantum electrodynamics (QED) [Bjorken 64] and was one of the early successes of that theory. In fact Eqn. 1.3 reduces to Eqn. 1.1 for small k. The angular distributions for Thomson scattering and Compton scattering are plotted in Figure 1.1 to show the effect of higher photon momentum.

It should be noted that due to the mass difference between the proton and the electron, the Compton effect for protons is 3.36×10^6 times smaller in cross section than that for electrons. So while the electron Compton effect is a standard experiment in undergraduate labs, the smaller nuclear cross sections have made accurate measurement of this effect very difficult until recently.

1.2 Photon Scattering From Multiple Point Charges

In the case of scattering from many particles each particle contributes a Thomson or Compton scattering amplitude. However, the distribution of these particles must be taken into account in the calculation of cross sections. The scattering amplitude for the j-th particle at point $\vec{x}_j$ has a phase factor of $e^{i\vec{k}\cdot\vec{x}_j}$, for the incident photon, and $e^{-i\vec{k}'\cdot\vec{x}_j}$, for

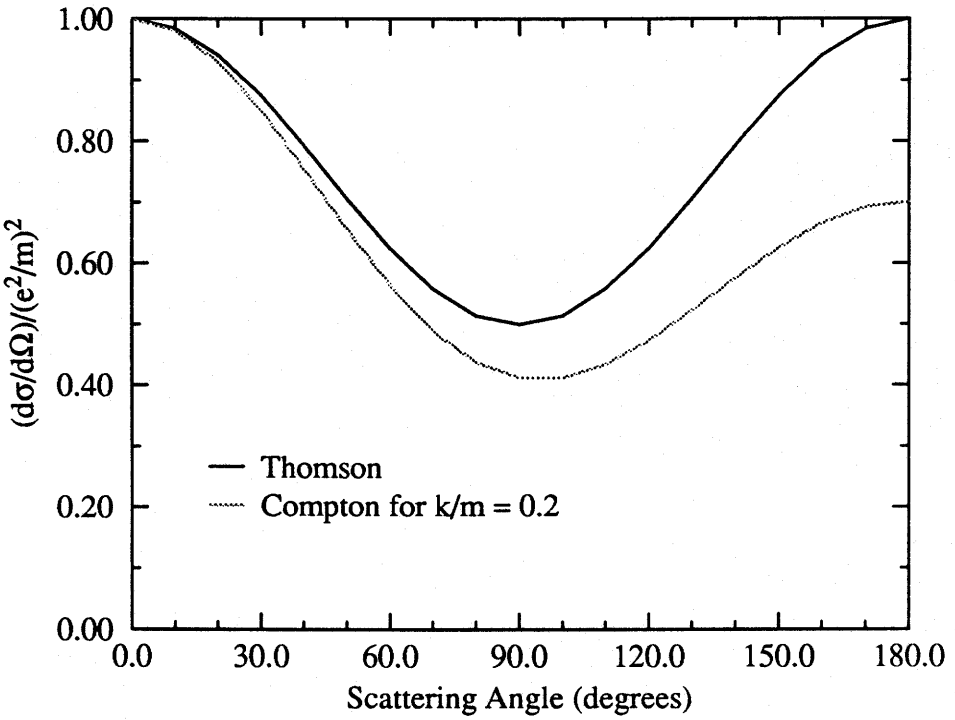

Figure 1.1: Differential Cross Sections for Thomson Scattering and Compton Scattering

the outgoing photon. If these charged particles are unbound, or can be treated as unbound, the amplitudes for Z particles may be summed [Jackson 75b] such that Eqn. 1.1 becomes

$$\frac{d\sigma}{d\Omega} = \left| \sum_{j=1}^{Z} \frac{e_j^2}{m_j} e^{-i\vec{q}\cdot\vec{x}_j} \right|^2 \frac{(1+\cos^2\theta)}{2} \tag{1.4}$$

where e_j and m_j are the charge and mass of the j-th particle, and $\vec{q} = \vec{k}' - \vec{k}$. For identical particles, this becomes

$$\frac{d\sigma}{d\Omega} = \left(\frac{e^2}{m}\right)^2 \left| \sum_{j=1}^{Z} e^{-i\vec{q}\cdot\vec{x}_j} \right|^2 \frac{(1+\cos^2\theta)}{2} \tag{1.5}$$

Now suppose that the charges are electrons freely distributed within a finite sphere of radius *a*. It must be stressed that this is not a model for an atom since it lacks a nucleus. The significance of this will be made apparent shortly. For wavelengths that are long

compared to *a*, or for small angles, qa << 1 and the argument of the exponential is near zero, so that the exponential is near unity [Jackson 75a]. Then the sum is simply the number of particles, Z, and the scattering cross section becomes

$$\frac{d\sigma}{d\Omega} = Z^2 \left(\frac{e^2}{m}\right)^2 \frac{(1 + \cos^2\theta)}{2}. \tag{1.6}$$

This is the Thomson formula for a point particle of charge Ze and mass Zm. Alternatively, this expression arises when the scattering from each of Z centers is in phase.

At the other extreme, qa >> 1, the cross terms of the sum average to zero so only the square terms are significant. There are Z terms from the sum of magnitude unity so that the cross section becomes

$$\frac{d\sigma}{d\Omega} = Z \left(\frac{e^2}{m}\right)^2 \frac{(1 + \cos^2\theta)}{2} \tag{1.7}$$

This is the cross section due to Z isolated particles where the photon effectively scatters from only one of the Z particles rather than the whole system of particles.

One can see that in the qa << 1 case, the whole system of particles is affected in unison and is left essentially in the state in which it started. This is called coherent scattering and is directly related to elastic scattering from a system of bound charges. On the other hand, in the qa >> 1 case, only one of the particles has experienced the effect. Then it may have changed its status with respect to the other particles and the system does not end in its initial state. This is called incoherent scattering and is related to inelastic scattering from a bound system of particles.

In the intermediate qa range, it is useful to define the form factor, F(q), for the sum over the individual particle phases:

$$Z^2F^2(\vec{q}) = \left| \sum_{j=1}^{Z} e^{-i\vec{q}_j \bullet \vec{x}_j} \right|^2 \tag{1.8}$$

so that the cross section for a particle with a charge distribution is related to the cross section of a single point particle by

$$\frac{d\sigma}{d\Omega} = \left(\frac{d\sigma}{d\Omega}\right)_{\text{point}} |F(\vec{q})|^2. \tag{1.9}$$

This concept can be extended to more complicated charge distributions or continuous charge distributions if the sum is replaced with an integral of the charge density and the particle phase,

$$ZF(\vec{q}) = \int \rho(\vec{x}) e^{i\vec{q}\bullet\vec{x}} d^3x \tag{1.10}$$

where $\vec{q} = \vec{k}' - \vec{k}'$ and $\rho(x)$ is the charge density. Thus these form factors are Fourier transforms of the structure of the charge distribution.

1.3 Bound Particles and Particles with Structure

The ideas from the previous section can now be extended to a group of particles that make up larger objects like atoms and nuclei. Atoms are electrically neutral, so that as a single particle, they do not Thomson scatter photons. However, a photon will still cause the constituent electrons and nucleus to oscillate. Since the electrons and nucleus are oppositely charged, the atom becomes polarized in the field of the photon with an induced dipole moment $\mathbf{p} = \lambda_{mol}\,\mathbf{E}$, where λ_{mol} is the molecular electric polarizability. This dipole moment oscillates in the field of the photon. The resulting cross section, derived by Lord Rayleigh, has a k^4 dependency

$$\frac{d\sigma}{d\Omega} = \lambda_{atom}^2 k^4 |\varepsilon \bullet \varepsilon'|^2 F^2(\vec{q}). \tag{1.11}$$

where ε and ε' are the polarizations of incoming and outgoing photons. This process of photon scattering from electric dipoles is called Rayleigh scattering [Jackson 75c].

Nuclei have net charge, Ze, so that at the long wavelength limit Thomson scattering can occur on the center of mass, mass Am, which, according to Eqn. 1.1, has a cross section of

$$\frac{d\sigma}{d\Omega} = \frac{Z^4}{A^2}\left(\frac{e^2}{m}\right)^2 \frac{(1+\cos^2\theta)}{2}. \qquad (1.12)$$

This does not match Eqn. 1.6 which is the coherent scattering from a system of Z particles. The problem, of course, is due to the neutrons. The discrepancy is again resolved by decomposing the coordinates in Eqn. 1.5 into center of mass and internal coordinates [Silbar 68]. Because neutrons, which make up part of the mass of the system, do not move, the center of mass motion does not correspond to proton oscillations and a polarization occurs. Then the expected Thomson cross section for a particle of mass Z and charge Z (Eqn. 1.6) must be summed with a Rayleigh type term (having a NZ/A dependence) yielding Eqn. 1.12 [Arenhovel 86]. Eqn. 1.12 is the correct expression for the scattering cross section at the zero energy limit, or long wavelengths, and Eqn. 1.6 is a finite energy expression.

Up to this point, all particles were assumed to be point (Dirac) particles. For nucleons which make up the nuclei that interest us, this is not true. They are extended structures of radius about 1 fm and interact through the strong force for which we have substantially less understanding than electromagnetism and modify the scaling factors for cross sections.

1.4 Dispersion Relations

In photon scattering, dispersion relations can be used unambiguously to provide a very useful tool for predicting cross sections. Being somewhat phenomenological, these cross sections do not reveal as much as full calculations but they can yield some interesting information about strengths of contributions. These relations in a classical context are attributed to Kramers and Kronig[1] and were extended to quantum theory by Gell-Mann

et al [Gell-Mann 54]. In the present context, they relate the real and imaginary parts of the 0 degree scattering amplitude, S(E,0) to each other [Bjorken 65, Hayward 70, Ziegler 86] through the following principle value integrals:

$$\mathrm{Re}\{S(E,0)-S(0,0)\} = \frac{2}{\pi}P\int_0^\infty \frac{E^2\,\mathrm{Im}\{S(E',0)\}}{E'(E^2-E'^2)}dE' \tag{1.13}$$

$$\mathrm{Im}\{S(E,0)-S(0,0)\} = \frac{2}{\pi}P\int_0^\infty \frac{E\,\mathrm{Re}\{S(E',0)\}}{E'^2-E^2}dE' \tag{1.14}$$

With the optical theorem

$$\sigma_{tot}(E) = \frac{4\pi}{k}\mathrm{Im}\{S(E,0)\} \tag{1.15}$$

where for photon scattering σ_{tot} is the total absorption cross section, Eqn. 1.13 becomes

$$\mathrm{Re}\{S(E,0)-S(0,0)\} = \frac{E^2}{\pi hc}P\int_0^\infty \frac{\sigma_{tot}(E')}{E'^2-E^2}dE' \tag{1.16}$$

The scattering amplitude can then be expressed by

$$S(E,\theta) = S(E,0)g(\theta) \tag{1.17}$$

where $g(\theta)$ is the appropriate angular distribution. This becomes quite useful if one assumes that electric dipole scattering is dominant so that $g(\theta) = \hat{\varepsilon}' \bullet \hat{\varepsilon} \;/\; 2$, which becomes $(1 + \cos^2\theta)/2$ for an unpolarized photon beam.

More generally, but non-relativistically, if a multipole decomposition is possible such that

$$S(E,\theta) = \sum_{\lambda,L} S^{\lambda,L}(E,\theta) \tag{1.18}$$

where λ is either E (electric) or M (magnetic) and L is the order of the multipolarity, and if the total cross section for that multipolarity is known, then

1. [Jackson 75], p. 310.

$$S(E, \theta) = \sum_{\lambda, L} S^{\lambda, L}(E, 0) g_{\lambda, L}(\theta) \tag{1.19}$$

and

$$\mathrm{Re}\{S^{\lambda, L}(E, 0) - S^{\lambda, L}(0, 0)\} = \frac{E^2}{\pi hc} P \int_0^{\infty} \frac{\sigma_{tot}^{\lambda, L}(E')}{E'^2 - E^2} dE' \tag{1.20}$$

The usefulness of the Dispersion Relations then hinges on knowing the appropriate total absorption cross section, either from measurements or from models. A problem may exist since few cross sections are known to E'=∞. However the difference in the denominator places emphasis on the cross section in the energy range of E and suppresses contributions far away from E so that the integration can be terminated at a finite limit. Also, Eqn. 1.20 is strictly non-relativistic. The relativistic expression is somewhat more complicated, but the difference is that the integrand consists of higher order terms in E/m due to amplitudes of opposite helicity [L'vov 90].

One last consideration is the effect of the structure of the target with increasing momentum transfer, that is, the form factor. Each multipole has a corresponding form factor so that Eqn. 1.19 becomes

$$S(E, \theta) = \sum_{\lambda, L} S^{\lambda, L}(E, 0) g_{\lambda, L}(\theta) F_{\lambda, L}(q) \tag{1.21}$$

which reduces for the dipole approximation to

$$S(E, \theta) = S(E, 0) \left(\frac{\hat{\varepsilon}' \bullet \hat{\varepsilon}}{2}\right) F(q). \tag{1.22}$$

It is assumed that the form factor is known, and for the dipole case this is true due to extensive measurements by electron scattering [Fregeau 55, Ehrenberg 59, Herman 60,

Frosch 61, Crannell 64, Crannell 66]. The differential cross section for unpolarized photons from Eqn. 1.22 is

$$\frac{d\sigma}{d\Omega}(E, \theta) = \frac{d\sigma}{d\Omega}(E, 0)|F(q)|^2 \frac{(1 + \cos^2\theta)}{2} \tag{1.23}$$

which is the dominant term for photon scattering, where the zero degree cross section is from the amplitude derived from Eqn. 1.20. Again, the θ=0 cross section component is derived from total cross sections (measured or modelled) by the dispersion relations.

Thus, using this scheme, called a Schematic Model, the complexities of the reaction mechanism and particle structure can be completely sidestepped. It has been used extensively for comparison to photon scattering data with the dipole approximation [Fuller 56, Hayward 57, Penfold 59, Williams 61, Leicht 81, Hayward 84] and with higher multipole contributions [Pfeil 74, Dodge 80, Wright 85, Nathan 86,Schelhaas 88, Schelhaas 90].

1.5 Intermediate States

Up to this point, photon scattering has been described in terms of inducing oscillations of a particle or its multipoles, and re-radiation. There can be additional quantum mechanical effects. Particles bound in a potential well are limited to absorbing certain amounts of energies or occupy specific energy levels. There is a lowest possible energy they can have, called the ground state, but the particles can be moved or excited to higher energy levels or resonances. In photon scattering, an incident photon with enough energy may be absorbed, induce a short lived excitation which immediately returns to the ground state, and emits a new photon. This short excitation is called an intermediate state or a resonance. The atomic analog of this mechanism is shown in Figure 1.2. There are many possible excited states and they all can serve as intermediate states for photon scattering. Therefore, the cross section must include a contribution from all of these states. This can become quite complicated.

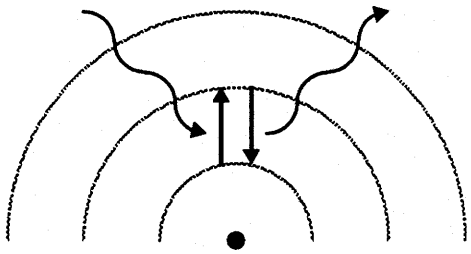

Figure 1.2: Photon Scattering Through Intermediate State

A simple case of this mechanism is resonant scattering through a single intermediate state. In this case, the incident photon energy is at or near the energy of an excitation. Resonance fluorescence through the 15.1 MeV level in carbon is an example of this where the scattering cross sections rise to the resonance by a factor on the order of hundreds [Hayward 57, Kuehne 67, Schelhaas 90].

The above discussion can be expressed in more formal quantum mechanical terms. The presence of the electromagnetic field perturbs the nucleus. Second order perturbation theory considers the perturbed state to be the superposition of unperturbed states. The cross section computation then starts with the following form,

$$\frac{d\sigma}{d\Omega}(\sigma) \propto |S(E,\theta)|^2 \tag{1.24}$$

where the amplitude, S(E,θ), is

$$S(E,\theta) = \langle f| H_{int} |i\rangle + \sum_n \frac{\langle f| H_{int} |n\rangle\langle n| H_{int} |i\rangle}{E_n - E_0} \tag{1.25}$$

where E_0 is the total energy of the initial state. The first term leads to the coherent Thomson cross section for Z particles, Eqn. 1.6, at the E=0 limit. The second term is the sum over all intermediate states, $|n\rangle$. At the E=0 limit, this term added to the first term results in the Thomson cross section, for a particle of charge Z and mass A, Eqn. 1.12. Away from the E=0 limit, complications arise from determining what all the necessary

states are, how to describe them, and the interference terms resulting from squaring the amplitude. However some such calculations do exist for the deuteron [Weyrauch 88, Weyrauch 90a].

1.6 Polarizabilities

The above problem can be reduced to finding the value of polarizabilities and has the advantage of introducing a physical interpretation. The interaction Hamiltonian for a photon scattering from a charged particle is

$$H_{int} = \frac{e^2\vec{A}^2}{2m} - \frac{e\vec{p}\bullet\vec{A}}{m} - \frac{e(\vec{\nabla}\times\vec{A})\bullet\vec{S}}{m} \tag{1.26}$$

where **p** is the particle momentum operator, **A** is the photon field operator, **S** is the particle spin. This is inserted into Eqn. 1.25 and with a low energy expansion the transition amplitude becomes [Petrunkin 64, Baym 69, Ericson 73, Friar 75]

$$S_{fi} = \frac{1}{\sqrt{\omega_f\omega_i}}\{\frac{e^2}{m}\hat{\varepsilon}_f\bullet\hat{\varepsilon}_i + \omega_f\omega_i\varepsilon_{fj}\varepsilon_{ik}\alpha_{jk} + (\hat{k}_f\times\hat{\varepsilon}_f)_j(\hat{k}_i\times\hat{\varepsilon}_i)_k\beta_{jk}\} \tag{1.27}$$

where

$$\alpha_{jk} \equiv \sum_n\left(\frac{\langle f|\,d_j\,|n\rangle\langle n|\,d_k\,|i\rangle + \langle f|\,d_k\,|n\rangle\langle n|\,d_j\,|i\rangle}{E_n - E_i}\right), \tag{1.28}$$

$$\beta_{jk} \equiv \sum_n\left(\frac{\langle f|\,\mu_j\,|n\rangle\langle n|\,\mu_k\,|i\rangle + \langle f|\,\mu_k\,|n\rangle\langle n|\,\mu_j\,|i\rangle}{E_n - E_i}\right), \tag{1.29}$$

$\vec{d} = e\vec{r}/m$ is the electric dipole operator and $\vec{\mu} = e(\vec{L} + g\vec{S})/2m$ is the magnetic dipole operator, and g is the gyromagnetic ratio (2 for Dirac particle, 2.79 for real proton, -1.91 for real neutron). Experimenters can compare to, or fit to their data with, the resulting cross section equation for varied α and β [Williams 61, DeWire 61, Baranov75, Genzel 76], and theorists compute α and β from Eqn. 1.28 and Eqn. 1.29 using their models, e.g. dispersion theoretic calculations [Baldin 60, Petrunkin 64, Gerasimov 65, Guiasu 78, L'vov 90] or "direct" calculations [Weyrauch 90a].

This scheme has primarily been used for nucleons [Baldin 60, Petrunkin 64, DeWire 61, Baranov 75, Genzel 76, Guiasu 78], because the determination of the proton and neutron electric and magnetic polarizabilities is considered to be of fundamental importance. The mechanism is similar to the discussion in Section 1.3. In this case, quarks are the charged point particles which make up the nucleon and which can oscillate and radiate. Since there are oppositely charged quarks in nucleons, a polarization of the nucleon occurs in the field of the incident photon. Hence, the polarizabilities are an indication of the quark structure of nucleons. The measurement of proton polarizabilities in the energy range of 150 MeV to 290 MeV was the goal of the proton part of the experiment described in this thesis and was analysed by E. Hallin [Hallin 93].

1.7 The Delta Resonance

Another consequence of the quark structure of nucleons is the existence of excited states. Thus nucleon intermediate states contribute to the scattering in the same manner as discussed in Section 1.5. Calculations with quark models have been attempted with some promising results [Huber 90, Weyrauch 90b]. These calculations were meant for energies above pion threshold but were not meant for extracting accurate information about the nucleon resonances. Instead, it was shown that assumptions made about quark dynamics had very significant effects and that further measurements of photon scattering data might lead to a better understanding of these resonances through quark models.

The lowest energy nucleon excitation is called Δ resonance. It has mass 1232 MeV, spin 3/2, isospin 3/2, and positive parity. It is sometimes referred to as the (3,3) resonance. Above pion threshold (135-140 MeV), the delta resonance becomes significant by allowing the delta nucleon state as a viable intermediate nuclear state. A Δ can be viewed as a nucleon which had the spin orientation of one of its quarks flipped so that all three quarks have the same spin orientation (Figure 1.3). In general, the Δ can be produced by any $\Delta S=1$ reaction, but the mechanisms may differ. For example, the pion-nucléus coupling to the Δ is dependent on $\hat{s} \bullet \vec{k}$ [Hirata 79] which is longitudinal and the

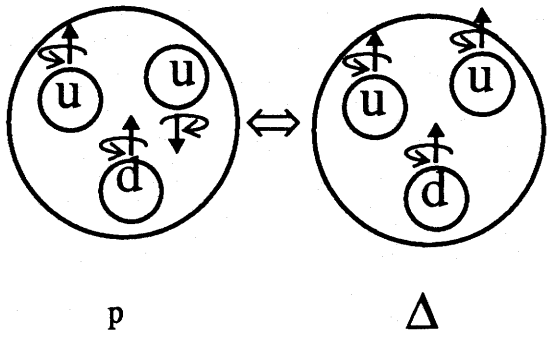

Figure 1.3: Simplistic Representation of Δ State

photon-nucleus coupling is dependent on $\hat{\varepsilon} \bullet (\hat{s} \times \hat{k})$ [Koch 84] which is transverse, where $\hat{s}$ is the nucleon spin, $\hat{k}$ is the photon or pion momentum, and $\hat{\varepsilon}$ is the photon polarization.

In nuclei, this delta is produced in the presence of other nucleons. This leaves a vacancy, or hole, in the state that the converted nucleon had occupied (see Figure 1.4).

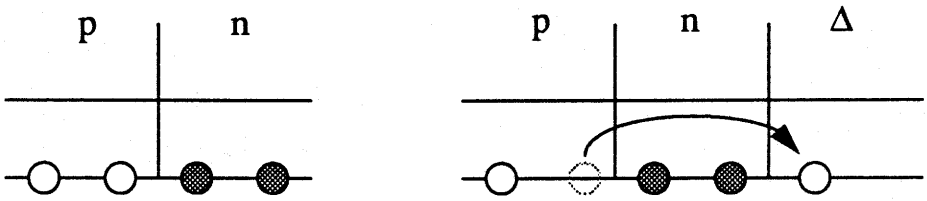

Figure 1.4: Formation of Delta-hole pair

The propagation of this delta and hole pair must be described in the context of nuclear matter.

Attempts to describe the physics of photon scattering above pion threshold use the Δ isobar-hole (Δ-hole) models [Koch 84]. These calculations had their beginnings in attempts to describe pion scattering data [Hirata 79, Kisslinger 76] (Figure 1.5). Then one of the πNΔ vertices was substituted by a γNΔ vertex to describe photopion reactions

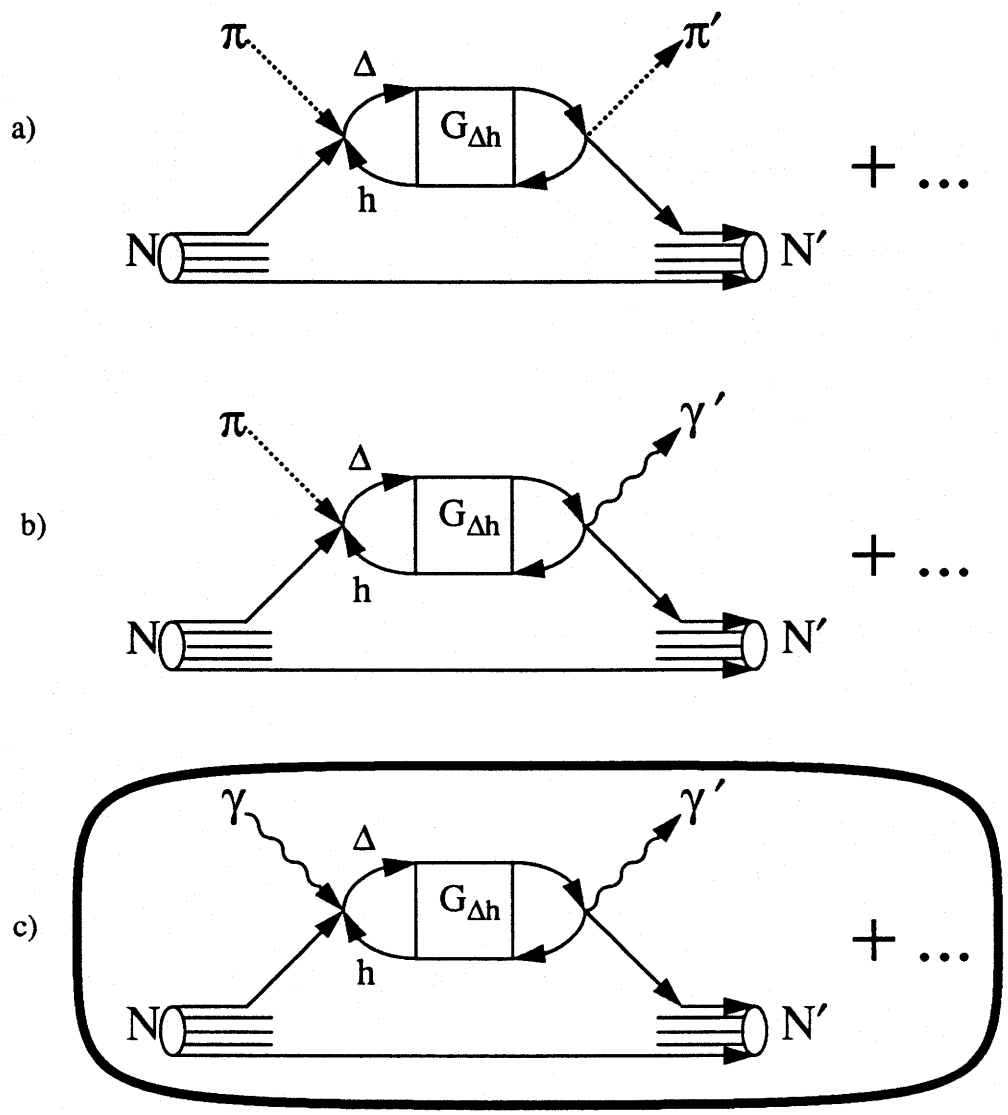

Figure 1.5: Schematic representation of Δ-hole models
a) pion scattering, b) photopion reactions, c) photon scattering

[Woloshyn 78, Oset 81, Saharia 81, Koch 83]. The final step was to make the same substitution on the remaining pion vertex to try to describe photon scattering.

The Δ resonance is the dominant feature between pion threshold and 350 MeV. The Δ resonance is associated with pion reactions which have been used extensively to study this resonance. The attraction of performing photon scattering in this region is that this reaction has the potential to reveal more about the mechanisms involved with the Δ-hole

state than pion scattering can. One reason would be that since the pion interacts strongly with nuclei it is absorbed near the surface, whereas the more weakly interacting photon probes the whole nuclear volume.

From the Δ-hole approach, the value of photon scattering in the region of this resonance can be appreciated by examining the interaction Hamiltonian for the Δ-hole model of Koch et al [Koch 84],

$$H_{\Delta h} = \gamma(E)\, H_{\Delta} + \delta W + W_{\pi} + V_{sp} \qquad (1.30)$$

where H_{Δ} is the one body Δ Hamiltonian, γ(E) is a kinematic factor relating the free Δ propagator to the Δ propagator in the system CM frame[2], δW is a Pauli blocking term, W_{π} is due to a pion propagating in the presence of the nuclear ground state, and V_{sp} is the spreading potential. W_{π} is a background term which can mask the true behavior of the Δ. When the real part of W_{π} is plotted against excitation energy for pion induced reactions and photon induced reactions, shown in Figure 1.6, a suppression of this component is seen with the photon reaction. V_{sp} depends on a parameter that is derived from a fit to pion scattering data. So photon scattering provides a means to suppress non-delta contributions and is a complimentary way of testing the parametrization of the delta resonance.

A measurement of elastic photon scattering from carbon by Hayward and Ziegler [Hayward 84] disagreed with the Δ-hole model of Koch et al [Koch 84]. However, one of the possible reasons for the discrepancy was cited to be the use of detectors with insufficient resolution (10%) for this type of experiment. This conclusion was supported by calculations by Vesper et al [Vesper 85] and Arenhovel et al [Arenhovel 85] who showed that at the measured angles, inelastic scattering dominates over elastic scattering. Thus, detector resolution has, until recently, been a factor that made such photon scattering experiments difficult.

2. That is, given that D(E) is the Breit-Wigner denominator for a free Δ, then for a Δ in the nucleus, the (internal) energy available for Δ excitation $E \rightarrow E - H_{\Delta}$ and $D(E) \rightarrow D(E - H_{\Delta}) \sim D(E) - \gamma(E)H_{\Delta}$

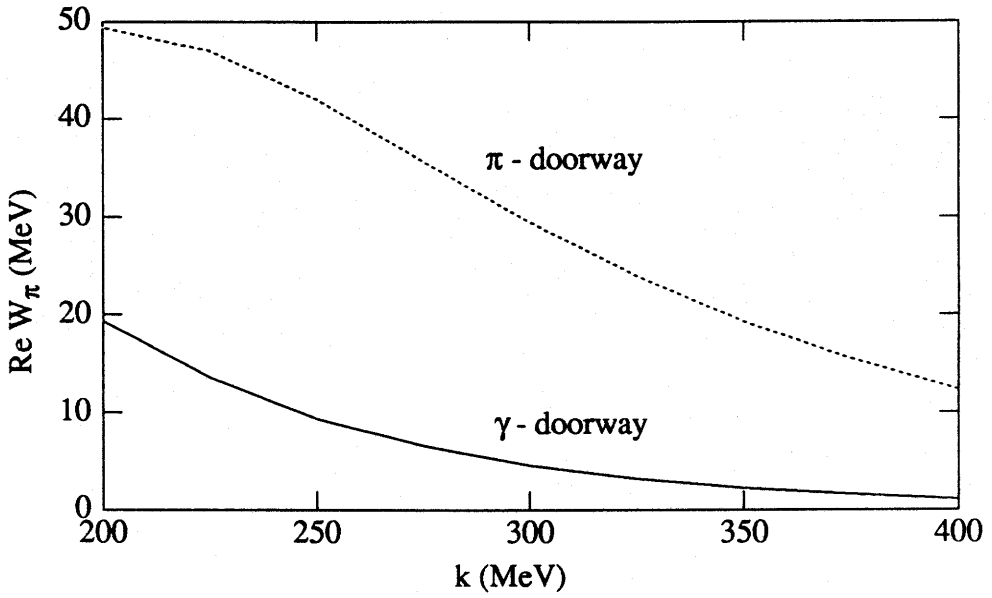

Figure 1.6: Real part of W_π versus excitation energy [Koch 84]

To mitigate the resolution problem, a measurement of coherent photon scattering on helium was performed by Austin et al [Austin 86] at 180 MeV. Helium has a large energy gap between the ground state and its first excited state so that even if the detector resolution was not high, the risk of including inelastic scattering was lower than with carbon. Nonetheless, a substantial deviation from the Δ-hole model was found. The differential cross section was lower than the Δ-hole prediction at forward angles, it had a minimum at middle angles, and at the one point measured at a back angle was much higher than predicted (see Figure 1.7). It could be argued that 180 MeV was so far below the peak of the resonance that the Δ-hole mechanism was not dominant. To make the measurement at the peak of the resonance required the construction of a large, high resolution photon spectrometer [Miller 88]. It was used in a later experiment on helium at 320 MeV by Austin et al [Austin 88a]. That measurement found agreement at forward angles with the Δ-hole model at the resonance energy but the back angle cross sections, where the earlier disagreement was found, were not accessible due to the low cross sections.

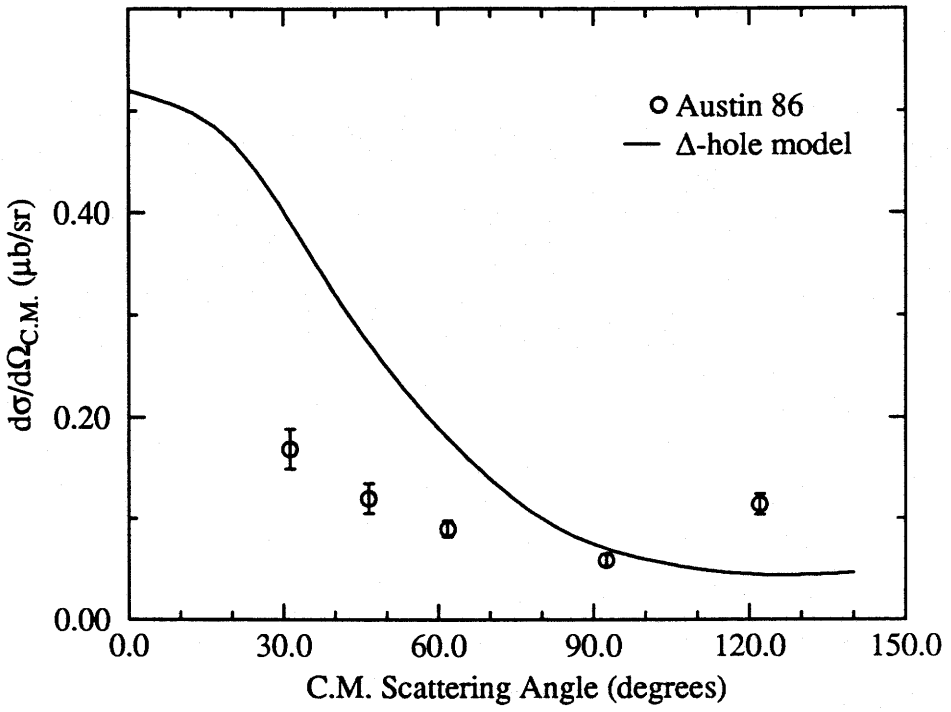

Figure 1.7: Elastic Photon Scattering from Helium at 180 MeV Compared to Δ-hole model of [Koch 84]

This thesis also describes the photon scattering from helium at SAL but the analysis was done by Delli Carpini et al [Delli Carpini 90, Delli Carpini 91]. It fully explored and confirmed the size of back angle cross sections at 187 MeV. At 280 MeV, the differential cross section from this experiment had the same shape as the model, but differed in magnitude (see Figure 1.8).

It has now been generally acknowledged that the current Δ-hole models can only be applied very near the resonance. It is believed that the increase in cross section at back angles away from the resonance for helium is due to the effect of meson exchange currents (MEC) [L'vov 90]. The same consideration was also investigated below pion threshold by scattering from deuterons by [Weyrauch 83] and lead to the conclusion that MEC effects must be significant in the Δ resonance. Furthermore, it was stated that such calculations might benefit from photon scattering cross sections for heavier nuclei.

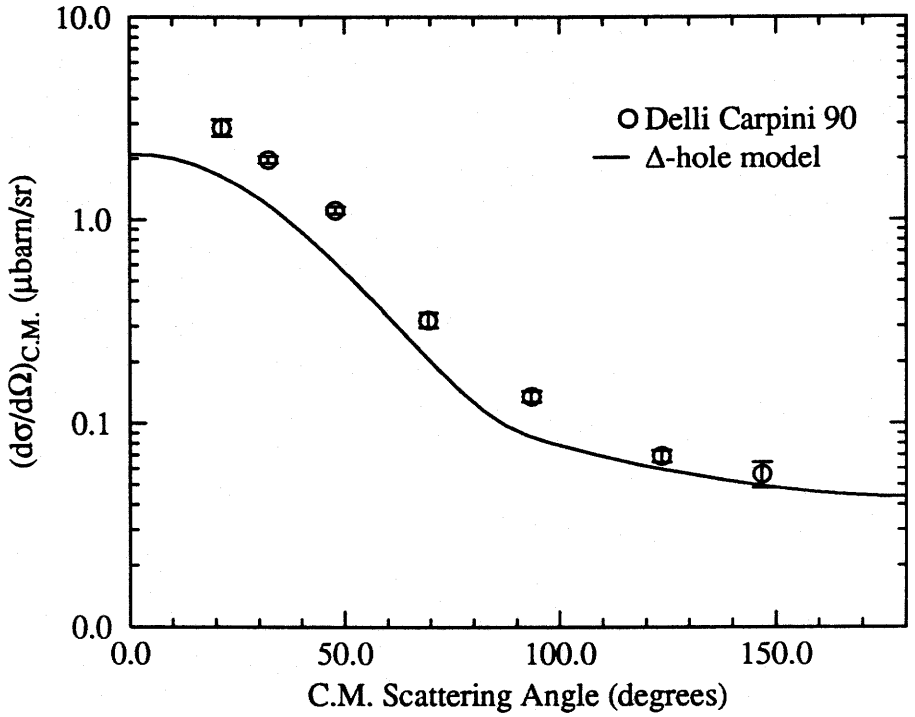

Figure 1.8: Elastic Photon Scattering from Helium at 280 MeV Compared to Δ-hole model of [Koch 84]

Photon scattering from carbon is of interest from historical and theoretical aspects. It would be interesting to see to what extent the results of Hayward and Ziegler [Hayward 84] had suffered from inelastic contributions. With the high resolution detector available, it was thought that the elastic scattering process could be unambiguously separated from the inelastic process. Indeed, if that were possible then the differential cross sections from inelastic cross sections from the low lying states might be measurable. These have not been measured in the energy range of the Δ resonance. Theoretically, it would be interesting to see if the Δ-hole model is more successful with a heavier nucleus. Perhaps, the helium nucleus is not as conducive as heavier nuclei to the assumptions made in the Δ-hole model because it has only 4 nucleons. Also, the helium results show that the greatest sensitivity is at back angles so that angular distributions must be measured. The measurement of photon scattering differential cross sections in the Δ resonance region for carbon is the goal of this thesis.

Chapter 2. GENERAL ARRANGEMENT, EXPERIMENTAL EQUIPMENT AND DATA ACQUISITION

The experiment was performed at the Saskatchewan Accelerator Laboratory (SAL). This facility has a 300 MeV linear accelerator (linac) that injects electrons into a Pulse Stretcher Ring (PSR). The ring provides a high duty factor electron beam which can in turn produce bremsstrahlen for experimental use. The high duty factor makes it possible to accurately measure the low cross sections expected for this experiment.

2.1 Accelerator Facilities

The linac at SAL currently consists of 6 accelerating sections, each capable of boosting the energy of electrons by about 50 MeV (Figure 2.1). Because the energy spread from the linac is too wide for use in the pulse stretcher ring (PSR), an energy compression system was placed at the end of the linac. This system consists of a chicane of 3 dipole magnets and a low power RF accelerating section. The energy spread is easily improved by a factor of 10 [Dallin 90].

The electron pulse is then injected into the pulse stretcher ring where it circulates. The ring is "tuned" in such a way that a small number of these circulating electrons of a given energy exceed the orbital acceptance parameters. These electrons are extracted continuously from the ring, resulting in a high duty factor beam with well defined energy delivered to the experimental areas (EA). The bremsstrahlung facility for this experiment was in EA2 which is at the east end of the building (Figure 2.1).

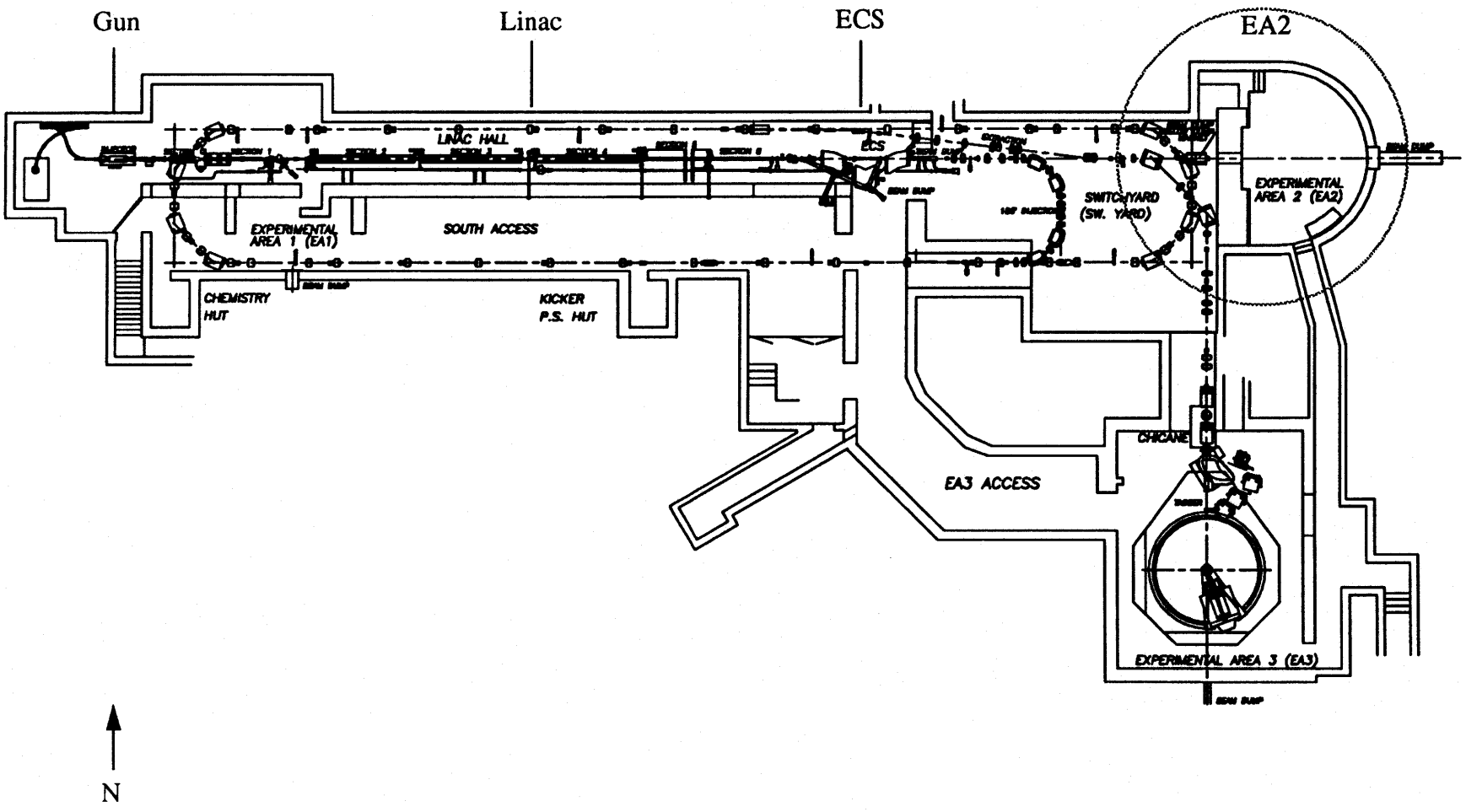

Figure 2.1: Plan View of SAL Facilities

2.2 Experimental Arrangement

The bremsstrahlung facility and the placement of apparatus for this experiment is shown in larger scale in Figure 2.2. The electron beam from the PSR passed through a 0.936 mm thick (1% radiation length) aluminium foil radiator producing bremsstrahlen. A dipole magnet then swept the electrons downwards into a deep pit which contained an electron beam current monitor. The photons were not affected by the magnet and passed through a lead collimator. The collimation process itself produces secondary charged particles which were swept away from the beam axis by a 3.5 kG dipole sweep magnet immediately after the collimator. The resultant photon beam then passed through the target and proceeded to a Wilson type quantameter [Wilson 57] for flux measurement at the end of the photon beam dump channel. Photons scattered by the target were detected in a large sodium iodide (NaI(Tl)) gamma ray spectrometer contained in a shielding house mounted on a steel table.

The spectrometer was sensitive to neutrons, in addition to the photon and electron background associated with electron accelerators. In order to measure the expected low cross sections, the background had to be radically reduced. The neutron background was reduced by shielding. Unused space between the electron dump and the experimental set up was filled with high density concrete blocks, adding 1.5 m to the existing concrete. This was called the Concrete Castle because of the way the sweep magnet seemed to be walled in. The beam entry hole into EA2, in which the collimator resided, was filled in, around the beam, with lead bricks and a stacked iron plate pre-collimator placed on the upstream end of the beam entry hole. This reduced the aperture through which neutrons from the radiator area could pass.

The photon dump was collimated with about 1 meter of concrete rings to allow the photon beam to enter the quantameter sitting at the end of the dump but restrict back-streaming.

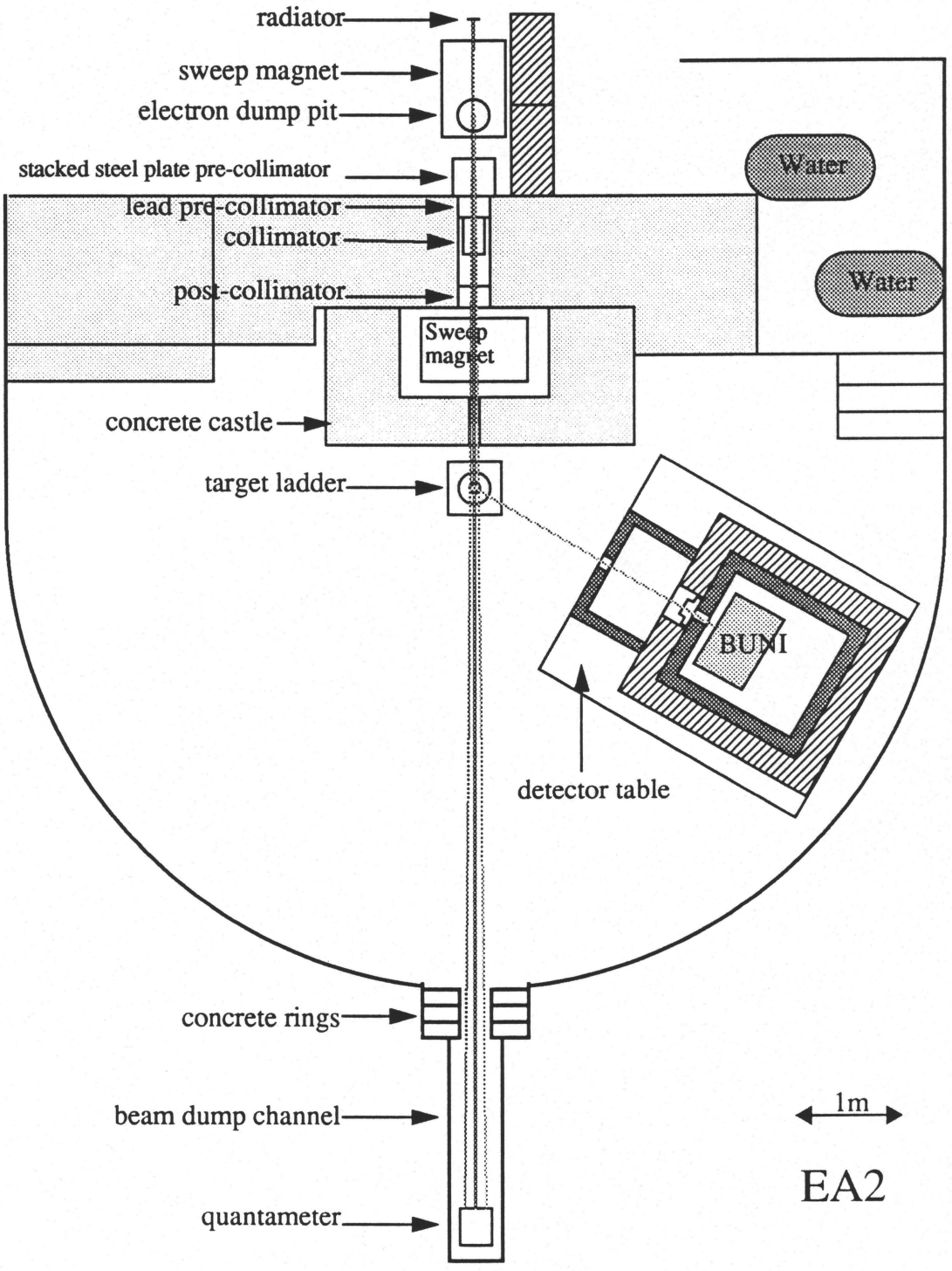

Figure 2.2: Layout of Experimental Apparatus in EA2

Finally the detector was shielded to further reduce neutron background. The shielding consisted of 17.8 cm of lead and steel plates, each plate 2.54 cm thick, surrounded by 35.6 cm of borated wax on the sides and underside of the table surface and 35.6 cm of borated water in a tank on top (see Figure 2.3). The front face of the house had a 15 cm diameter aperture cut out to allow the scattered photons to enter the spectrometer. This aperture had a 12.70 cm inside diameter tungsten insert to define the detector solid angle. A cylindrical lead snout was placed on the front face of the house as a pre-collimator. A beryllium cylinder was inserted into the aperture snout to absorb low energy photons to reduce some of the background (see Section 2.8.1). A lead shielding hut in front of the aperture protected aperture scintillation counters, discussed later, and acted as a pre-collimator.

Due to the restricted size of EA2, an angle change not only involved revolving the detector about the target, but also shifting the target stand along the beam line. The table, which weighed 20 tonnes with the shielding, floated on 4 air pads for angle changes. The whole maneuver was done by muscle power, with some people pushing and others pulling by block-and-tackle and required a coordinated effort. This process was aggravated by the inertia of the 20 tonnes of shielding and detector lifted by those air pads.

The spectrometer angle was measured by a laser goniometer built into the lower section of the target stand. Independent screw jacks at the corners of the table were used to bring the detector up to beam height and level the table.

Some of the electronics for data acquisition were situated on the spectrometer table but most was in the counting room upstairs 100 meters away. All computers were also located in the counting room.

2.3 Beam Flux Monitor

With the high photon flux used in this type of experiment, it was impossible to count individual incident photons. Instead, an ionization shower chamber that measured the total energy content of the beam was used. The device used for this experiment was the

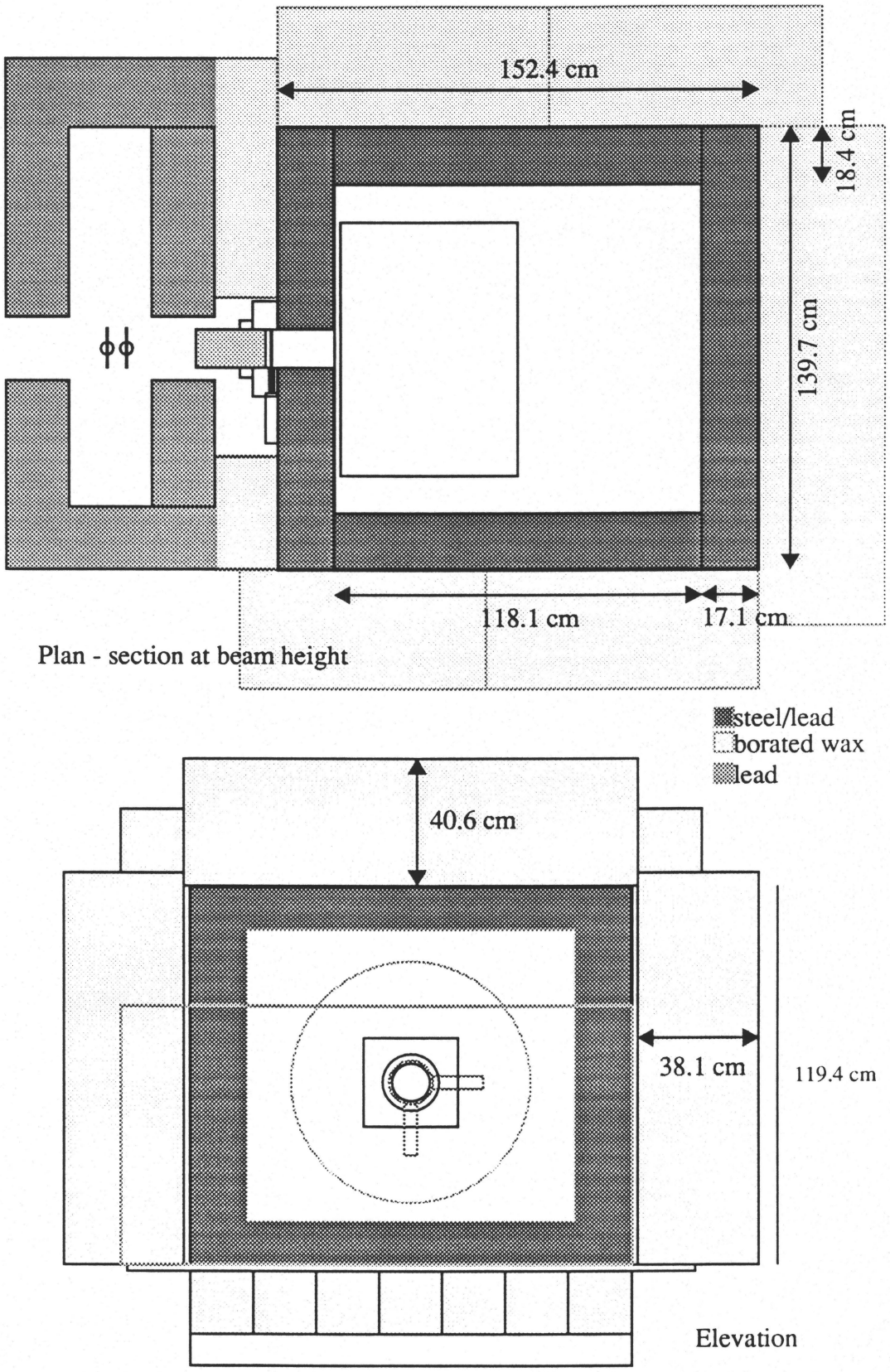

Figure 2.3: Spectrometer shielding

QB1 quantameter, shown schematically in Figure 2.4, whose design was based on the Wilson type quantameter [Wilson 57]. It consisted of thick parallel plates with dual roles of inducing a shower and, in alternating series, of collecting charge or applying high voltage bias. The chamber gas was a 95% argon, 5% CO_2 mixture. The bias used was -450 V. The advantage of this device over other types of ionization chamber was that the calibration constant that relates charge collected to the energy deposition was independent of the photon energy.

The quantameter integrates the energy content of the whole spectrum, U, and produces charge, Q, by

$$U = \int_0^\infty N_{\gamma t} A(E)\, n(E)\, E dE = U_q Q \tag{2.1}$$

where U_q is the quantameter calibration constant, n(E) is the photon spectrum shape, A(E) is the transmission spectrum for material in the beam (e.g. target and air), and $N_{\gamma t}$ is the photon flux. It follows that the fraction of energy deposited between E_1 and E_2 scales by $\int_{E_1}^{E_2} A(E)\, n(E)\, dE$. So, if the shape of the photon spectrum is known and the calibration has been measured, one can obtain the photon flux between E_1 and E_2 by

$$N_\gamma = U_q Q \frac{\int_{E_1}^{E_2} A(E)\, n(E)\, dE}{\int_0^{E_0} A(E)\, n(E)\, E dE}. \tag{2.2}$$

where E_0 is the maximum photon energy of the incident spectra, the endpoint energy for bremsstrahlung. The linearity of response of the quantameter with energy was examined and verified with Monte Carlo simulations.[1]

1. E. Hallin, private communication

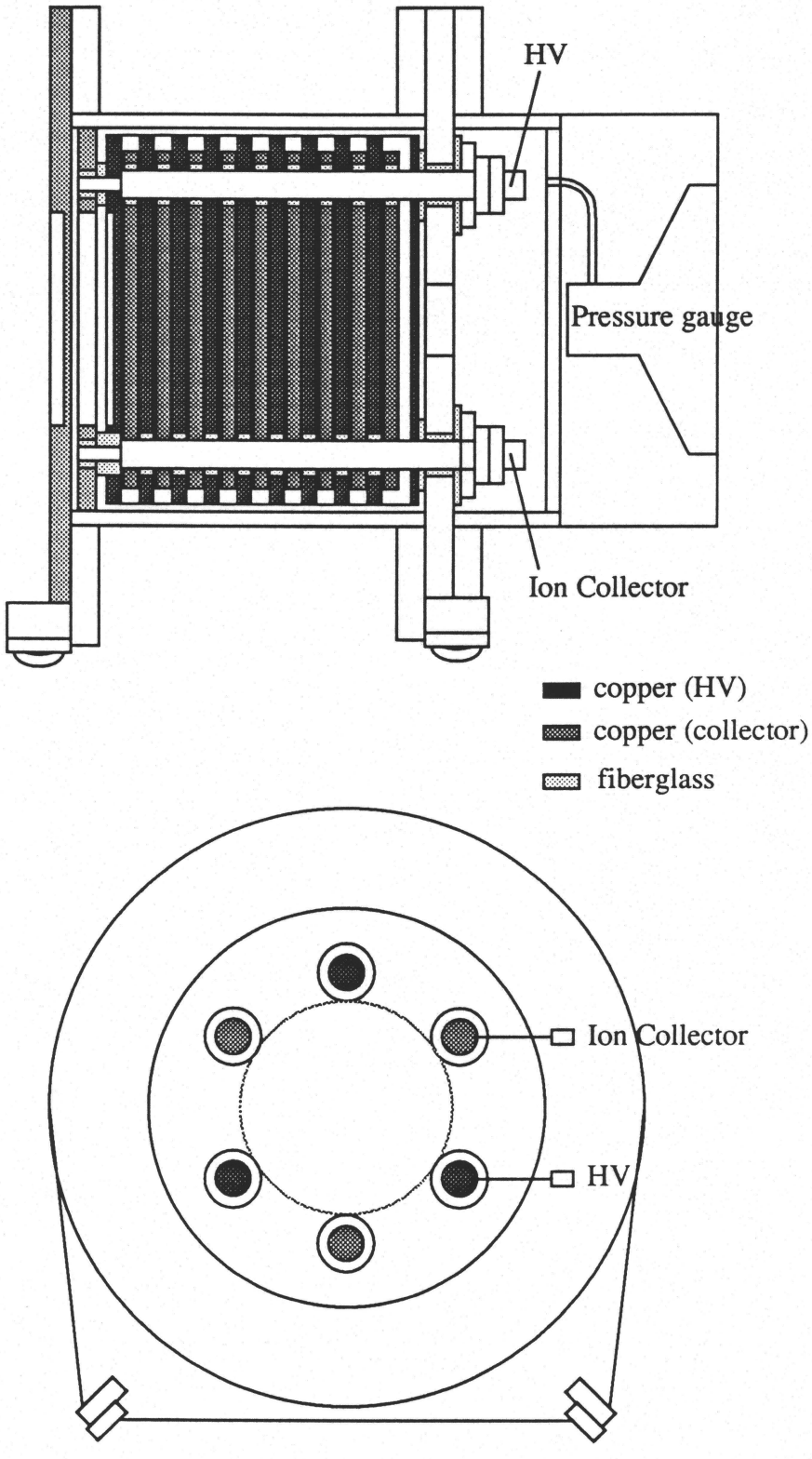

Figure 2.4: QB1 Version of the Wilson Type Quantameter

2.4 Targets

Three nuclei were studied in this experiment, ^{12}C, ^{4}He, and ^{1}H. There were two carbon targets made of graphite and mounted on circular protractors. One was 15.01±0.05 cm wide, 11.50±0.05 cm high, and 1.01±0.05 cm thick, and weighed 276.40±0.05 g yielding a target thickness of 1.60±0.01 g/cm^2. The other was 15.14±0.05 cm wide, 11.92±0.05 cm high, and 2.55±0.05, and weighed 717.5±0.1 g yielding a target thickness of 3.98±0.03 g/cm^2. The choice of target thickness depended on background rates. For scattering angles forward of 60 degrees, it was found that the background rate was high enough to require low beam flux and thinner targets. Beyond 90 degrees, there was little or no background so the thicker target was used to compensate for the lower cross sections. The protractor provided stability and adequate angular positioning of the target with respect to the beam. The target was turned so that the normal to its face subtended half the angle that the detector subtended (see Figure 2.5).

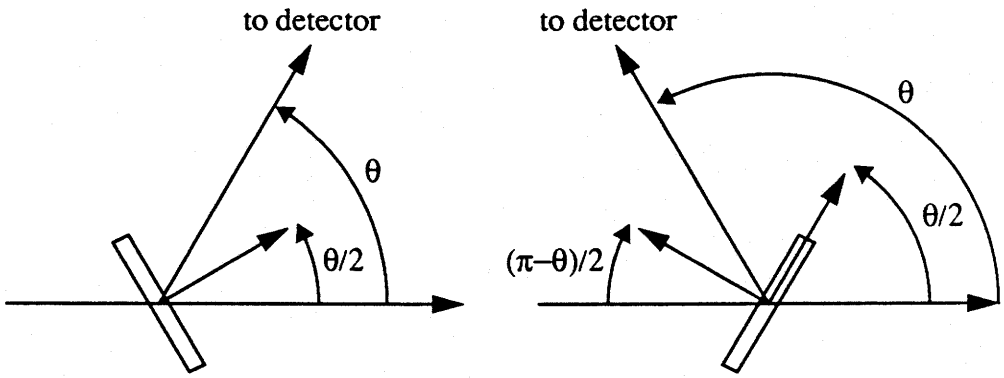

a) forward angle scattering b) back angle scattering

Figure 2.5: Alignment of Carbon Target with Respect to Beam

Both the ^{4}He and ^{1}H targets were liquid. The ^{4}He target was a passive cryostat (Figure 2.6), brought to SAL by the University of Illinois, Urbana-Champaign collaborators[2], which was merely filled with purchased liquid helium (LHe) in bulk. Such a target must be designed for a maximum storage time, like a dewar, but still have as little structural material as possible for a photon beam to pass through. It consisted of a 1 litre target cell attached to an 8 litre reservoir, both kept in vacuum. The cell was a cylinder with rounded ends, 10.2 cm in diameter and 12.7 cm long, loosely wrapped with 5 layers of 12.7 μm thick mylar with a 200 Å thick aluminum coat. The LHe reservoir was surrounded by an LN_2 jacket. A 1.6 mm thick heat shield extended from the LN_2 jacket around the mylar target cell. The thickness of the LHe cell was 0.158 ± 0.002 g/cm^2. Further details of this target can be found in the thesis of Wells [Wells 90].

Since in the above arrangement the target cell must always remain full, an evacuated mock up of the target portion was used for target empty background measurements. This, of course, required that the cryostat and its mock up be physically moved into the beam line for target in and target empty measurements.

Since the angle changes were so time consuming, difficult, and risky, the carbon measurement was alternated with a helium measurement made for another thesis [Delli Carpini 90]. A target ladder was constructed that carried the liquid helium cryostat, the cryostat mock-up, the carbon target, and a space (for carbon target out) (Figure 2.7). The carbon target was held inside a cylinder with slots cut out for the beam to pass through. The cylinder was taller than the carbon target by 10 cm for the space for carbon target-out measurements. The cryostat mock-up was clamped on top of this cylinder. The cryostat was clamped on top of the mock-up. This stack was mounted on a hand powered cross drive for left-right alignment adjustment. All of this was mounted on a platform that was lifted by a screw jack. The jack was powered by a heavy duty servo. This ladder was

2. M. Lucas, A. Nathan, D. Wells.

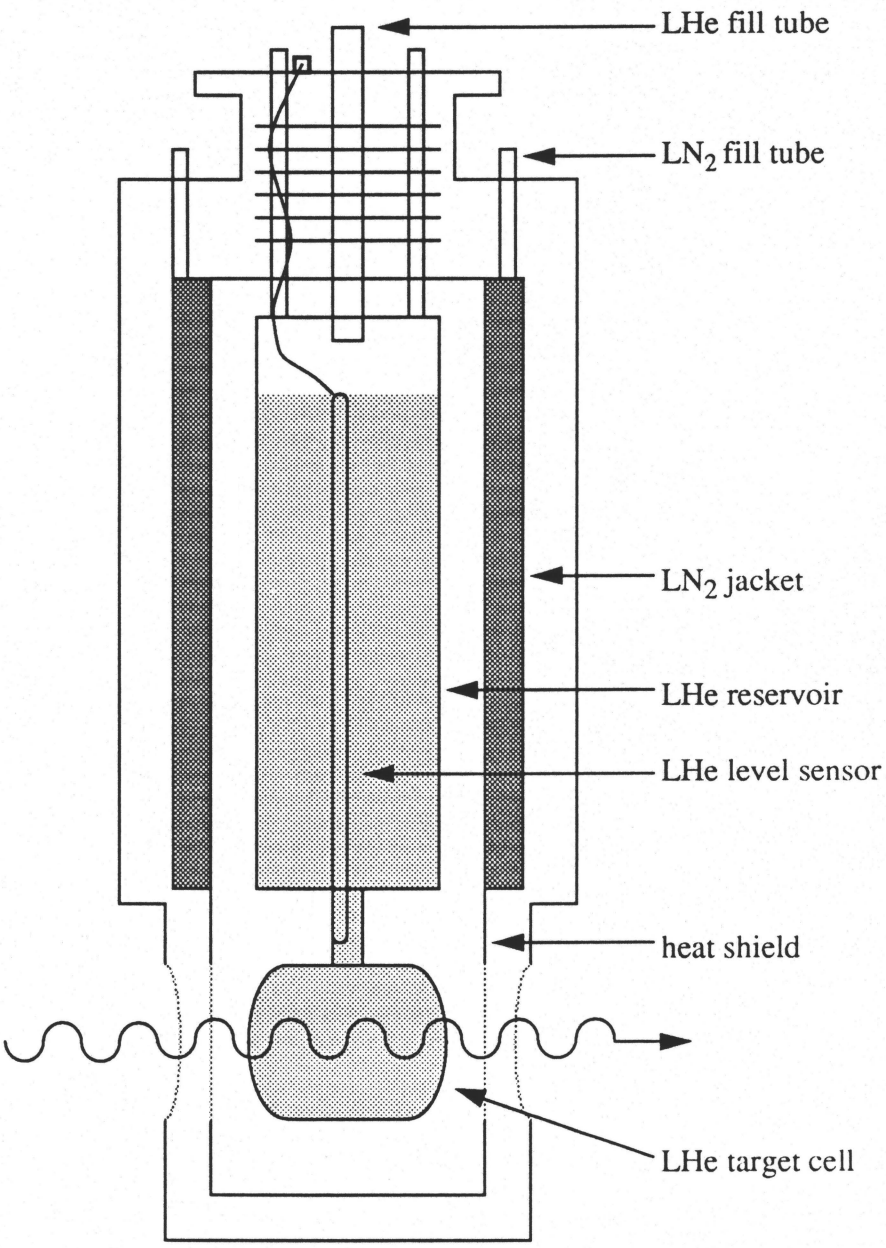

Figure 2.6: Liquid Helium Cryostat

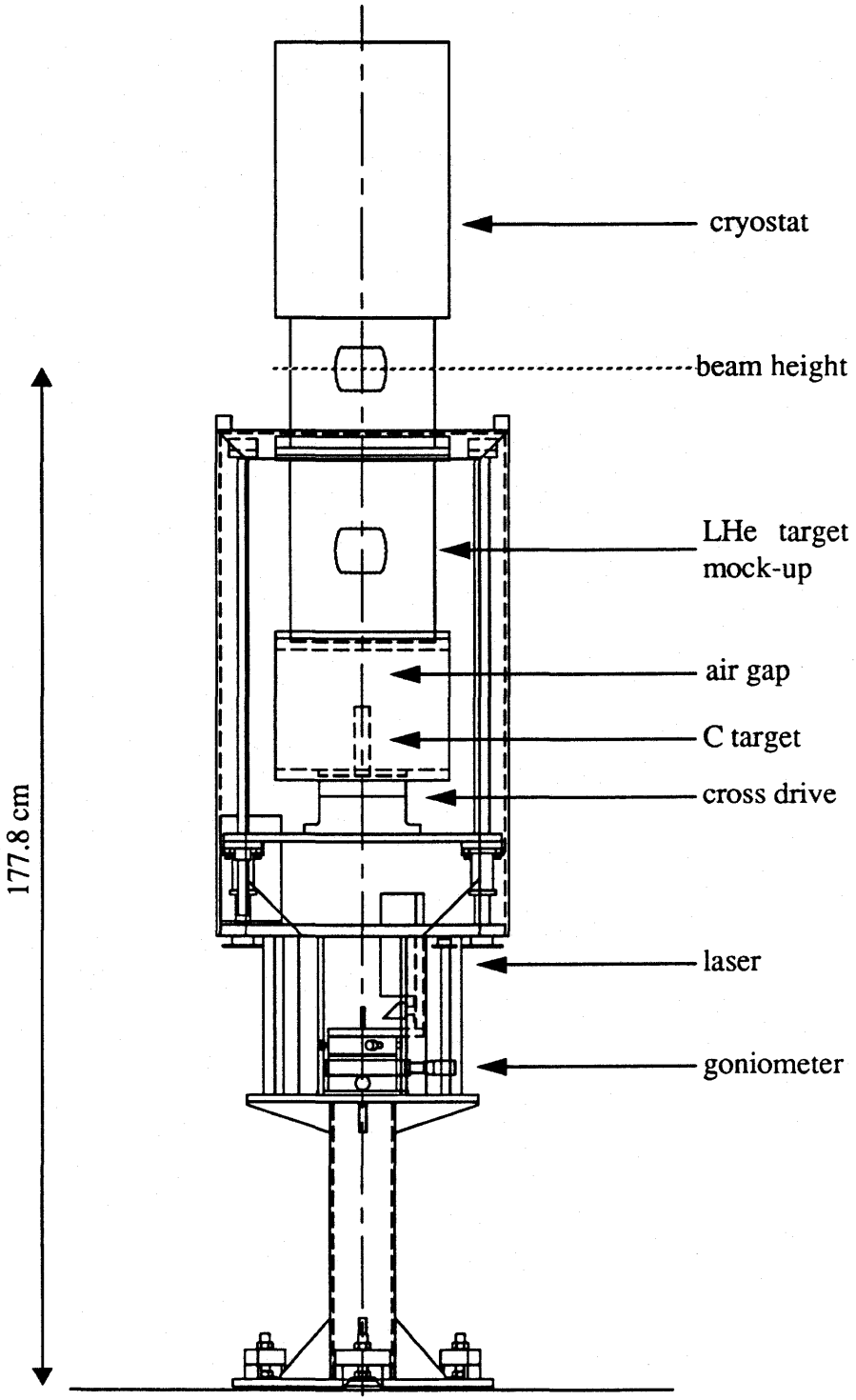

Figure 2.7: Target Ladder for ^{12}C and ^{4}He targets

remotely controlled. There was a scale on one of the support struts with target position indicators marked on it. A pointer attached to the platform indicated the target position on this scale. A video camera, also attached to the platform, viewed the pointer and scale so that the experimenters could determine the target position.

The ^{1}H target, also brought to SAL by the U. of Illinois group, utilized an active cryo-cooling system (shown schematically in Figure 2.8). The power required to lower hydrogen to its 20 K liquefaction point is about 600 times less than that for helium, and was well within the capabilities of an available cryocooling system. The target cell was a cylinder with rounded ends, 12.7 cm long and 10.2 cm in diameter and was made of 0.25 mm mylar. For insulation, the cell was wrapped with 10 layers of thick aluminized (200 Å thick) mylar and surrounded by vacuum. The target was filled by cooling hydrogen gas in the reservoir until it liquefied. The condensate then flowed through a thin tube to the target cell, gradually cooling those components by evaporation. The vapor returned to the reservoir for condensation via a vent tube from the target cell. Eventually, the fill tube and target cell were cool enough to hold liquid. In this case, it was practical to empty and fill the target cell repeatedly rather than to move the target out and insert a dummy into the beam. To empty the target, the vent tube was closed and power applied to a small resistor to heat the cell. The resulting boil-off pressurized the cell, and forced liquid up the fill tube to the reservoir. Since the cryocooler was an elaborate system, measurements on ^{1}H were done with that target alone. Further details of this target system can be found in [Amendt 91].

2.5 Spectrometer

Scattered photons were detected in the **B**oston **U**niversity Sodium Iodide (**NaI**(Tl)) (BUNI) gamma ray spectrometer. What was impressive with this detector was the size of its crystals and its characteristics. At high energies, electromagnetic showers spread over more than 10 radiation lengths in diameter. For NaI, one radiation length = 2.5 cm, therefore these detectors tend to be large, as shown in Figure 2.9. The only way to

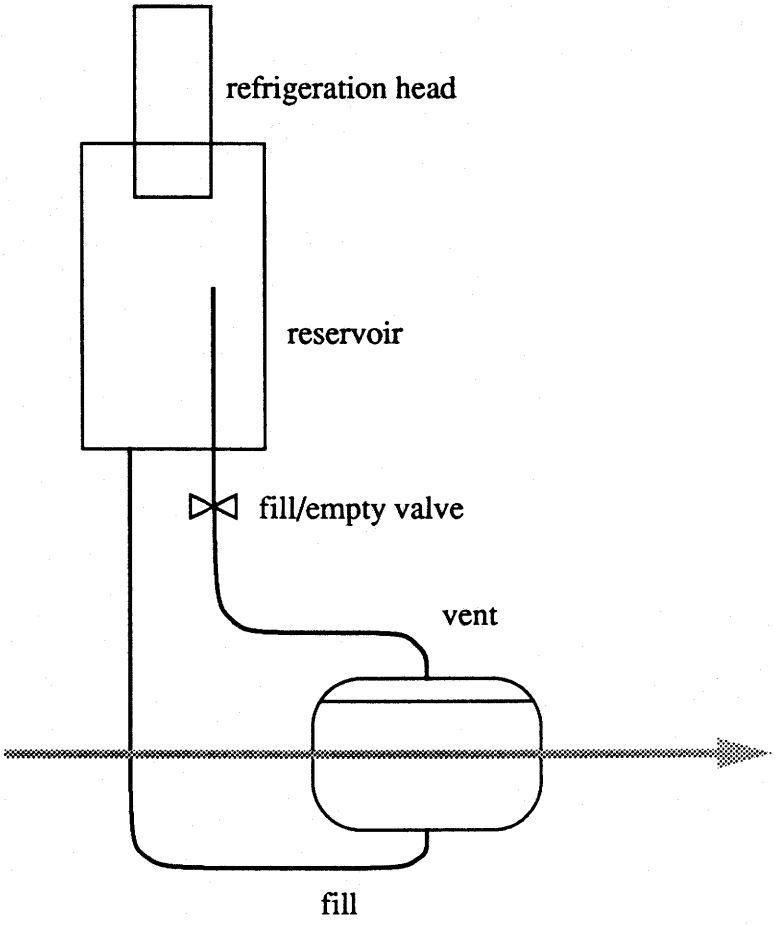

Figure 2.8: Schematic Diagram of Liquid Hydrogen Cryocooler System [Amendt 91]

completely contain a shower would be to use an infinitely large crystal, otherwise with a finite sized detector there is a finite probability that one or more interactions within the shower produces a photon that escapes from the detector volume, irretrievably carrying away energy. This shower leakage is the dominant mechanism in defining the probability distribution of deposited energy, or response function, and ultimately the resolution of the spectrometer. Ultimately, the design of an NaI detector is a compromise between crystal growing capabilities, cost, and resolution.

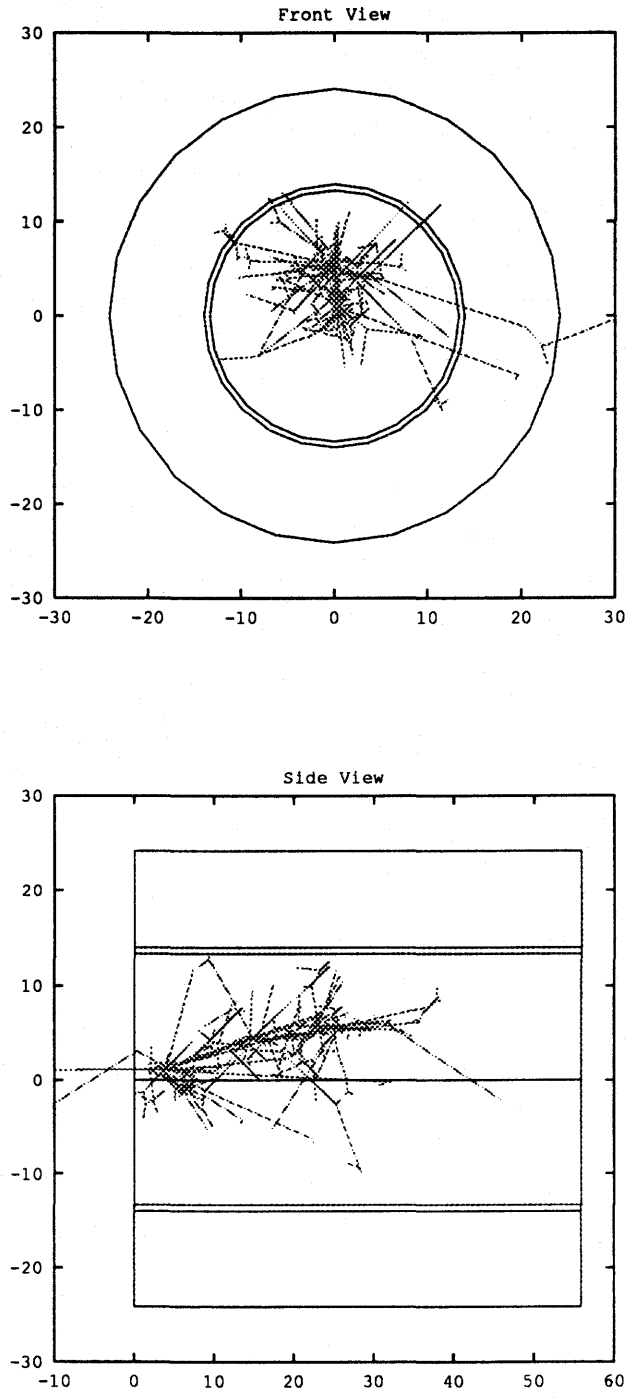

Figure 2.9: Simulation of Electromagnetic Shower in a Large NaI. Axes in cm.

At the time of BUNI's construction, the largest crystals that could be grown were 30 cm thick. To increase the detector volume, BUNI consisted of a cylindrical core and 4 annular segments, all optically isolated, to form a cylinder totalling 53.3 cm in diameter and 55.8 cm in length [Miller 88] (see Figure 2.10). NaI detectors produce photon energy information by inducing an electromagnetic shower with a fraction of the ionization energy of that shower being converted to visible light. This light is in turn converted to electrical signals by photomultiplier tubes (PMT). Seven PMTs were coupled to the core, 12 to the quadrants (three each). For cosmic ray background suppression, the NaI is surrounded by a plastic annulus which has 12 PMTs. Each PMT had a signal and high voltage cable running from it (see Figure 2.11). This instrument had been used to make similar measurements on helium at the MIT-Bates Accelerator Lab [Austin 88], so its characteristics were well understood and most of the required structural and electronic support for the present experiment accompanied it to SAL.

Energy resolution is extremely important for this experiment because of the narrow energy regions that must be measured. This is ultimately the reason for the size of the spectrometer. BUNI had a measured resolution of 1.3% at 130 MeV [3]and estimated resolution of 1.8% at 300 MeV. This is considered to be an excellent resolution for a high efficiency photon spectrometer in this range.

The excellent quality of BUNI would be advantageous only if the calibration of the detector were fixed. However, PMT gain changes are inevitable in this type of detector and it was not uncommon to see a 10% shift from the beginning of a series of measurements to the end. To be able to compensate for this later, a system for monitoring the gain was implemented (Figure 2.12). A Xenon flasher sent a pulse of light to the NaI segments via fibre optics (3 to the core, 2 to each quadrant). If the flasher was stable, tracking the flasher pulse height in the energy spectra would suffice. In reality, the flasher also was

3. E.C. Booth, Private communication.

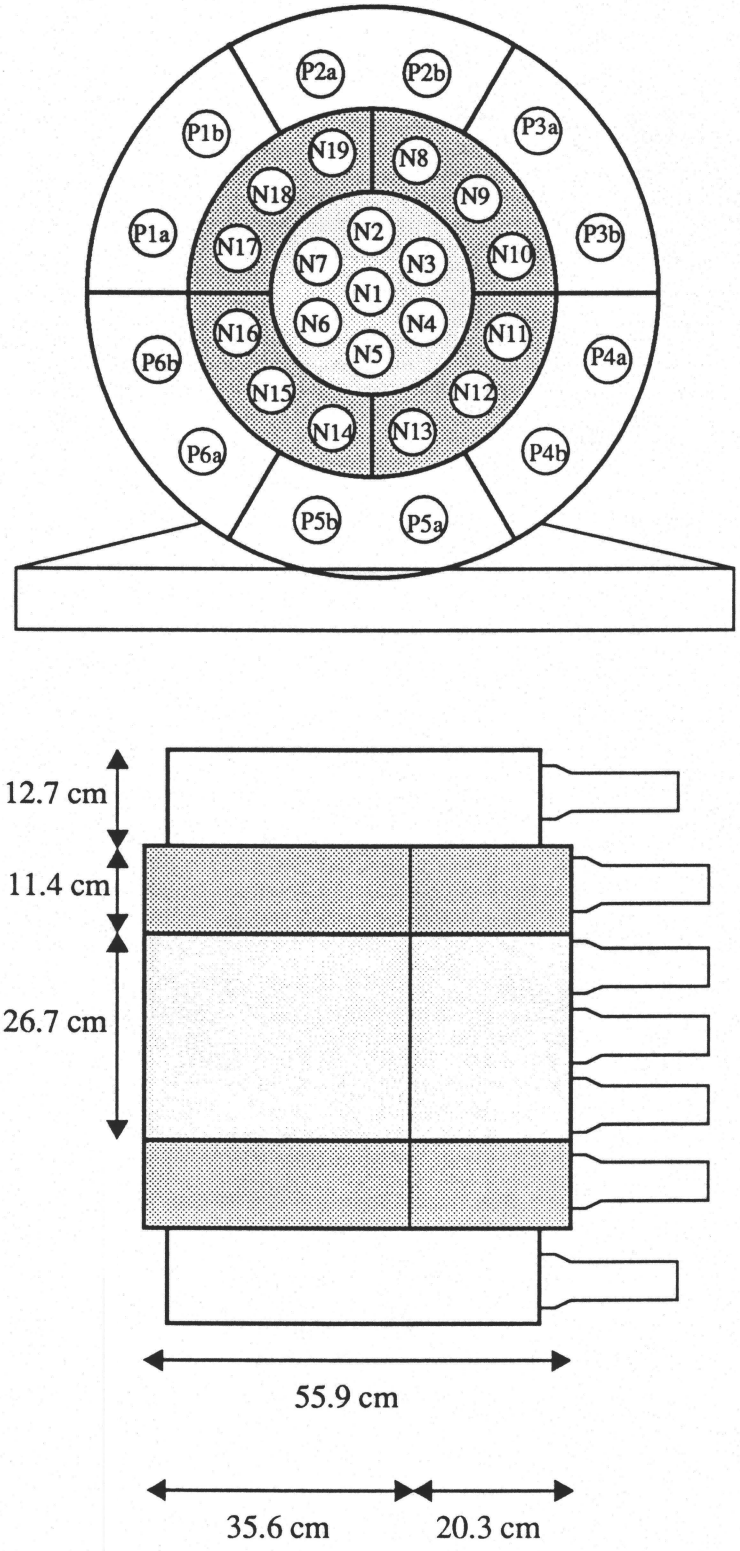

Figure 2.10: BUNI

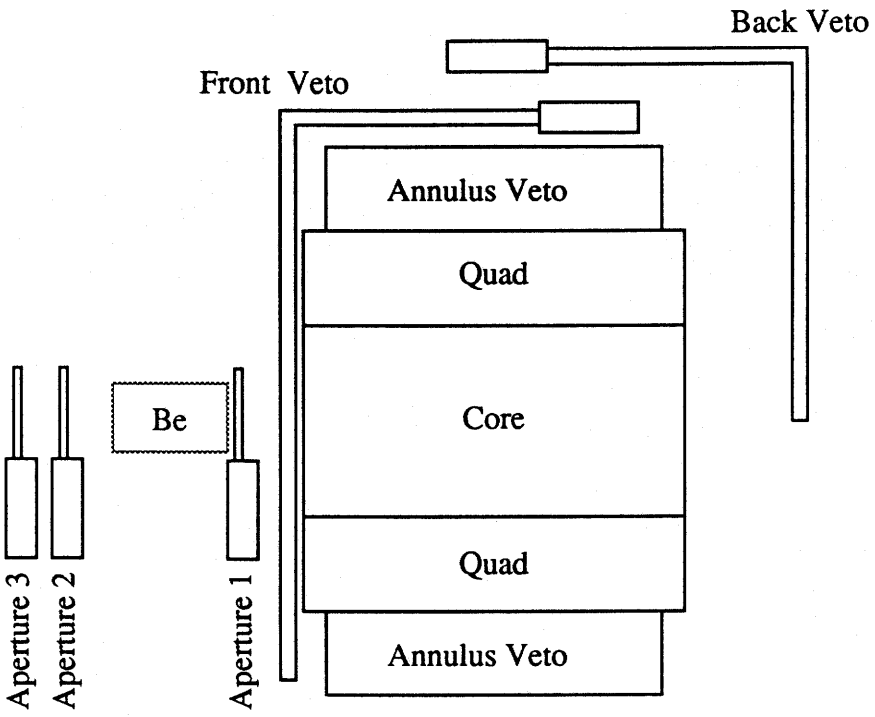

Figure 2.11: Placement of Plastic Scintillator Veto Detectors

not stable and sometimes experienced long term 10% shifts. Therefore another fibre optic cable also sent flashes to a small 2 inch NaI detector to which a weak Th-C source was also attached. By comparing the flasher pulse height in the 2 inch NaI spectra to the reference source peak position, the flasher signal could be normalized. By tracking the 2 inch NaI normalized flasher signal, the base gains from calibration runs could be compensated on a run by run basis.

Because the NaI scintillator was so thick, the energies deposited by cosmic rays extended over the range of interest for the experiment, at a rate similar to the anticipated scattered photon event rate. The annulus of 12cm thick plastic scintillator surrounded the

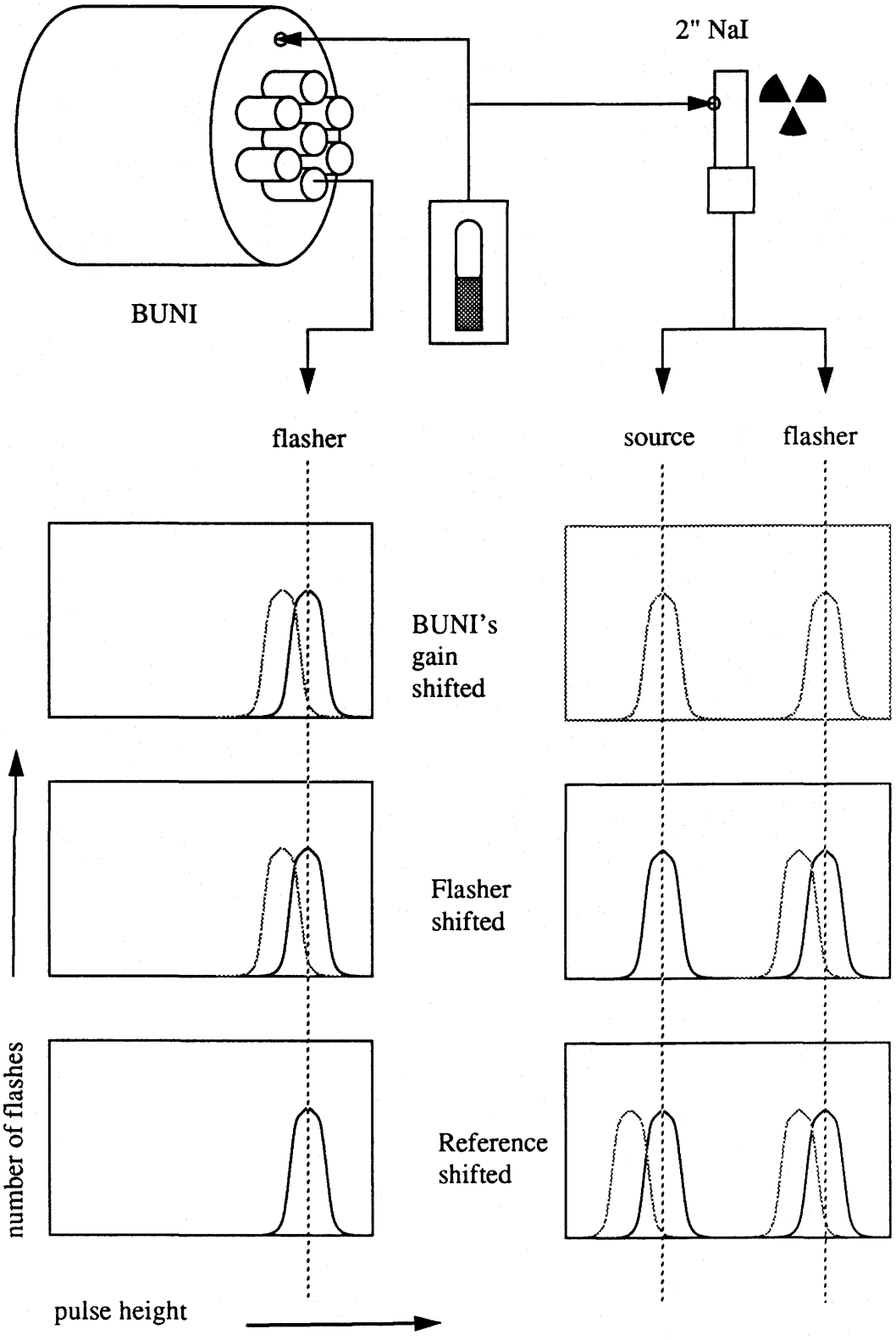

Figure 2.12: Flasher Gain Monitoring System

NaI to serve as a cosmic ray veto. The vetoes were thick enough to discriminate between the low energy shower leakage from the NaI and the high energy deposited in the plastic by cosmic rays.

The annulus cosmic vetoes could not cover the front and back of the detector. Three 2.54 cm thick plastic scintillator paddle counters were used for the front. The multitude of cables made complete coverage of the rear impossible, but three short plastic counters covered it partially (see Figure 2.11), leaving only a very small contribution from cosmic rays that enter from the lower rear and stop in the detector.

The beryllium hardener placed in the aperture to reduce low energy background sometimes produced a shower whenever a high energy photon was absorbed. Such events were deemed unreliable so a thin plastic scintillator veto (Aperture 1 in Figure 2.11) was placed in the aperture snout after the hardener. A coincidence between it and the Front Mid cosmic veto paddle rejected such converted photons.

Electrons produced anywhere between the target and the detector were of particular concern at forward angles. To distinguish such events from photon events, 2 thin plastic paddle counters were placed in front of the hardener, inside the front shielding hut (see Figure 2.11 and Figure 2.3). A coincidence of events in this pair constituted a charged particle event and these were rejected in software.

2.6 Signal Processing and Data Acquisition

Signal processing and data acquisition may be divided into 4 components: transmission and processing of linear signals, generation of triggers, conversion of data, and display of data. Events, such as detected photons, generated electrical pulses. This information was typically split, with one branch sent to logic electronics to generate triggers. These triggers were used to signal acquisition electronics to read out the signals from the second branch of the split. The electronics converted the pulse information into digital information that could be read, analyzed and stored on tape by a computer. Data acqui-

sition was controlled and data analyzed and displayed by the LUCID Data Acquisition and Analysis System [Lucid 91] designed at SAL for general nuclear physics data acquisition.

2.6.1 Electronics

In the first sections, the processing and transmission of linear signals from scintillators are discussed. Although the generation of logical trigger signals will be mentioned, these are treated more systematically later.

2.6.1.a Core Signal Processing and Conversion

The pulses from all the core NaI photomultiplier tubes (PMT) were immediately passively split (see Figure 2.13). One set of signals went upstairs to the counting room where the bulk of the acquisition hardware resided. The second set was summed and fanned out before also being sent upstairs.

The first set of signals were delayed by 330 ns to match the delay for generating triggers. The linear signals were clipped because the raw NaI detector signals were over 1 microsecond long. By reducing the length of the pulses, the acquisition gate could be made shorter and thus the rate of accidental coincidence with background, or **pileup**, could be reduced. The clipping circuit contained a passive split with one arm delayed and terminated with low impedance (see Figure 2.14). This reflected a smaller, inverted, and delayed signal back onto the main signal on the other arm, cancelling the long tail of the raw signal as it exited the clipping circuit (see Figure 2.15). The clipped signals were then converted by a LeCroy 2249W charge integrating Analog-to-Digital Converter (ADC) module.

The summed core signals shown on the lower part of Figure 2.13 were used for sum ADCs, a Waveform Digitizer (WFD), and trigger generation.

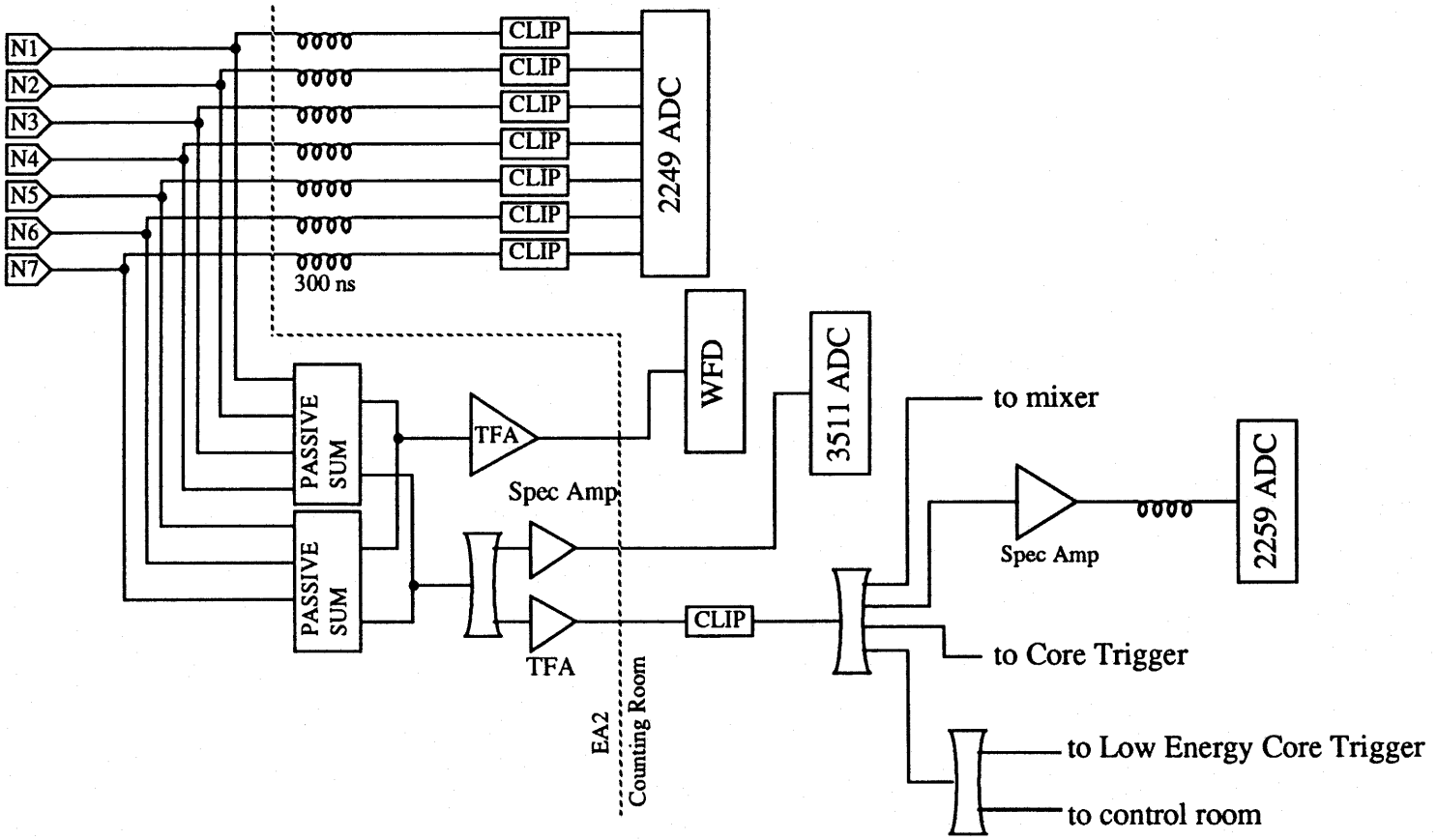

Figure 2.13: Core electronics

Two core sum signals were shaped in spectroscopy amplifiers and went to a LeCroy 2259B Peak Sensing ADC and a LeCroy 3511 Spectroscopy ADC. These ADCs were used for monitoring the core energy spectrum on-line but were mostly ignored during later analysis which relied on the individual ADC's.

The last summed core signal was amplified in a Timing Filter Amplifier (TFA) and digitized using a LeCroy 2256A Waveform Digitizer module set with 50 ns windows and 8 bit conversion. The information from this module would subsequently be used to identify pileup events from the pulse shape. Piled up events have deviations ("bumps") when compared to the standard shape obtained at low rates.

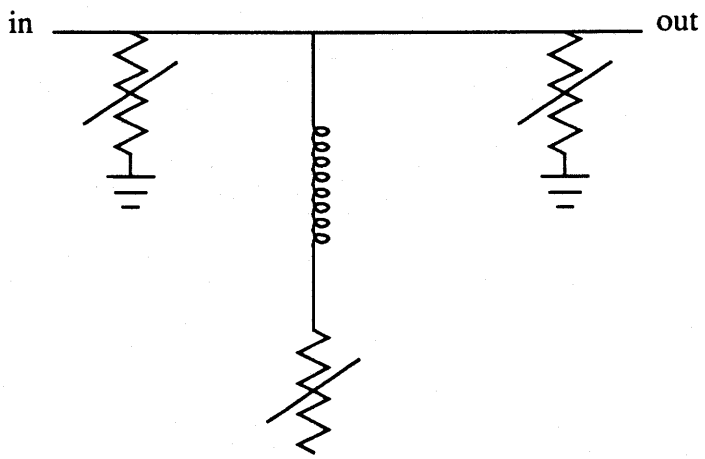

Figure 2.14: Clipping Circuit

The core signal destined for the triggers was amplified by a T FA[4], clipped and fanned out. One copy of this signal went to the High Energy Core Trigger logic and another to the Low Energy Core Trigger logic and to the accelerator control room so that the machine operators could monitor beam fluxes according to our requirements.

4. The TFA was used strictly in an amplifying but non-shaping mode. Though this was not its primary design application, this was a secondary capability, and a shortage of electronics necessitated its use.

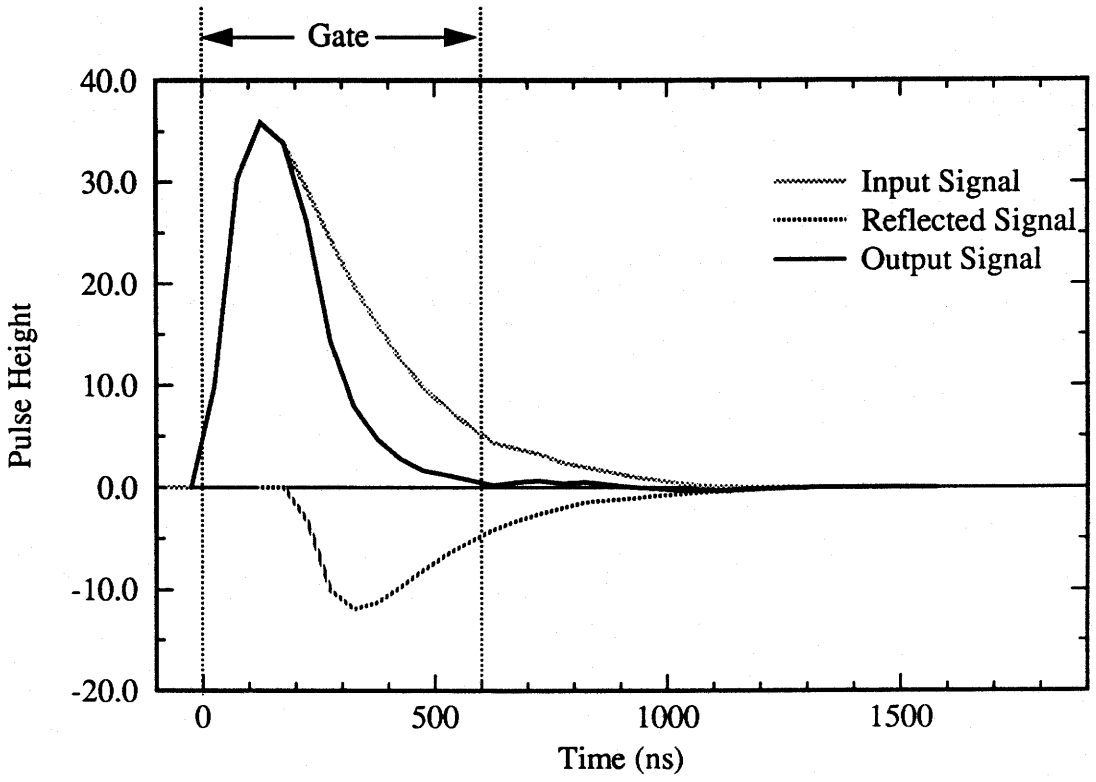

Figure 2.15: Pulse clipping

2.6.1.b Quadrant Signal Processing and Conversion

Each quadrant was viewed by three phototubes. The signal from each of the tubes was also split but both arms were immediately amplified (see Figure 2.16). One set was sent upstairs for conversion. The other set was summed first and then sent upstairs.

The first set of signals were delayed by 330 ns. Most events deposited less than 10 MeV of the shower in the quadrants, but there were a significant number of events that deposited up to 30 MeV. To accurately accommodate this large range of energy deposition, the linear signals were passively split again and sent to two different types of circuits. One of these sets were passed through a clipping circuit and converted by a 2249W ADC. This comprised the low energy quadrant signal. The other set of signals was attenuated and converted by a 2249W ADC for high energy quadrant data.

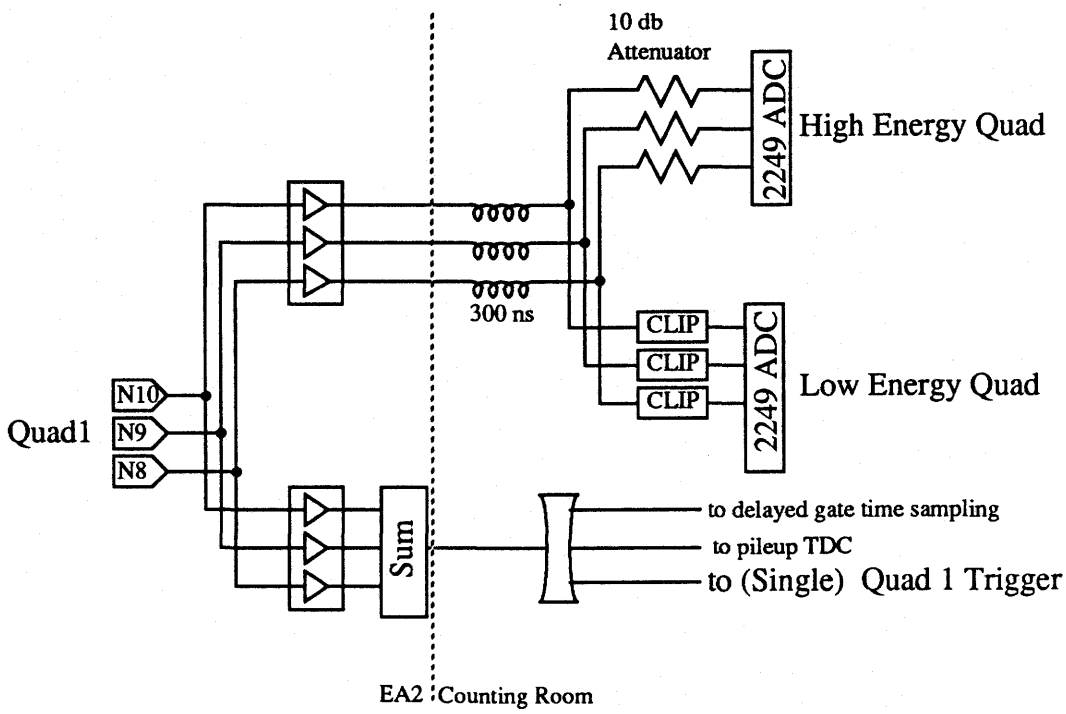

Figure 2.16: Single Quadrant Electronics

Each of the summed quadrant signals from EA2 was fanned out. Two sets of fan-out signals were used for quadrant pileup identification electronics. One channel went to the Single Quad Trigger logic.

The primary scheme for pileup identification in the quadrants was waveform digitizing. Unfortunately, four WFD modules were not available, so a delayed gate time sampling scheme was set up (see Figure 2.17). The summed signal from a single quadrant was split into seven separate signals. Each of the seven were increasingly delayed by 100 ns steps and converted in a LeCroy 3400B Fast Encoding and Readout ADC (FERA) with a 100 ns gate. The result was that 100 ns pieces of the quadrant pulse shape were sampled. If an accidental coincidence occurred, at least one of these sample channels would be abnormally high.

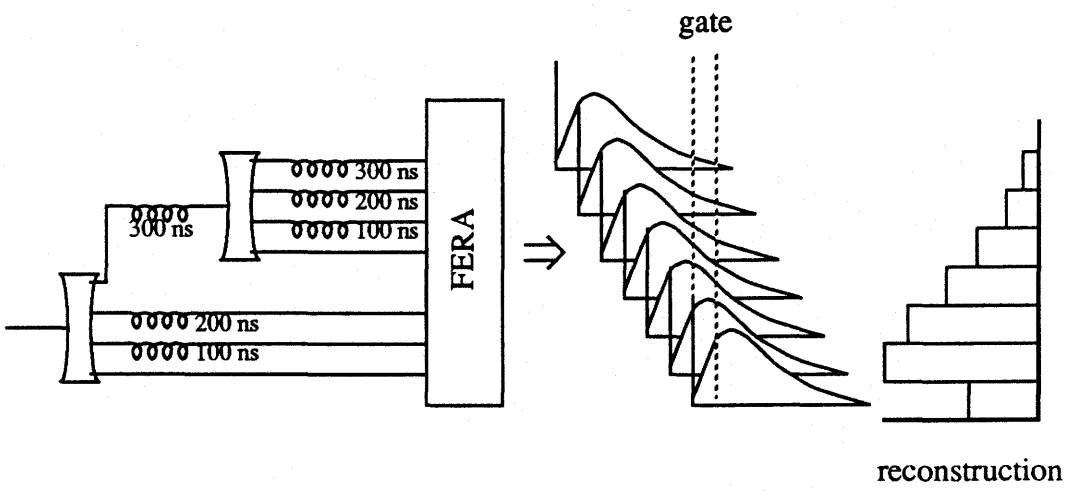

Figure 2.17: Delayed gate time sampling of quadrant pulse shape

The second pileup identification scheme employed a pair of Time-to-Digital Converters (TDC). The start signal was generated by the core trigger logic, and then split. One start signal went promptly to one TDC, and the other was delayed before going to a different TDC. The stop signal was generated by the respective Single Quadrant trigger from a Leading Edge Discriminator (LED). For a good data event the TDC with the delayed gate would receive a stop signal before the delayed start. This would result in an overflow and an empty timing spectrum. The prompt TDC would produce a timing spectrum characteristic of the shower production time. If another signal immediately preceded the main signal, the delayed gate TDC would start before the stop instead of overflowing. Then any event found in the delayed gate TDC spectrum must be a pileup event. In hindsight, the use of an LED was a mistake. Because LEDs trigger at a fixed level and because pulses of various size have different leading slopes, LEDs trigger at different times depending on the size of the input pulse. The result was a timing spectrum that was too difficult to use for more than basic pileup rate calculations. Instead of using an LED, the Constant Fraction Discriminator (CFD) output from the Single Quadrant trigger circuit (see Section 2.6.2) should have been used.

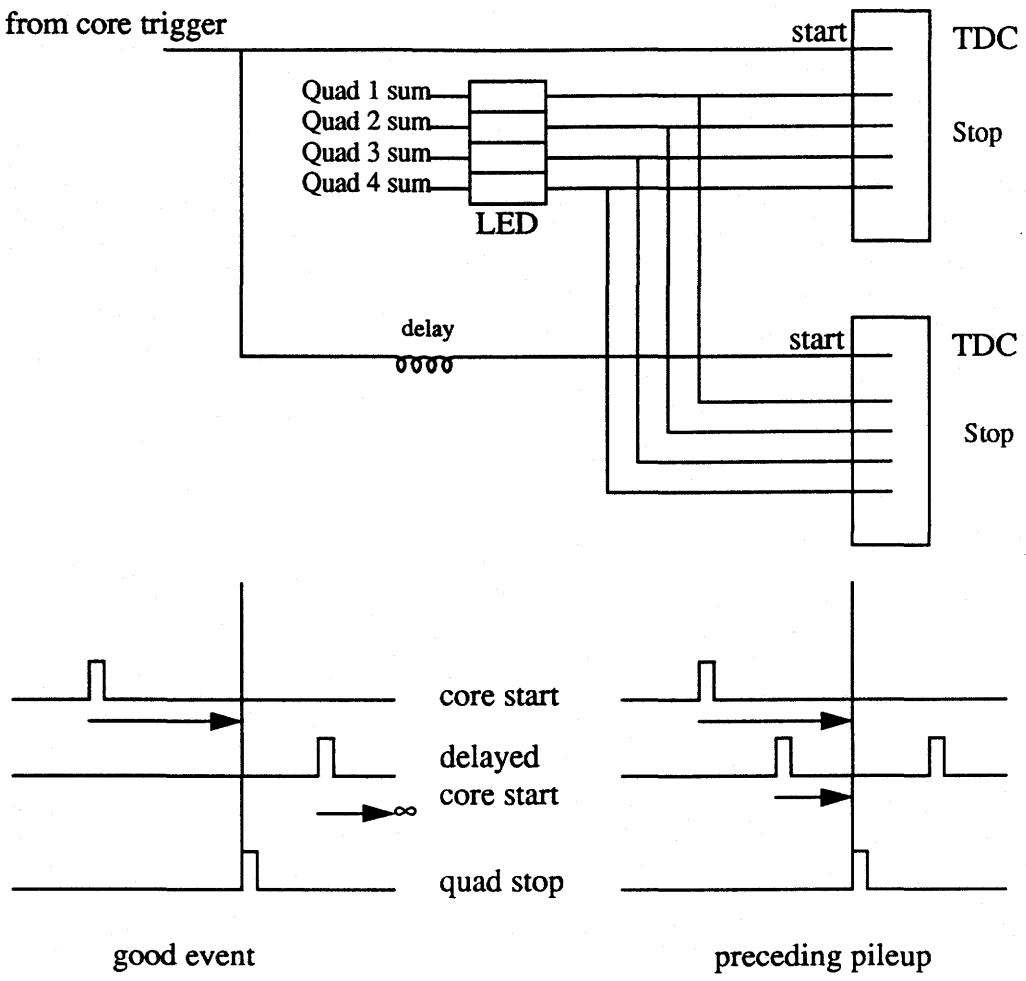

Figure 2.18: Pileup TDC

2.6.1.c Two Inch NaI Signal Processing and Conversion

The two inch NaI source spectrum was required for the gain compensation system. Therefore it required its own ADCs and trigger (see Figure 2.19). The PMT signal was split and then amplified. Both branches were sent upstairs. One signal was delayed by 330 ns, clipped, attenuated, and converted in a 2249W ADC. The second arm went to the 2 inch NaI Trigger logic.

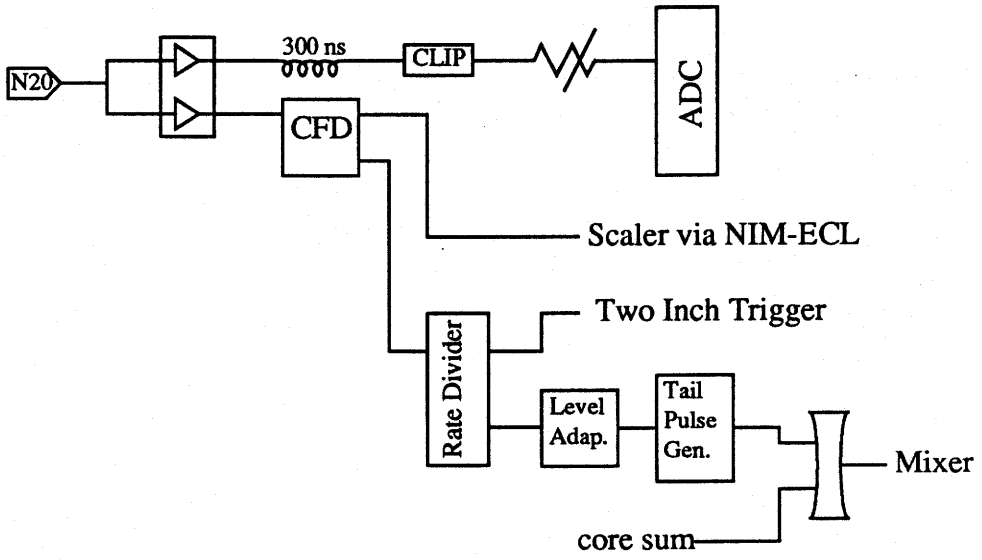

Figure 2.19: Two Inch Detector Electronics

2.6.1.d Anti-Cosmic Annulus and Paddle Scintillator Signal Processing

The anti-cosmic annulus and paddle cosmic ray veto counters, with the exception of the Front Mid veto counter, were delayed then converted in a FERA (see Figure 2.20). The annulus signals actually were summed in pairs so that 6, instead of 12, signals were sent upstairs. The Front Mid veto was in the aperture so it was fanned out to a delay and FERA and to a discriminator for coincidence assessment with the aperture counters.

Aperture 2 and 3 were clipped because of the anticipated high rate of electron background. Aside from that, all 3 apertures were each fanned out to a FERA and to an LED. The signals destined for the FERAs were first delayed by 330ns then AC coupled with external 0.05 μF capacitors. The latter was necessary because the FERAs on hand for these detectors had DC coupled inputs. The discriminator outputs were fanned out to a set of coincidence modules with different combinations of coincidence levels.

Many of the ADC's were meant to provide energy information. Since ADC's generally offset output so that an input of zero produces a non-zero output, this offset or pedestal must be measured. This was simply done by triggering a readout of all ADC's

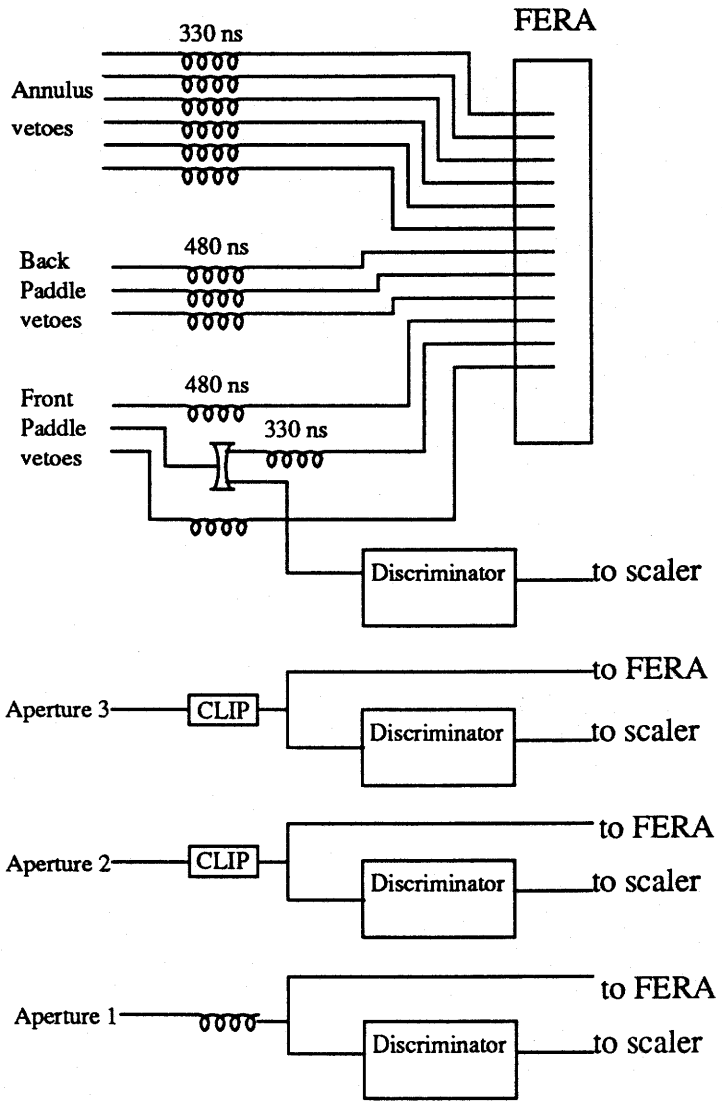

Figure 2.20: Veto Electronics

at random times. This also serves the purpose of monitoring the effects of random background. This will be discussed later. The resulting spectra were ideally spikes 1 or 2 ADC channels wide and the position of those spikes indicated the pedestal values.

2.6.2 Triggers

There were 4 primary triggers: Core (for data events), Quad (for quadrant calibrations), "Two inch" (for pedestals and reference source spectra), Flasher (for gain monitoring). Two secondary triggers were Low Energy Core and Extraction Gate. The OR of these signals generated the Master Trigger. When this occurred, all acquisition modules,

except for scalers, were read via CAMAC.

The Core Trigger logic pulse was generated by a Constant Fraction Discriminator (CFD) from one of the summed and clipped core signals (top of Figure 2.21). One core trigger signal was sent to a visual scaler, the other to a NIM-to-ECL converter for the Master Trigger generation.

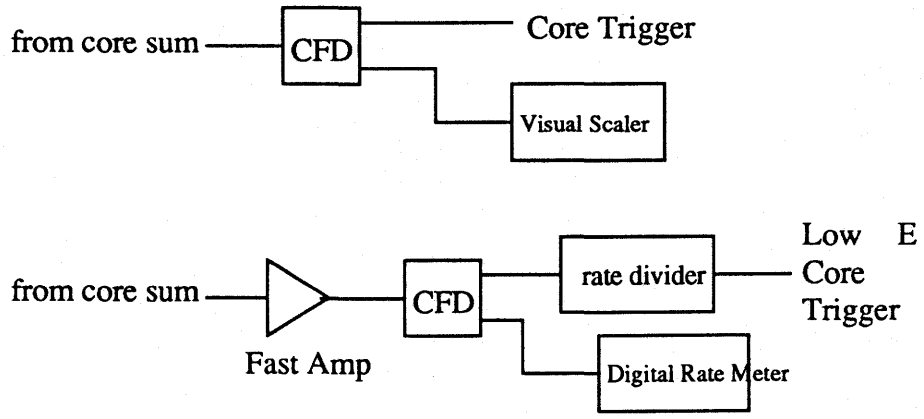

Figure 2.21: Core Triggers

A Low Energy Core trigger was sometimes used for diagnostic purposes with radioactive sources (bottom of Figure 2.21). A core sum signal was amplified before entering a CFD. One discriminator output was prescaled by a rate divider module to reduce the high trigger rates to about 5 Hz. Another output went to a Digital Rate meter. This was the more useful on-line signal from this circuit since it indicated the overall count rate in BUNI. The data rates displayed by this meter were used to determine the maximum acceptable beam flux.

A Single Quadrant trigger (Figure 2.22) was generated from each of the four summed quadrant signals by a CFD. A second CFD output went to a scaler to measure the raw quadrant event rate. The Quadrant trigger was the OR of the four CFD outputs and was prescaled by a rate divider to a rate of 5 Hz. The rate divider was necessary since the

radioactive source flux could not be regulated. This trigger was used only for quadrant source calibrations. A second output of the OR was sent to a scaler to measure the prescaled quadrant rates.

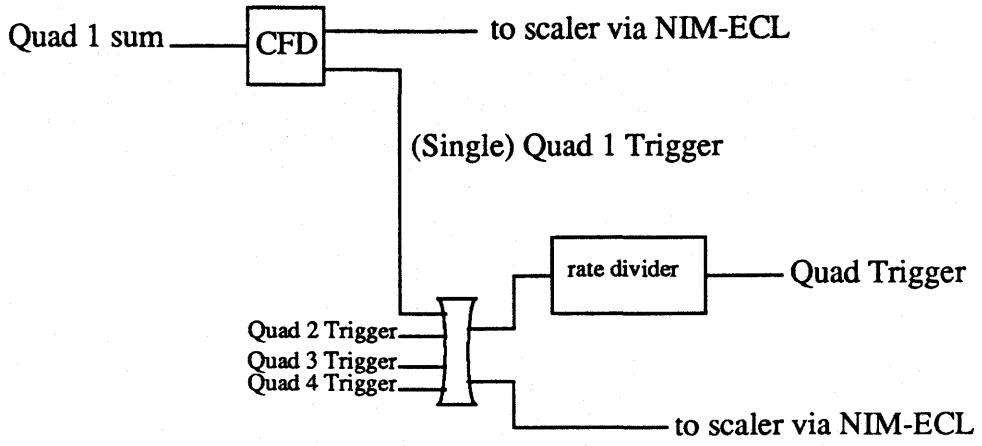

Figure 2.22: Quad Trigger

The Two inch NaI trigger (Figure 2.23) was generated by a CFD and was prescaled to 5 Hz by a rate divider. A second rate divider output triggered a Tail Pulse Generator. The pulse was shaped with time constants similar to NaI pulses and mixed with core input. The core energy spectrum from this "mixer" should be a narrow spike in the pulse height spectrum and the amount of broadening was a measure of the pileup rates. A second output from the CFD went to a scaler to measure the raw Two Inch NaI count rate.

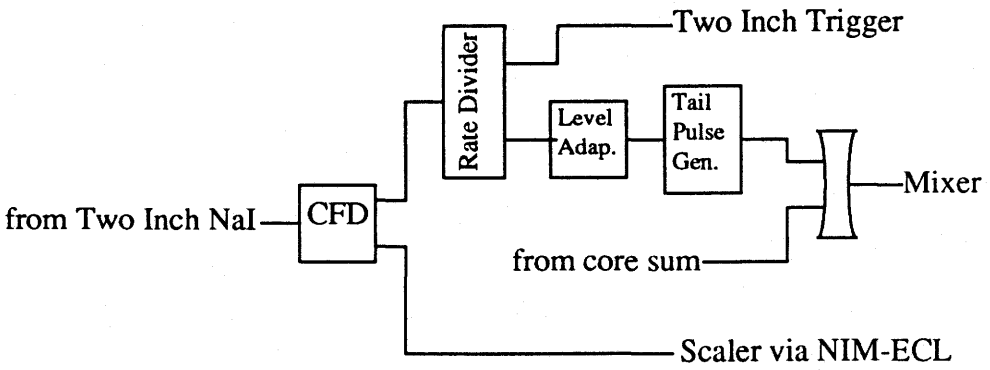

Figure 2.23: Two Inch NaI Trigger

The trigger used for pedestals was the "Two inch" trigger since the source that triggered it could be counted on to be random. Later, it was realized that since the beam duty factor was not 100%, completely random triggers would not properly sample the beam dependent background. To correct for this, a trigger was set up using a plastic scintillator on the opposite side of the beam from BUNI.

The flasher was externally triggered by one output of a pulse generator. The flasher trigger came from the second output of the pulse generator pulser which was delayed to match the time for the flasher trigger to reach the flasher downstairs and the resulting NaI pulse to return upstairs (Figure 2.24).

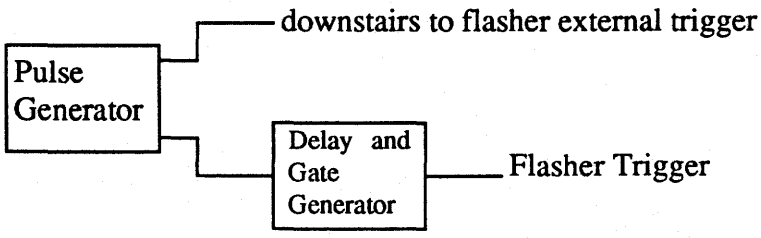

Figure 2.24: Flasher Trigger

Since EA2 is directly downstream of the linac, there was always a massive flux of background radiation during the acceleration of electrons in the linac. An electronic veto was required for this part of the pulse stretcher duty cycle. The primary timing signal was the electron gun trigger from the control room (Figure 2.25). An EG&G Delay and Gate Generator, GD 150 generated a 20 microsecond long logic pulse, 0.1 microsecond after the gun trigger. This pulse was fanned out into many copies. One output was the Extraction Gate trigger which was used in anti-coincidence with the other triggers to generate the Master Trigger. This prevented data acquisition during the injection burst. Another output was used for an oscilloscope monitor for debugging. The third was ORed with the output of a CAMAC output register and fanned out. One output went to a scaler and the

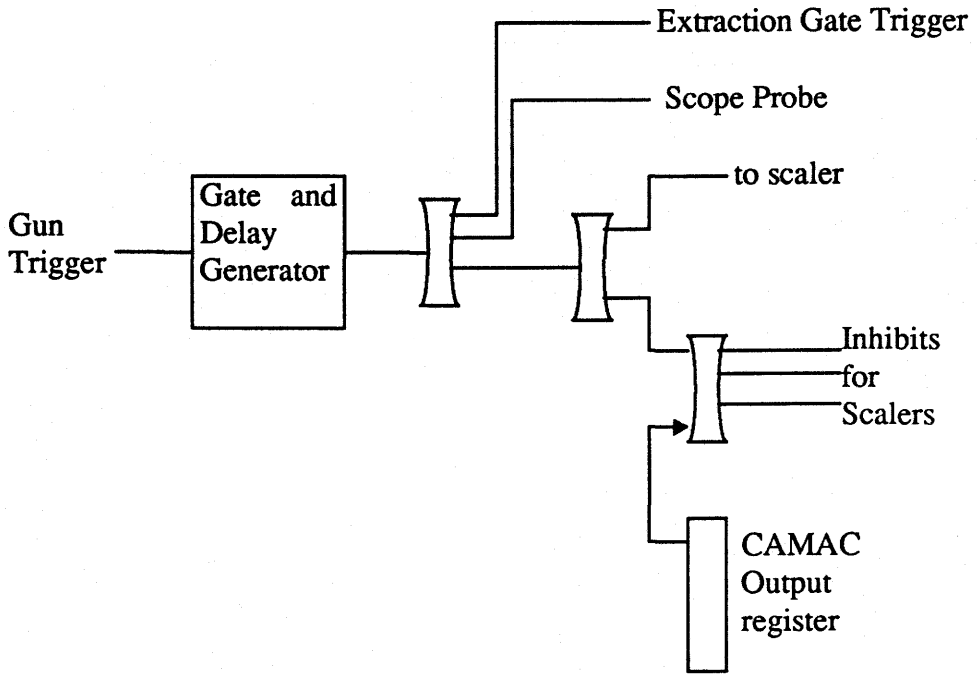

Figure 2.25: Extraction Trigger Electronics

other to a fan out. The output from this fan out was used to inhibit the 3615 hex scalers during the beam burst in the linac, during pauses in data acquisition, and at the end of a run.

Trigger signals were converted to ECL by a 16 channel NIM-ECL converter, and then split in a LRS 4418 delay module (Figure 2.26). ECL output was desired because high density scaler modules can be used. The delay module has 3 ECL output banks of 16 channels. The first bank was chained to a coincidence register to record which triggers fired (for some event types, more than one trigger fired) and to an ECL scaler.

Eight channels of the second bank went to the first input bank of a Programmable Logic Unit (PLU). The Master Trigger was generated from the other major trigger signals by the PLU. Logic expressions could be downloaded to this module for different combinations of eight input channels to produce signals in up to any of eight output channels, for each of two input banks. The logic for this experiment is shown in Figure 2.27. The Master trigger logic for a photon scattering run was an OR of the Core Trigger, Two inch

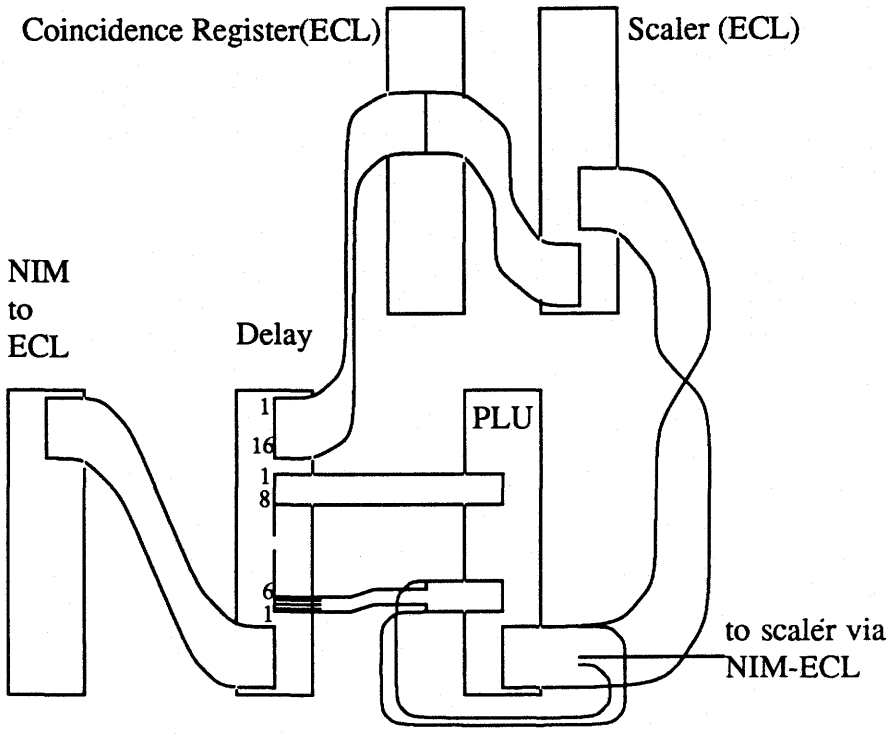

Figure 2.26: Trigger Handling

Trigger, and Flasher Trigger in coincidence with the Core Trigger. The quadrant calibration Master Trigger logic included the Quadrant Trigger signal. There were two output channels using the Master Trigger logic. One proceeded to a scaler. The other went to the second bank of the PLU. A feedback loop using input1, input8, and output8 was used to lock the first seven output channels during an event trigger. This was meant to allow time for acquisition of the current event before processing another event.

The first output channel of the second bank was used for gate generation. That signal went to a NIM-to-ECL converter. The ECL output went to a scaler. The NIM output was fanned out to gate generators and discriminators. There were not enough gate generators so discriminators were used for modules that required only short gates. NIM-to-ECL was used to convert the NIM gate signals to ECL for the modules that required ECL gate signals (e.g. FERA modules). One pair of gate signals was sent to the pileup TDCs in Figure 2.18.

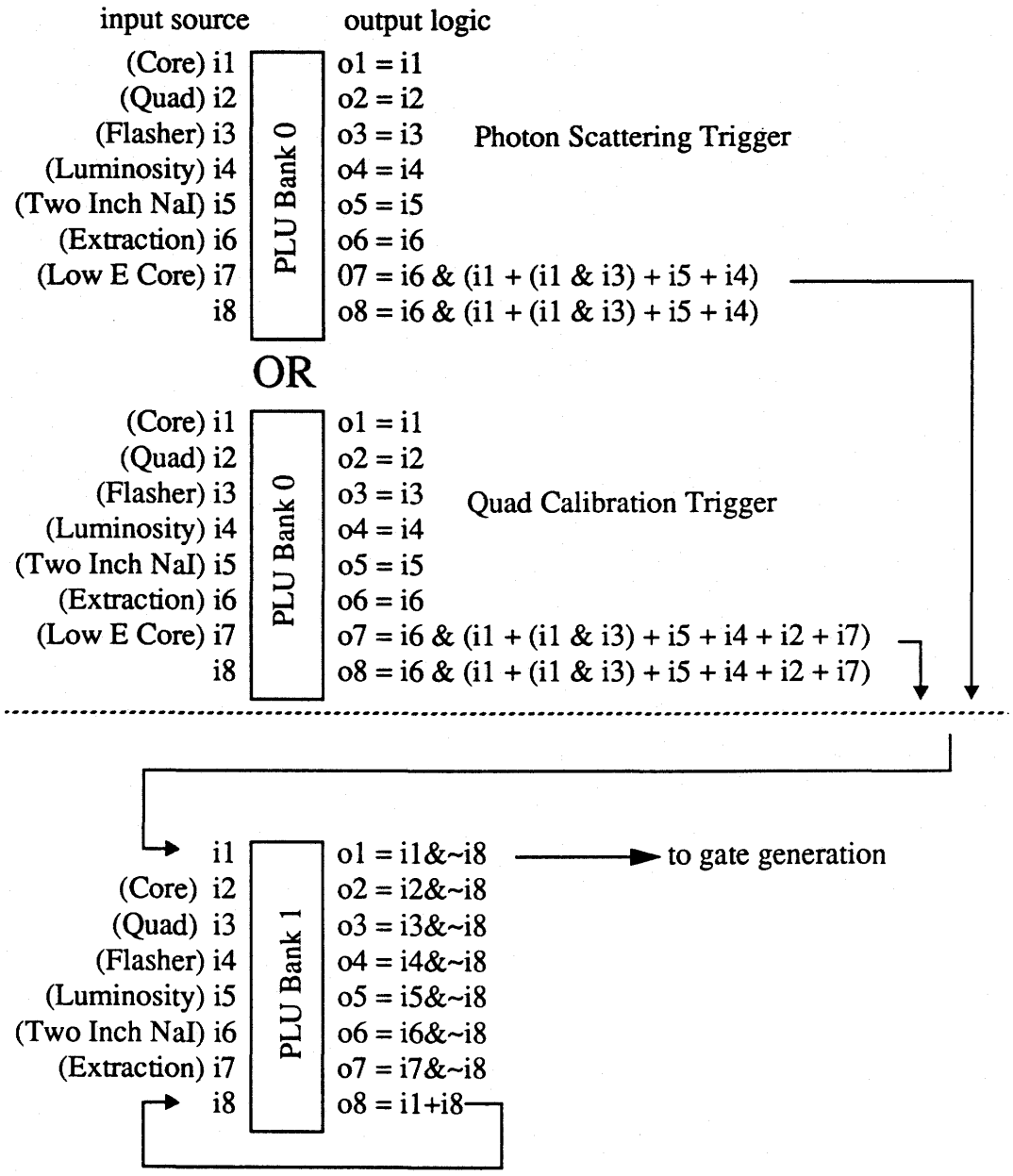

Figure 2.27: PLU Logic

It should be noted that the philosophy adopted in data acquisition was to accept everything: not just data thought to be useful, but also anything that might be conceivably relevant later. Thus, there was no hardware rejection of any data by veto detectors. Instead, the vetoes were to be performed in software.

2.6.3 Ancillary Electronics

The quantameter current was digitized by a current integrator. The output logic pulse rate was directly proportional to the input current, with the proportionality constant being user selectable by rotary switch. The output pulses were counted in a 3615 hex scaler. A second set of pulses were sent to the control room for machine operators to monitor.

The electron dump signal came from the control room, where a current digitizer converted the dump current in the same way as for the quantameter. The output was counted in a 3615 hex scaler.

A third current digitizing circuit was set up primarily for cross calibration of beam flux monitors. Some other secondary monitors were tested during runs with this circuit.

2.6.4 Software

The function of the software is to organize the data collected by the hardware, to analyze them, to display them to the experimenter, and to store them for later retrieval. To facilitate the writing of this software the Computer Systems staff of SAL developed the LUCID data acquisition and analysis system. The user writes the acquisition instructions in the LUCID program language in three separate description files: Reader, Writer, and Looker. To "Build" the acquisition programs, these files are translated to C and compiled. The user may also supply C or Fortran subroutines that are linked to LUCID acquisition programs.

The compiled LUCID software resides in three physically separate computers: a Front End processor, an analysis computer, and a control and display computer. For this experiment, the Front End processor was a CES J11 Starburst module residing in the

CAMAC crate with the other acquisition hardware. The analysis computer was a Digital Electronics Corporation microVAX. The control and data display computer was a Sun Microsystems workstation.[5]

A user interface program on the workstation allowed the user to command the data acquisition software and to display acquired data through a Manager process on the microVax (see Figure 2.28). Typical commands were to record data, pause, resume, and stop acquisition. Typical messages were software status messages (e.g. notification of a

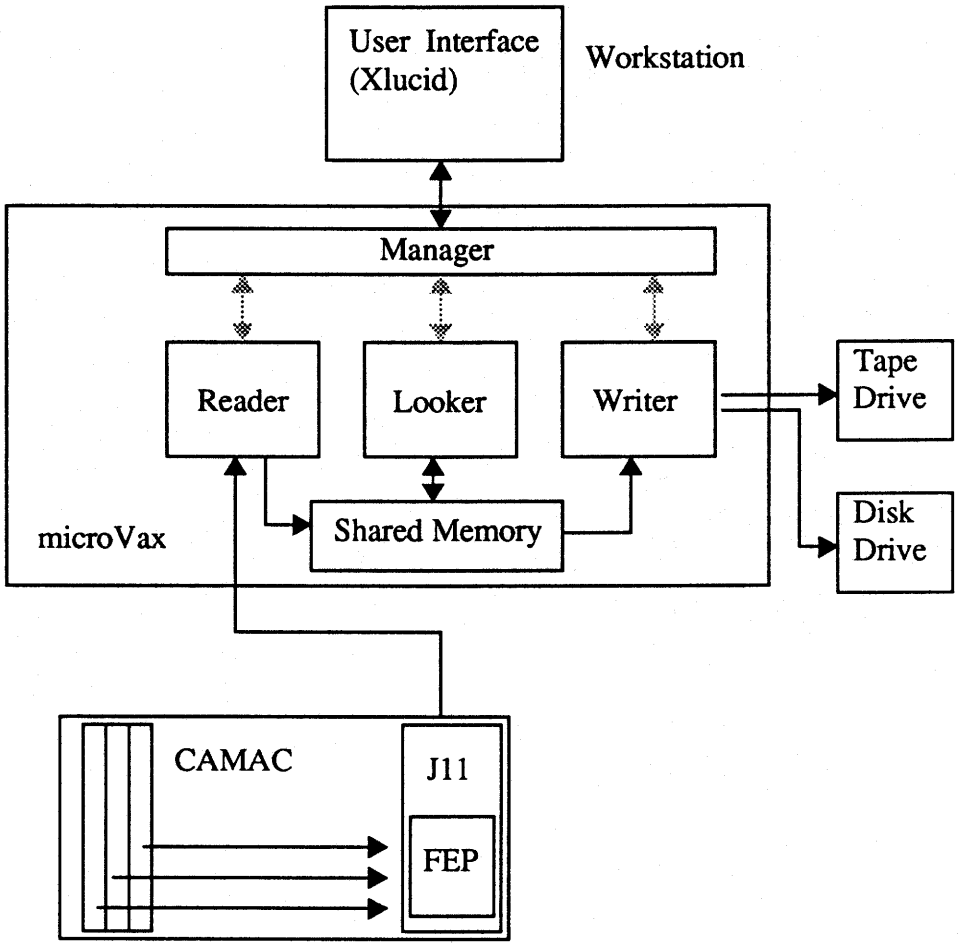

Figure 2.28: Schematic representation of LUCID processes

5. At the time this thesis was written, the acquisition system had upgraded to using a Motorola 68040 based VME system for the Front End processor, a workstation for the analysis computer, and another (or the same) workstation for the control and display computer.

successful compile), processed information from the analysis software (e.g. total counts and count rates), and prompts for user information at the beginning of a run(e.g. target and angle information).

Two programs are generated from instructions in the Reader description file. The Front End Process (FEP) is downloaded to the J11. The other program, the Reader, resides in the microVax. The Front End Process collects data from the acquisition electronics according to instructions in the Reader description file. These instructions dictate when the FEP should do something, i.e. what the acquisition trigger conditions are, and what is done, e.g. what modules are read. Data are classified according to the trigger conditions and put into a corresponding LUCID "event". There were four different LUCID event types for this experiment. The **startup** event was triggered by a **beginrun** signal from the Manager. The **nai** event corresponds to the Master Trigger discussed in Section 2.6.2. LAM (Look At Me) from the coincidence register module interrupts the Front End Process which then performs the collection of data from the electronics. The name **nai** is a misnomer because it includes photon events, Two inch NaI events, flasher events, and calibration events. Scalers were read in the **scalerread** event once every 5 seconds using a timer in the Front End Process. In the **windup** event, final scaler readouts were done. The data from all events were then sent to the microVax via serial highway, where the Reader puts the data into shared memory.

The Looker samples data in shared memory, and makes computations for each of the LUCID event types as directed by the user in a Looker description file. It is here that data can be calibrated, kinematics computed, tests made, and histograms be accumulated for the user to examine on-line. Understandably, this is usually the most complicated and time consuming process. If all data were examined by the Looker, it could impede the

rate of data throughput. To prevent this, the Looker was instructed to analyze only as many events as it could manage. In this experiment, 50% to 90% of the events were looked at on-line.

The major concern for on-line analysis was to ensure that all detectors and readout modules were functioning. To that end, histograms were made of all modules for the different types of event triggers in the **nai** LUCID event and reviewed regularly. The Reader was not instructed to generate different event types for the different triggers. Instead, the on-line analysis differentiated trigger types by the coincidence pattern from the coincidence register. In addition, a series of crude (by final analysis standards) total energy spectra were produced. These were crude with respect to calibrations which were determined by eye and were only good to 1%. However, they were sufficient for determining data rates. These histograms were reset in the **startup** event, and written to files for later perusal in the **windup** event. Scalers were also written to a file in this event.

Above compiling histograms, the generation of total energy spectra consumed a major part of the on-line analysis resources. In the **nai** event, a running mean peak position was computed for all NaI segments for flasher and Two inch NaI triggers. In the **windup** event, the final mean positions were written to a file and new gains computed from flasher and Two inch NaI information and Zero Degree calibration information. In the **startup** event of the next run, the new gains were read in and were applied to each PMT ADC. This allowed gain tracking on-line on a run by run basis. Because all seven phototubes on the core viewed the same volume, their energies were averaged to give a core energy. Similarly, the energies from the three phototubes of each quadrant were averaged to give 4 quadrant energies. The core and quadrants were optically isolated so the core energy and quadrant energies were summed to yield the total energy from the spectrometer. Crude thresholds were used to reduce cosmic ray background.

The Writer process can transfer data in shared memory to some output device or to another program. Its description file is the simplest: a file or device name and, optionally, which event type to write. For this experiment all events were specified and were saved on 8mm Exabyte Tape cartridges.

2.7 Calibrations

The equipment for this experiment needed to be calibrated before they could be used. Procedures will be discussed in this section for determining the energy scale of BUNI, the resolution of BUNI, and the conversion factor for the quantameter.

2.7.1 Zero Degree Calibrations of BUNI

The energies measured by BUNI in this experiment were more than 50 MeV which exceeded the energy of available radioactive sources (5-10 MeV). Most of this energy was deposited in the core. The energy scale for core pulse height spectra had to be determined by the beam. The primary method was measuring bremsstrahlung spectra and correlating the observed endpoint with the expected endpoint. Before, and sometimes after, a series of measurements, BUNI was swung directly into the photon beam line for energy calibration. Running the full beam into the detector would have been catastrophic. Since the accelerator could not be turned down low enough to provide a 50 kHz data rate, which was BUNI's upper limit, a 4 inch lead filter (a standard lead brick) was placed in the brems beam line on the target post to reduce the photon flux by a factor of 10^4 to 10^5. The detector was moved into place with the high voltage supply to its phototubes turned off. The accelerator was turned on with the current turned down as low as possible, then the high voltage was turned back on. If the low energy trigger rate was excessive, the beam was immediately shut off. Here the fear was not so much of catastrophic failure, but of PMT gain shifts. If the rate was good then acquisition of pulse height spectra proceeded as a normal photon scattering run. For on-line analysis, the endpoint was determined by eye for each core phototube and gains computed for use in the analysis software.

2.7.2 Source Calibration of Quadrants

The quadrants were calibrated with a Thorium-C source placed in the aperture during angle changes and any lengthy downtime. This process required the removal of the beryllium hardener and the thin paddle counters in its vicinity. This was a delicate operation. On a couple of occasions one of the scintillators was snapped from its tube and had to be re-glued. The Master Trigger logic had to be changed for these types of runs. However, this was straightforward, as the PLU instructions that were downloaded included the Quadrant Trigger. Data were acquired until there was about 3% statistics (1000 counts) in the calibration peak seen in a typical low energy quadrant energy spectrum (Figure 2.29). After the statistics were attained, the source was removed, the hardener replaced, the aperture paddles replaced, and the Master Trigger changed back to normal

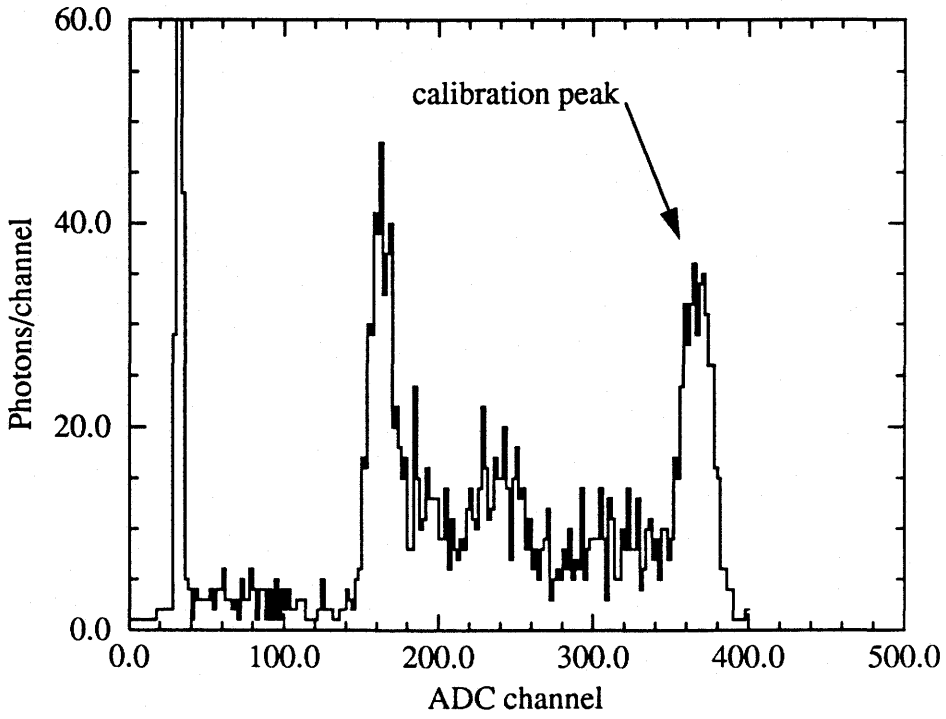

Figure 2.29: TH-C Source Spectrum in Quadrant PMT 1

2.7.3 Calibration of Quantameter by Photons

A P2 chamber [Pruitt 62] of known calibration was placed in the photon beam and the current from both the quantameter and the P2 were simultaneously measured (Figure 2.30). Of course, the beam that reached the quantameter was attenuated by the P2, so the absorption due to the P2 was to be modelled with EGS simulations. With the modelled correction on the photon spectrum for the quantameter, the calibration could be determined from the correlation with the P2.

2.7.4 Electron Scattering Calibration of BUNI and of the Quantameter

2.7.4.a BUNI

Since a monochromatic electron beam could be delivered to EA2, scattering of electrons was a viable method of measuring the resolution of BUNI as well as its energy calibration. The set up was somewhat different than for photon scattering (Figure 2.31). The electron beam dump magnet was turned off and degaussed. A vacuum pipe was extended from the dump magnet to the target post. This was connected to a vacuum chamber containing a small target ladder (Figure 2.32). The ladder held thin foils of carbon (0.48 mm), aluminium (0.25 mm), CH_2 (1.78 mm) and scintillating screen to view the beam. A vacuum pipe extended downstream from the target chamber to the quantameter so that

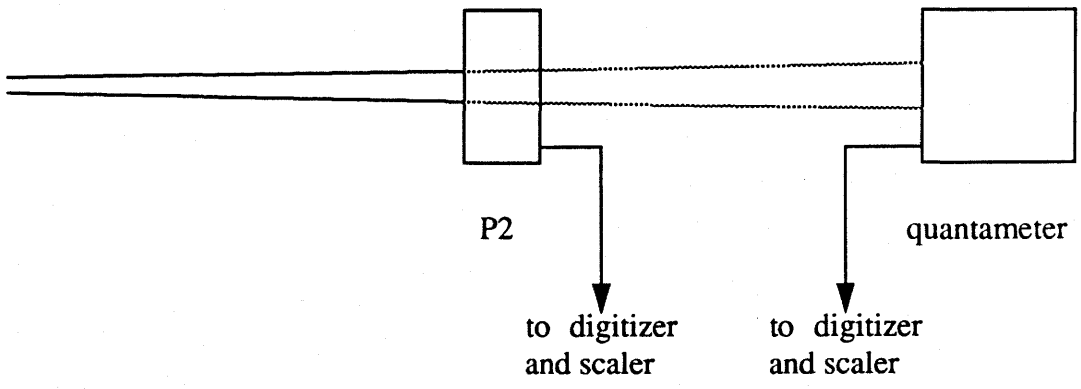

Figure 2.30: Calibration of the Quantameter by Photons

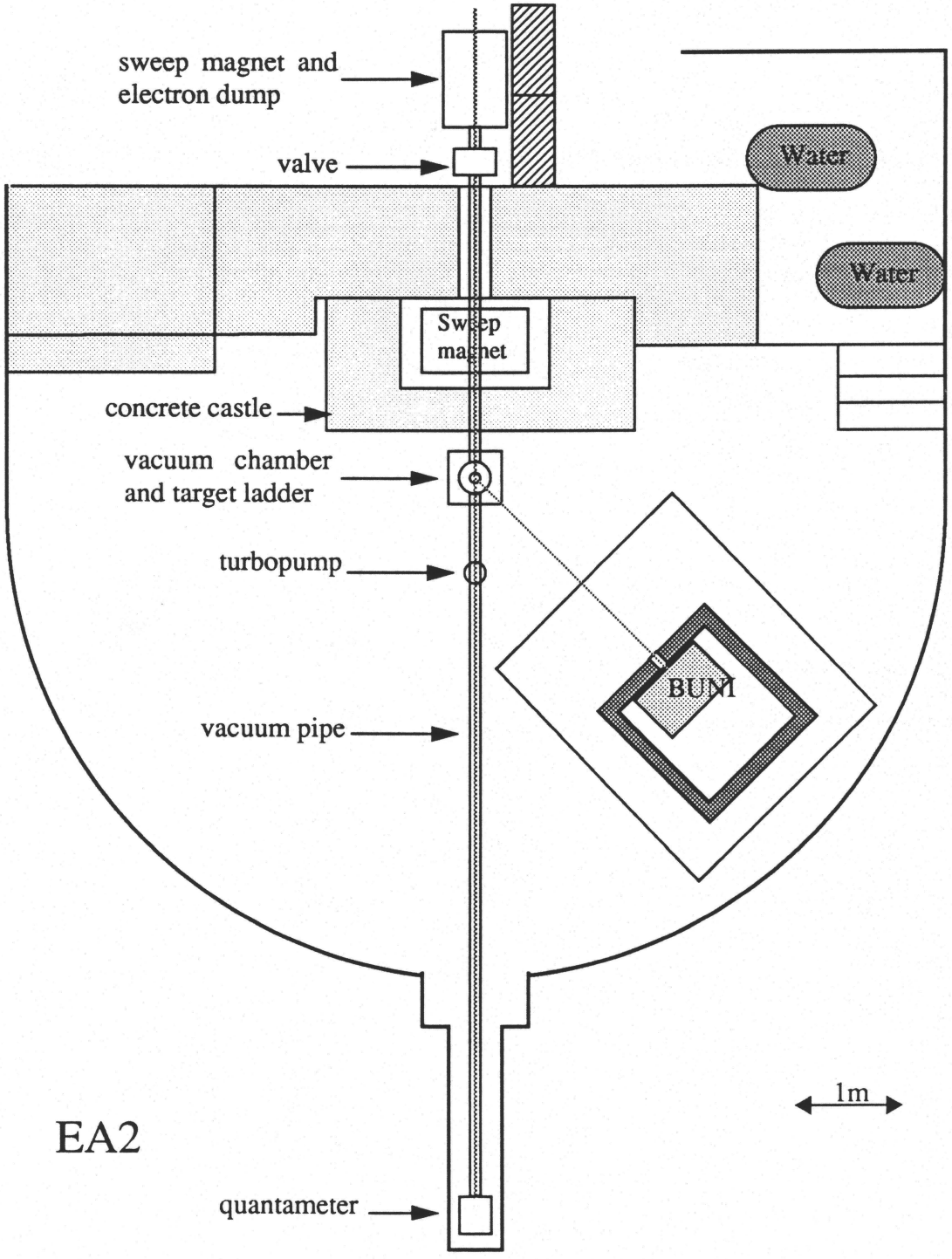

Figure 2.31: Electron Scattering Set Up for BUNI Resolution and Calibration

the electron beam passed through no material, other than the thin target. Scattered electrons exited through a thin foil window at a 45 degree exit port and then were collimated by a 1 cm hole machined through 5.08 cm of lead. This collimator shielded against multiple scattered electrons from the wall of the target chamber. The scattered beam spot size was determined by a 3.81 cm x 3.81 cm square aperture in the opening of the shielding hut at the front of the detector table. The scattered electrons were not contained in vacuum, so the measured spectra were actually a convolution of energy loss with detector response function. An EGS simulation would be required later to determine the extent of straggling and mean energy loss. The resolution and calibration could then be inferred. This method was used only once because the setup was too obtrusive to the photon scattering setup.

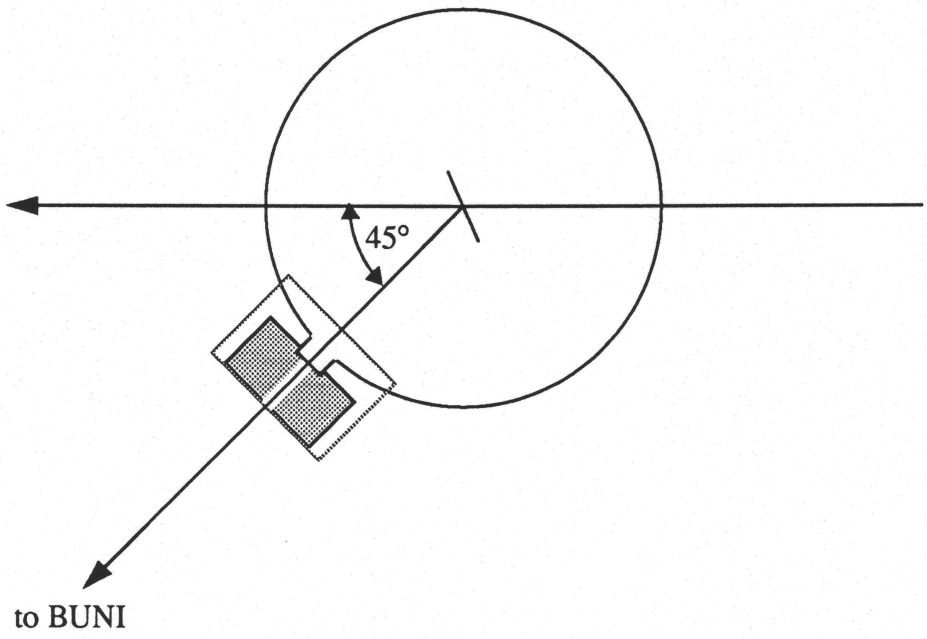

Figure 2.32: Target Chamber for Electron Scattering

Since the resolution of BUNI was energy dependent, these measurements were made at two energies, 201 MeV and 291 MeV. Spectra were measured until about 10000 events were accumulated in a 10 MeV region about the highest energy electron peak.

Spectra were measured for all of the targets in the ladder. The CH_2 and carbon targets were the key ones. Due to recoil, the hydrogen scattered electrons appeared 11 and 24 MeV below the carbon scattered ones at incident energies 201 and 291 MeV, respectively. This would provide the least ambiguous spectra for extracting the resolution. The carbon data was taken to subtract from the CH_2 data.

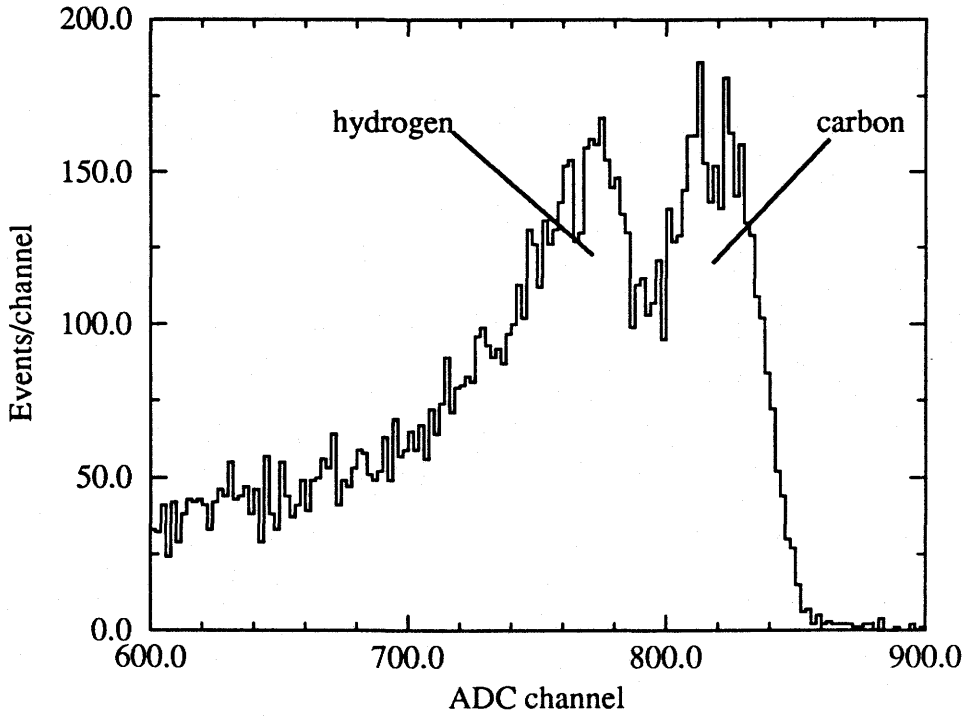

Figure 2.33: Electron Scattering Core Phototube Spectrum from CH_2

2.7.4.b Quantameter

Electron scattering was also used to calibrate the quantameter by measuring electron scattering yields with BUNI from various target materials while measuring the current in one of three different flux monitors. The setup was similar to the electron scattering calibration of BUNI, however the downstream beam pipe from the target chamber was

shorter to accommodate the other flux monitors. Electrons of 3 different energies, spanning our photon scattering measurements were used. A Faraday cup, dubbed "the purple pig", was the primary comparison flux monitor. A crane was used to lower the Purple Pig into the beam line downstream of the target, but upstream of the quantameter. The electron beam current was integrated by the Purple Pig while counting scattered electrons in BUNI (Figure 2.34a). Scattered electron energy spectra were accumulated until a standard count (about 1000 counts in a 10 MeV region around the electron peak) had been reached. This established the ratio of number of electrons in the beam to BUNI yield. The Purple Pig was lifted out of the beam line and the charge output of the quantameter was integrated, using roughly the same currents as for the Purple Pig measurements, while electron energy spectra were measured (Figure 2.34b). The integrated charge from the quantameter was compared to the BUNI yield which in turn was related to the electron beam flux. The correlation of yields and currents determined the calibration for the quantameter.

The P2 was used as a secondary comparison. The P2 chamber was placed in the beam and its charge output was integrated while scattered electron spectra were accumulated (Figure 2.34c). To ensure that the difference in positions of the Pig to the quantameter would not affect the perceived currents, a P2 chamber was cross calibrated near the target and then near the photon dump (Figure 2.34d).

In each case, measurements were done with different beam currents to determine if any of the ionization chambers were saturating. One of the difficulties encountered was that the electron beam currents required were below the sensitivity of beam monitors in the control room. Hence, even though an attempt was made to use the same currents for the different cases, this was not guaranteed.

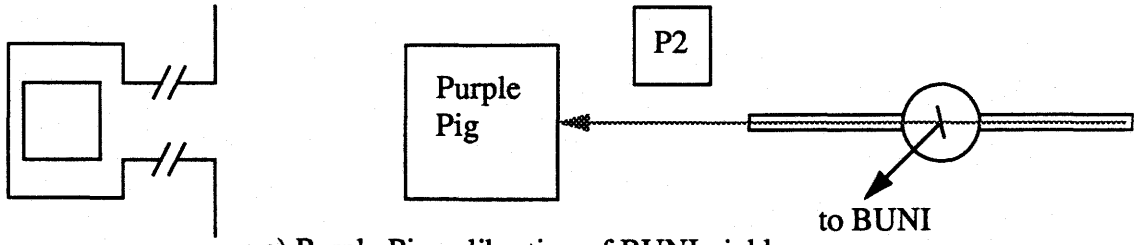

a) Purple Pig calibration of BUNI yield

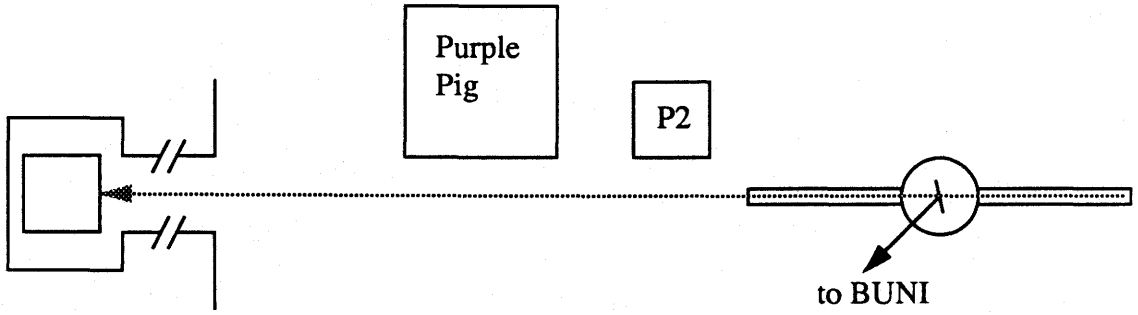

b) BUNI yield calibrates Quantameter

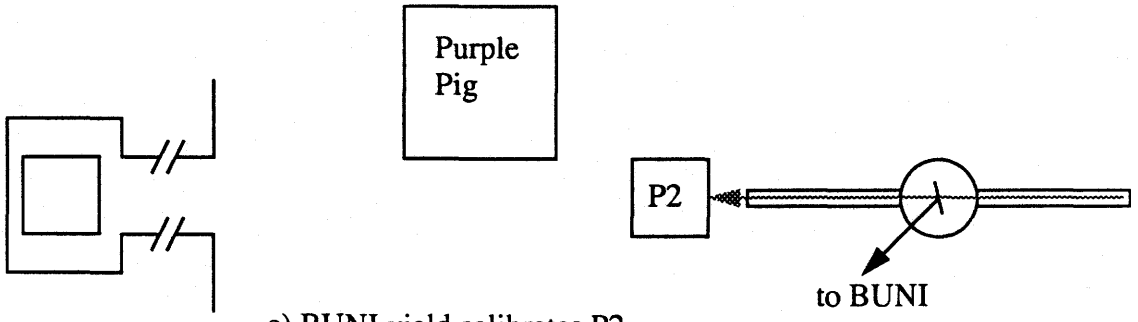

c) BUNI yield calibrates P2

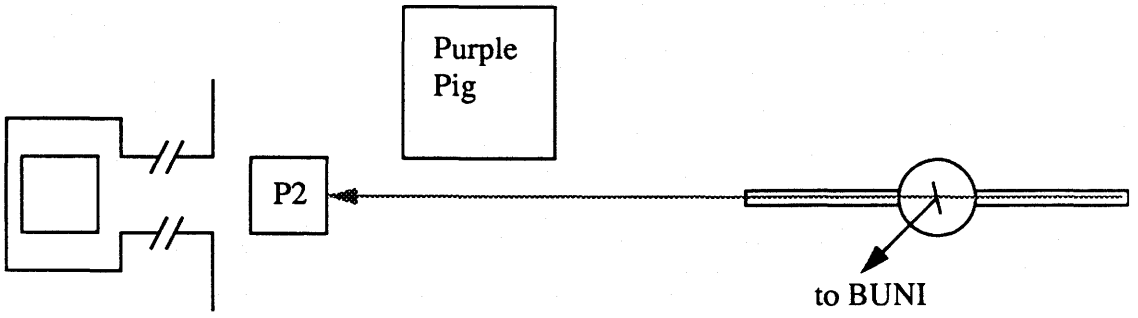

d) BUNI yield calibrates P2 downstream

Figure 2.34: Electron Scattering Setup for Quantameter Calibration

2.8 The Photon Scattering Experiment

2.8.1 Procedure

2.8.1.a Pre-run Procedures

At the beginning of the experiment, steel sheets were laid on the floor of EA2. This was to provide a smooth surface for the airpads and to prevent chipping of the floor. Then the detector was brought in and the shielding house assembled. The whole detector assembly was leveled and then the detector was brought up to beam height using a survey transit as a spotter. The target ladder positions were pre-determined and bolt holes were drilled into the floor to fasten the ladder down at three positions. Each position was used for a different angular range for the angular distribution measurements (see Figure 2.35).

The collimator housing was surveyed into place. A transit located on the beam line and at beam height sighted on a fiducial centered on the electron dump magnet exit port. Then a fiducial was placed on the collimator housing and the housing was shifted horizontally and levelled by adjusting screws (Figure 2.36). The collimator had a tapered bore which could be changed to match the divergence of the photon beam which in turn depended on the incident electron energy. The collimator assembly consisted of trimmed lead bricks with 5.08 cm inside diameter holes machined out and fixed between 2 steel plates, and a series of 5.08 cm outside diameter cylindrical inserts with different size holes machined out. These cylinders were made of brass cylinders filled with lead. The hole in each insert was larger than the hole in the insert upstream of it to match the beam divergence.

Two different sets of inserts were used. At high energies, the beam divergence was small, so there was no problem with ensuring that the beam spot did not exceed the size of the target or the quantameter. However, it was preferred to have a beam spot with fairly uniform intensity. Therefore the beam was cropped which also ensured that the wider divergence "tail" was eliminated. For lower energies, the beam's divergence would have

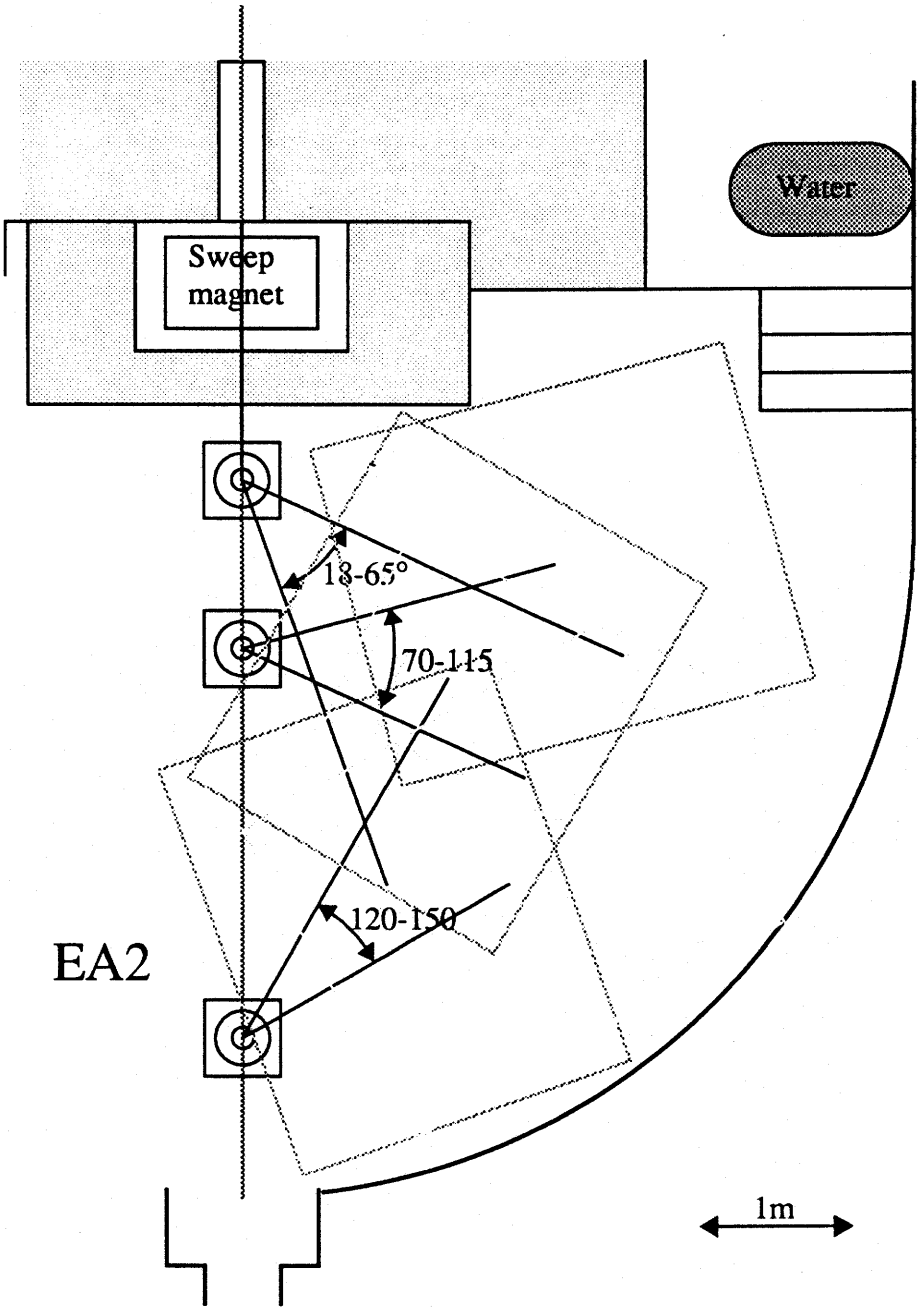

Figure 2.35: Target Positions and Corresponding Angular Ranges.
Length of delimiting lines indicates target to BUNI distance

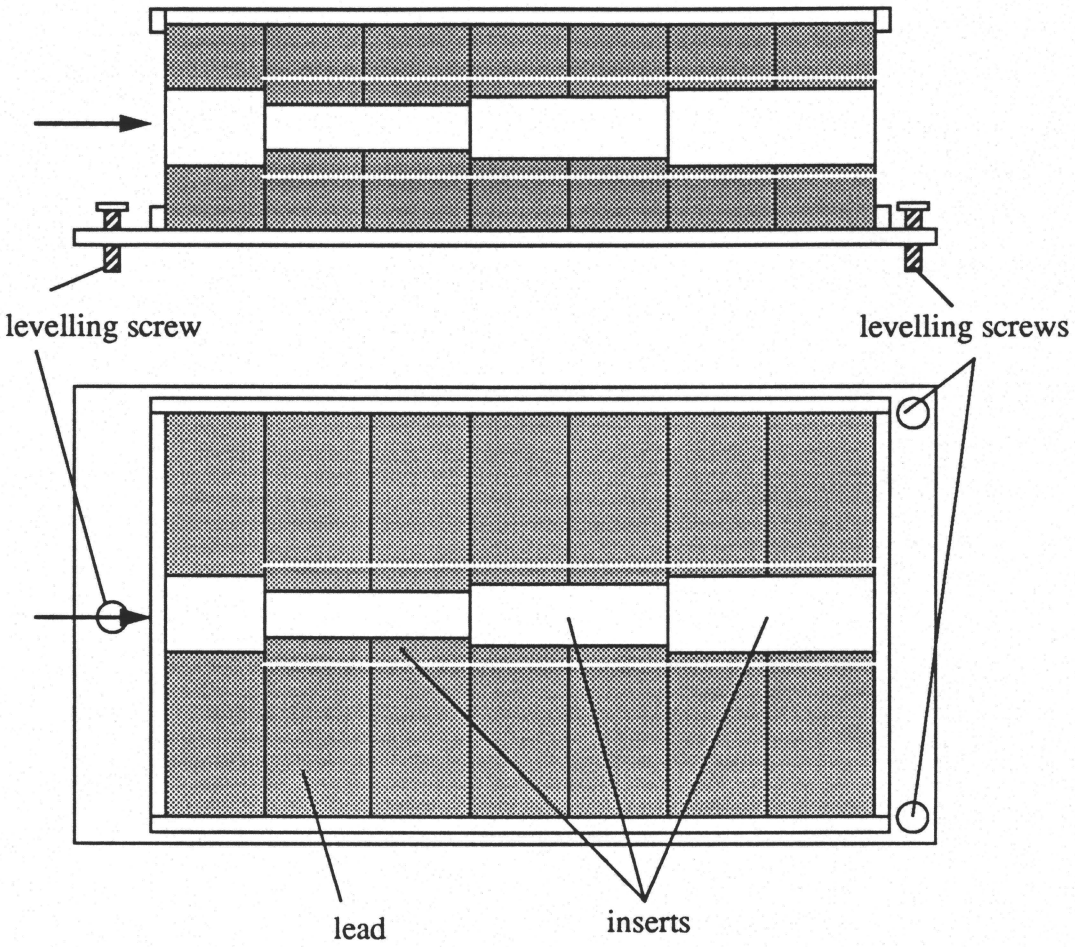

Figure 2.36: Collimator Assembly

caused its dimensions to exceed those of the target and quantameter if left uncollimated. Hence, the beam was collimated to ensure that the beam spot did not exceed the size of the active area of the quantameter (about 15 cm diameter).

After all the experimental equipment was in place, the accelerator operators tuned the linac and PSR to the energy requested by the experimenters and delivered beam to the radiator at EA2. Then the trajectory of the photon beam through the room had to be adjusted. This was controlled by two steering coils, one coil (M601) at the radiator and the other (M701) 3.5 m upstream of the radiator. Each coil controlled both horizontal and vertical parameters. As shown in Figure 2.37, M601 (at the radiator) affected the angle

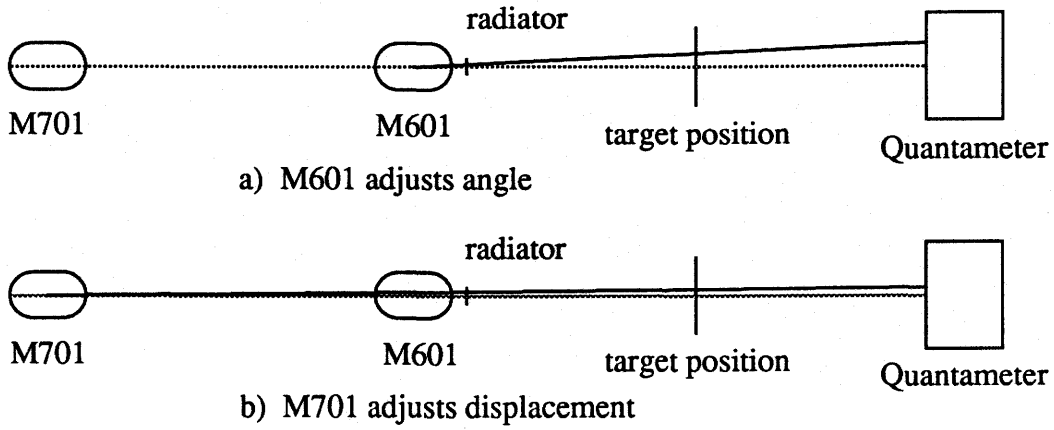

Figure 2.37: Steering Coils for Adjusting Angle and Displacement of the Photon Beam

of the photon beam. M701 had a long lever arm so it effectively adjusted the displacement of the beam from the proper beam axis. Coarse adjustments were made by maximizing the current from the quantameter. For this purpose, one current digitizer output from the experimental electronics was delivered to the control room. Final adjustments were made by taking beam spot photographs. For alignment purposes, a horizontal and a vertical line were drawn through the center of two Polaroid films. One film was placed on the downstream side of the helium or hydrogen target, and aligned with center lines on the target. The other was placed and aligned with center lines on a film mount at the entrance to the photon beam dump. After exposing the films to bremsstrahlung, but just before extraction from its paper backing, a small hole was punched in the middle of the crossed lines. This marked the proper beam axis and if the beam was steered correctly, the beam spot on the film would be centered on the hole. If not, the necessary steering correction was calculated from the divergence. Also, a properly exposed film at the target showed shadows of the vacuum containment and heat shield. This gave a secondary reference for beam steering.

2.8.1.b Moving the Detector

The detector was moved to measure cross sections at different angles. The procedure to do this was rather involved. Since the detector moved on airpads, a diesel air compressor located outdoors at the back of the building had to be turned on and warmed up, especially during the winter months. During this time, the floor had to be swept and wiped clean. This was important, because any greasy residue could cause the rubber coated airpads to stick, and any grit would damage the airpads. The quad calibration was started at this time. Also, if the target position had to be changed, the target ladder was unbolted from the floor and moved to its new location. The target was horizontally centered onto the beam axis using a plumb line from a line on the ceiling that parallels the axis. The cross drive was adjusted such that the intake spout on top of the cryostat was centered on the plumb line. In the case of the 20 degree and 150 degree measurements, the wax shielding had to be removed on the beam side of BUNI. Finally, people had to be enlisted to push the detector. Four airpads were inserted under the detector table, each covering approximately a quarter of the space occupied by the table. Compressed air was distributed to each pad by a manifold, and the respective hoses were connected to them. The table was then lowered onto the pads and the laser goniometer set to the desired angle.

Once the master valve on the compressed air manifold was opened, the flow to each pad had to be balanced to raise the table evenly and to prevent oscillations. Frequently, the operator of the manifold relied upon spotters at the back of the detector to inform him if the airflow distribution had to be changed. Once it was up, the detector was pushed, pulled and rotated, with the aid of one or two block-and-tackle, to roughly the correct position, then set down. During this time, one person was solely responsible for ensuring that no signal or HV cables were pulled or severed.

The final positioning and attitude was determined by the laser goniometer and a telescoping tongue from inside the detector table (see Figure 2.38). The laser was turned on, and the tongue extended towards the target post. With the compressed air turned back on,

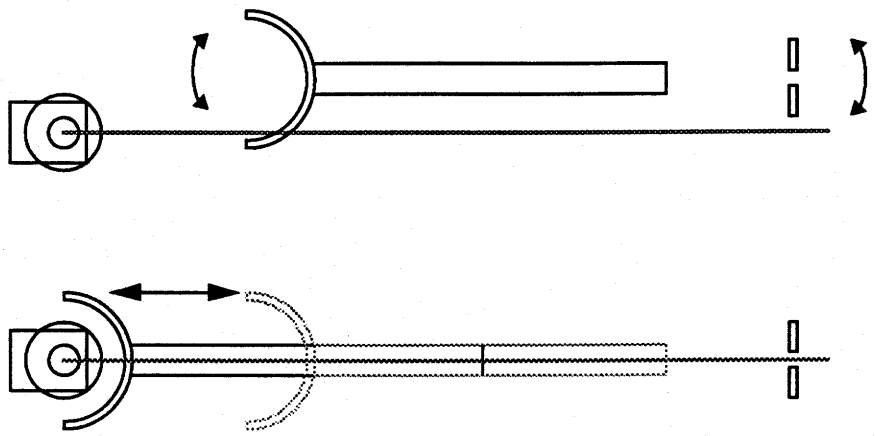

Figure 2.38: Angular Alignment of Table

the table was first rotated until the tongue coupled with the target ladder, but not locked. The angle was checked by observing whether or not the laser beam passed through a slit at the back of the table. If not, then the tongue was retracted and the table shifted. The process was repeated until the laser beam passed through the slits, and then the table was set down. The distance from the target post to the tube that the tongue slides out from (tube-to-post distance) was measured for later calculation of target to detector distances and solid angles.

The table was raised off the air pads and onto its feet and then approximately up to beam height. A bubble level was placed on a part of the table known to be level with the detector, and the table was levelled, front to back, then side to side. Finally, the table was brought to beam height and the level double checked.

After all accelerator areas were cleared and locked up and the beam positioned, data acquisition commenced.

2.8.1.c Run Considerations

Spectra were accumulated until about 1000 events were collected in a 20 MeV region near the endpoint. After accumulating part of the required statistics, target empty runs were made to determine the relative rates of target full and target empty runs. From the rates, a decision was made as to how much time could be allocated to target empty and target full runs. Generally, the time spent on target out runs, t_B, was calculated by,

$$t_B = \sqrt{\frac{R}{\alpha}} t_A \tag{2.3}$$

where t_A is the target in time, R is the ratio of target out and target in yield, and α is the ratio of target out and target in beam flux (this is derived in Appendix D). Since at least 6 people were needed to move the detector, angle changes could only be made during the waking hours of the day. Usually, the move was made first thing in the morning followed by an accelerator tune-up so that one angle was measured per day. In some cases, sufficient statistics could be accumulated in several hours so that an angle change could be made in the evening. An attempt was made to avoid detector moves after 22:00, but this was not always possible. These daily time blocks determined the total time available for all target configurations.

The beam current used was largely determined by background rates. There were three sources of background that comprised a major fraction of the raw data rate detected by BUNI: low energy scattered photons, electrons and neutrons. The bremsstrahl spectrum is a continuum that is heavily weighted towards low energies. These low energy photons are far below energies of interest but also have a larger scattering cross section, so that they represented a substantial background problem It was possible to reduce the amount of low energy photons by placing a beryllium beam hardener in the beam. This hardener consisted of three 7 cm diameter, 2.5 cm thick beryllium pucks inserted in the steel plate precollimator (see Figure 2.40). This was done only once, at 160 MeV, 20 degrees because the usual methods of dealing with background were inadequate.

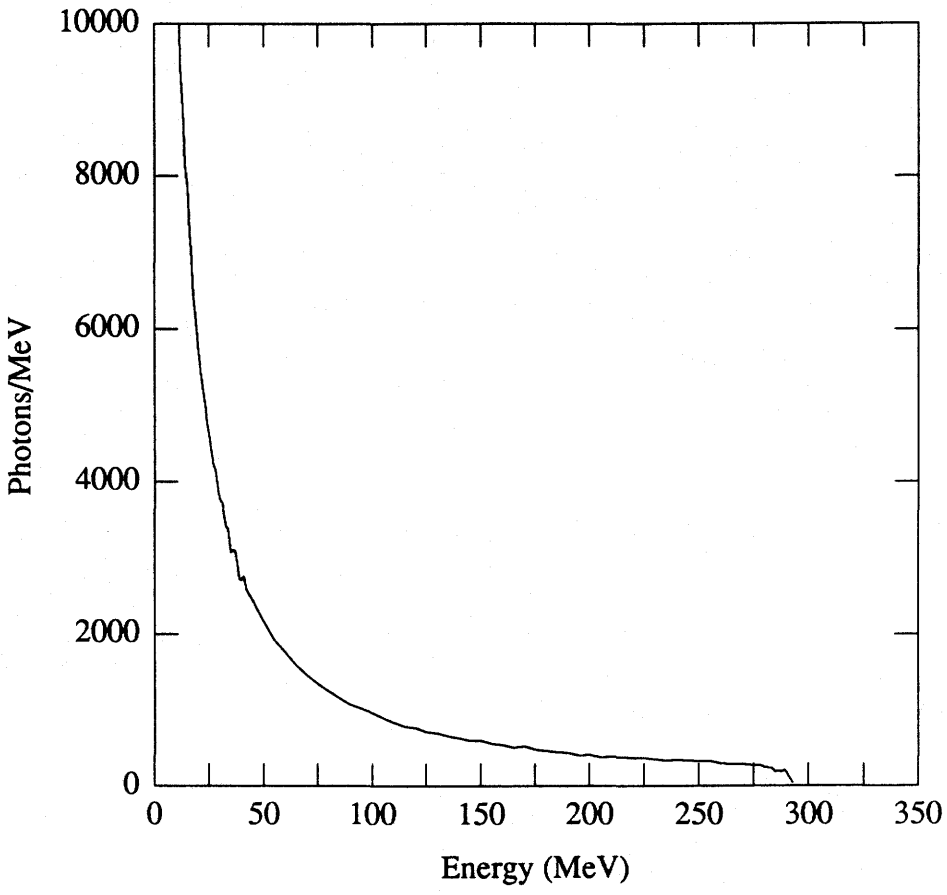

Figure 2.39: Bremsstrahlung Spectrum from 291 MeV Electrons

Pair produced electrons could be vetoed but they had to be considered for the background event rate. Thermal, slow, and fast neutrons were produced copiously in the electron beam dump, collimator, target and photon dump. EA2 was small enough and the flux high enough that the "neutron soup" in the room could overwhelm BUNI if the room and BUNI were not shielded.

These backgrounds had two adverse effects on BUNI. For raw event rates approaching 100 kHz, sampled with a lower threshold near 0.5 MeV, the PMT gains shifted rapidly. The data rate was easy to monitor with the visual scalers so this was not

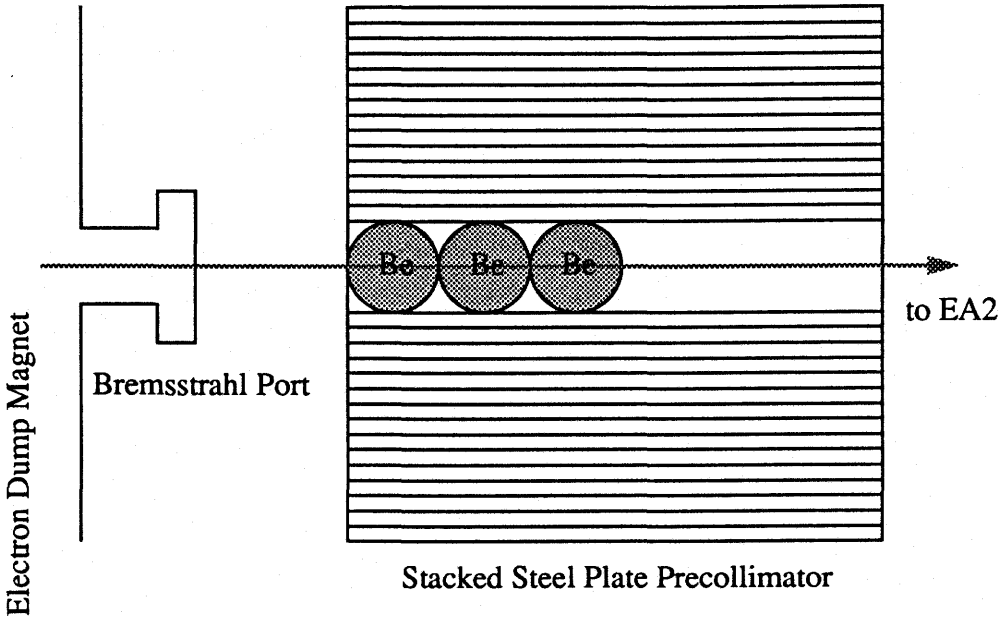

Figure 2.40: Placement of Beryllium Beam Hardener

necessarily a serious problem. However, the scalers were not interlocked and accidents did happen. On one occasion BUNI gains dropped suddenly and slowly recovered over a period of a week.

The more serious effect of the background was to cause pileup, where the detected energy gets shifted by some fraction of the energy of a nearly simultaneous background event. This leads to an effective loss of energy resolution and can change the count rates in regions of interest in energy spectra.

Pileup was dealt with on two levels. The pileup level could be monitored and the photon flux moderated to maintain some acceptable level. The primary monitors were the core PMT ADC pedestals. Since these events were randomly triggered at rates roughly the same as the data event rate, the resulting spectra would reflect the accidental coincidence distribution. For low background rates, hence low pileup rates, the pedestal spectrum would just be a spike occupying 1 or 2 ADC channels. For increasing background rates, this spike would suffer increasing distortion with a tail developing toward higher

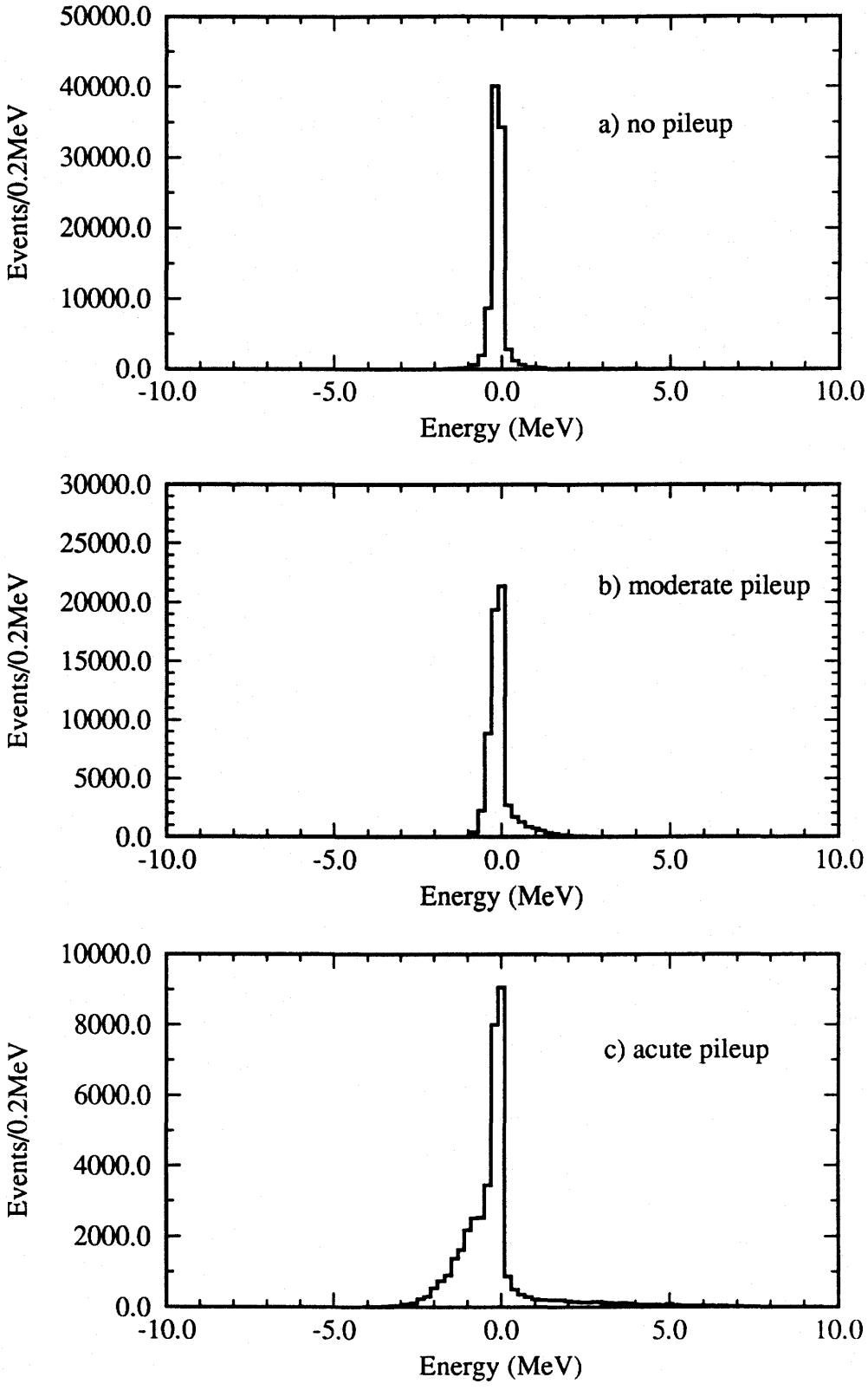

Figure 2.41: Pedestal as Pileup Monitor

energies from the background pulse. At extreme rates, a shoulder develops on the low energy side due to either the overshoot or the slow recovery time of the AC coupled charge integrating ADCs from a previous pulse. The fraction of events in this tail from the total triggered pedestal events corresponds to the pileup rate.

The second level of dealing with pileup is by rejection. Since this means a drop in efficiency, this option must be avoided by ensuring, through monitoring, that pileup levels be minimized during data taking. However, pileup rejection is possible using the waveform digitizer for the core, and delayed gate time sampling ADCs and delayed start TDCs for the quadrants (see Section 2.6.1)

2.8.2 Run Synopsis

Measurements were made in 5 run periods between November 1988 and April 1990. The Dec 1989 run and part of the Mar/Apr 1990 run were for the hydrogen component of the experiment and are discussed in detail in [Amendt 91, Hallin 93]. Angular distributions for carbon and helium were measured at 159.58, 196.0, 198.0, 248.0 and 291.10 Mev electron energies. Each angular distribution consisted of a base set of data point of angles at about 20, 30, 45, 60, 90, 120, and 145 degrees. Data at additional angles were taken when a distribution required more detailed study, particularly at 105, 110, 130, or 135 degrees. Such was the case for He where one previous measurement [Austin 86] seemed to indicate an upturn at back angles. The energies, angles, and run times are tabulated in Table 2.1 to Table 2.7.

Table 2.1: List of Data Points: Mar/Apr 1990: 159.58 MeV Electron Energy

Target	Angle (degrees)	Target Thickness (g/cm^2)	Tube To Post Distance (cm)	Target Full Time (s)	Target Empty Time (s)
He	20.00	1.58	147.60	85494	30195
He	40.20	1.58	79.60	45737	21800
He	60.88	1.58	87.80	35368	14449
He	89.85	1.58	49.30	11876	4616
He	119.98	1.58	66.60	8382	2198
He	145.28	1.58	113.70	11865	2632
C	20.00	1.60	147.60	53419	14447
C	40.20	1.60	79.60	59275	16651
C	59.68	3.98	69.10	35747	12987
C	89.85	3.98	49.30	13080	3001
C	119.98	3.98	66.60	35733	3237
C	145.28	3.98	113.70	26040	4401

Table 2.2: List of Data Points: Nov/Dec 1988: 196 MeV Electron Energy

Target	C.M. Angle (degrees)	Target Thickness (g/cm^2)	Tube To Post Distance (cm)	Target Full Time (s)	Target Empty Time (s)
He	18.73	1.58	162.10	13225	10748
He	30.0	1.58	152.88	8315	5061
He	45.0	1.58	83.19	8393	2726
He	60.0	1.58	85.09	8525	4224
He	120.25	1.58	46.80	15812	5051
C	18.73	1.60	162.10	7121	6727
C	30.0	1.60	142.88	6907	3205
C	45.0	1.60	83.19	8882	2958
C	60.0	3.98	85.09	2454	3502
C	60.0	1.60	85.09	3268	3502
C	90.27	3.98	42.00	17670	1987
C	120.25	3.98	46.80	5152	3384
C	150.0	3.98	79.40	13458	4063

Table 2.3: List of Data Points: Feb/Mar 1989: 198 MeV Electron Energy

Target	C.M. Angle (degrees)	Target Thickness (g/cm^2)	Tube To Post Distance (cm)	Target Full Time (s)	Target Empty Time (s)
He	30.0	1.58	139.86	9011	3100
He	90.00	1.58	46.80	14113	3322
He	104.67	1.58	62.23	7220	2275
He	131.63	1.58	71.91	7185	4083
He	143.85	1.58	123.19	18636	4887
C	30.0	1.60	139.86	7426	2411
C	90.00	3.98	46.80	5464	2007
C	90.00	1.60	46.80	7093	2007
C	104.67	1.60	62.23	3408	847
C	131.63	3.98	71.91	9029	3650
C	143.85	3.98	123.19	10371	2600

Table 2.4: List of Data Points: Feb/Mar 1989: 248 MeV Electron Energy

Target	C.M. Angle (degrees)	Target Thickness (g/cm^2)	Tube To Post Distance (cm)	Target Full Time (s)	Target Empty Time (s)
He	20.0	1.58	160.10	13657	3288
He	30.07	1.58	150.20	12893	3103
He	45.07	1.58	122.50	14551	2090
He	56.75	1.58	83.66	11058	2651
He	90.10	1.58	42.80	9966	3601
He	104.67	1.58	62.23	10498	2627
He	119.67	1.58	52.10	15829	2806
He	129.33	1.58	76.52	9979	3014
He	146.48	1.58	124.10	16137	6213
C	20.0	1.60	160.10	21949	2270
C	30.07	1.60	150.20	6633	1437
C	45.07	1.60	122.50	7730	698
C	59.92	1.60	93.66	12412	2181
C	91.02	3.98	42.00	13043	934
C	104.67	1.60	62.23	4213	1497
C	119.67	3.98	52.10	9105	2382
C	129.33	3.98	76.52	11224	1736
C	146.48	3.98	124.10	7433	2086

Table 2.5: List of Data Points: Sept/Oct 1989: 291.10 MeV Electron Energy

target	C.M. angle (degrees)	Target Thickness (g/cm^2)	Tube To Post Distance (cm)	Target Full Time (s)	Target Empty Time (s)
He	19.97	1.58	156.1	38960	4553
He	30.12	1.58	139.7	21744	3088
He	45.00	1.58	137.6	26497	9818
He	65.75	1.58	110.8	14653	4785
He	89.35	1.58	48.8	20500	5857
He	120.17	1.58	60.6	29897	8003
He	144.58	1.58	128.1	18392	8729
C	19.97	1.60	156.1	14115	2322
C	30.12	1.60	139.7	25914	6730
C	45.00	1.60	137.6	11273	3711
C	65.75	1.60	110.8	19188	2799
C	89.35	1.60	48.8	18121	3936
C	90.05	1.60	49.6	12303	5024
C	120.17	3.98	60.6	17333	5814
C	144.58	3.98	128.1	25716	8635

Table 2.6: List of Data Points: Dec 1989: Proton Compton Effect

Electron Energy (MeV)	C.M. Angle (degrees)	Tube To Post Distance (cm)	Target Full Time (s)	Target Empty Time (s)
293.42	31.38	104.85	25207.00	14014.00
293.42	49.10	79.40	19972.00	7882.00
293.42	72.18	65.00	17567.00	7543.00
293.42	90.98	49.50	15065.00	5865.00
293.42	122.58	51.50	10603.00	7490.00
293.42	144.00	75.30	23598.00	15471.00
239.88	30.23	104.84	85698.00	26688.00
239.88	53.47	65.20	25042.00	7171.00
239.88	88.86	52.60	10824.00	8288.00
239.88	119.16	50.20	7919.00	8621.00
239.88	139.62	78.90	17943.00	15615.00
239.88	142.03	66.60	20179.00	13885.00

Table 2.7: List of Data Points: Mar 1990: Proton Compton Effect

Average Photon Energy (MeV)	C.M. Angle (degrees)	Tube To Post Distance (cm)	Target Full Time (s)	Target Empty Time (s)
200.22	30.69	105.30	80170.00	38912.00
200.22	59.45	63.30	25930.00	18943.00
200.22	89.47	47.90	73079.00	28883.00
200.22	113.49	50.80	21271.00	15629.00
200.22	141.08	76.80	19905.00	13193.00
181.10	67.21	69.00	15621.00	7264.00
169.78	66.69	69.00	3947.00	5986.00
172.86	140.47	69.30	13173.00	8944.00
172.86	91.23	52.50	29295.00	13430.00
172.86	50.94	67.30	48257.00	31816.00

Chapter 3. DATA ANALYSIS

The on-line analysis presented enough information to give the experimenter confidence that the equipment was working properly and that data, background, and pileup rates were acceptable. In these circumstances, a full analysis to extract cross sections was impractical. A thorough analysis is only possible in off-line analysis and is the subject of this chapter.

3.1 Backup Tapes and Filtering Data

Backup copies of all data tapes were made as soon as possible. For the early runs some tapes were difficult to read because at that time 8mm digital data tape technology was quite new. A total of 86 tapes with about 1 Gigabyte of data each were written during the experiment and each copy took from 4 to 6 hours, so every failed copy represented a noticeable setback. However, all such tapes were salvaged with the help of the manufacturers of the drives and with improvements in design. After copying, the original tapes were stored, hopefully to remain unused.

There was extraneous data stored on tape. The hardware trigger threshold was set at about 80 MeV which was considerably below any region of interest in the total energy spectra. This was because the core signal was used as a trigger and many events deposited energy out of the core into the quadrants. Also, no events were rejected in hardware by cosmic veto detectors. So a sizeable fraction of events on tape were cosmic rays, events too low in energy to be of interest, or charged particles in the acceptance of the detector.

To make the volume of data on tapes more manageable, the data were filtered using a custom C language program, **filter7**[1], written around LUCID subroutines that rejected undesired events and wrote the remainder to a new tape.[2] A cut was made on the cosmic ray veto counters at a threshold that would eliminate about 90% of the cosmic background (see Figure 3.1). This threshold was intentionally inefficient because the thresholds could not be accurately determined at this stage of analysis. This threshold will be optimized in later analysis. Note that a majority of the low energy events in Figure 3.1, which is a histogram for one veto counter, are due to cosmic rays that passed through a neighboring veto counter or another veto counter altogether. Eventually, events that are rejected by other counters will deplete all but 10% of the low energy events for this histogram.

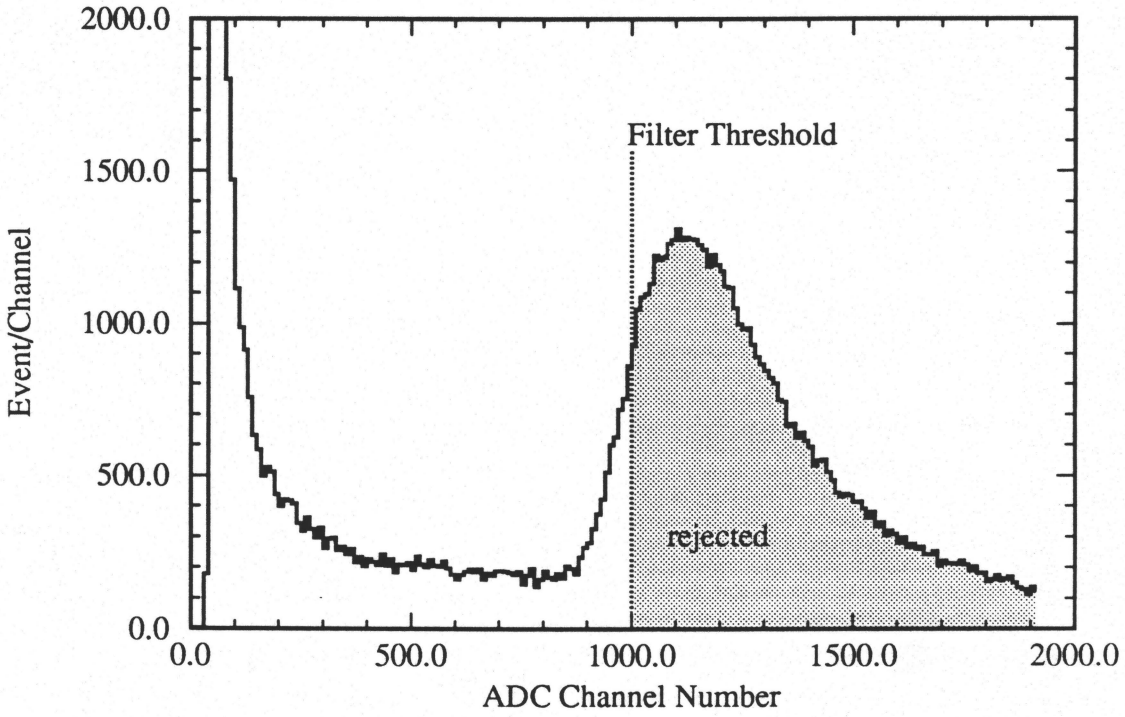

Figure 3.1: Cosmic Ray Veto Cut on Annulus Tube 0

1. Filter7 was written by Dr. Emil Hallin for this experiment.
2. At the time that the filtering was being done, LUCID was still not capable of writing data to tape in off-line analyses. This capability has, since then, been installed and LUCID is now routinely used for filtering data.

Another cut to eliminate useless events was a total energy cut at about 70 MeV down from the endpoint (shown shaded in Figure 3.2). Again, the actual energy of this threshold was approximate since the crude on-line calibrations were used to determine the energy of photons. Since the π^0 decay spectrum is largest at low energies, this reduced the photon

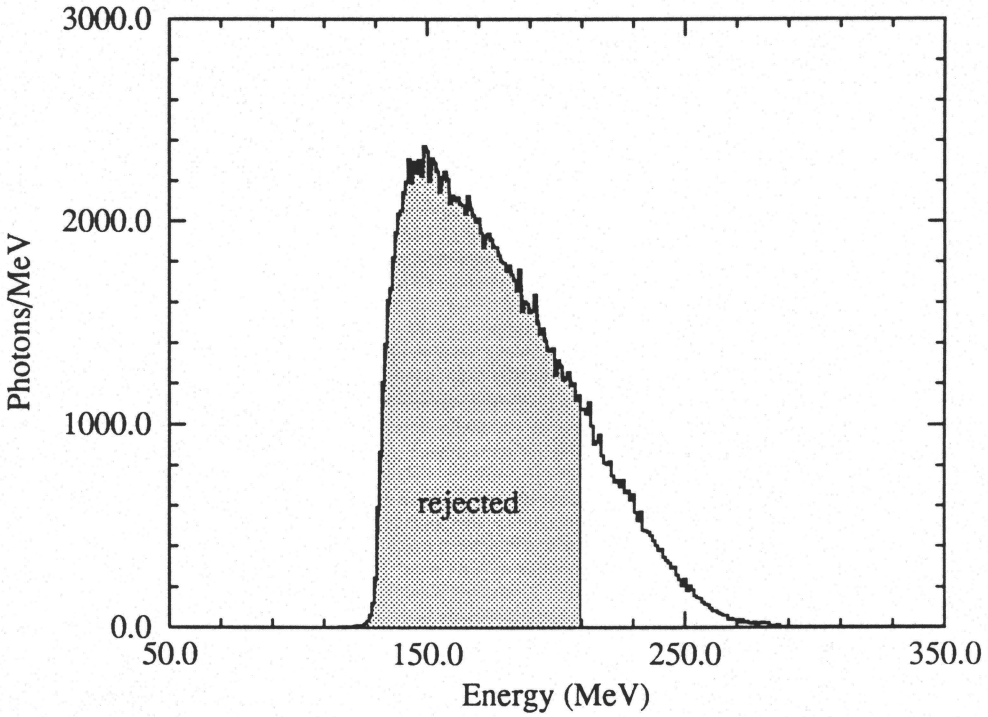

Figure 3.2: Total Energy Cut

related data volume by 80%.

The flasher and Two Inch events were retained on output data tapes for future gain compensation schemes. As a result the data volume was reduced to only 50% rather than the expected 70%. Fortunately, this extra bulk of data required little data processing and a significant net analysis speed increase was obtained in later replays.

As well as transferring "good" events to the output tape, histograms of other events were formed during filtering. Some of these were written to a disk file for fitting after filtering was finished, others were fit by the filter program at the end of each run and then the results were written to a file.

For each run, histograms were built up for the Two Inch NaI source spectra and flasher pulse height spectra, and saved in a file for subsequent fitting. The Two inch NaI fits typically yielded four apparent peaks, of which the 2.62 MeV peak was of interest (see Figure 3.3). The flasher pulse height spectrum almost always had a single well defined peak (see Figure 3.4) so fitting was easy. Fit results were written to files for later extraction of peak position values.

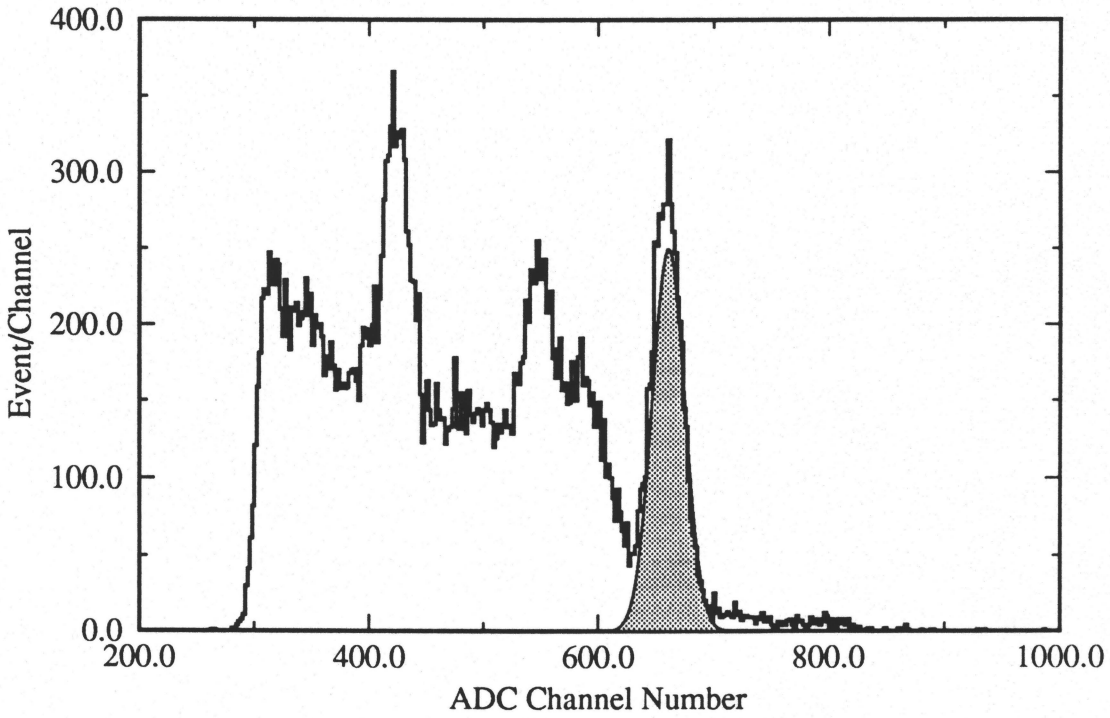

Figure 3.3: Two Inch NaI Spectrum and Fit

Since calibrations would eventually require pedestal subtraction also, these data were extracted during filtering. The pedestal typically occupied no more than two channels, so a simple maximum height peak position was extracted for all detectors. A mean position

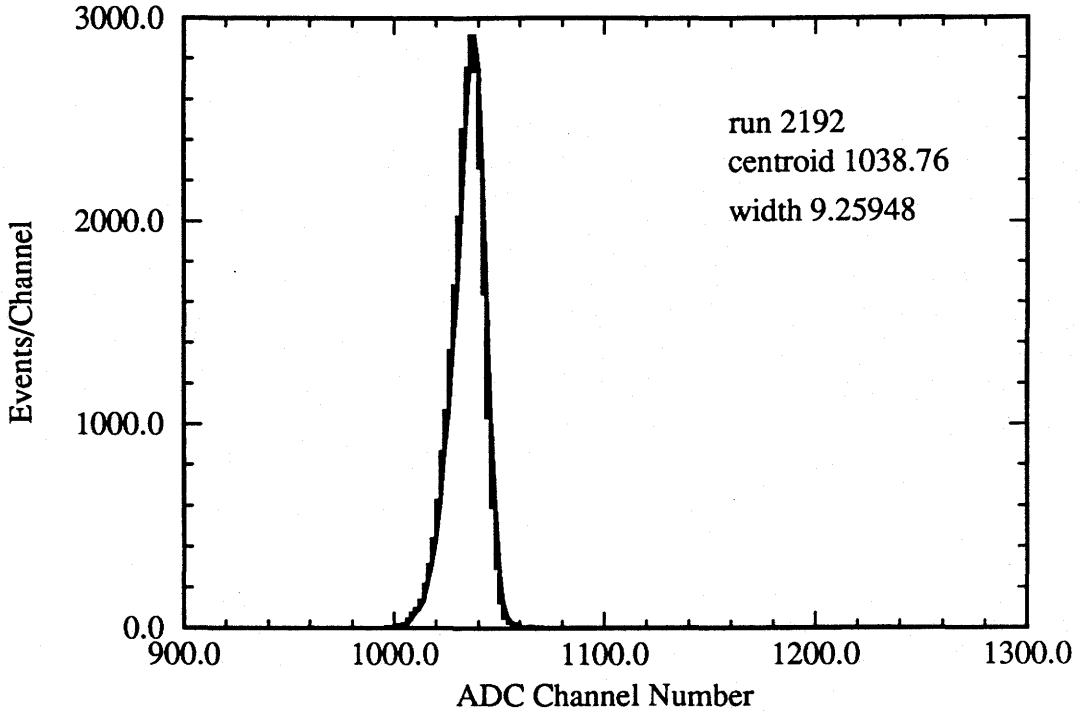

Figure 3.4: Flasher Spectrum and Fit

was not used because if the pedestal suffered from an asymmetric distortion, like pileup, the mean value would be offset from the true pedestal position. However, the mean position could be compared to the maximum value position to verify that the peak searching algorithm was working properly.

Every core event triggered a low energy and high energy quad readout, and every low energy quad event triggered a high energy quad readout. Hence, nearly every data and calibration run contained a large number of events in which low energy events (up to 10 MeV) registered in both low and high energy ADCs of the quadrants. A linear least squares fit of low E quad ADC readout versus high E quad ADC readout was performed for each run for cross calibrations later on (see Section 3.2.2).

The fit, pedestal, and cross calibration files were filtered to extract peak positions using a C program, **filter2list**, which wrote the results to a list file for use in gain compensation calculations (Section 3.2.3). The correct Two Inch NaI peak was selected according to whether a peak was above ADC channel 590, if the chi-squared of the fit was

less than 2.0, and if the uncertainty of peak position was less than 1.2 channels. For the flasher, as long as the width parameter was non-negative (a negative width indicated a failed fit) and the peak position was below 2000 channels, the position was accepted. In the cases of double peaking, the cause was usually physical activity near the flasher during accesses, and the secondary peak was less well defined. Then the peak with the narrower width was chosen.

Since the filtering process rejected events but did not decrement the scaler counts for these events, accepted and total events had to be counted for eventual deadtime calculations. In particular, the accepted and discarded cosmic count and the number of total, accepted and discarded core, flasher and reference source events were output to files for later use.

3.2 Calibrations

The information required for computing the change in gains on a run-by-run basis was extracted in the filter pass as discussed in the previous section. The next piece of information needed was the absolute gains from the calibration runs. This was obtained from a calibration pass of data tape replays. Data was replayed using LUCID in off-line analysis mode, schematically shown in Figure 3.5. Basically, the Build software generated a tape/file Reader instead of a FEP and its corresponding Reader. The format of data stored on a LUCID data tape is written on that tape so the build uses the tape instead of a Reader description file. For this analysis, the data was already filtered so a Writer was not required either. However, the Looker description file is still required. The core code of the off-line Looker was not much different than the on-line one. The major difference was that all events were examined, and as a result, the tape playback time was longer than the on-line analysis.

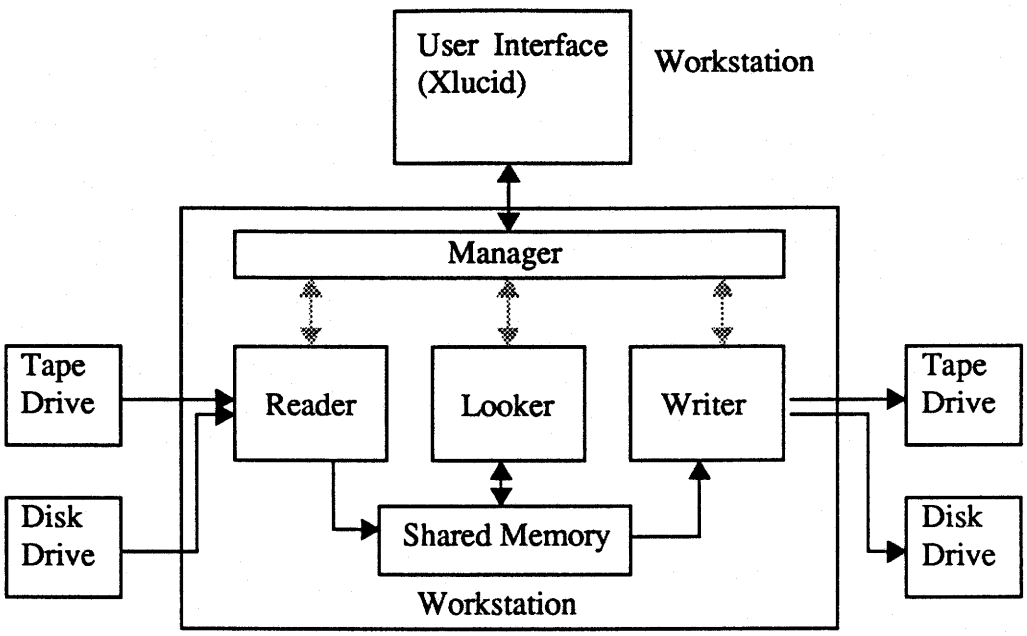

Figure 3.5: Schematic Representation of Off-line LUCID Processes

In parallel with this pass, was a preliminary replay pass through all filtered tapes to extract the quantameter calibration, cosmic veto thresholds, and waveform digitizer parameters. These parameters were necessary for the final playback of data tapes.

3.2.1 Core Calibration

The energy calibration of acquired data was the primary concern of this analysis. A one percent error in energy calibration corresponded to a 1.5 to 3 MeV shift of the endpoint. This could easily result in a factor of 10 change in the final cross section. Since most of the energy of a photon detected by BUNI was deposited in the core, the greatest care was taken with core calibration.

3.2.1.a Zero Degree Data

The core was calibrated using zero degree data which were essentially direct measurements of bremsstrahlung spectra. Pulse height spectra from each core PMT for these runs were produced and written to files for each run in the calibration pass of tape replays. The only definitive feature in the bremsstrahlung spectra were the endpoints. The most reli-

able way of extracting the endpoint was to fit a modelled spectrum to the pulse height spectra. The software required to do these fits had to satisfy several requirements. It had to accommodate a table of numbers for the fit function because the input spectrum varied in a way that could not be easily expressed algebraically. It had to adjust an x-axis scale parameter, corresponding to the gain factor being sought, for this histogram. And, since pileup was a possibility, it had to be able to convolve a secondary spectrum with the fit function. These are not typical requirements. Thus a series of custom programs were written around a standard weighted least squares algorithm. The principle was to calculate first and second derivatives, analytically if possible, of χ^2 and vary each parameter using Newton's method. It is the derivatives that the user must supply and these can be complicated, especially if convolution was involved (see Appendix B).

The model spectra for fitting were generated with a series of EGS (Electron Gamma Shower [Nelson 85]) Monte Carlo simulations. Bremsstrahlung spectrum curves were generated by an EGS simulation called **brem** that simulated the beam line layout from the radiator to the beam dump. Because the lead attenuator filter used for these runs had an energy dependent effect, EGS simulations were run for monochromatic photons at 10 MeV intervals to model the dependence. Simulating photon transmission through 4 inches of lead results in poor statistics so 1 inch of lead was used and the transmission coefficient scaled exponentially. These coefficients were spline fitted to produce a transmission curve with the same intervals as the **brem** curves (see Figure 3.6). Another EGS program, **buni_sim**, was written to simulate all the elements in the acceptance of BUNI and showers in BUNI, and used the modified bremsstrahlung spectrum as input. **Buni_sim** could produce histograms for all regions coded, particularly the core of BUNI. This histogram was used as the function to fit to the Zero Degree core data.

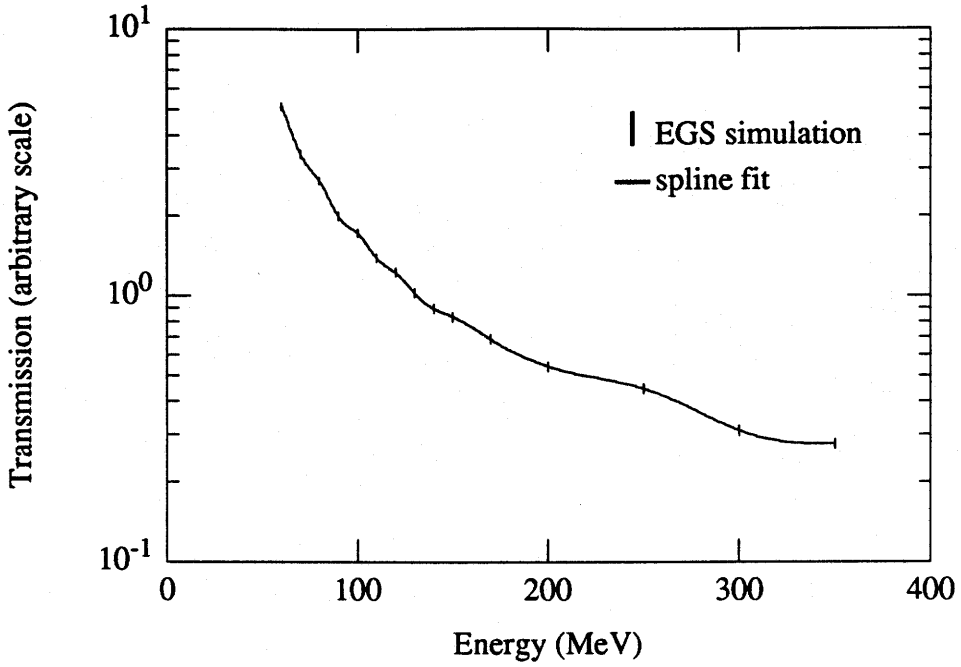

Figure 3.6: Transmission of Photons through 4 inches of Lead

Fitting proceeded in stages. The first iteration was done with an extremely crude first guess. This was an automated pass, a Unix shell script running the fitting program, **endfit**, for each calibration run, in a region 20 MeV from the endpoint, and writing the results to a file. Fits were made with a weighted least squares (χ^2) algorithm described inAppendix B. The resulting fit histograms were manually compared to the corresponding data by eye to determine if the fits had converged on a reasonable solution. If not, the errant fit was retried manually with a different (and usually more reasonable) first guess. The fit parameters from first iteration were used as initial guesses to the second iteration. Figure 3.7 shows a successful fit. The shape near the endpoint, which was the most important region, fits well and the fit is good for a large energy range. This was an indication that the simulation code accurately emulated BUNI's response.

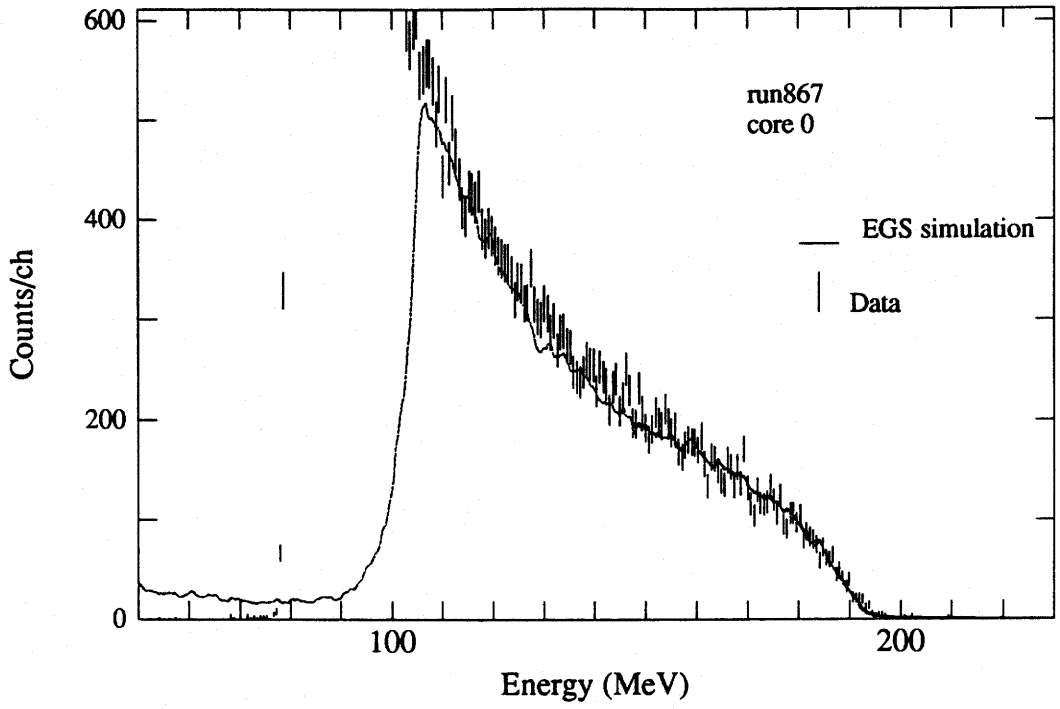

Figure 3.7: EGS Fit to Zero Degree Spectrum with 195.2 MeV Endpoint. The drop at low energies in both spectra are thresholds.

Because some runs had noticeable pileup, a third pass fit was run using a fitting program with pileup simulated in it. Since pileup had the effect of moving counts from one bin to others around it, the function spectrum was convoluted with the pileup spectrum. Since the energy calibration and the pileup fraction were being adjusted, this convolution was computed at every iteration.

After many trials with data in which different first guesses were used, and trials with mock data, a systematic uncertainty of 0.5 MeV was estimated for the calibrations determined by the fitting program. When all core calibration fits were finished, the calibration constants were stored in a file for gain stabilization computations (Section 3.2.3).

3.2.1.b Electron Scattering Data

The 291 MeV data were calibrated by the electron scattering measurements. The procedure for this analysis was an analogue of the Zero Degree analysis. Data from electron scattering was only filtered in the sense that the gain stabilization information and the other easily extracted information were obtained. The filtered data were not used for further analysis because the filtering process rejected charged particles passing through the Front Mid cosmic veto and because the majority of events were near the electron energies. Pulse height spectra were extracted in a replay pass but with the Front Mid cosmic veto and the three thin aperture vetoes disabled so that the electron events would not be rejected.

The modelling for this was much more simple than for the bremsstrahlung calibration scheme. The kinematics was computed for the scattered electron and the energy deposition histogram accumulated for events depositing energy in the core in the EGS simulation of BUNI. Since all of the material in the acceptance of BUNI was included in the simulation, the energy loss and straggling effects were accounted for in this histogram. The fitting procedure was the same as for the bremsstrahlung fitting procedure.

3.2.2 Quadrant Calibration

The quadrants were calibrated by fitting to the peaks of a Thorium-C source in low energy quadrant pulse height spectra from quadrant calibration runs. The source data was taken at nearly every angle change (51 measurements), so quadrant calibrations were obtained more frequently than core calibrations. The calibration replay of these runs produced histogram files for each run, for each of the 12 phototubes, with each spectrum containing 4 to 6 viable peaks. A typical spectrum is shown in Figure 3.9. To ensure that the background under the calibration peak (shaded Gaussian) did not bias the extracted centroid, the whole spectrum was fit using a weighted least squares (χ^2) algorithm. Complications occurred when it was realized that some runs did not accumulate enough statistics to yield reliable peak information. This was in contrast to Two inch Nai source

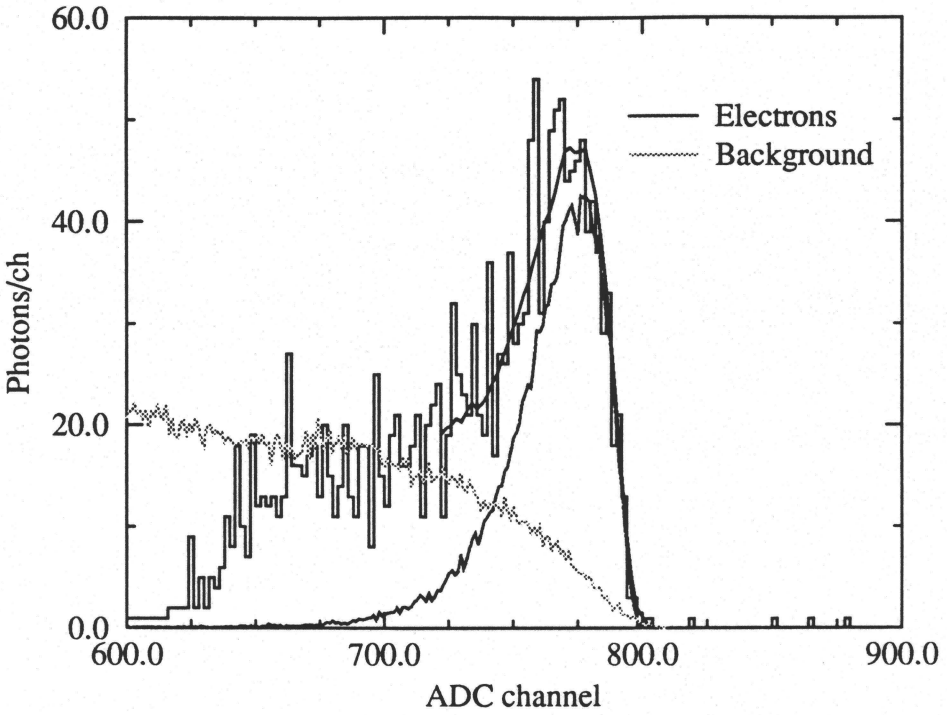

Figure 3.8: EGS fit to Electron Scattering Data at 291.1 MeV

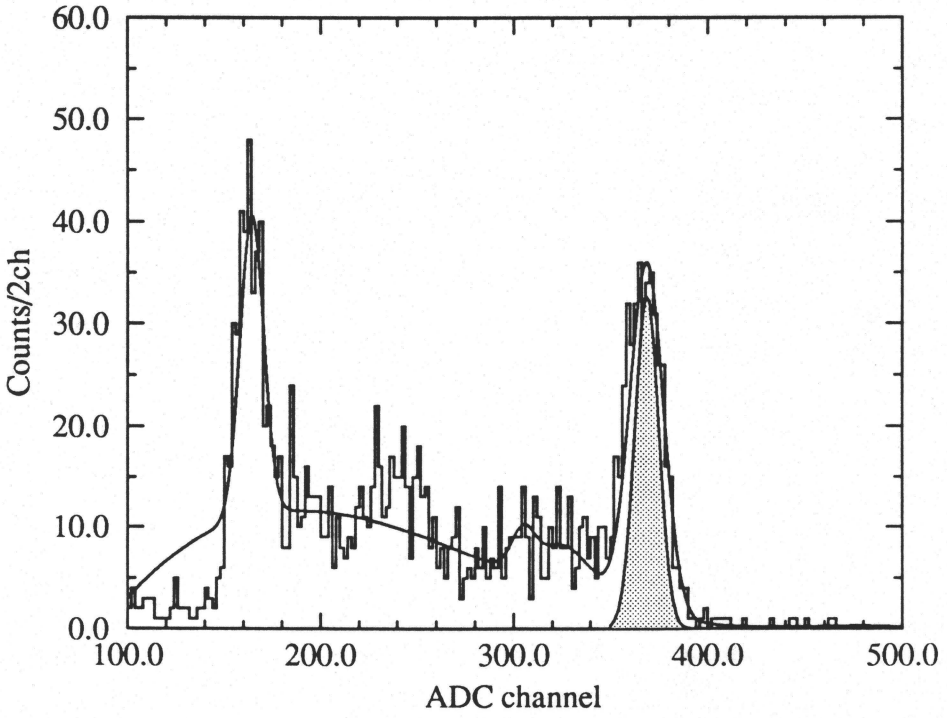

Figure 3.9: Fit to Th-C Spectrum in Quadrant

peak fitting which typically accumulated statistics over periods of hours instead of a period of half an hour typical of quad calibration runs. In some cases, some of the photo-tubes were difficult to fit or could not be fitted automatically. So while the volume of fitting was made manageable by automation, there was still a fair amount of human intervention. The criteria for peak selection also required a lot of tuning because some of the difficult fits either had too large an uncertainty or visual examination of the fit was showed the fit to be unsatisfactory.

The fitting program produced a list of peak positions corresponding to the many peaks found for the Th-C source. To select the correct peak, a similar peak selection algorithm as the Two inch NaI peak selection was used (Section 3.1). A peak had to be above 300 channels, and its reduced chi-squared had to be less than 2.0. The peak at the highest channel that passed these restrictions was chosen. This was supposed to be the 2.62 MeV line for Th-C. There were situations where fits were unsuccessful for individual quadrant PMTs, so that the peak positions were unavailable for them. Then, if only one or two quadrant PMTs out of the twelve were missing, a gain was interpolated from adjacent runs, otherwise the whole run was discarded.

There was no means of calibrating the quadrants for events with quadrant deposition energies above 10 MeV, so the high energy ADC signals were calibrated by scaling the low energy ADC calibration with the cross calibration factors from the filter output.

The final gains from the quadrant calibration runs were written to a file for gain stabilization computations (Section 3.2.3)

3.2.3 Flasher Gain Stabilization and Gain Computation

The flasher and reference source peak positions were extracted, run by run, during filtering. Gains were then calculated for each run by normalizing gains from calibration runs by the ratios of reference source position and of flasher positions from the current run and the calibration runs, in accordance with the stabilization system described in Section 2.5. That is

$$G_c = \frac{P_{2i}}{P_{2c}} \frac{P_{fc}}{P_{fi}} G_i \tag{3.1}$$

where P_{2i} , P_{fi} , and G_i are reference source peak position, flasher peak position, and gain for the calibration run, and P_{2c} , P_{fc} , and G_c are reference source peak position, flasher peak position, and gain for the current run. Because gains had to be calculated for about 1000 runs, a C language program, **list2gain**, was used to read base gain files, the peak position file and the list file, and the gains for all NaI PMTs were written to a file for each run for use in the final replay of data tapes. In the cases where some runs were lacking sufficient input (e.g. Two Inch NaI source fit failures), the gain of the nearest run was used. A test of the success of this compensation was to plot gains from Zero Degree calibration against the gains computed from the gain monitoring data (Figure 3.10). The gains track from initial calibrations to final calibrations for each run period.

3.2.4 Quantameter Calibrations

3.2.4.a Photon Data

As mentioned in Section 2.7.4, one method of quantameter calibration was to measure currents from flux monitors of known calibration using BUNI as a reference. For this, only the energy spectra and scaler counts were necessary from the playback of the data. The calibration of the P2 chamber was assumed to be the standard as documented in [Pruitt 62]. The absorption of photons in the P2 was modelled by EGS. The absorption spectrum was convoluted with the bremsstrahlung spectrum and the resulting spectrum was used in evaluating the integrals in Equation 2.2. N_γ was computed by scaling the P2

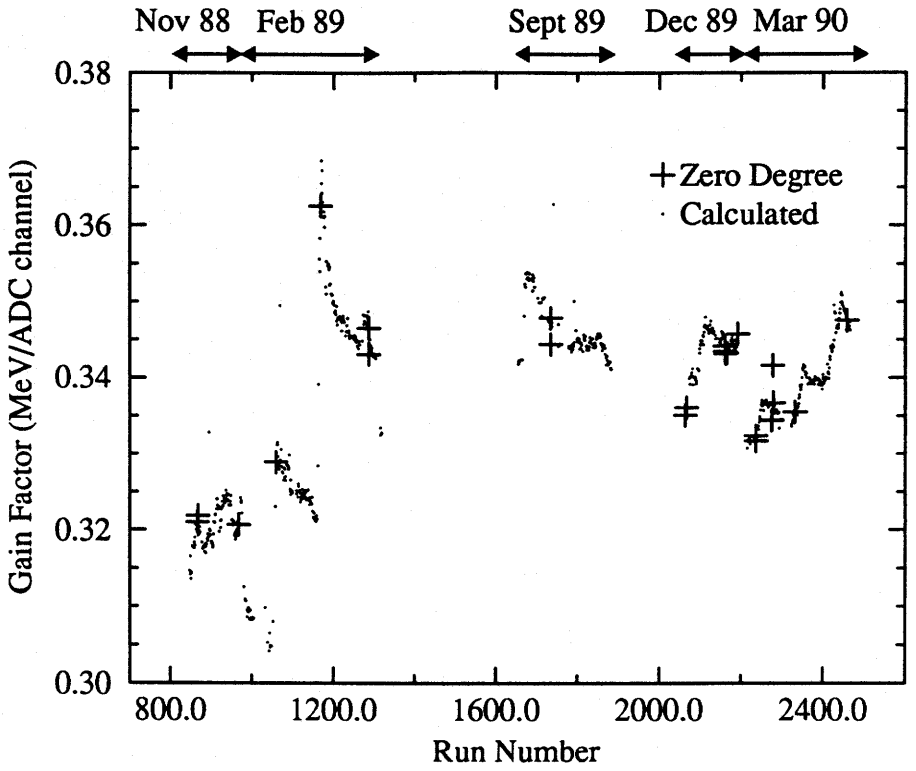

Figure 3.10: Gain Factor from Gain Monitoring and Zero Degree Calibrations for Core PMT 1

photon count. The ratio of this photon count and the integrals was the quantameter calibration. This analysis is detailed in [Delli Carpini 90], and yielded a quantameter calibration of $(1.02 \pm 0.03) \times 10^{19}$ MeV/Coulomb.

3.2.4.b Electron Scattering Data

The analysis of quantameter calibration by electron scattering was similar to the core calibration by electron scattering (Section 3.2.1.b), except that the total energy spectra were the primary concern. The detector calibrations were installed in the analysis software, and a total energy spectrum was produced. Yields were extracted from the spectrum or from a fit to the spectrum.

Equation 2.2 must be altered for use with mono-energetic electrons. The energy spectrum shape is now $\delta(E_e)$ to within 0.01% [3], where E_e is the electron energy, and the trans-

3. L. Dallin, private communication

mission spectrum is assumed to be unity because most of the beam line was in vacuum. Then the particle count simplifies to

$$N_e = \frac{U_q Q}{E_e}. \tag{3.2}$$

The BUNI electron count for the quantameter is related to the total electron count by the Purple Pig yield by

$$N_e = \frac{C_q}{C_{PP}} \frac{Q_{PP}}{1.602\times10^{-19}} \tag{3.3}$$

so that the quantameter calibration is found by

$$U_q = \frac{C_q}{C_{PP}} \frac{Q_{PP}}{Q} \frac{E_e}{1.602\times10^{-19}} \tag{3.4}$$

There were some complications. One problem was an unexplained background, even after accounting for inelastically scattered electrons. The magnitude of the background was energy dependent, being larger for the 291 MeV spectra than the 201 MeV spectra. Since this background was not fully understood, its contribution could only be estimated. It was assumed that the background was roughly triangular in shape under the electron peak since this was the region of maximum accelerator energy. Then a rough estimate for the background contribution was about 2% for 201 MeV spectra, and about 17% ± 5% for the 291 MeV spectra. The results of this analysis are shown in Table 3.1.

Table 3.1: Quantameter Constants from Electron Scattering

Energy	C_{PP}/Q_{PP}	C_q/Q	U_q (x10^{19} MeV/ Coulomb)
200.8	0.05858 ± 0.00096	0.04470 ± 0.00086	0.956 ± 0.025
291.1	0.00538 ± 0.00022	0.00314 ± 0.00029	1.06 ± 0.10

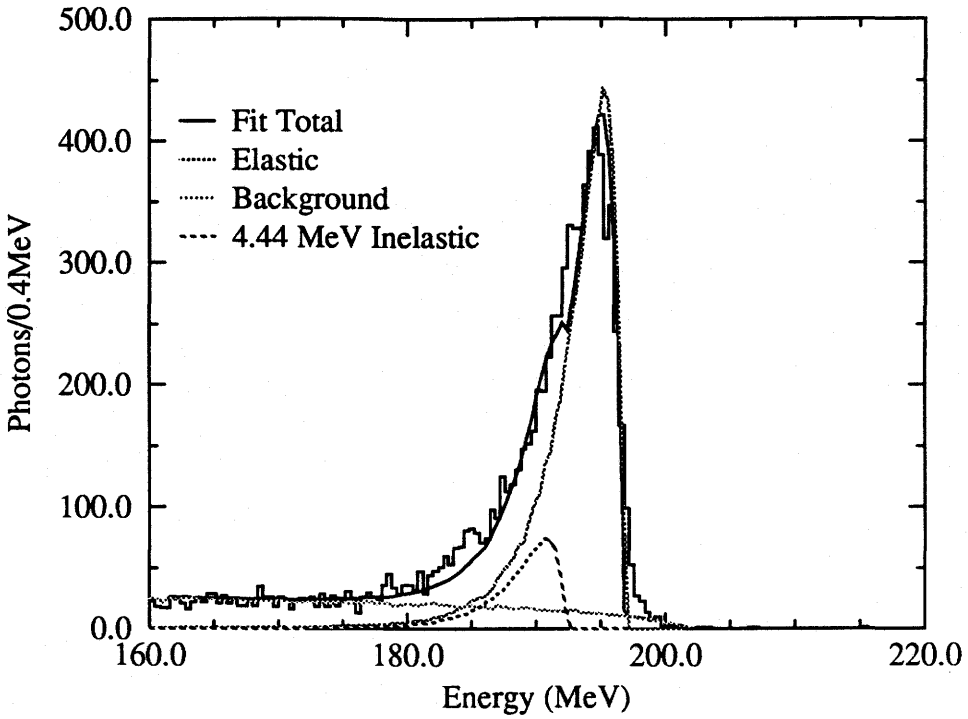

Figure 3.11: 200.8 MeV Electron Scattering Spectrum for Quantameter Calibration

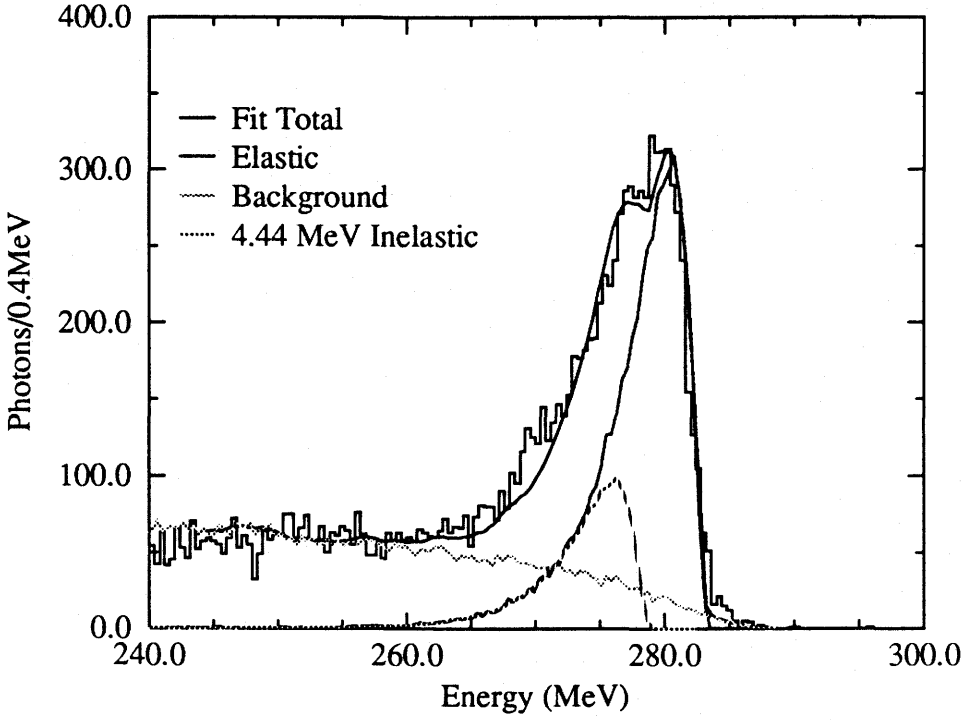

Figure 3.12: 291.1 MeV Electron Scattering Spectrum for Quantameter Calibration

An attempt was made to improve this analysis by fitting to the scattered electron spectra assuming a bremsstrahlung shaped background. These fits used the same EGS simulations as from the calibration of BUNI core PMTs by electron scattering, but the total energy deposition was considered here. The quality of fits was good but yielded similar results as in Table 3.1, and the magnitude of the uncertainties in this analysis

Table 3.2: Quantameter Constants from Fits to Electron Scattering Spectra

Energy	C_{PP}/Q_{PP}	C_q/Q	U_q ($x10^{19}$ MeV/ Coulomb)
200.8	3.242 ± 0.052	2.315 ± 0.037	0.95 ± 0.025
291.1	1.340 ± 0.031	1.400 ± 0.032	1.08 ± 0.08

makes this data unsuitable for accurate determination of the quantameter constant.

However, the more relevant reason for performing the fits was to determine that the detector resolution had not deteriorated. Since there was material in the aperture causing energy loss and straggling, the resolution was extrapolated by comparing widths of simulated peaks with and without that material. The results were consistent with the design and measured values of 1.6% to 1.8% [Miller 88, Booth 90].

3.2.4.c Correlation of Quantameter with Electron Dump

Since the electron beam current was measured by a Faraday cup below the electron dump magnet, it should have been possible to determine the flux of the bremsstrahlen on the target by integrating the charge deposited in the cup, calculating the rate of photon production at the radiator by the corresponding number of electrons, calculating the number of photons that are within the solid angle of the collimator, and comparing that with the output of the quantameter. In practice, this was not possible since the field strength of the electron dump magnet tended to drift periodically, thus steering the beam

towards the side of the Faraday cup in the dump. This made absolute measurements of electron current unreliable. However, the ratio of quantameter current versus the electron dump current provided diagnostic information for the subsequent analysis.

3.2.5 Thresholds for Cosmic Ray Veto Counters

A few runs were made with the beam off and with acquisition running as though they were production runs. These runs accumulated cosmic ray spectra as seen by BUNI and the cosmic veto scintillators but without scattered photons. The BUNI data were used with time normalization for cosmic ray subtraction from data runs. However, cosmic veto scintillator spectra from all runs were used to determine thresholds for cosmic rejection in software. In the preliminary replay pass, histograms were accumulated for the

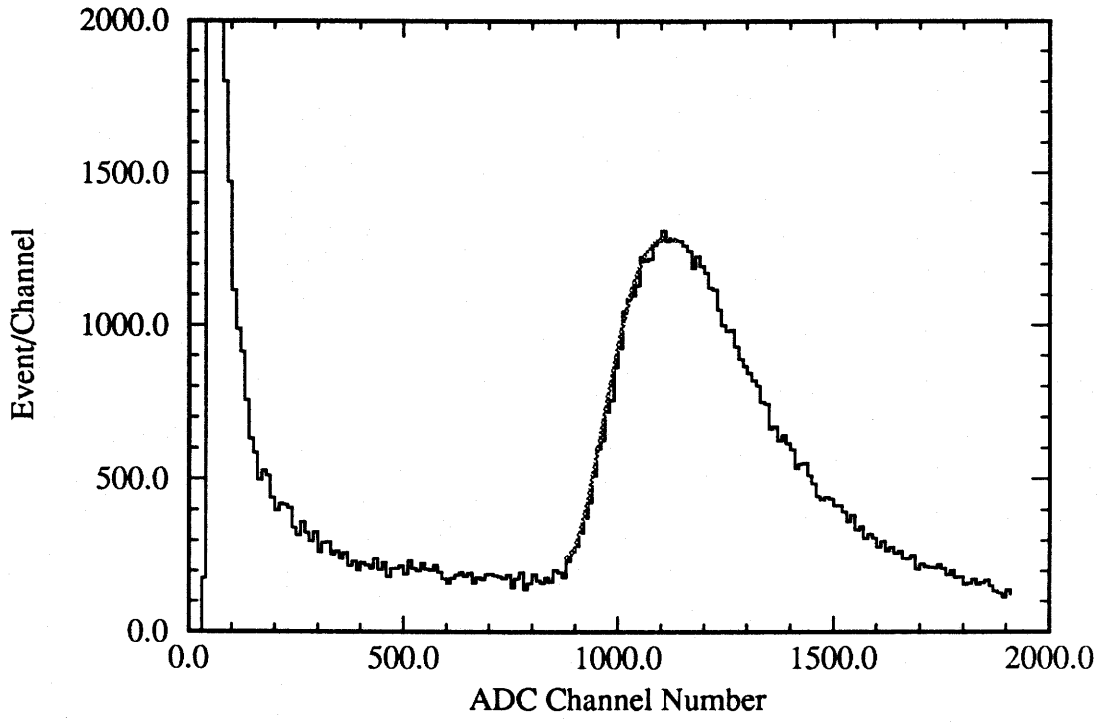

Figure 3.13: Cosmic Veto Scintillator Spectrum (histogram) with Fit (smooth line)

Annulus, Front, and Back cosmic ray veto detectors and written to files at the end of each run. A C language program, **findthresh**, was written to systematically extract these thresholds. Since the spectrum of cosmic rays passing through the vetoes is a broad peak,

the algorithm looked for the ADC channel which was 10% of the height of the peak analogous to a CFD. A fourth order polynomial was fit to the peak, as shown in Figure 3.13, and the channel for the 10% of maximum was computed. After performing these fits on all runs, it was found that there was some drift of threshold values in the annulus vetoes within a series of measurements, but none for the front and back paddle vetoes (see Figure 3.14 and Figure 3.15). The added background from shower leakage reduced the reliability

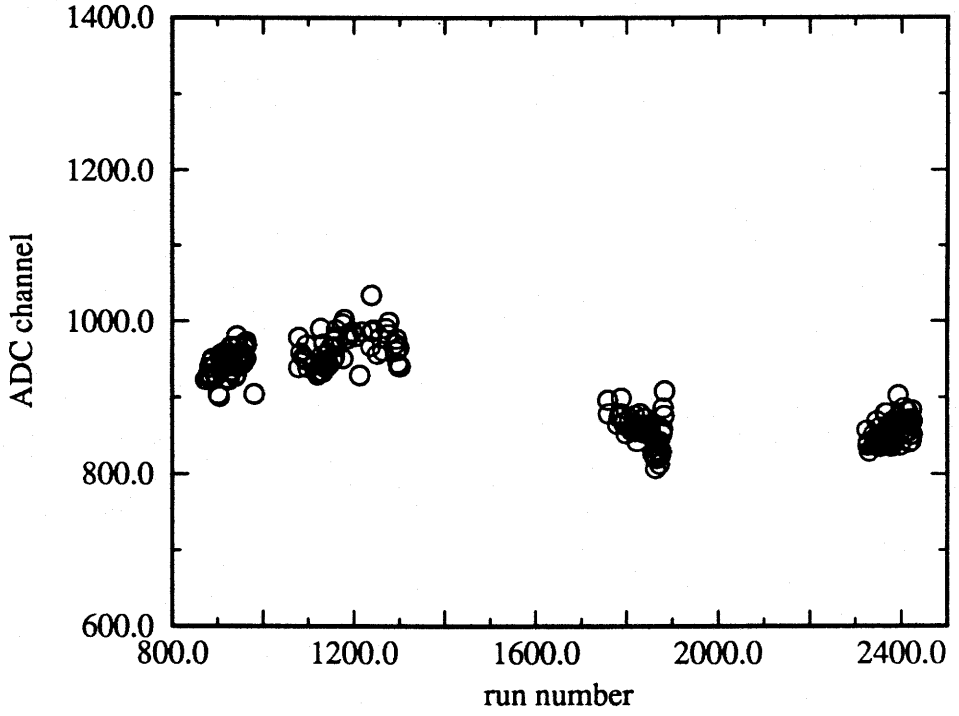

Figure 3.14: Annulus Cosmic Veto 0 Thresholds

of these data. Since a second level of cosmic rejection was available, a small loss in efficiency with the cosmic ray veto counters was acceptable and mean value was taken. This mean was found by making a histogram of the threshold for each cosmic ray veto PMT, then fitting a Gaussian to the histogram (see Figure 3.16). This was done separately for each run period and the peak positions were written to a file containing thresholds for all of the cuts used in the final replay of data tapes.

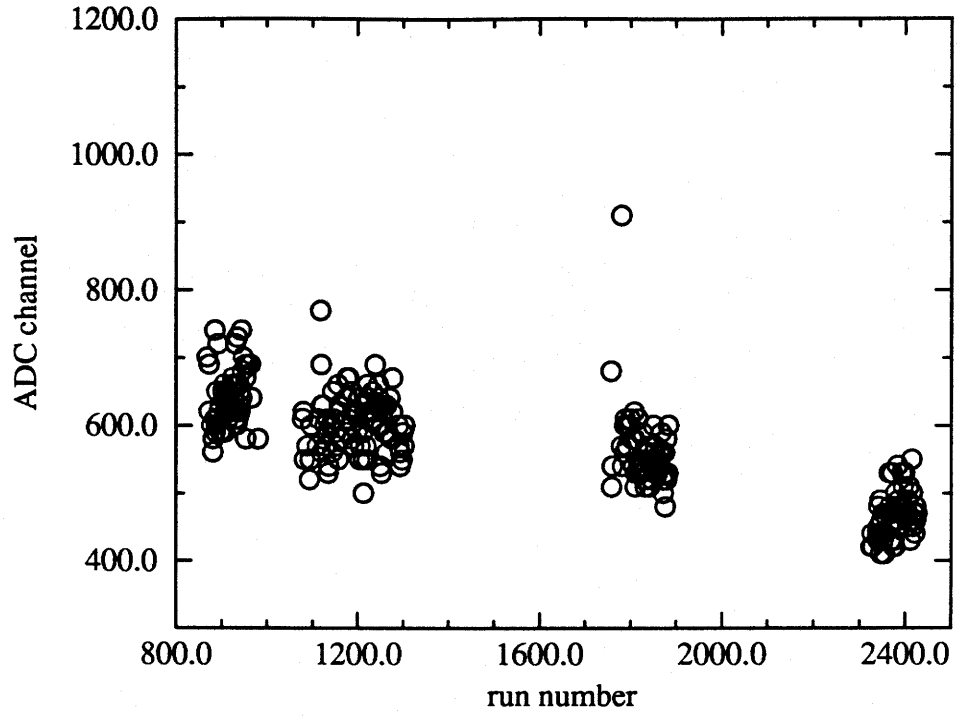

Figure 3.15: Front Right Cosmic Veto

3.3 Computation of Differential Cross Sections

The analysis to obtain differential cross sections consisted of replaying the data to produce energy spectra, grouping runs according to energy, angle and target type, summing together total energy histograms for these runs, counting the number of events in the appropriate region of interest, and normalizing the counts by flux, target thickness, solid angle and efficiency. Most of the normalization factors required some modelling. The cross sections in most cases in this chapter were calculated using the following formula:

$$\frac{d\sigma}{d\Omega} = \frac{t_b \; C(E_1, E_2)}{\varepsilon(E_1, E_2) N_\gamma(E_1, E_2) N_t \Delta\Omega} \tag{3.5}$$

where C is the yield extracted from a region of interest (ROI) in scattered spectra, t_b is the fraction of photons in the beam that do not get absorbed on the way to the quantameter, N_γ is the total number of photons in the incident beam corresponding to the ROI, N_t is the

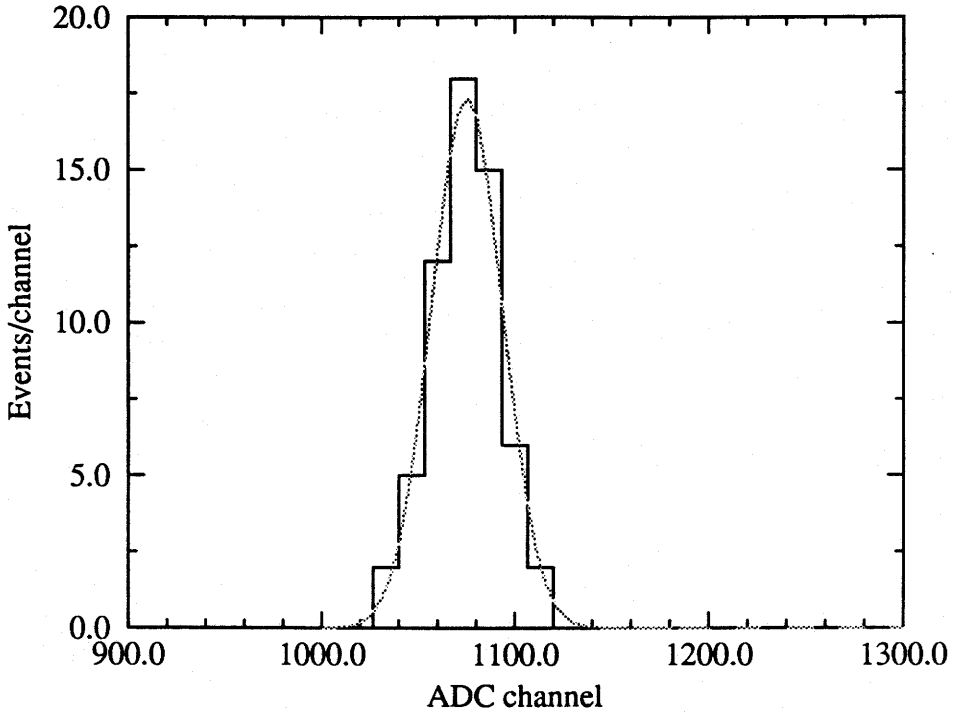

Figure 3.16: Fit for Annulus Cosmic Veto 4 Threshold, Feb 89 runs

target thickness (in g/cm^2), $\Delta\Omega$ is the solid angle, and A is the detector efficiency in the ROI.

3.3.1 Replay

This was essentially the final pass of data tape replay. The basic code of the off-line Looker for the final replay was similar to the on-line one. The gains were input from a file, but this file contained the larger and more accurate data base for all runs as described in Section 3.2. A C language subroutine compatible with LUCID was written for the Looker to read the file and identify the appropriate set of gains. Other subroutines were added to read pedestals, cuts and other parameters at the beginning of each run, and to perform the more complex analyses.

Each of the core ADCs was scaled by its gain factor. Since the seven phototubes on the core saw the same volume, these energy calibrated values were averaged (not summed) to yield the core energy. The same was done for each of the quadrants, yielding four quadrant energies. However, the quadrants had two sets of read-outs: high energy deposition and low energy deposition. If a photon deposited less than 10 MeV in the high energy quad ADC, the low energy quad ADC was used for the rest of analysis for this photon. The four quads were then added to yield the total quad energy. The sum of the core and the total quad energies was the total energy.

Next, the cosmic ray vetoes were checked. Any events that deposited energy above a threshold in any of the vetoes were rejected. The threshold was determined from cosmic ray runs (see Section 3.2.5) and this rejection resulted in a 98% reduction of cosmic ray events (Figure 3.17a). Next, a quad-to-total energy deposition ratio cut was applied. This made use of the concentric segment design of the spectrometer. Good events rarely deposited more than 20% of the total energy in the quads. Cosmic rays typically deposit more than 30% in the quads (Figure 3.18). So a simple threshold of 20% on the ratio of deposition resulted in a powerful cosmic rejection. The overall cosmic ray rejection was better than 99.99% (Figure 3.17b). The efficiency of this rejection scheme was determined by EGS simulations and by examining graphs like Figure 3.18 for real data before making the 20% cut. The estimated loss of good events was less than 1%.

Finally, the aperture scintillators were checked to determine whether or not the event was a charged particle or if the photon had initiated a shower in the Be hardener. Any events with energy deposited above the respective aperture scintillator thresholds were rejected. Examination of the rejection rates indicated that the 2.54 cm thick Front Mid cosmic veto eliminated 99% of the charged particle event before the aperture vetoes were even checked. Ultimately, 99.9% of charged particles were rejected.

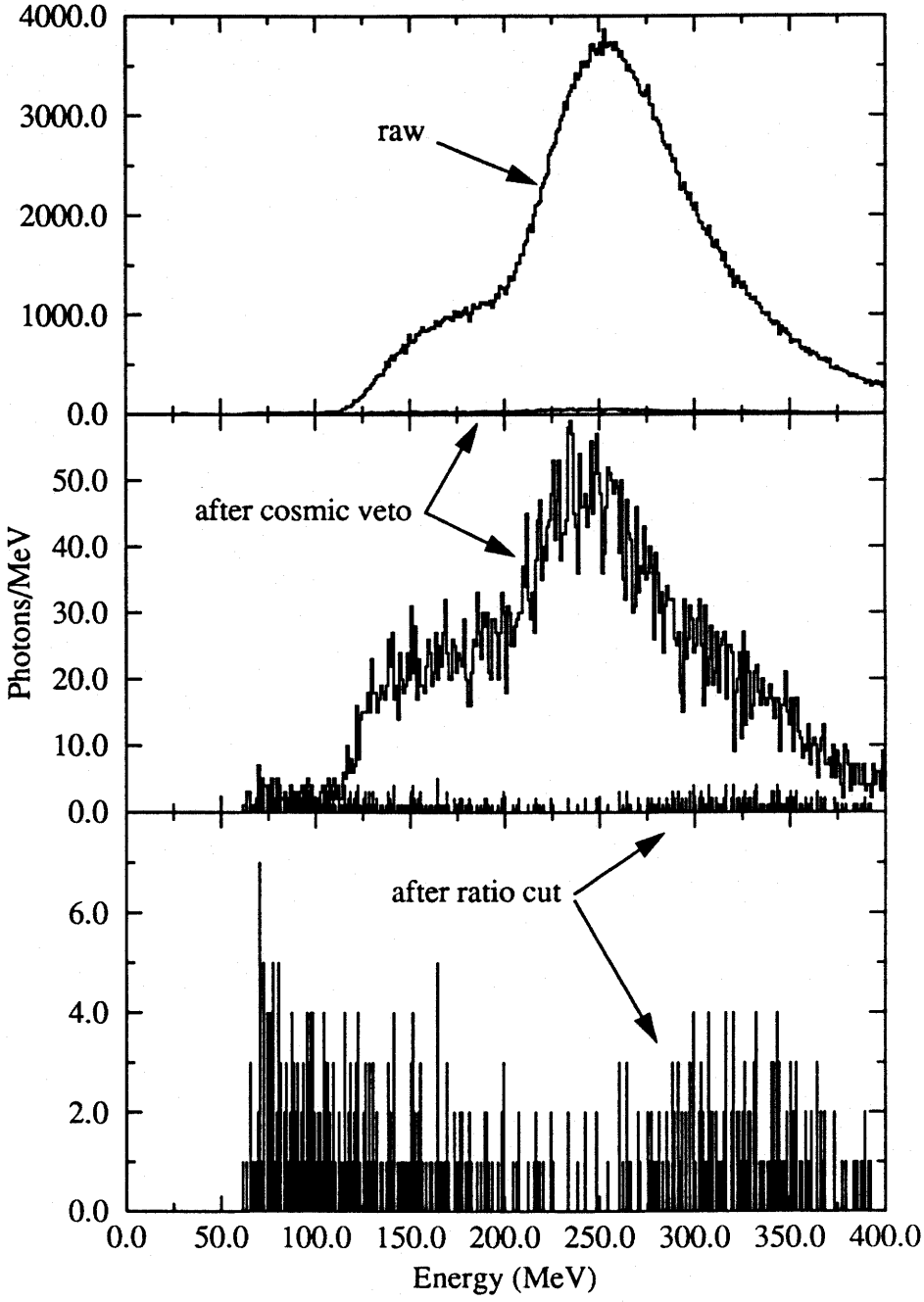

Figure 3.17: Cosmic Ray Spectra Showing Effects of Rejection

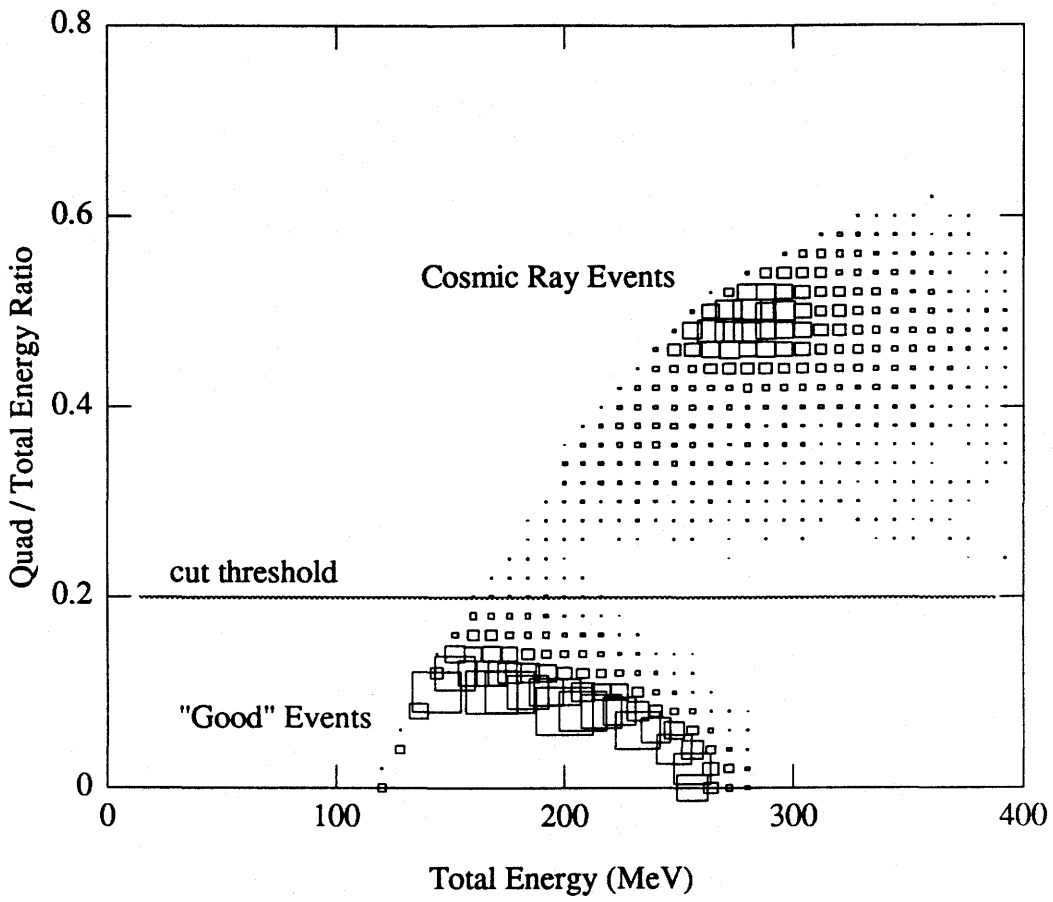

Figure 3.18: Quadrant / Total Energy Ratio vs. Total Energy for Scattered Photons at 290.2 Mev Maximum Energy

Total energy histograms were made for each run with events passing all of the vetoes and these histograms were written to a file at the end of each run for the extraction of yields (Section 3.3.2).

3.3.2 Extraction of Yields

The use of bremsstrahlung poses a unique problem in extracting cross sections. The incident photon spectrum is a continuum, so without tagging or coincidence with the recoiling nucleus, some sort of unfolding is required employing a theoretical bremsstrahl spectrum. Even then, the discrimination of different scattering channels may be difficult or outright impossible.

To attempt to isolate the elastic scattered photons detected by BUNI, the analysis of most of the data from this experiment relied on photons from a region near the endpoint. Even though more copious, decay photons from neutral photopion production have a maximum energy that is 15 to 30 MeV lower than that of elastically scattered endpoint photons because the second (undetected) photon from the decay must carry some of the decay energy (see Section A.3). Furthermore, elastically scattered photons will carry more energy than inelastically scattered ones, the deficit for the latter being due to the excitation of the target nucleus (see Section A.2). The endpoint positions of various scattering channels for carbon and helium are shown in Figure 3.19. From this figure, it can be seen that only elastically scattered photons are contained in the region above the endpoint for inelastic scattering to the first excited state. For the helium data, this means events in a region 17 to 20 MeV wide are available, making it possible to obtain high statistical certainty. However, for carbon the region is only 4.4 MeV wide. This means that to get the same statistical certainty as for helium with the same cross section, 4 to 5 times more beam would be needed. This was not possible in the time allotted so the expected statistical certainty will be poorer. The major effect on the analysis of this narrow region is to require that the energy calibration be known to much better than 1%. This is why a major effort went into the determination of calibrations described in the previous section.

A C language program (**sumetotal**) was written to extract the histograms dumps after all tapes were replayed, collate them according to an instruction file, sum them, subtract cosmic ray background, and write to individual summed energy spectra. These spectra were ready for yield extraction. A C language program, **extract.data**, was written that accepted spectrum file name, energy, angle, target type, and ROI from the user, and integrated the appropriate ROI in the spectrum file and outputted the yield.

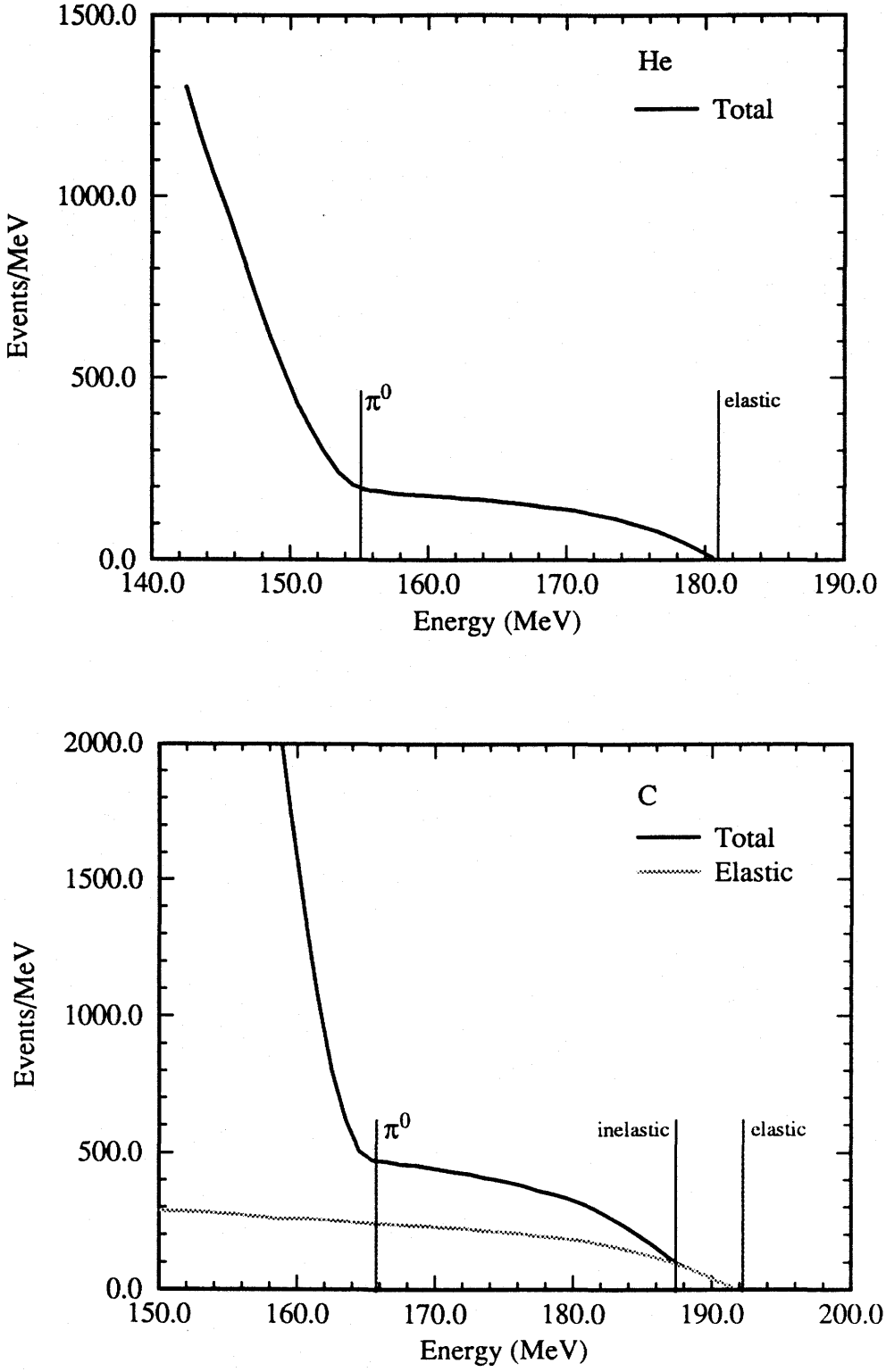

Figure 3.19: Typical scattered photon spectra.

It should be noted that there were 88 combinations of energy, angle, and targets, when the helium analysis is included. The extraction of all the information for this many measurements, in addition to their many permutations, would be cumbersome without the use of computer programs. The repetitiveness of all of the tasks lead to the writing of a master program (**buildresults**) that read a parameter file and generated all of the required scripts and input files for any permutation and combination of analysis conditions. The use of scripts allowed the recomputation of individual classes of information, e.g. if a bug was found and corrected in **extract.data**, the corrected yields can be generated without having to extract the efficiencies (which were correct already), and so on.

At this stage of the analysis, it was assumed that there was no energy dependence in the yield from the chosen region of interest (ROI). That is, the cross section was assumed to be constant with energy. For small ROIs, such as those used for ^{12}C, this is quite reasonable. However, where there was strong energy dependence and seemingly weak inelastic contributions, it was deemed possible to attempt extracting energy dependences by using a wider part of the scattering spectra, and breaking it up into 5 MeV ROIs. The computation of cross sections is the same, regardless of which portion of the spectrum is used. This will be discussed further in Section 3.4.2.

3.3.3 Flux

The bremsstrahlung curves were generated by an in-house program called **bremss** which uses the Mathews and Owens calculation [Mathews 73]. The bremsstrahlung EGS simulation (**brem**) used in core calibrations (Section 2.7.1) indicated that the Mathews and Owens calculation accurately described the full bremsstrahl spectrum for this experiment. A comparison resulted in 0.1% difference (Figure 3.20). It was decided to use **bremss** spectra instead of the EGS spectra for the sake of speed of computation and uniformity in yield. The EGS simulation **brem** was modified to determine the transmitted/incident ratio of photons in the beam line in 1 MeV steps. This simulation was meant to ascertain the relative variation of absorption rather than an absolute value. For

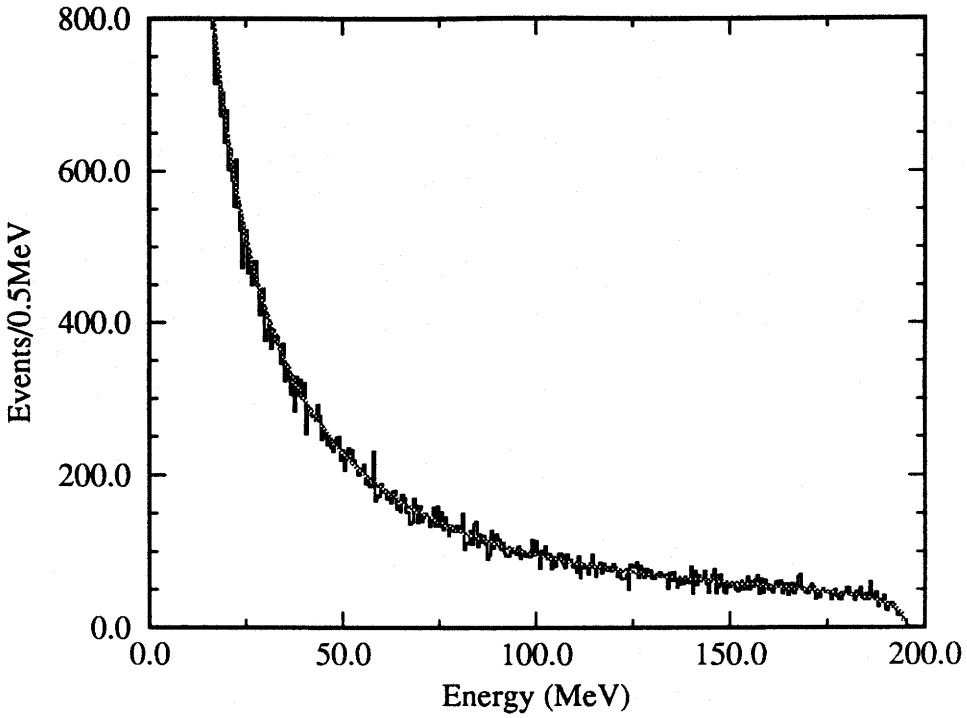

Figure 3.20: Comparison of Simulation (histogram) and Mathews and Owens calculation (smooth line)

helium, one simulation at each energy was sufficient for all angles, except when a beam hardener was in place, in which case a second simulation run was needed. For carbon a simulation had to be run for each angle because the target was rotated depending on the detector angle so that the target thickness changed for each angle. The photon flux at the quantameter was then computed by a C language program, **brem_e_ave**, which read the **bremss** file and the EGS file for use with Equation 2.2

The absolute effect of photon absorption was determined by yet another version of the EGS **brem** which used the Mathews and Owens spectrum for the bremsstrahl spectrum and histogrammed, in 0.1 MeV bins, the number of photons incident on target and the number of photons incident on the quantameter. The ratio of counts on target, within the ROI, and counts on quantameter, within the same ROI, was computed, and was used as an absolute scale factor on the cross section.

3.3.4 Efficiency

The detector efficiency was estimated using the EGS simulations for BUNI detecting scattered photons, **buni_sim**. Every data point had a corresponding EGS run to simulate run conditions (e.g. target to detector distances, target angles). These runs accumulated histograms for photons just after scattering and for the photons that eventually deposited energy in BUNI. The ratio of counts within the ROI in these histograms is the efficiency of detection. A C program (**extract.eff**) was written to extract efficiencies from EGS output. The major contributors to the loss of efficiency were photon absorption and scattering by the beryllium hardener (50%) in the aperture and the long tail of the response function. Secondary contributions were absorption and scattering within the target and target support structures, in one or more of the 4 plastic vetoes, and in the air.

3.3.5 Solid Angle

Solid angles were computed by a Monte Carlo method. The EGS code for simulating scattered spectra contained an accurate description of the geometry, so a streamlined version of it was used. Basically, the events in these runs were terminated before entering BUNI and all material except the collimator were switched to vacuum. The ratio of the number of photons within a known, oversized solid angle that arrived at BUNI is the solid angle of the spectrometer. A C program (**extract.msr**) was written to extract solid angles from the EGS output. An independent and more simplistic Monte Carlo was also run and its results compared within statistical error.

3.3.6 Number of Target Nuclei

The number of target nuclei was simply calculated from the target thickness using

$$N_t = \frac{t_t N_A}{A} \tag{3.6}$$

where t_t is the target thickness in g/cm^2, A is the atomic mass, and N_A is Avogadro's number. The thickness of the helium target was the same for all angles because the target cell was a cylinder whose axis had to remain aligned with the beam axis. The number of

target nuclei for the carbon target varied with angle because the target slab was rotated as shown in Figure 2.5. The modification of Equation 3.6 is

$$N_t = \frac{t_t N_A}{A\cos(\frac{\theta}{2})} \tag{3.7}$$

for forward angles, and

$$N_t = \frac{t_t N_A}{A\cos(\pi - \frac{\theta}{2})} \tag{3.8}$$

for back angles.

3.4 Analysis by Fitting

Fitting to the zero degree energy spectra was done initially to extract the calibration constants for BUNI. It should also be possible to check the accuracy of the calibration by fitting measured spectra with the EGS simulation **buni_sim** for the detector with a scattered spectrum, in a similar manner. Any deviation in the gain factor from 1.0 would indicate that the gain compensation system did not function adequately. This scheme was only partially effective as some data points did not have sufficient statistics, and the shape of some spectra were changed by the processes to be measured. For example, the back angle carbon data was dominated by a mixture of inelastic scattering channels (see Figure 3.21). The forward angle data for helium and carbon actually showed the effect of the rising delta amplitude. This overcame the usual monotonically falling bremsstrahl spectrum so that a "dip" appeared in some spectra and noticeable modulation occurred in others (see Figure 3.22).

This analysis used a version of the fitting program mentioned in Section 3.2.1. This program, **bunifit**, inputs EGS generated response functions, modelled bremsstrahlung spectra and, modelled pion decay spectra. It then internally generates detected scattered

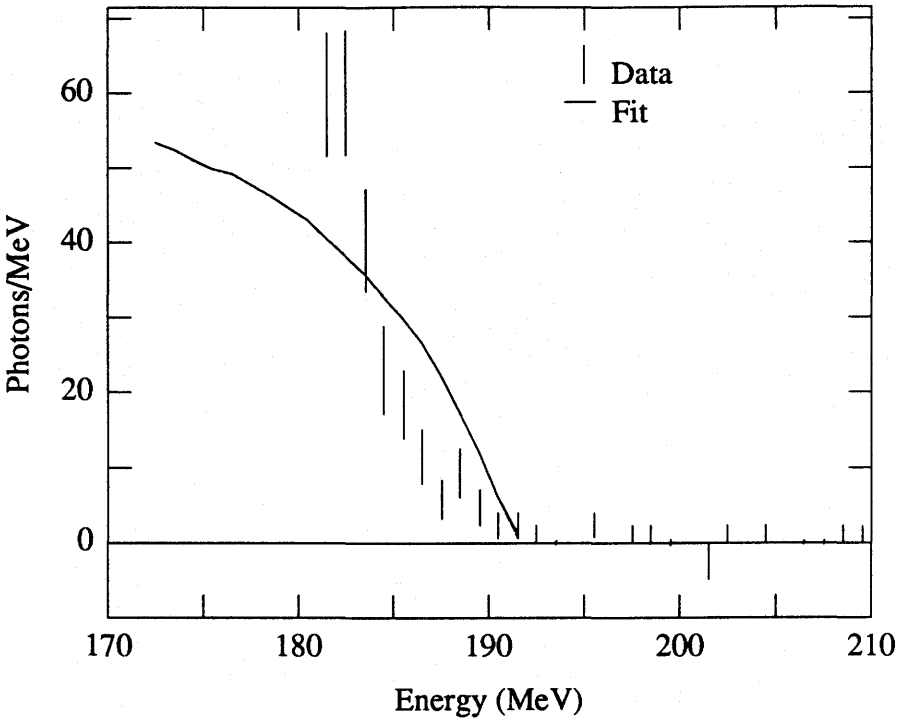

Figure 3.21: Detected spectrum for $^{12}C(\gamma,\gamma)$ at 120, 158 MeV incident endpoint

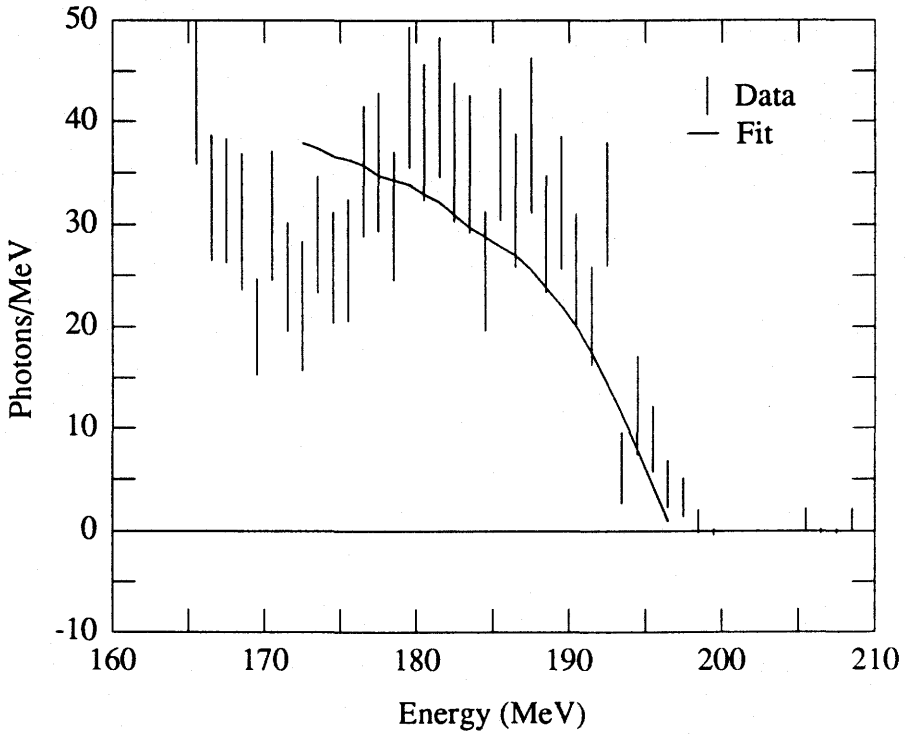

Figure 3.22: Detected spectrum for 12C(γ,γ) at 30 degrees, 198 MeV incident endpoint

spectra for elastic scattering, any number of inelastic photon scattering channels, and pion decay by convolving ideal scattering spectra with detector responses. Finally, these modelled detected spectra are fitted to actual detected energy spectra.

The advantage of this scheme over the one used for finding calibration constants is the flexibility afforded by internally building scattered spectra, thus eliminating the repeated long simulations required to generate spectra for every measured spectrum. The strengths of inelastic scattering channels can be studied by adding or removing candidate reaction spectra. The π^0 production channel can be studied by simply changing the theoretical production cross sections. Finally, the energy dependence of cross sections in scattered bremsstrahl spectra can be studied by weighting the bremsstrahlung spectrum with an energy dependence function.

There was a practical reason for pursuing fits into regions with many possible excitations, even into pion production. As will be discussed in Section 3.5, pileup was a concern. One approach to dealing with it was to model the effects of pileup. To do this, a model of the pileup free inclusive spectrum was necessary. The only requirement of the model was that it had the correct shape, rather than have the correct cross sections. Extending fits into these regions generated these inclusive spectra.

3.4.1 Inelastic Scattering

If the problem of pileup is disregarded for a moment, the well defined endpoint of the bremsstrahlung makes the elastic channel clearly extractable. A sizeable 4.44 MeV channel at back angles would manifest itself by the appearance of a second bremsstrahl spectrum shape, starting 4 to 5 MeV from the elastic endpoint, on top of the elastic, as was shown on the bottom plot of Figure 3.19. However it was not clear what, or even if, any other channels are significant, as even approximate strengths of all inelastic scattering

channels were unknown. The first guess is any transition leading to a 0^+ or 2^+ state. The levels chosen for use in the fits were the 4.44, 7.65, 10.3, and 16.1 MeV [Ajzenberg 89] excited states.

Fitting the ^{12}C data proceeded in stages, mainly to facilitate automation. The first stage consisted of a series of iterations in which the elastic ROI was fitted first. Then in successive passes, each of the inelastic channels are added and the ROI extended. The program was by no means infallible, so each one was reviewed, and any fits with reduced $\chi^2 > 2$ were manually repeated.

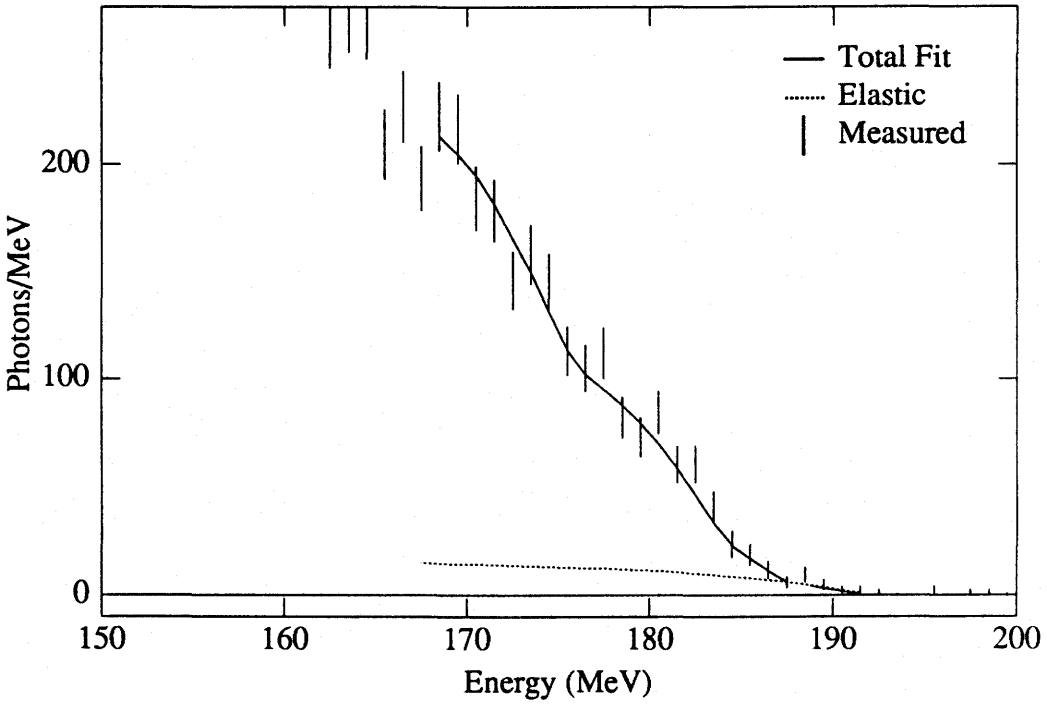

Figure 3.23: Fit to Scattered Photon Spectrum at 198 MeV Endpoint Energy, 132 Degrees

Once the fits were completed, a C language program, **extract.bunifit**, integrated the fit functions over the same ROI as those used in the analysis for elastic cross sections. From this point on, the computation of cross sections is as described in Section 3.3.

3.4.2 Energy Dependences

As discussed in Chapter 1, the scale factor for the differential cross sections come from total absorption data. This was used to model the energy dependence effect in fitting to forward scattering spectra. Using **bunifit**, the energy dependence, for the elastic channel only, was applied by multiplying the input bremsstrahl spectrum by the total absorption cross section derived from beryllium data, and then fitting proceeded similarly to the fits for inelastic scattering. The results, such as the fit shown in Figure 3.24, indicated that the shape of the forward angle spectra could be explained by the energy dependence in differential cross sections.

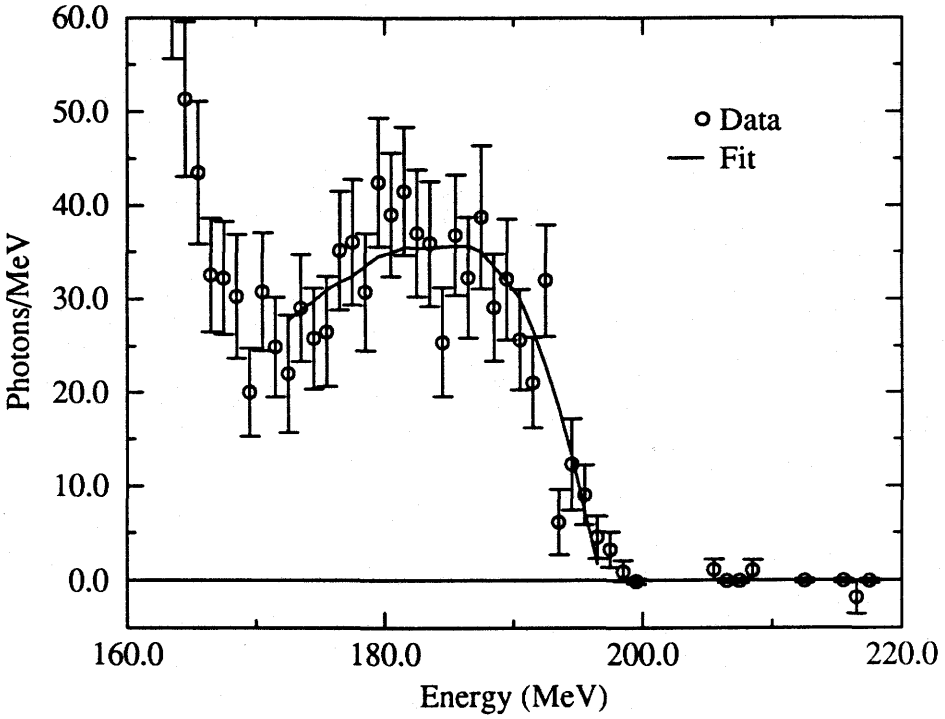

Figure 3.24: Fit to Scattered Photon Spectrum at 30° for C at 198 MeV with Energy Dependence from Be Absorption Cross Sections

An effort was then made to try to measure this energy dependence. For carbon, this analysis was restricted to the forward angle spectra, since the elastic scattering dominates here and inelastic contamination can be neglected. The helium data was also analyzed for the energy dependence, since this had not been done by Delli Carpini [Delli Carpini 90, Delli Carpini 91]. However, all angles could be analysed for helium since there were no

excited states to cause any ambiguities. Spectra were sectioned in 5 MeV regions between the π^0 decay endpoint and elastic endpoint, and cross sections calculated for each interval.

The energy dependence of cross sections was fitted by a Gaussian with a flat background. This new energy dependence derived from the data was used in place of the Be absorption cross sections in the next iteration of fitting. The effect of energy dependence on the analysis was to change the efficiencies used in the cross section calculations. New values for efficiencies were computed by **extract.bunifit** and used with the original extracted yields to re-calculate the cross sections, with the proper efficiencies, for demonstrating energy dependence.

3.5 Pileup Analysis

For the most part, pileup was kept under control during the runs. However, the offline analysis showed that some runs were badly piled up. A few methods were conceived to study its effect and to try to account for it in the cross section computations. An enormous amount of effort was expended on pileup with only modest success and the complicated procedures tried are described in this section.

3.5.1 Waveform Digitizer Analysis

The primary goal of this analysis was to use the waveform digitizer (WFD) to identify piled up events. From this, it was hoped that the pileup rate could be ascertained to provide an estimate of the effect on yields. A secondary consideration was the possibility of correcting individual pileup events.

For this waveform analysis, a standard waveform was required. A problem in generating such a standard was that the normalized NaI pulse shape exhibited an energy dependence, as illustrated in Figure 3.25. To account for this dependence, a series of

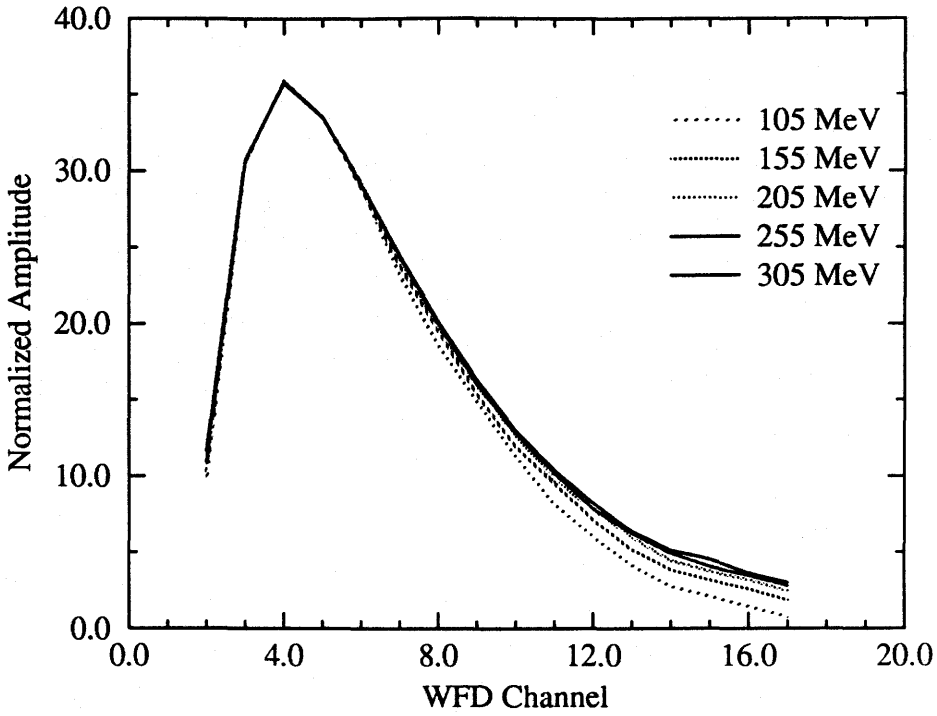

Figure 3.25: Energy Dependence of NaI Waveform

waveforms were generated from which the appropriate energy waveform could be selected during the final playback. These were extracted in a WFD replay after detector calibrations were finalized.

During this playback, waveforms were normalized, event by event, with respect to a 150 ns wide area of the pulse centered on the peak. The WFD was set for 50 ns wide bins so this area corresponded to 3 WFD channels. The delay between the pulse arriving at the WFD and the digitizer stop signal changed by as much as 20 channels between run periods. A simple peak searching algorithm was used to locate the peak and the waveform was shifted such that the peak was always at WFD channel 3. This put the start of the pulse on WFD channel 2. The waveforms were classified by energy in 10 MeV intervals and mean, normalized waveforms were calculated for each energy interval. These mean pulse shapes were written to files at the end of each run.

After all runs were replayed, the contents of the files that had been written at the end of each run were distributed to a new set of files according to channel number. These channel files contained the mean amplitude and standard deviation for every energy interval from all runs for a single channel. Figure 3.26 shows the contents of one of these files. The crosses are the mean values for channel 6 for all 248 MeV runs plotted against energy. The weighted mean channel amplitude from all runs, for each energy interval, was computed and written to mean files for each channel. This yielded the energy dependence for each channel and is shown as the solid line in Figure 3.26. These energy depen-

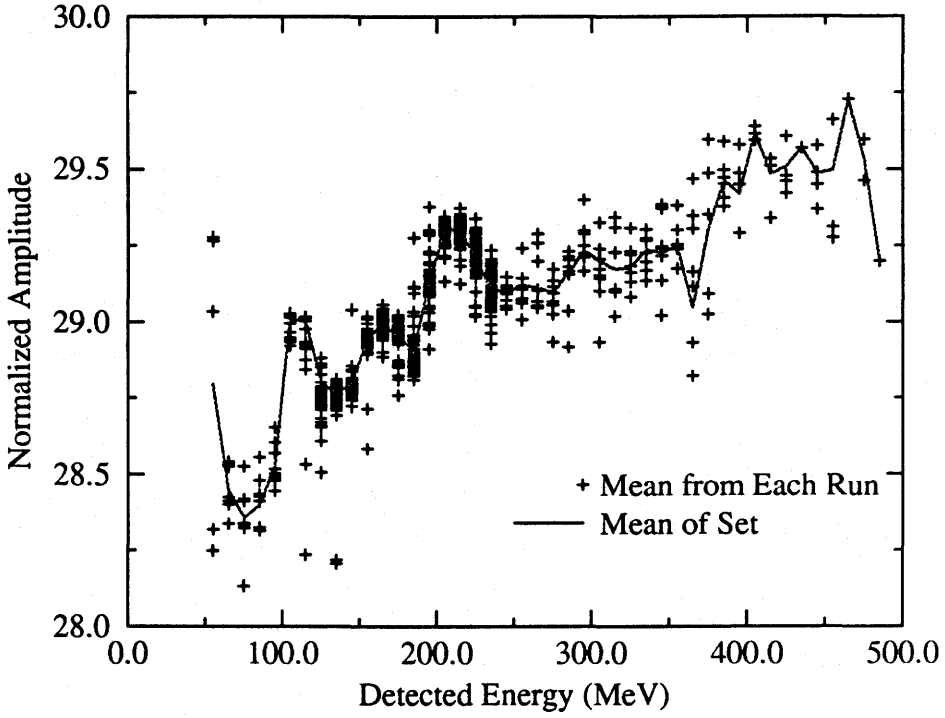

Figure 3.26: WFD Channel 6 Mean Amplitudes in 10 MeV Intervals from 248 MeV Data Runs

dences were then collated according to energy and eventually a file was written that contained one complete waveform for each of the energies. This waveform database file was used by the Looker as the standard waveforms for different energies in 10 MeV intervals.

The major problem encountered with the waveform digitizer was that it continuously digitized, regardless of whether or not there was a pulse present. The digitizer stopped only when a pulse did arrive and an external stop signal was received. As a result, the pulse's leading edge never started at a consistent time with respect to the digitizer's clock. A jitter was observed in the reconstructed waveform and a major part of the WFD analysis then went into correcting this.

The procedure for dealing with the jitter was as follows. At the beginning of each run on tape, the waveform database was read. The waveform for 185 MeV photons was selected as the standard shape to which all data waveforms would be compared. Then the waveform for each energy interval was parametrized for quadratic interpolation, that is, the i+1, i, and i-1 element were fit to a quadratic. This was for the interpolation that would be required for determining the correction factors for the jitter. The peak channels, 2 to 6, were fit by a third order polynomial for determining the amount of jitter.

For each data event first and second derivatives of the data waveform were calculated. The amount of jitter was found using Newton's method for finding the zero of the least square between the five channels nearest to the peak in the data and the standard waveforms. It was then used to calculate, by trapezoidal integration, the corresponding fraction of each channel to shift to the next channel. Finally, the pulse shape was corrected for energy dependence by subtracting from it the difference between the standard waveform for the event energy and the absolute standard waveform (the 185 MeV waveform) as indicated by

$$wfdc_i = wfdn_i - (wrds_i(E) - wfdS_i) \tag{3.9}$$

where i is the WFD channel number, wfdc is the corrected waveform, wfdn is the original data waveform, wfds(E) is the standard waveform for energy E, and wfdS is the absolute standard waveform.

Once the correction algorithm was in place, the corrected event waveform was compared to the standard waveform and its "derivative" to determine if it was piled up. The derivative was actually the current WFD channel height minus the previous channel height. For each channel, the difference between the data height and the standard's height was computed as well as the difference in derivatives. Then for a typical data pulse the differences would be zero, and a piled up pulse would deviate from zero. A cut could then be applied to identify piled up events. For each channel, the derivative difference was plotted against the height difference, as shown in Figure 3.27. An ellipse that represented

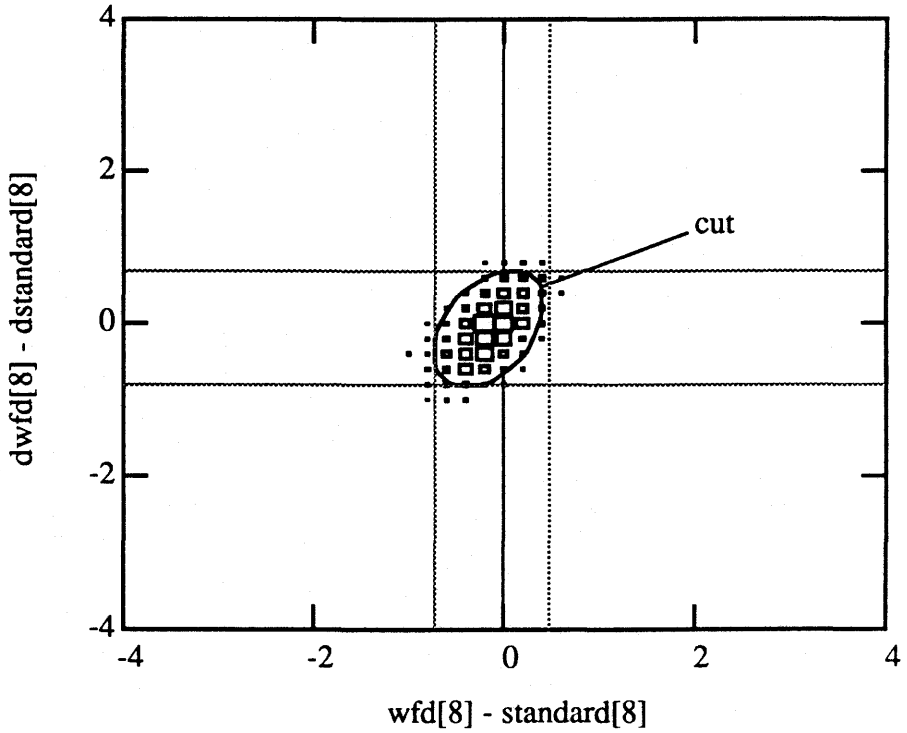

Figure 3.27: Difference of Data and Standard Derivative versus Difference of Data and Standard height for WFD channel 8

the maximum allowable deviation for each channel was determined and used as a two dimensional cut for identifying pileup. The parameters for these ellipses (semi-major axis, semi-minor axis, and rotation) were read and computed at the beginning of each run.

An elliptic cut was found to be appropriate, rather than a rectangular one, by dividing up this plot into slices and looking for correlations on the plot for the next channel. What was observed was that from one slice to the next on one plot, a band appeared on the next that rotated. This indicated that the peak implied in Figure 3.27 was truly elliptical. The rotated axis of the ellipse is further evidence of this and it can be seen that if only horizontal and vertical cuts were made as indicated by the grey lines, there would be events that would improperly pass the pileup identification cut.

A C language subroutine was called during the analysis to make the cut. In order for the event to be tagged as piled up, two adjacent channels had to exceed the positive half of the elliptic cut. If a piled up event was found, the net difference between the data pulse and the standard was proportional to the fraction of energy from that event that was due to the pileup. From that, it was possible to make a histogram of the pileup spectrum as shown in Figure 3.28. However, it was found that the ADC conversion resolution and width for each WFD channel were too coarse to properly resolve pileup below 3 MeV, which were the most copious. Hence, pileup rates could not be accurately determined and accurate pileup spectra could not be compiled. However, these spectra were still useful for identifying runs that were badly piled up because the higher energy pileup became observable, as shown in the bottom plot of Figure 3.28.

Since 3 MeV is comparable to the energy resolution of the detector, the effect of pileup of this energy is largely to make the energy resolution worse. For pileup larger than 3 MeV, the WFD could make a correction to recover the unpiled up energy. This corrected energy was used to produce a pileup corrected scattered energy histogram. The main problem encountered with this was that due to the 50 ns bin size, there was no way of identifying an event where two pulses coincided within 200 ns of each other. As a result, the efficiency of the pileup correction scheme could not be better than 60%. This was not adequate for this method to be used for correcting pileup, but it was an effective

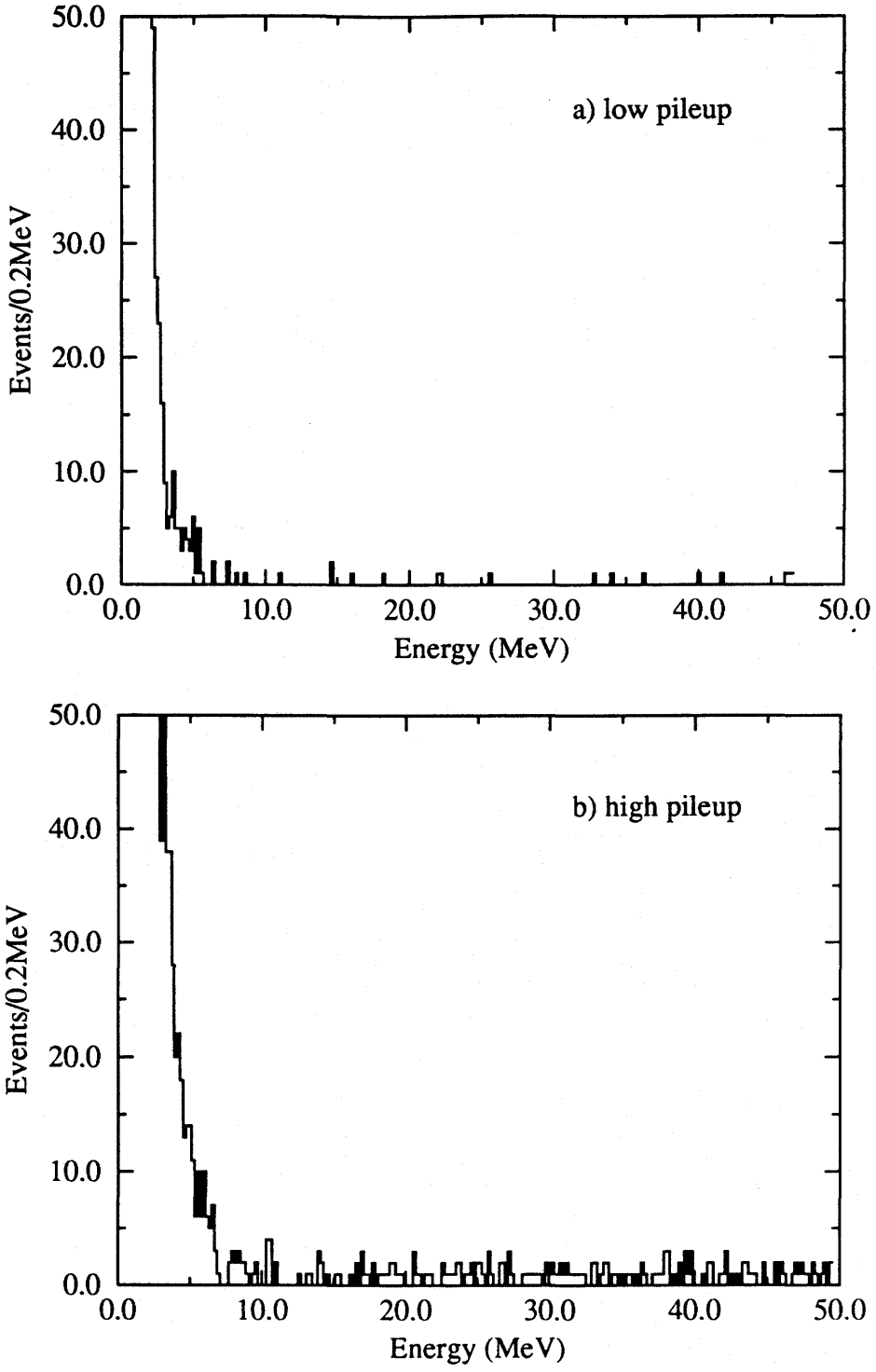

Figure 3.28: Pileup Energy Spectra for a) Low Pileup Rates and b) High Pileup Rates

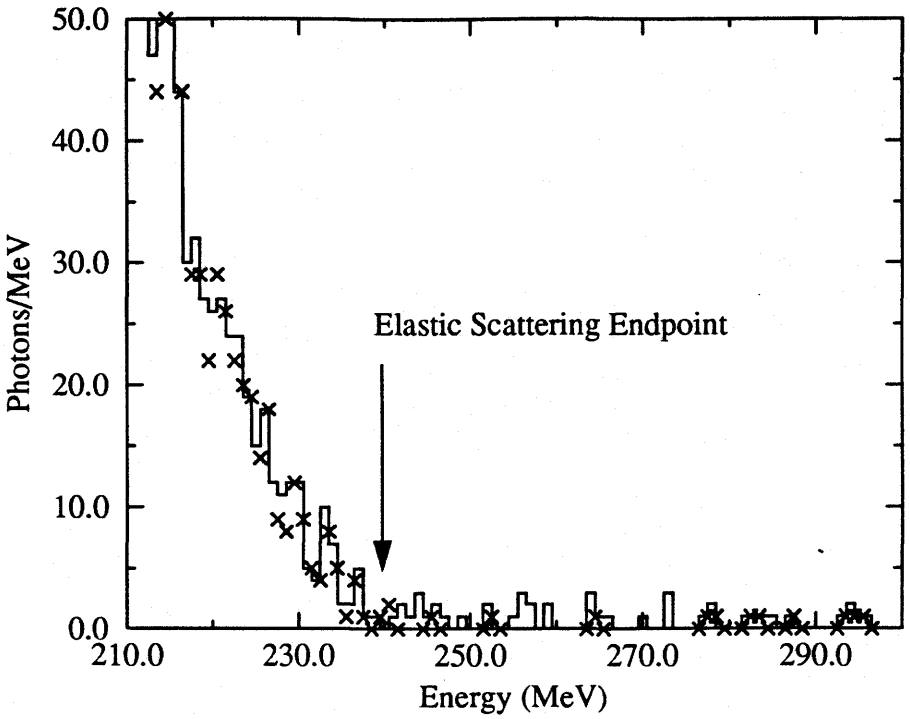

Figure 3.29: Energy Spectra Without WFD Pileup Correction (Histogram), And After WFD Pileup Correction (X)

way of determining the source of background, as shown in Figure 3.29. The amount of background above the endpoint for this run was reduced by about 50% using the WFD corrections. Thus the WFD indicated that the major source of high energy background, in this case, was not cosmic rays but pileup, and that this run required more attention.

3.5.2 Pedestal and Mixer Analyses

Pedestal events were meant to indicate which ADC channel corresponded to a zero input, that is, the channel offset of the ADC. Random pulses from background which contribute to pileup spread the pedestal response, as discussed in Section 2.8.1.c. Not only should the pedestal spectra have indicated the pileup rate, but the actual form of the pileup should have been recorded. Similarly, Mixer spectra should be narrow peaks and would be affected by pileup by the broadening of the peak. These spectra could then be used to determine the effect of pileup on energy spectra, e.g. they could be convolved with simulated scattering spectra to make fits to piled up spectra.

The first step was to replay the data treating the pedestal event in the same manner as photon scattering events. That is, ADC values, were scaled by gain factors, summed and averaged. The result was an energy calibrated histogram of the pileup spectrum. Histograms were grouped and summed by a C language program, **evalpile**, in the same way as total energy spectra. While the Mixer histogram was not calibrated, it was also grouped and summed by **evalpile.**

Evalpile also computed the pileup rates according to both the pedestal and Mixer histograms. Since pileup effects are, by definition, the deviations from the true pedestal and Mixer spectra, it was necessary to subtract true spectra from the spectra being analysed. The pedestal spectrum from the nearest cosmic ray run or quad calibration run was assumed to be free of pileup and were scaled by peak height and subtracted from the current spectrum. The peak area for scaling was between -0.5 and 0.5 MeV for pedestals and -2.0 and 2.0 units from the peak in the Mixer. These values roughly corresponded to 4 channels in their respective ADCs and were chosen because when various peaks were overlaid, the shape of the peaks in this range did not seem to change with pileup. The remainder from the subtraction were the piled up events. Pileup rates were calculated by integrating the subtracted pedestal histogram outside of the region of -0.5 and 0.5 MeV and the subtracted Mixer histogram outside -7.0 and 7.0 units, and then dividing by the respective total counts.

When the pedestal and Mixer estimates of pileup rates were compared with WFD pileup spectra and total energy spectra, discrepancies appeared. Many of the spectra were visibly free of pileup, yet the corresponding computed pileup rates from the pedestal for some of these spectra were above 20% which was considered excessive. To add to the confusion, some of the WFD spectra and total energy spectra were visibly piled up, yet the computed rate from their pedestal and Mixer indicated low pileup rates.

The cause of this discrepancy was due to the trigger used for pedestal events. It was assumed that sampling completely at random would be adequate because of the high duty factor of the photon beam. However, this assumption was based on duty factors approaching 100%. The real duty factor was closer to 50% with drops in some runs to 30%. This meant that the pedestal could have been sampling during the irrelevant periods when the cycle was in the low flux phase. When this was realized, a trigger was set up using a plastic scintillator placed at 90° from the target about 1 m away which provided a beam dependent trigger. However, by then the run constraints were well established and pileup problems never occurred thereafter.

This failure of the on-line method of pileup monitoring eventually caused the loss of some elastic scattering data. Some other means had to be devised to determine and account for pileup to try to recover some of the piled up data.

3.5.3 Fitting with Pileup

Up to now we have discussed techniques to try to deal with pileup based on the pulse shape. This section describes attempts to deal with pileup in the final energy spectra by fitting techniques. Two methods of dealing with pileup through fitting were attempted. The first was to assume a pileup spectrum shape and to convolve it with a simulated spectrum. Since the pileup rate was one of the parameters being sought in the fit, this convolution had to occur at every iteration of the fitting algorithm. The problem was in finding a suitable pileup spectrum.

The second method took advantage of the linear effect of pileup on histograms. The spectrum suffering from pileup can be decomposed into a piled up spectrum and a pileup free spectrum with the pileup rate as a proportionality factor (see Appendix B). Then it should be possible to include in the fitting procedure, outlined in Section 3.4.1, a spectrum that is totally piled up. This spectrum can be generated by convolving a previous fit that

assumed no pileup with a pileup spectrum in a single pass. With the proper preparation of this spectrum, the pileup rate can be extracted from the fit parameters. The problem, again, lay in finding the appropriate pileup spectrum.

Since the WFD analysis showed direct, but not quantitative, evidence of pileup, and since the erroneous pedestal spectra had too few statistics at the higher energies, an input spectrum for fits with pileup had to be improvised. The shape of pedestal spectra below 10 MeV is not easily modelled so this part of these spectra must be retained. These spectra also usually lack the statistics for the higher energy part to be used in a convolution or Monte Carlo simulation. However, this region should resemble the inclusive photon scattering plus neutral pion decay spectrum. So, fits were made to total energy spectra including about 15 MeV of decay photon spectrum (decay photon spectra were simulated by a C language Monte Carlo program, **pilesim**, described in Appendix C). Then a C language program, **pilegen**, generated simulated piled up total energy spectra (see Appendix C). It reconstructed the inclusive scattering spectrum from 0 MeV to the elastic endpoint from the fit results. The 0 to 10 MeV region from the pedestal spectrum was spliced in. The final piled up spectrum was generated by Monte Carlo, using the constructed pileup spectrum as a probability function and simulating two pulses with random delay within a 600 ns gate.

Fitting proceeded the same way as outlined in Section 3.4.1. As expected, the spectra that showed little or no pileup required no pileup spectrum in the fits. Most of the spectra that showed significant pileup were back angle spectra. For these, the cross section is very low and these fits seemed to indicate 100% pileup for them. The affected runs are tabulated in Table 3.3. Moderately piled up runs can be corrected using the pileup rate extracted from the fit. The rate is calculated using Equation B.30 from Appendix B. The ROI count from the simulated elastic spectra is then divided by the rate to yield the estimate of true counts.

Table 3.3: List of Data Points Suffering Significant Pileup

Energy (MeV)	Lab Angle (degrees)	Pileup Rate (%)	Note
248	91	28.4 ±8.6	Moderate pileup
248	105	100	Acute pileup
248	120	100	Acute pileup
248	129	100	Acute pileup in some data
291	66	100	Acute pileup
291	89	100	Acute pileup
291	90	100	Acute pileup
291	120	100	Acute pileup
291	145	100	Acute pileup

In the case of acute pileup, only an upper limit on the cross section can be obtained. Since the fit of the pileup spectra was usually good, the original fits that were used to generate the simulated pileup spectra were not overestimates of the true spectra. These fits were mistakenly fitting elastic spectra to pileup. Had they been overestimating the contribution of the elastic channel, the simulation would have either overestimated the counts below the endpoint and fit well above the endpoint, or underestimated the counts above the endpoint and fit well below the endpoint. In either case, the overall fit would have been poor. Since this was not the case, the yield could then extracted from the previous fit rather than the pileup spectrum fit.

3.6 Final Analysis

The energy dependence analysis described in Section 3.4.2 turned out to be a much more sensitive tool for assessing the accuracy of detector gains. As shown in Figure 3.30, the data points corresponding to the endpoint sometimes deviated substantially from data points derived from below the endpoints. This indicated that the assumed flux normaliza-

tion was from an energy bin shifted from the correct energy. Generally, the discrepancy was an overestimation of cross section indicating that the flux normalization was too small for the ROI and that the gains were too high.

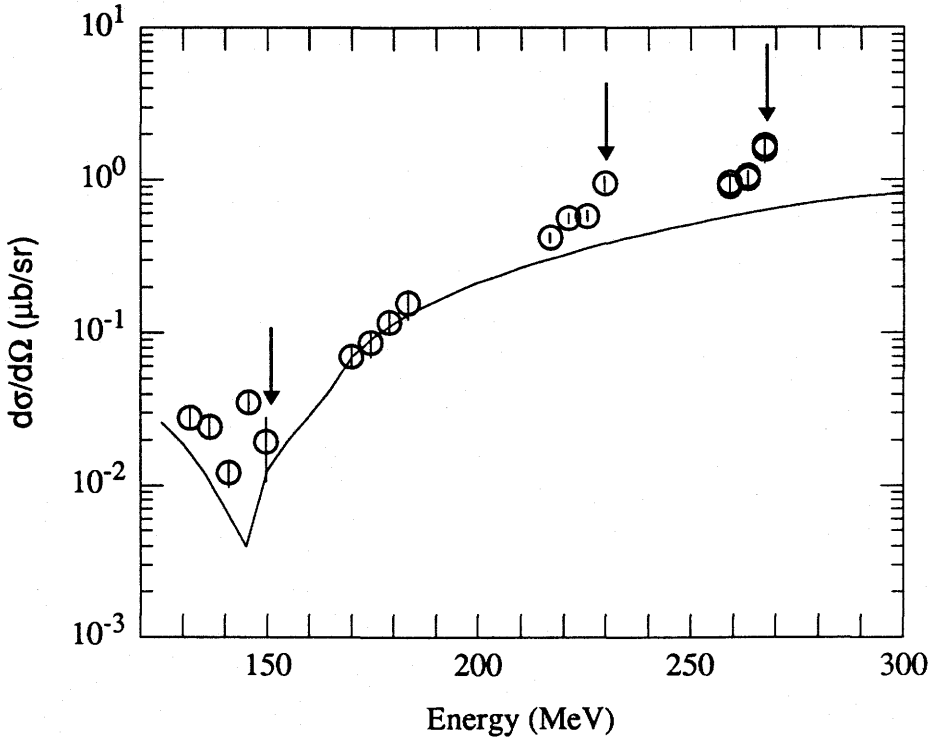

Figure 3.30: Energy Dependence of Cross Sections at 45 Degrees from Helium Before Correction. Circles are present data. Arrows indicate endpoint data. Line is to guide the eye.

In an iterative procedure, the yields were extracted with varied energy correction factors until most helium energy dependences became consistent, as shown in Figure 3.31. The carbon cross sections were not used for assessing gain corrections because of the possibility of misinterpreting inelastic contributions. However, since the helium and carbon data were taken in alternating sequence, the corrections from the helium data could be applied to the carbon data. Typical corrections were of the order of 0.2-0.5% in energy.

Not all the data could be corrected this way because pileup could have the same effect on the energy dependences, particularly the data points indicated in Section 3.5.3 and Table 3.3. In those cases, gain corrections were extrapolated from the data points chro-

nologically nearest to them. The latter correction was not crucial because the extracted cross sections were already compromised by pileup.

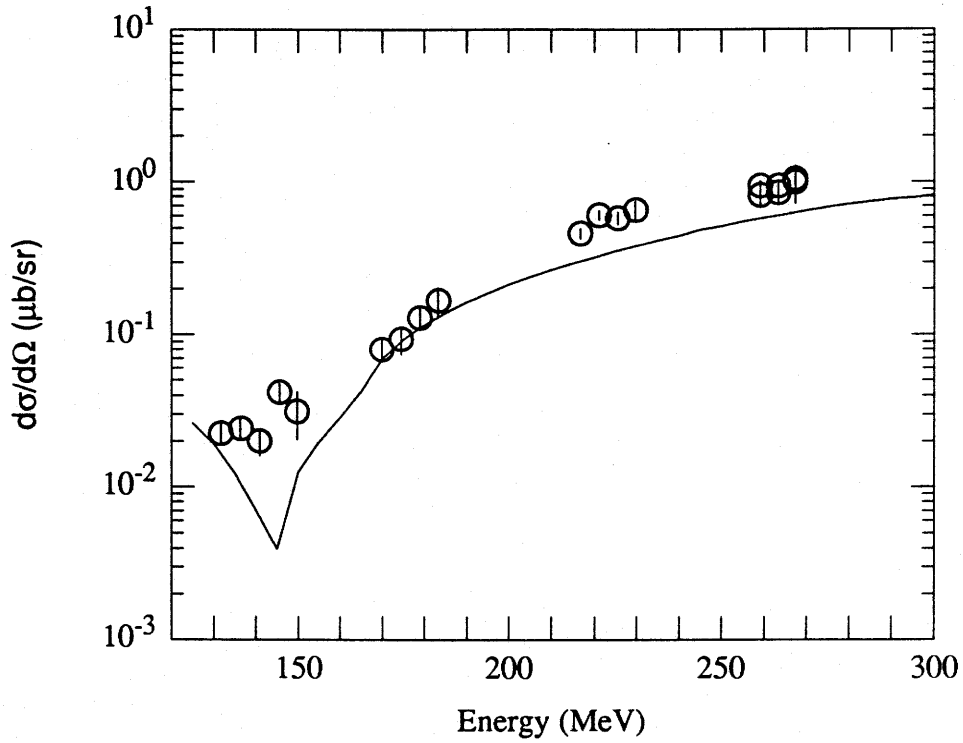

Figure 3.31: Energy Dependence of Cross Sections at 45 Degrees from Helium After Correction. Circles are present data. Line is to guide the eye.

The corrected yields were then used to calculate cross sections as described in Section 3.3. The inelastic cross sections and pileup corrected cross sections were also re-evaluated as described in Section 3.4.1 and Section 3.5.3, respectively, but with the new gain corrections.

3.7 Error Analysis

The major sources of systematic errors in measurements or calibrations and their estimated effect on cross sections are listed in Table 3.4.

Table 3.4: Summary of Systematic Errors

source of error	%error
quantameter calibration	3%
tube to post distance	0.3%
energy of electron beam (energy spread: 0.1%)	0.1%
BUNI PMT calibration	10%
Total	13.4%

The sources of error introduced by the simulations in the analysis are listed separately, in Table 3.5, because they have already been incorporated in the error propagation during cross section computations. They are predominantly due to statistical errors of the Monte Carlo simulations. They are shown here for the sake of completeness.

Table 3.5: Summary of Errors Introduced by Simulations

source of error	%error
transmission of photon to quantameter	0.2-0.6%
efficiency	1-3%
solid angle	0.1-0.4%

For the cross sections which required further analysis, there were additional errors to consider. These are tabulated in Figure 3.6, with the exception of errors in fit parameters. The fitting errors were computed by the fitting program from error matrices. The major source of uncertainty in making pileup corrections was the improvised pileup spectrum. A change in the normalization could easily change the computed pileup rates, but this is

countered by the tendency of getting poorer fits if the pileup spectrum is incorrectly constructed. The inelastic cross sections suffer from one continuum having to be extracted from on top of another at the endpoint. However, in most of the cases, the first inelastic spectrum is quite visible, so the fits should be fairly reliable. The uncertainty for the energy dependence is small because the fits, and hence the efficiencies, are unambiguous.

Table 3.6: Summary of Error For Other Analyses

source of error	%error
Pileup Correction	20%
Extraction of Inelastic Yields	10%
Extraction of Energy Dependence	1%

3.8 Results

The graphs in Figure 3.32 to Figure 3.35 are the differential cross sections for elastic scattering of photons from carbon. The circles are results extracted directly from the total energy histograms, as described in Section 3.3.2. The error bars are statistical. The triangles are pileup corrected results as outlined in Section 3.5.3. Vertical lines represent upper limits for data that suffered from acute pileup. The results from the previous measurement by Hayward and Ziegler [Hayward 84] are also shown.

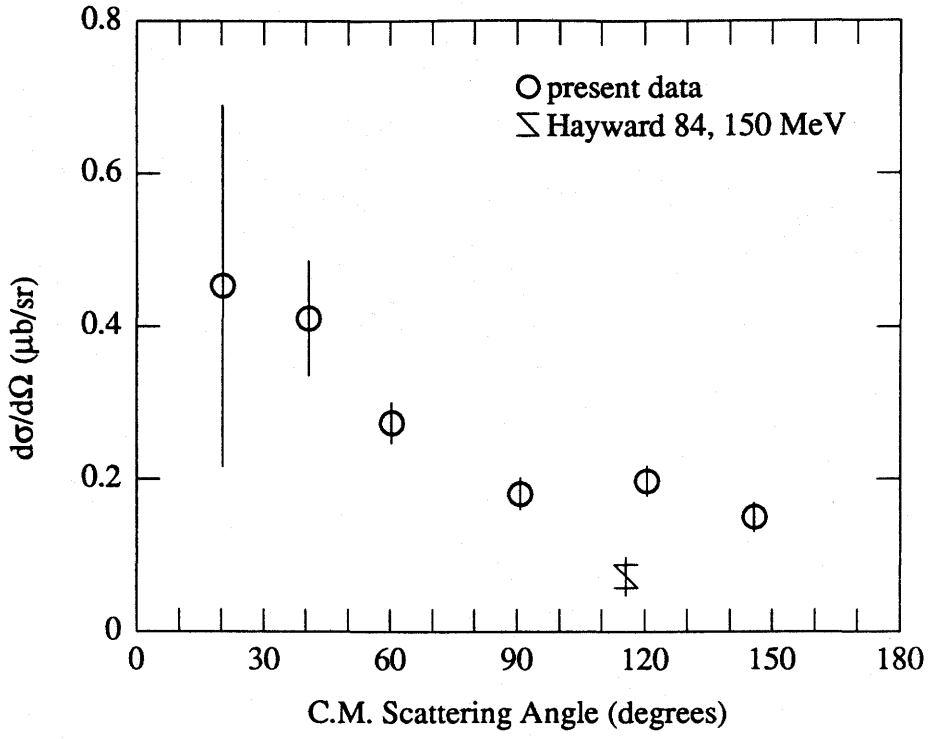

Figure 3.32: Differential Cross Section for Elastic Photon Scattering from Carbon at C.M. Energy of 156.2 MeV

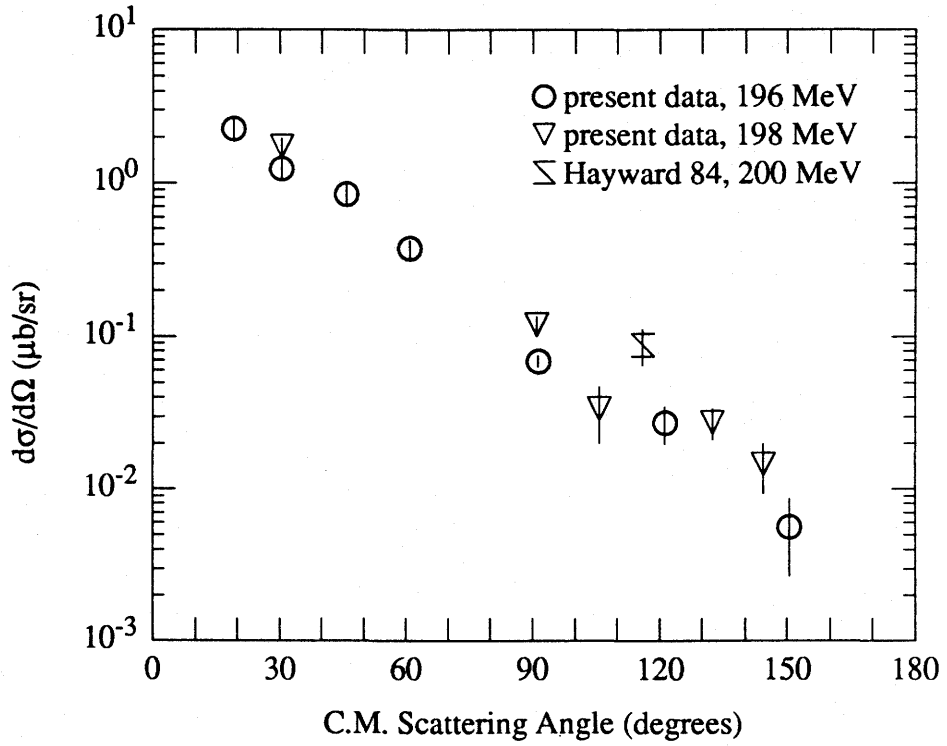

Figure 3.33: Differential Cross Section for Elastic Photon Scattering from Carbon at C.M. Energies of 192.7 and 194.7 MeV

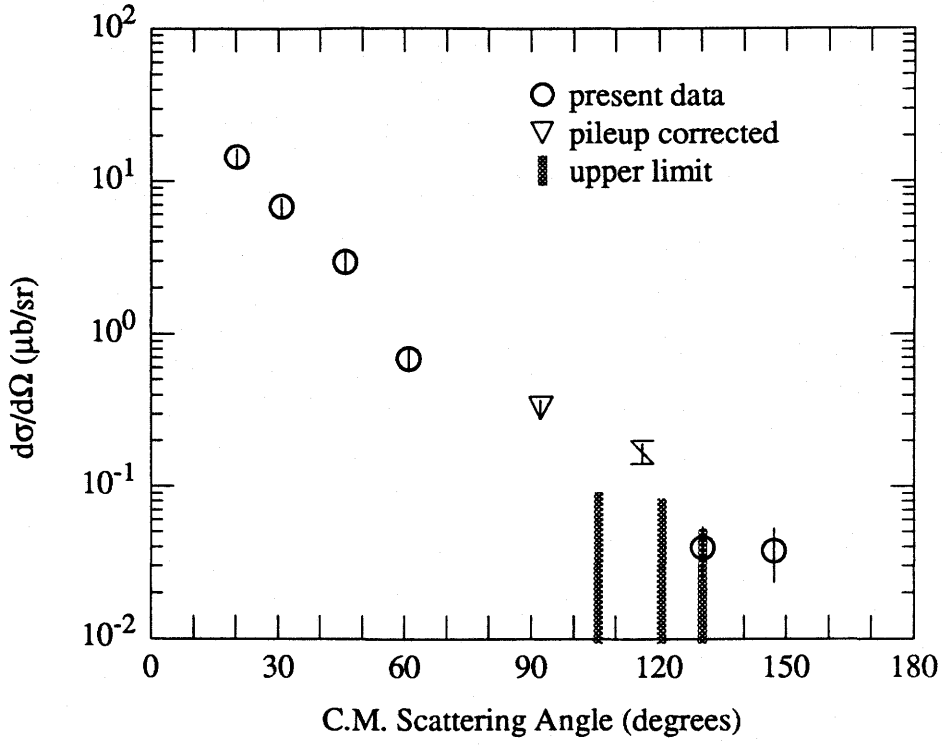

Figure 3.34: Differential Cross Section for Elastic Photon Scattering from Carbon at C.M. Energy of 244.7 MeV

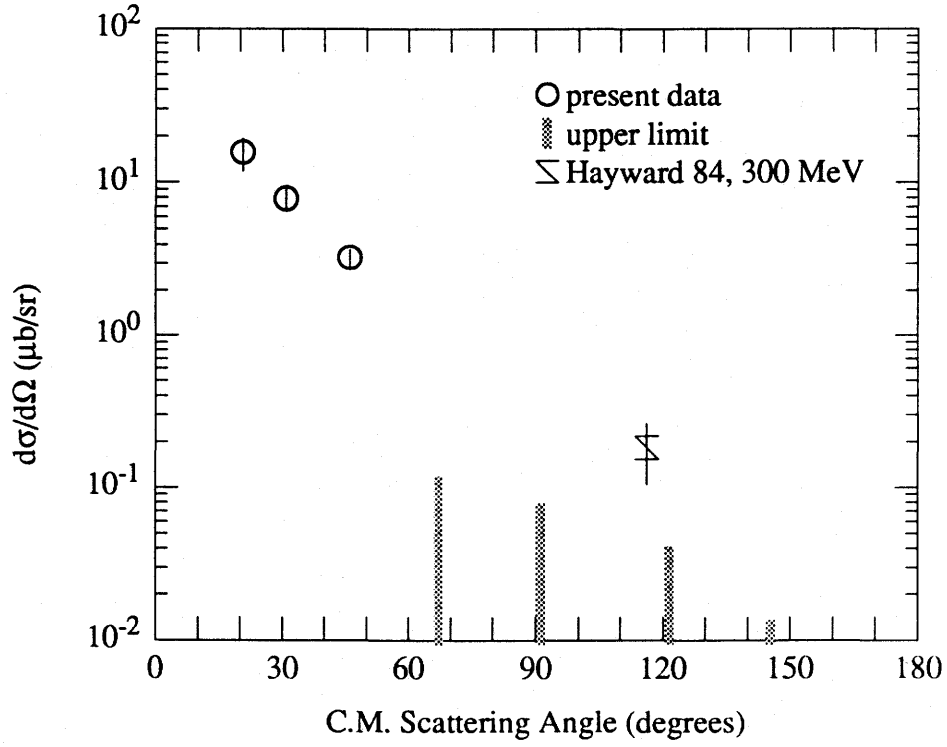

Figure 3.35: Differential Cross Section for Elastic Photon Scattering from Carbon at C.M. Energy of 287.7 MeV

Figure 3.32 to Figure 3.35 are the differential scattering cross sections for inelastic photon scattering leading to the 4.44 MeV first excited state of ^{12}C as derived by fitting to scattered photon energy spectra as described in Section 3.4.1. The elastic scattering data and the [Hayward 84] points are shown for comparison.

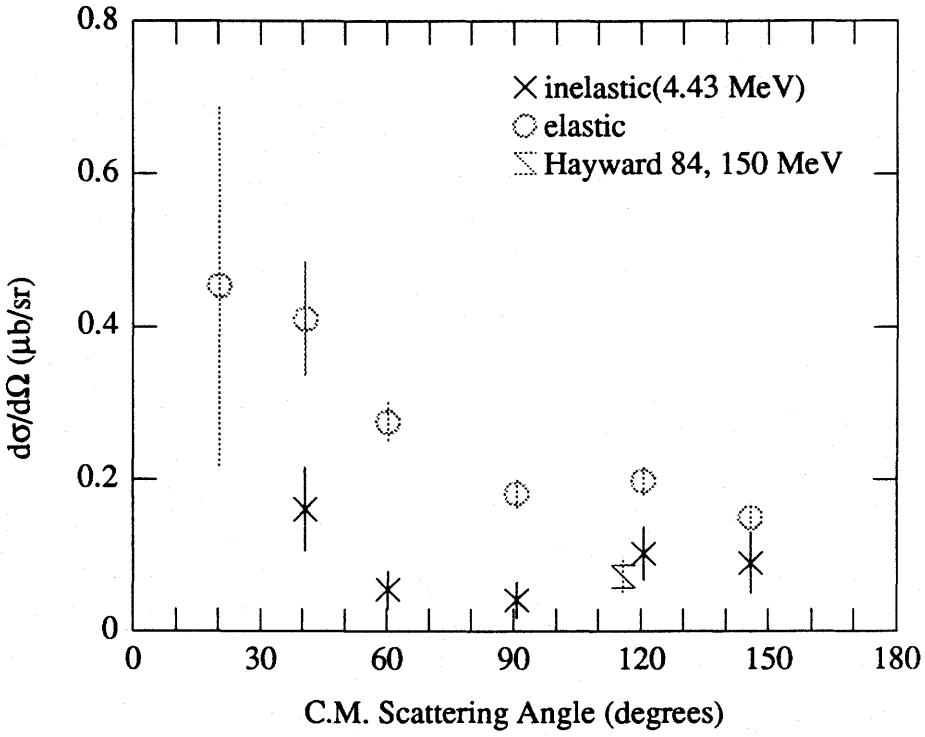

Figure 3.36: Differential Cross Section for 4.44 MeV Inelastic Photon Scattering from Carbon at C.M. Energy of 156.2 MeV

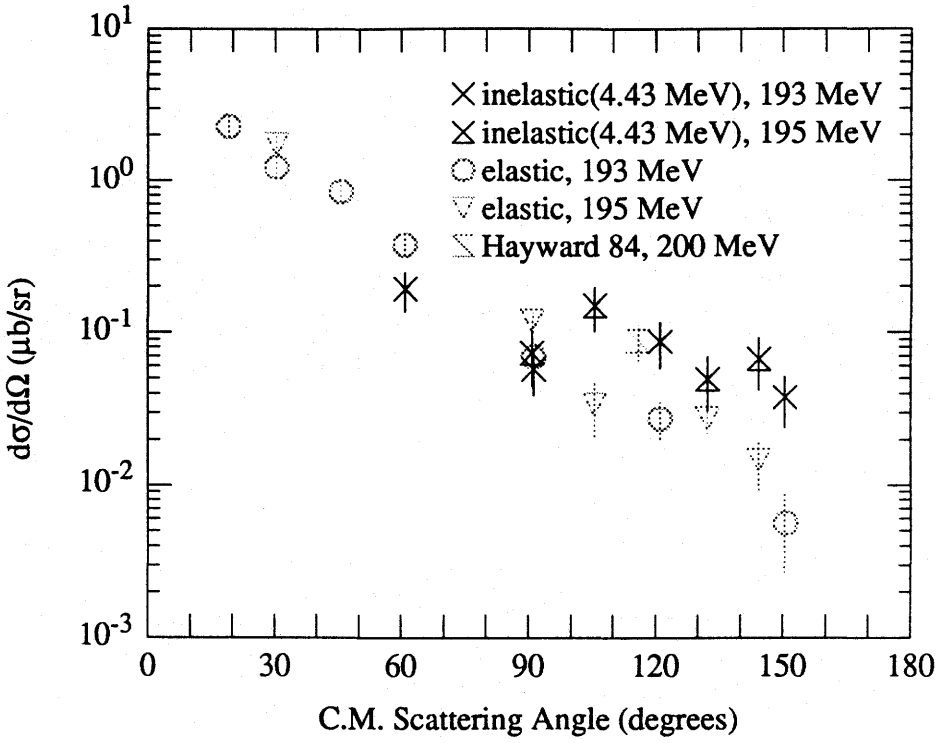

Figure 3.37: Differential Cross Section for 4.44 MeV Inelastic Photon Scattering from Carbon at C.M. Energies of 192.7 and 194.7 MeV

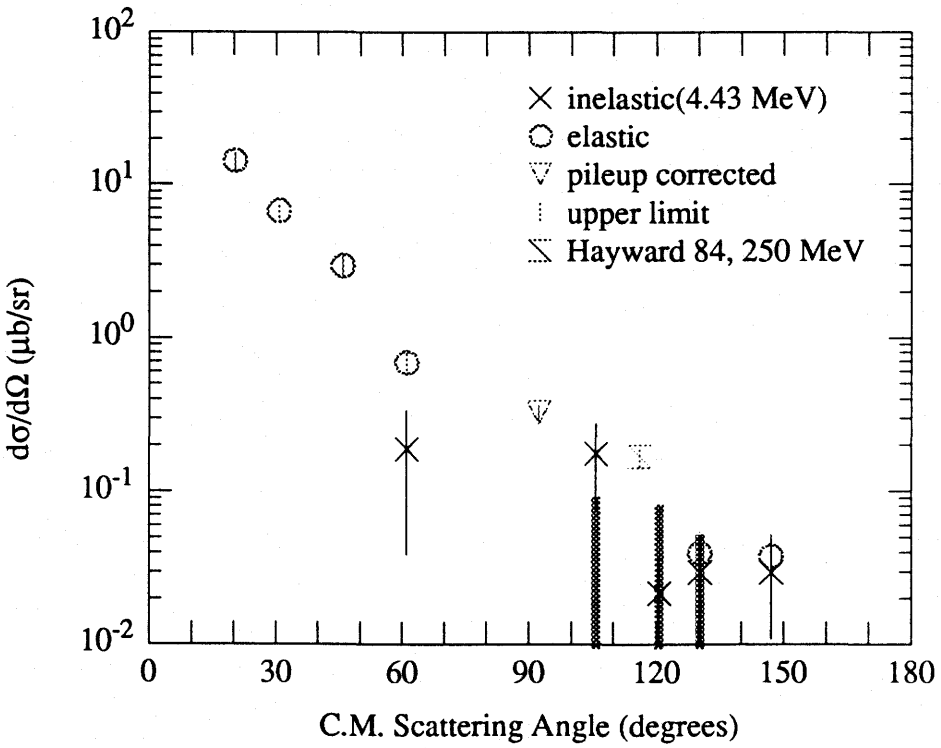

Figure 3.38: Differential Cross Section for 4.44 MeV Inelastic Photon Scattering from Carbon at C.M. Energy of 244.7 MeV

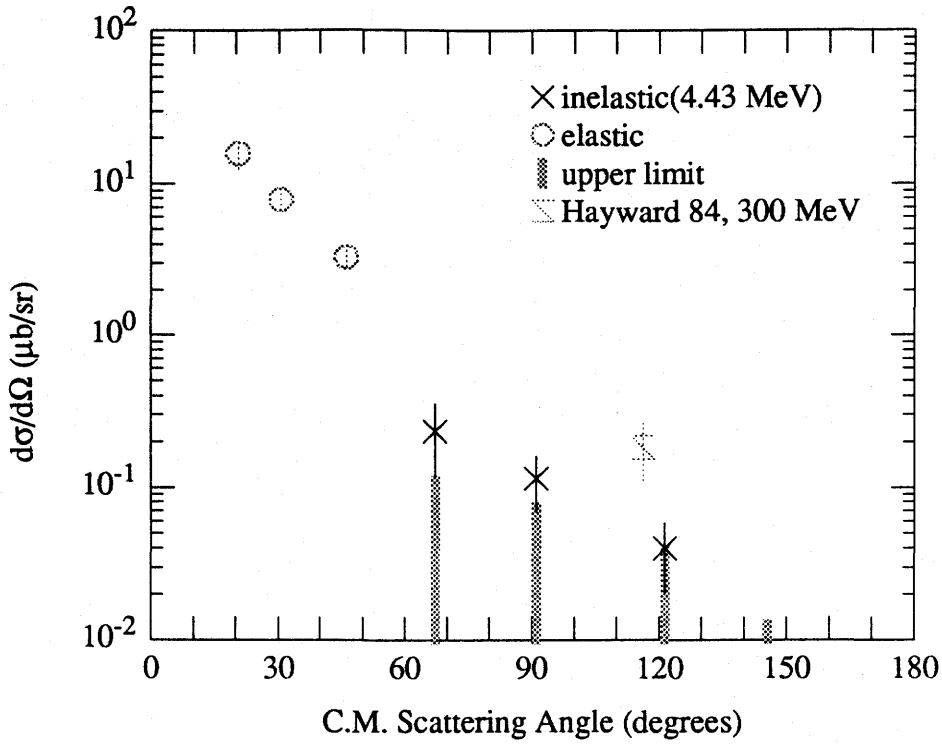

Figure 3.39: Differential Cross Section for 4.44 MeV Inelastic Photon Scattering from Carbon at C.M. Energy of 287.7 MeV

Chapter 4. CONCLUSIONS

4.1 Elastic Scattering Results and Discussion

The experiments described in this thesis were the photon scattering from ^{1}H, ^{4}He, and ^{12}C using a high duty cycle photon beam and a high resolution photon spectrometer.

The proton data were analysed by E. Hallin and constraints on the electric and magnetic polarizabilities of the proton were derived [Hallin 93]. These data have shown the first evidence for the unitarity cusp in the Compton scattering channel at photoproduction threshold [Bergstrom 93].

Most of the helium data was quickly analysed by D. Delli Carpini, for his Ph.D. thesis, to confirm the dramatic rise in the cross section at backward angles at 180 MeV [Austin 86] which disagreed with the Δ-hole model [Delli Carpini 90, Delli Carpini 91]. However the data for cross sections for the photon energy of 145.9 MeV were taken later and analysed by the present author. Indeed, all the helium data were re-analysed with more sophisticated programs before tackling the more difficult task of analysing the carbon data. While there were some disagreements, there was no systematic discrepancy between the present results and the earlier analysis. This gives some measure of confidence in the new analysis code.

The results for the angular distribution at 145.9 MeV in helium are presented here, in Figure 4.1, as they have not been published elsewhere. Although there are no Δ-hole calculations for helium at this energy, this model is not expected to succeed because the rise in cross section at back angles is similar to the 180 MeV [Austin 86] and 187 MeV [Delli Carpini 90]. The measured cross sections agree well with the Schematic model [Booth 90] at forward angles and then rise above the zero degree cross section at back

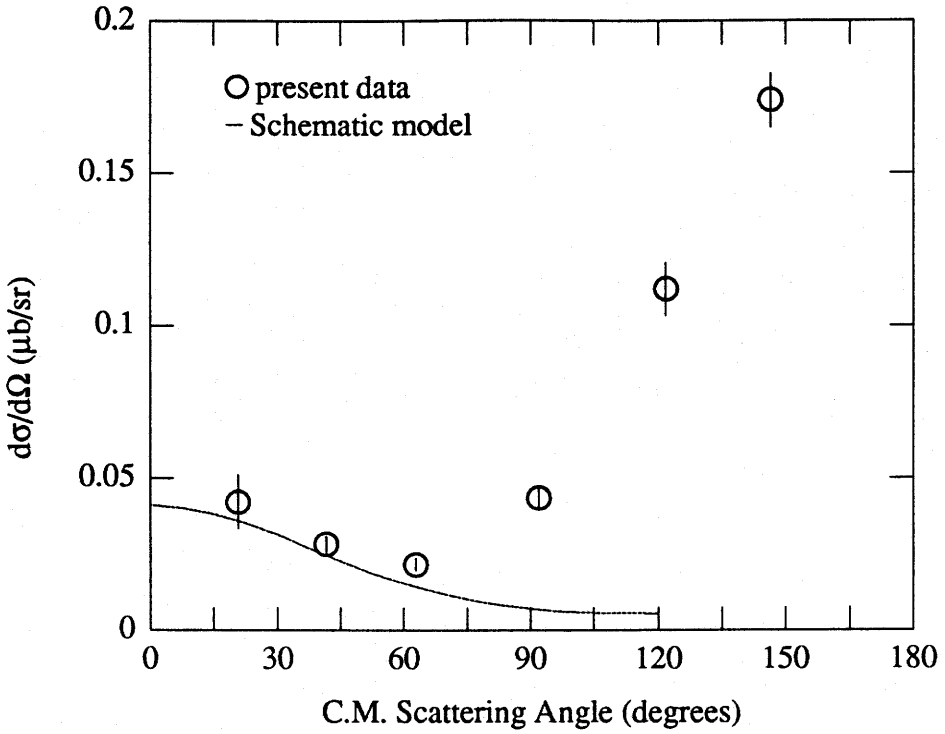

Figure 4.1: Differential Cross Section for Elastic Scattering of 145.9 MeV Photons from He

angles. It would be interesting to see if calculations of the type mentioned by L'vov [L'vov 90] would show that this back angle increase is really due to MEC effects, and if quark calculations would also show this.

The results for elastic scattering of photons from carbon are shown with the Schematic model (see Section 1.4 and Appendix F) and the previous Hayward and Ziegler [Hayward 84] measurement in Figure 4.2 to Figure 4.4. The results from the 196 MeV and 198 MeV runs are shown together in Figure 4.3 because difference in cross sections due to a 2 MeV energy difference is assumed to be negligible. Figure 4.4 and Figure 4.5 show data points that have been pileup corrected (triangles) and data points where only upper limits could be extracted (vertical bars). The only Δ-hole calculation that is relevant to the data in the measured energy range was done for 200 MeV photons (see Figure 4.3). In contrast

to the helium results (Figure 1.7 in Chapter 1), the model is higher than the data at back angles. It would be interesting to see if this is true nearer to the resonance, however that calculation has not been done.

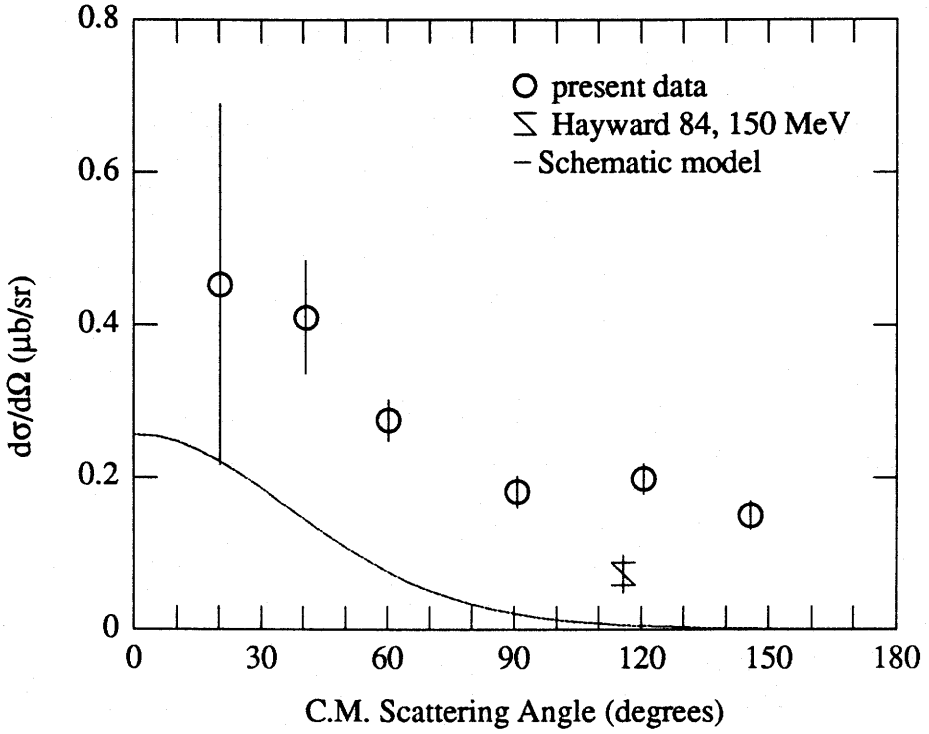

Figure 4.2: Differential Cross Section for Elastic Scattering of 154.0 MeV Photons from Carbon

The Schematic model is expected to apply at 0° since at this angle it is tied directly to measured total absorption cross sections via the optical theorem and the dispersion relations. The necessary total absorption data for carbon do not exist and, instead, the total cross sections were extrapolated from beryllium cross sections (see Appendix F). Thus any peculiarities that may exist in the carbon absorption cross section would not be accounted for. This has been remarked upon for helium [Delli Carpini 90, Delli Carpini 91] where the calculated forward cross sections do not match extrapolations of the angular distribution data to 0°. This could be the cause of the discrepancy in the 154 MeV carbon data (Figure 4.2). At 195 MeV, the model seems to slightly overestimate the data (Figure

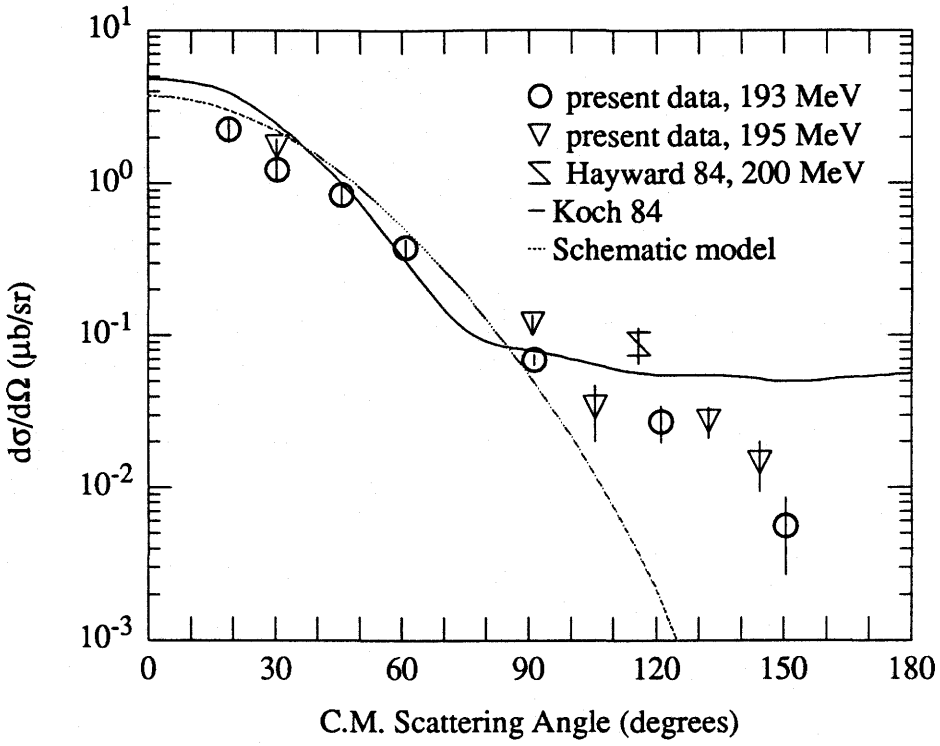

Figure 4.3: Differential Cross Section for Elastic Scattering of 192.7 MeV and 194.7 MeV Photons from Carbon

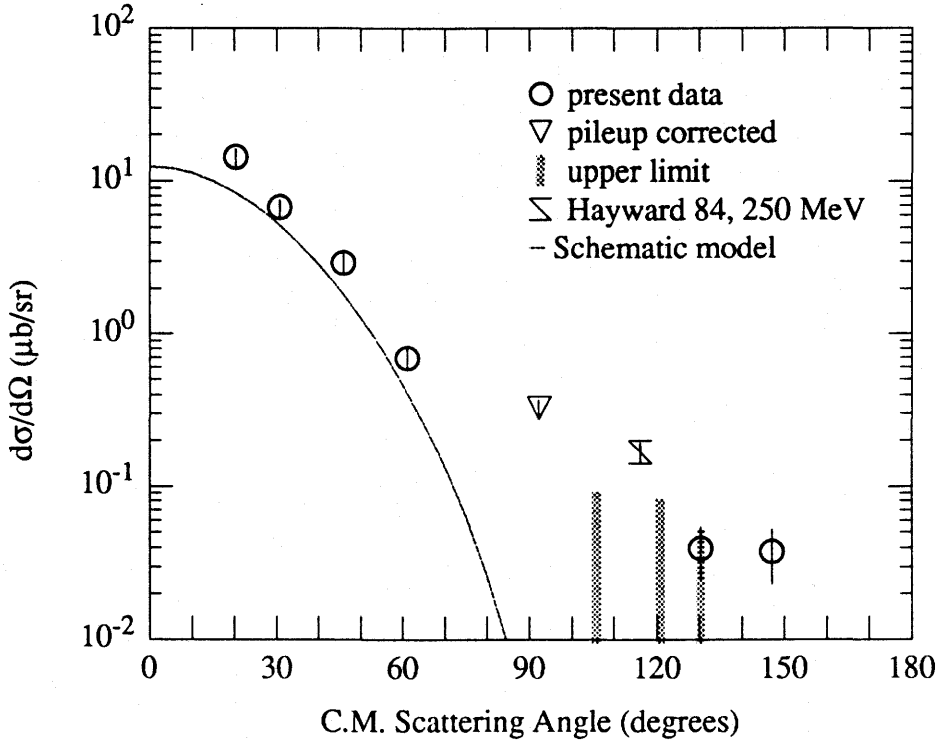

Figure 4.4: Differential Cross Section for Elastic Scattering of 244.7 MeV Photons from Carbon

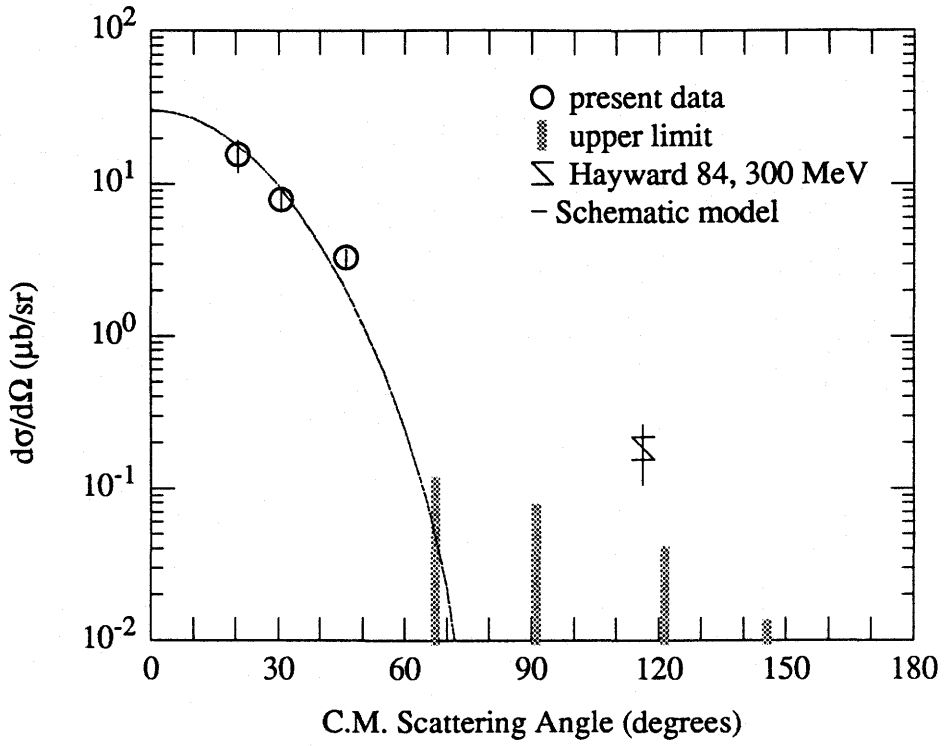

Figure 4.5: Differential Cross Section for Elastic Scattering of 287.7 MeV Photons from Carbon

4.3), whereas the 244 MeV model seems to slightly underestimate the model (Figure 4.4). Nonetheless, the Schematic model describes the present measured forward angle cross sections within a factor of 2.

The fit at finite angles requires assumptions about multipolarity, form factor, and other possible contributions, as discussed in Chapter 1. The Schematic model shown in Figure 4.1 to Figure 4.5 assumes only dipole radiation is involved. Because there are probably additional mechanisms involved, like MEC effects, the model is expected not to fit well, or at all, at more backward angles. This is supported by the measurements. However, there is a strong suppression of carbon cross sections at these angles, at the lower energies, in contrast to the enhancement of cross sections for helium at similar angles and energies. This may simply be due to the difference in magnitude of the form

factors for helium and carbon. The carbon form factor is typically on the order of 10 to 100 times smaller for the present range of momentum transfer (see Figure F.2 and Figure F.3 in Appendix F).

4.2 4.44 MeV Inelastic Scattering Results and Discussion

The differential cross sections for inelastic photon scattering leading to the 4.44 MeV excited state of carbon are shown in Figure 4.6 to Figure 4.9. These cross sections have not been measured before because of the inability to construct high energy, high resolution photon spectrometers. Such a detector was used for this experiment. These results show that at back angles the inelastic scattering process is comparable to or dominates the elastic process. It is therefore not surprising that the Hayward and Ziegler measurements exceeded Δ-hole predictions for elastic cross sections in some cases.

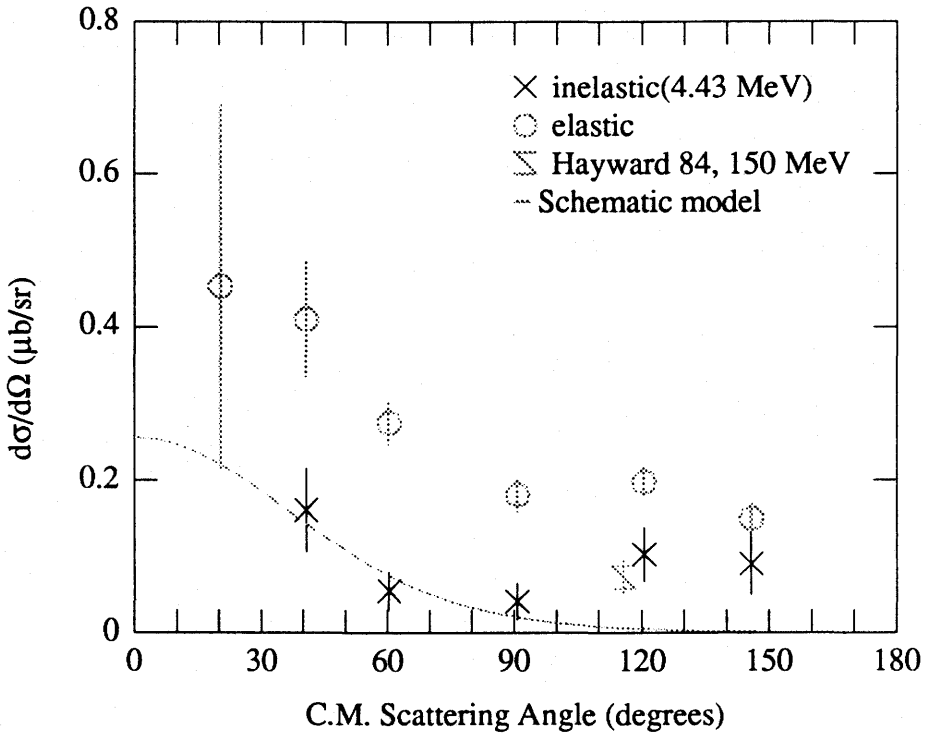

Figure 4.6: Differential Cross Section for Inelastic Scattering of 154.0 MeV Photons from Carbon Leading to the 4.44 MeV State

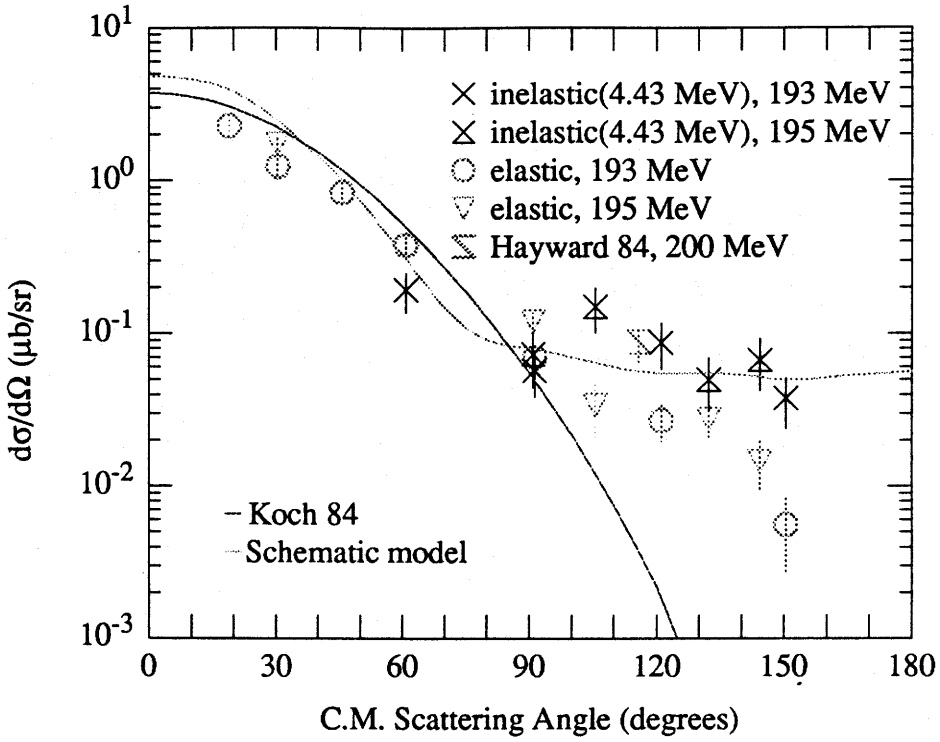

Figure 4.7: Differential Cross Section for Inelastic Scattering of 192.7 MeV Photons from Carbon Leading to the 4.44 MeV State

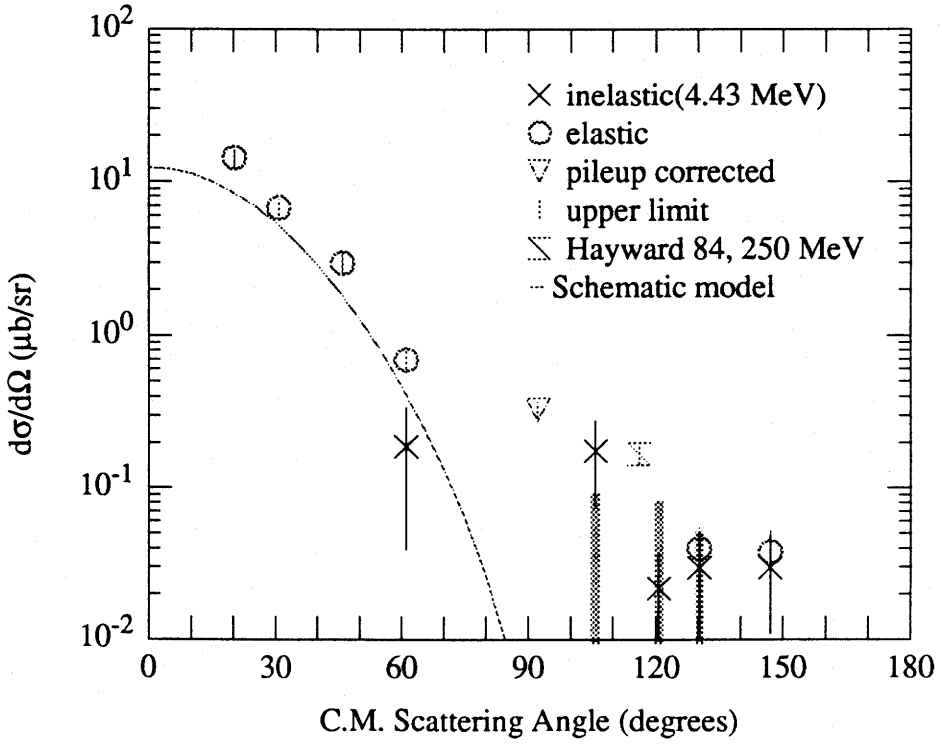

Figure 4.8: Differential Cross Section for Inelastic Scattering of 244.7 MeV Photons from Carbon Leading to the 4.44 MeV State

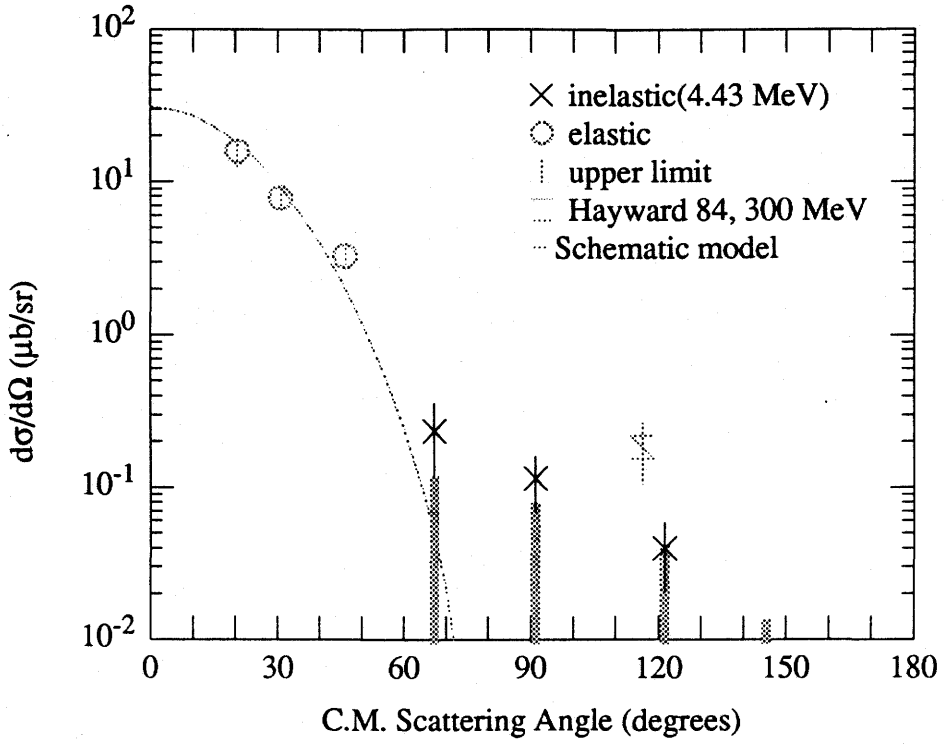

Figure 4.9: Differential Cross Section for Inelastic Scattering of 287.7 MeV Photons from Carbon Leading to the 4.44 MeV State

4.3 Energy Dependences

The energy dependence of the elastic differential cross sections in ^{4}He and ^{12}C are shown in Figure 4.10 to Figure 4.29. The Schematic model for the respective nuclei are also plotted for comparison. As shown in Section 4.1 the Schematic model describes the forward angle cross sections fairly well, so that the model's satisfactory energy dependence is expected to be reflected in plots of cross section versus energy at forward angles. The data show that this is true up to 70° for C and up to 90° for He (Figure 4.10 to Figure 4.20). This indicates, at least qualitatively, that the Be energy dependence is valid for helium and carbon. For helium at back angles beyond 90° (Figure 4.22 to Figure 4.28), the cross section seems to be constant and larger than the Schematic model predictions. For carbon, some of the plots (Figure 4.25 and Figure 4.29) seem to hint at underlying structure, but the magnitudes do not correspond to that predicted by the Schematic model. Unfortunately, at higher energies and back angles, the cross sections are small and the data

dominated by pileup. This means that only upper limits can be set, which make comparison with predictions more difficult. However, where data points do exist, they are higher than the Schematic model predictions, similar to the case of helium.

The difference between the Schematic model and the data indicates the presence of other internal processes which tend to move diffraction minima and fill them in. So not only are the back angle cross sections large compared to the Schematic model, but the magnitude does not change dramatically. Thus a realistic model must predict this back angle behavior and this presents a challenge for the theorists.

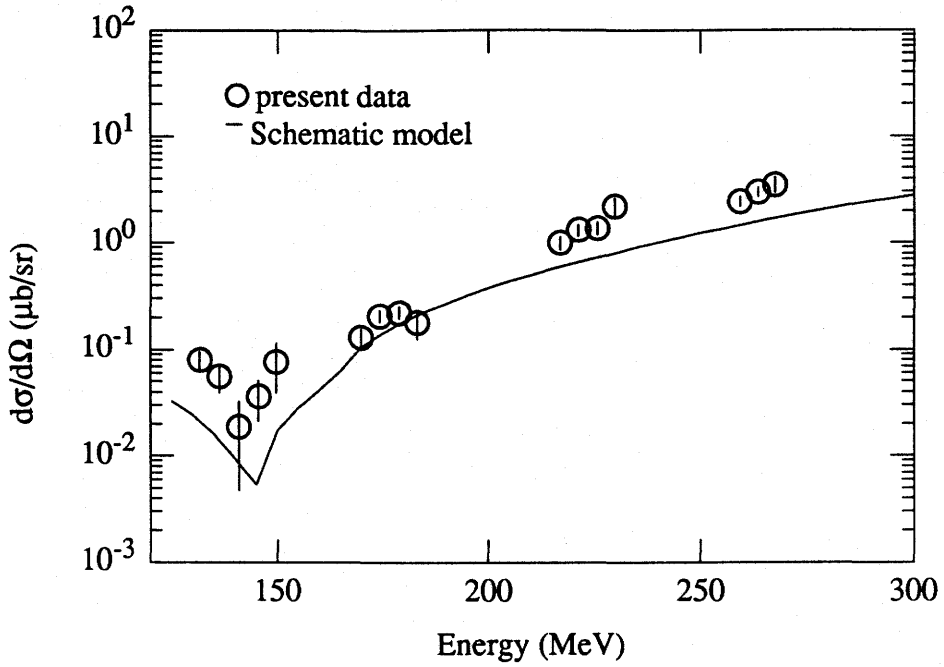

Figure 4.10: Differential Cross Section for Elastic Photon Scattering at 20° from He

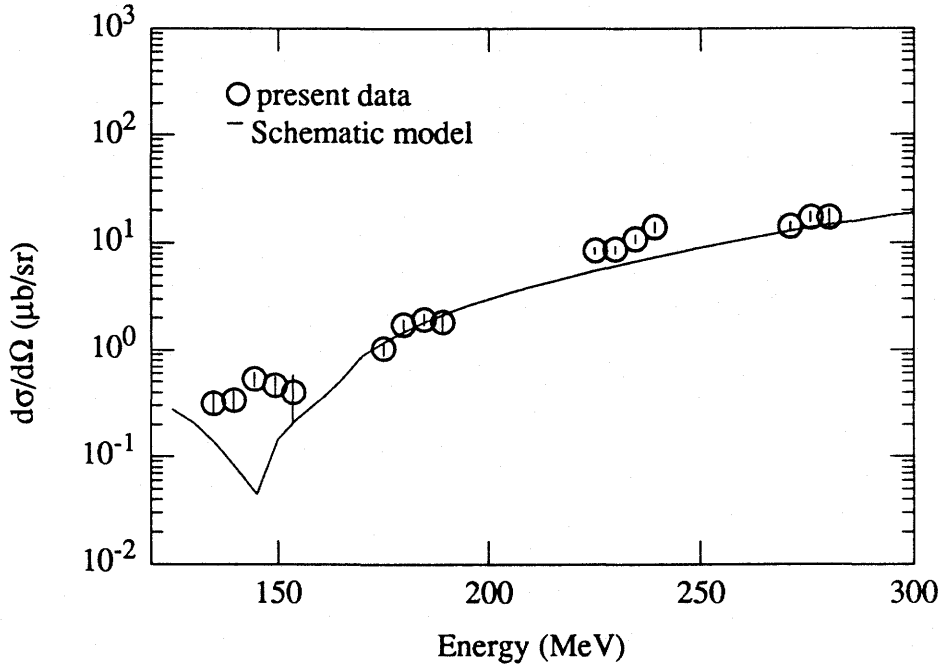

Figure 4.11: Differential Cross Section for Elastic Photon Scattering at 20° from C

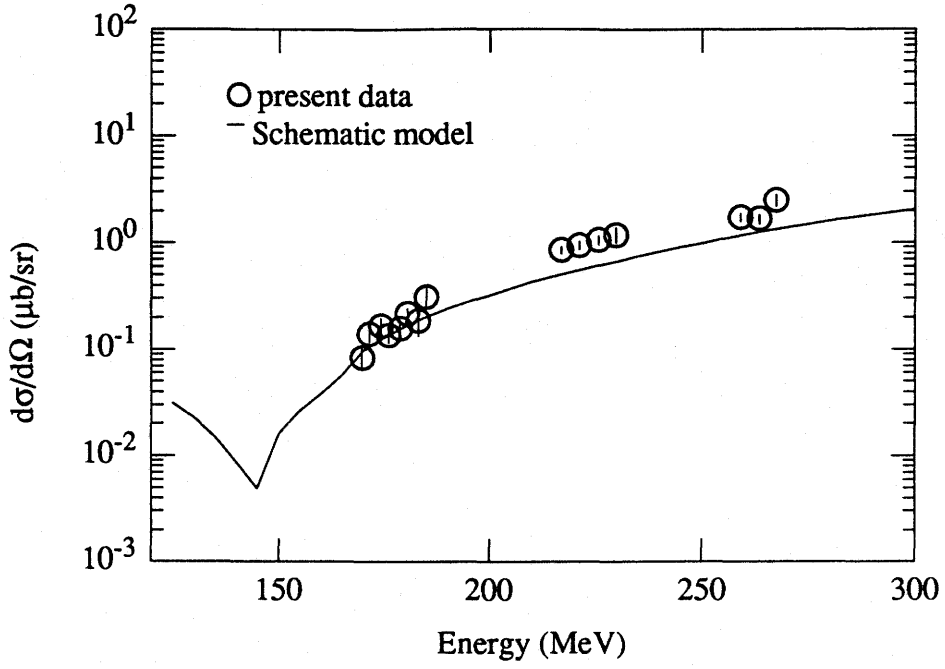

Figure 4.12: Differential Cross Section for Elastic Photon Scattering at 30° from He

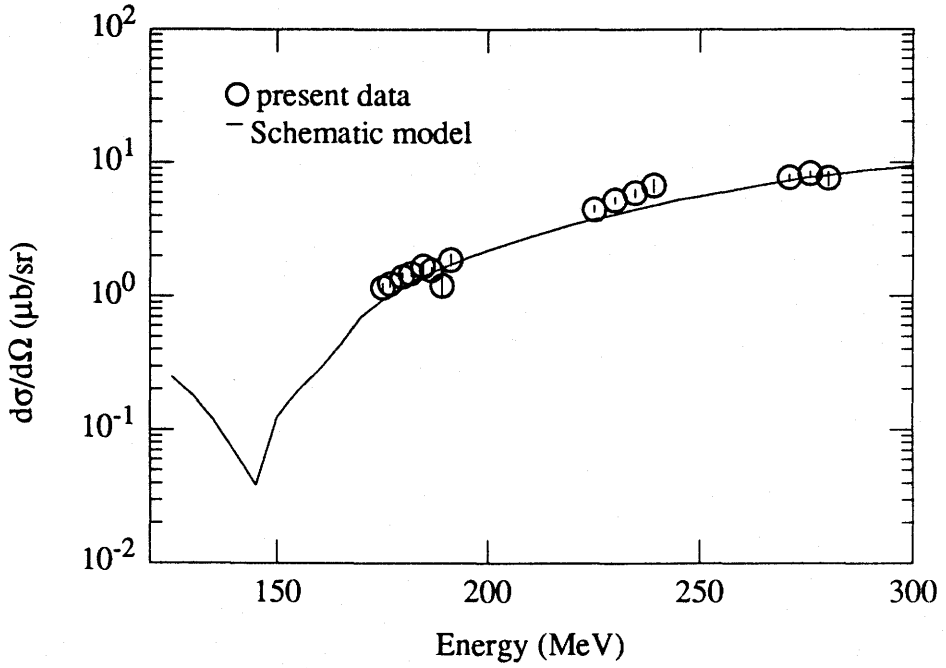

Figure 4.13: Differential Cross Section for Elastic Photon Scattering at 30° from C

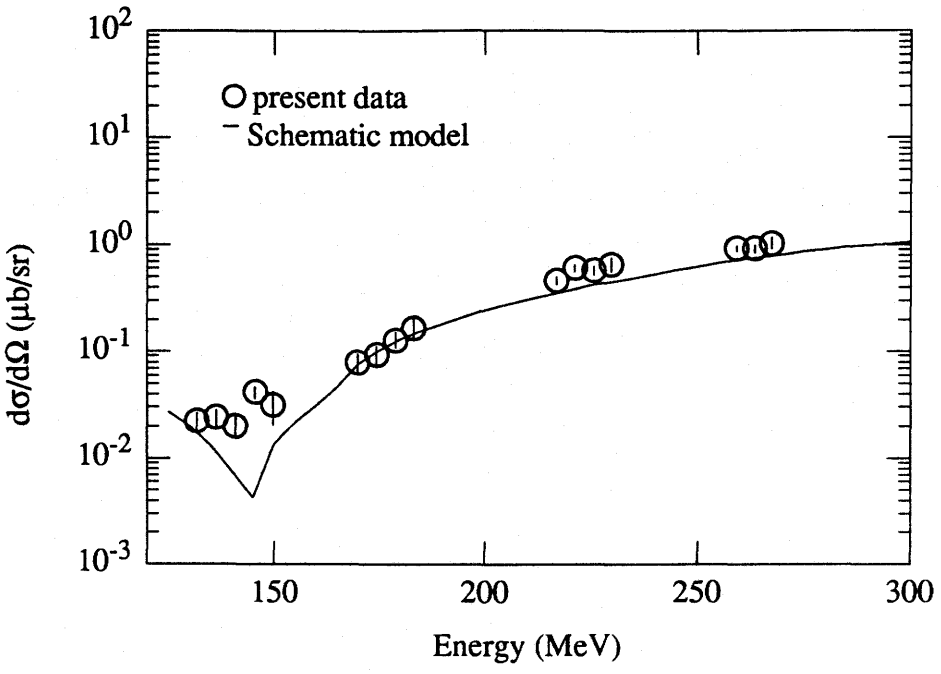

Figure 4.14: Differential Cross Section for Elastic Photon Scattering at 45° from He

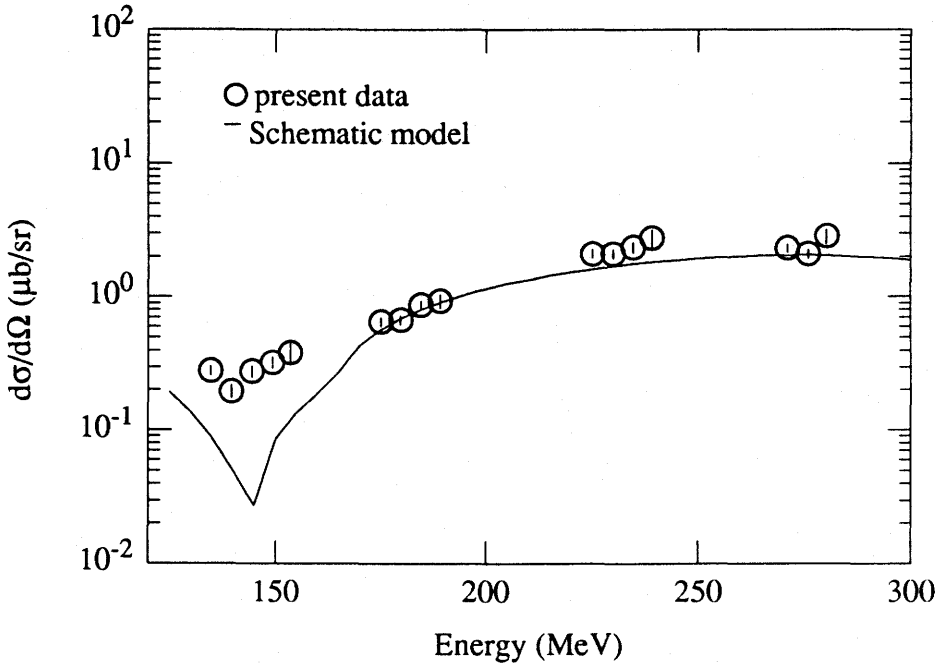

Figure 4.15: Differential Cross Section for Elastic Photon Scattering at 45° from C

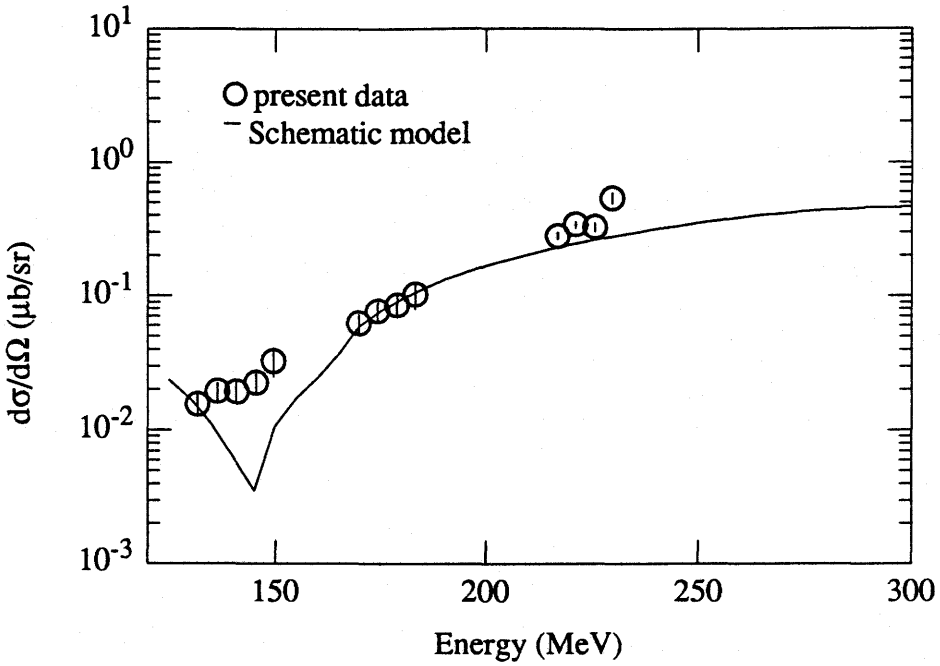

Figure 4.16: Differential Cross Section for Elastic Photon Scattering at 60° from He

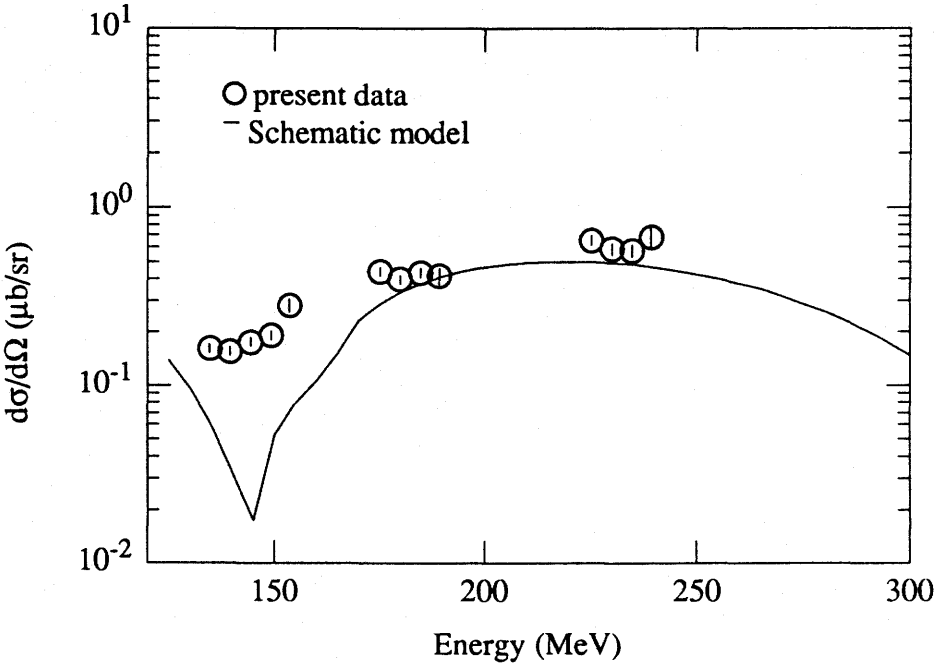

Figure 4.17: Differential Cross Section for Elastic Photon Scattering at 60° from C

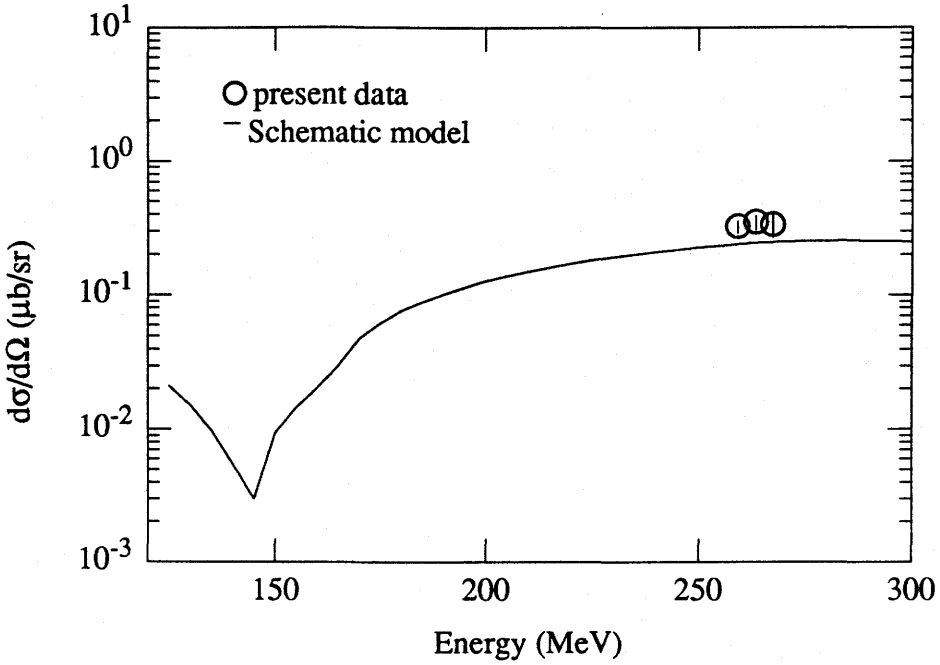

Figure 4.18: Differential Cross Section for Elastic Photon Scattering at 70° from He

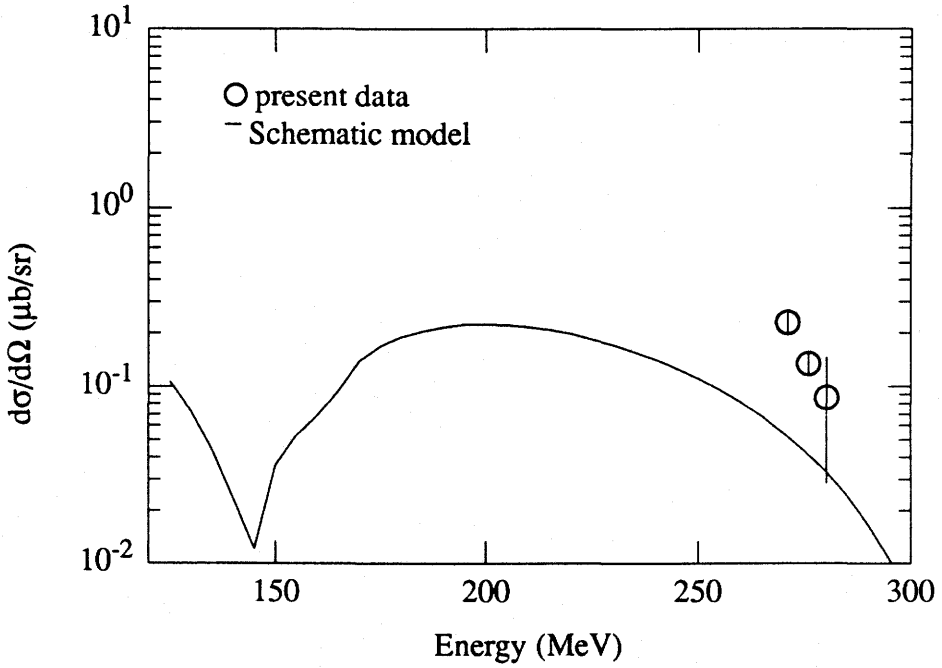

Figure 4.19: Differential Cross Section for Elastic Photon Scattering at 70° from C

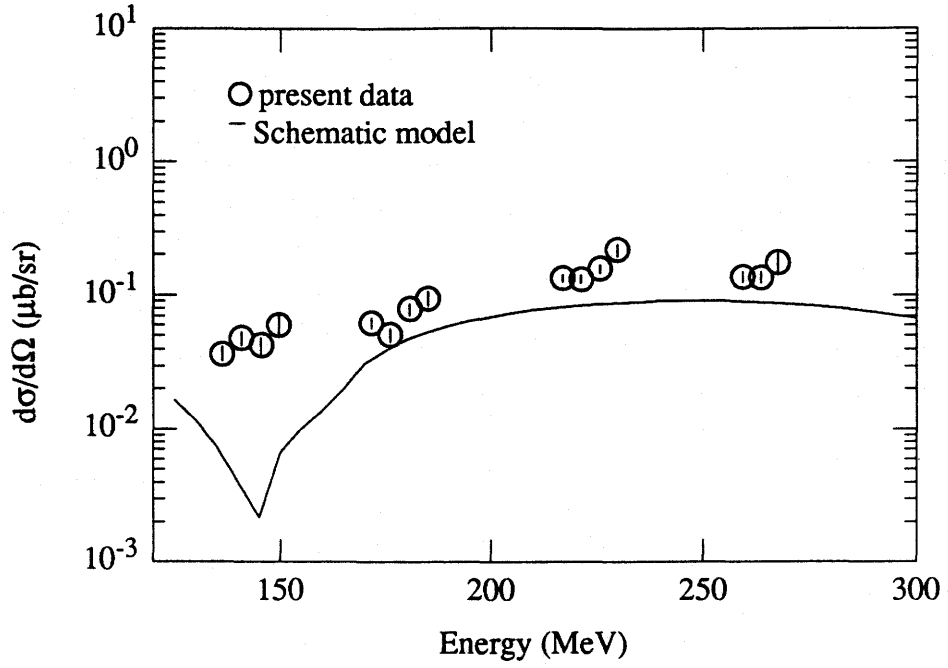

Figure 4.20: Differential Cross Section for Elastic Photon Scattering at 90° from He

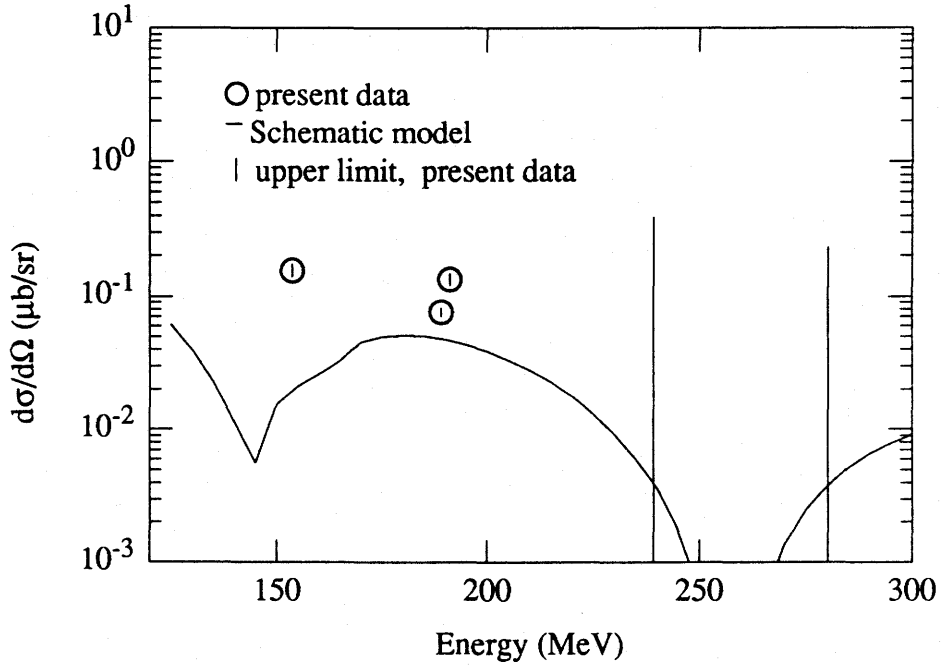

Figure 4.21: Differential Cross Section for Elastic Photon Scattering at 90° from C

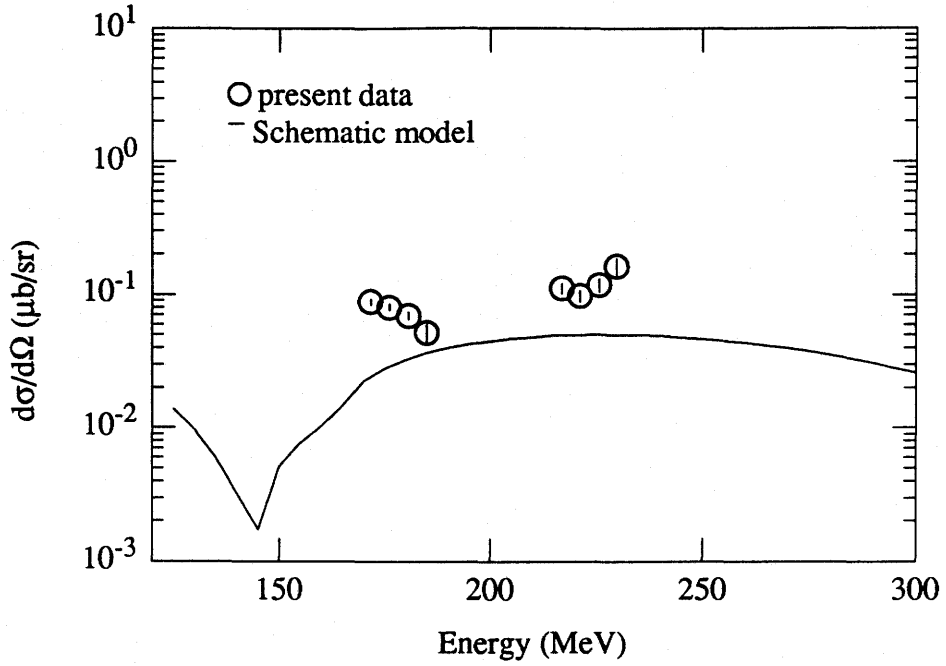

Figure 4.22: Differential Cross Section for Elastic Photon Scattering at 105° from He

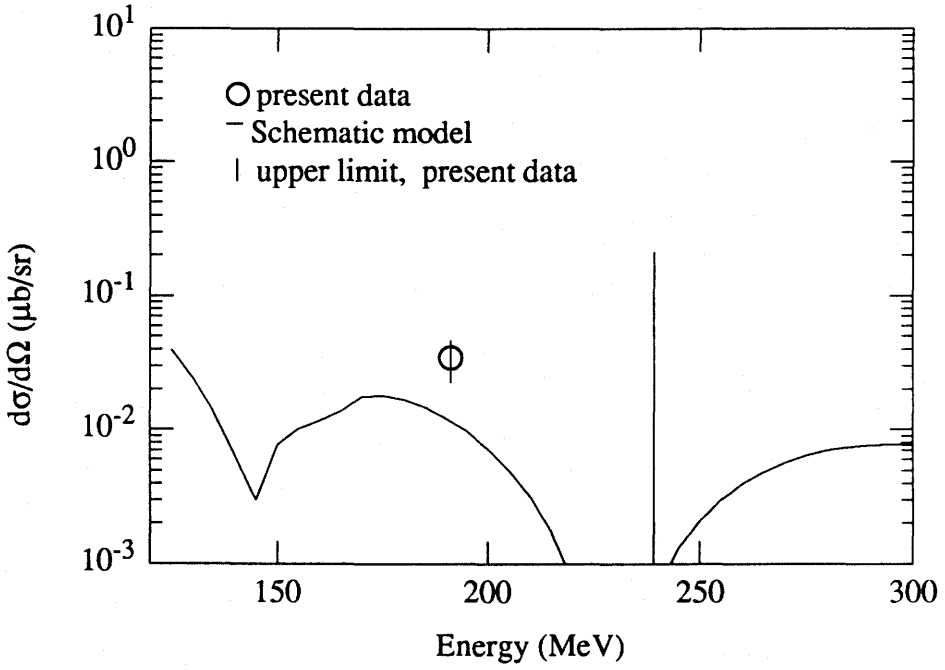

Figure 4.23: Differential Cross Section for Elastic Photon Scattering at 105° from C

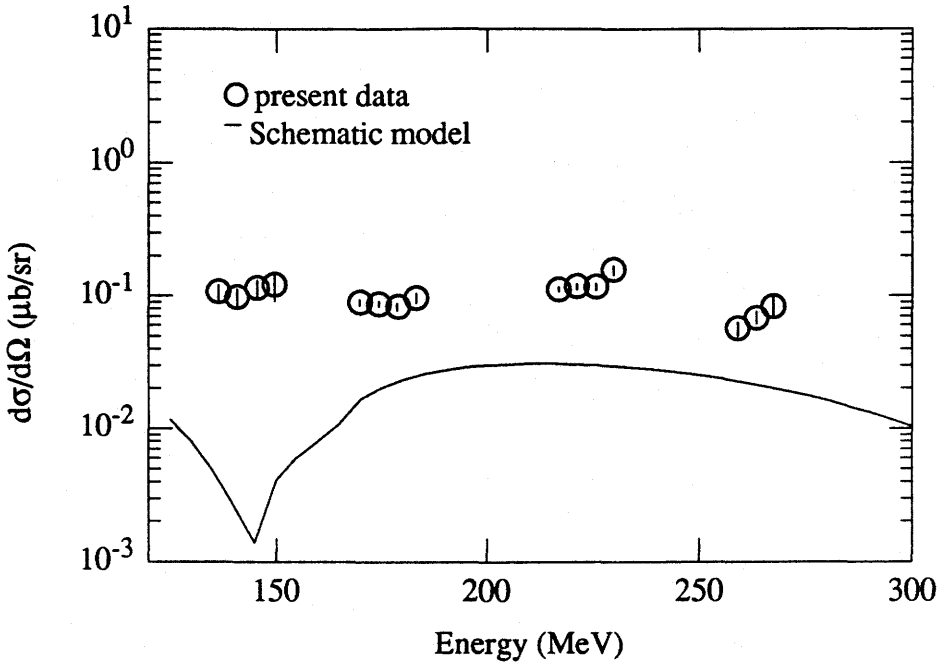

Figure 4.24: Differential Cross Section for Elastic Photon Scattering at 120° from He

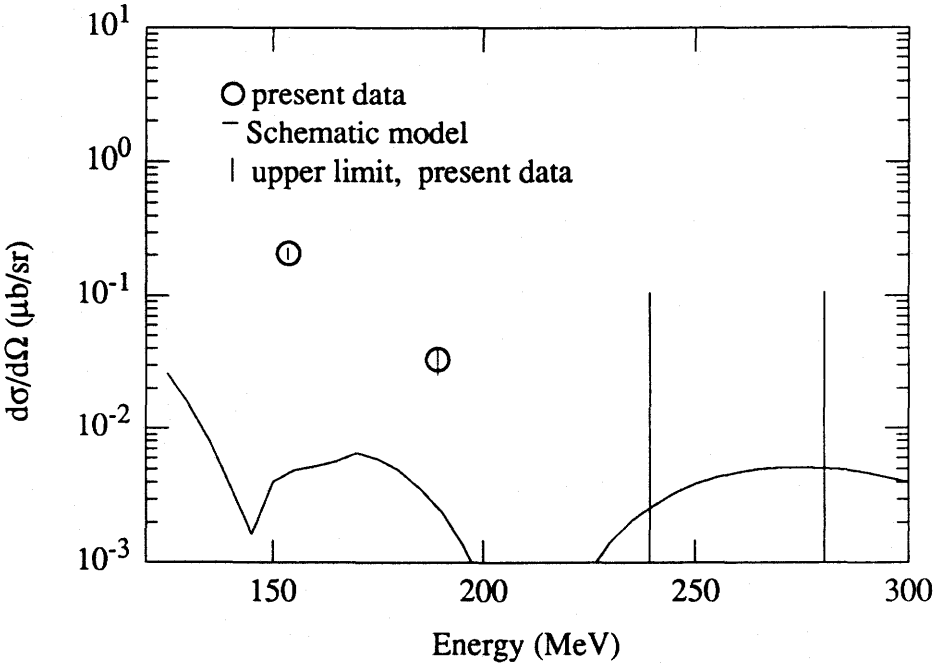

Figure 4.25: Differential Cross Section for Elastic Photon Scattering at 120° from C

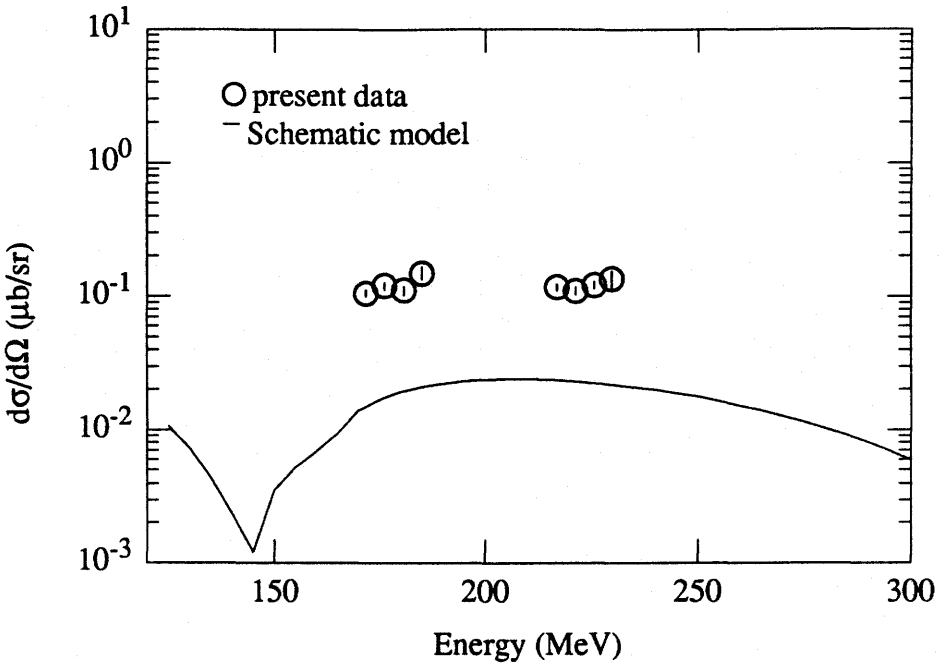

Figure 4.26: Differential Cross Section for Elastic Photon Scattering at 130° from He

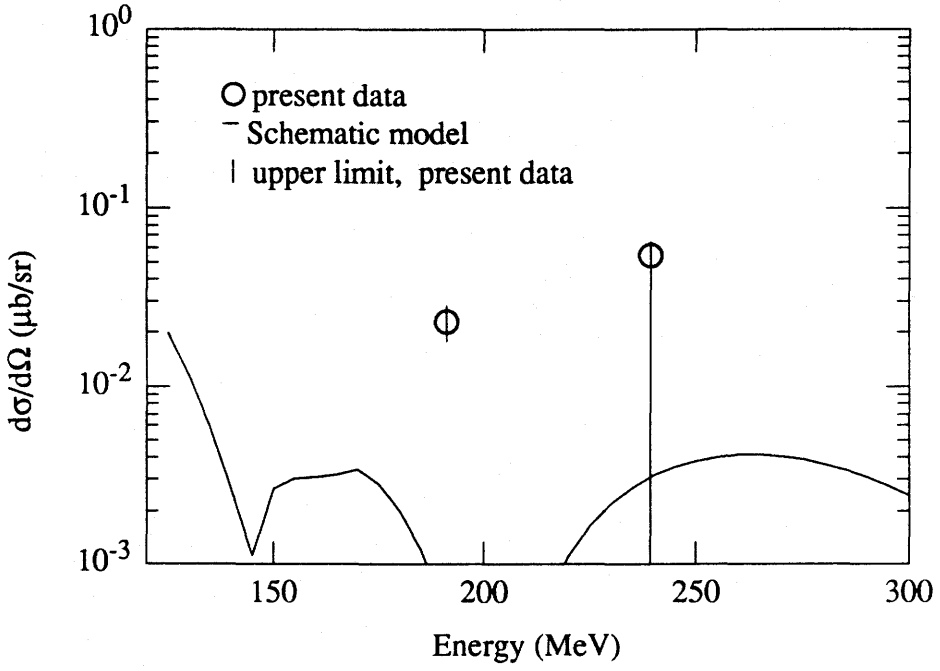

Figure 4.27: Differential Cross Section for Elastic Photon Scattering at 130° from C

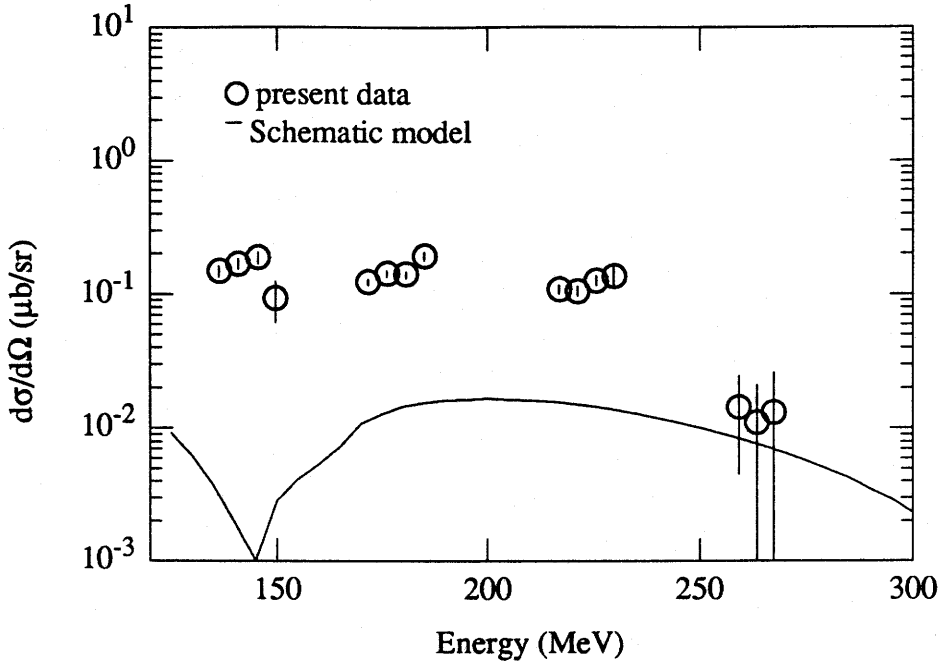

Figure 4.28: Differential Cross Section for Elastic Photon Scattering at 150° from He

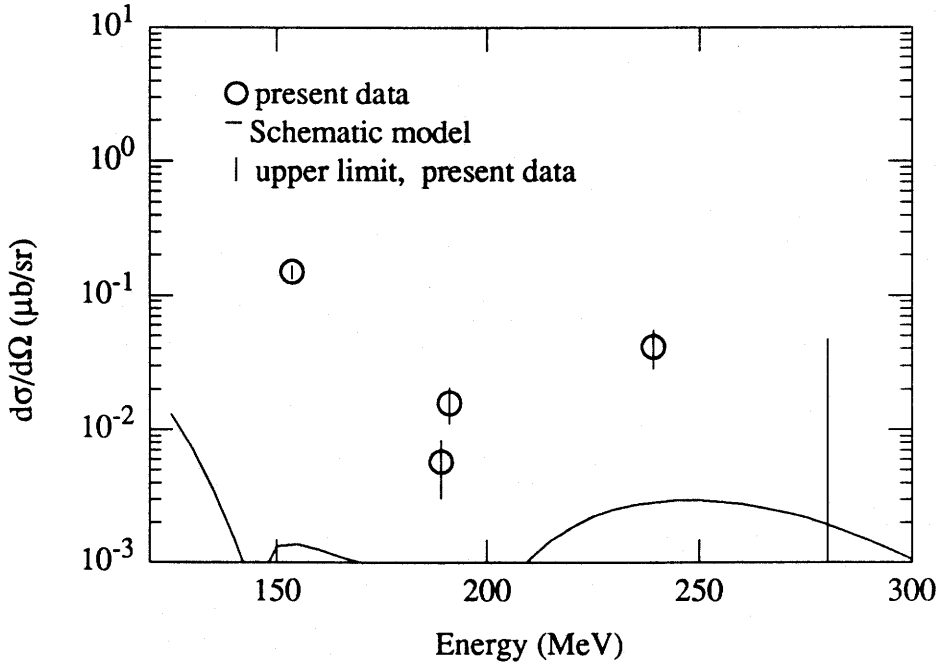

Figure 4.29: Differential Cross Section for Elastic Photon Scattering at 150° from C

4.4 Summary and Future Experiments

Photon scattering experiments performed at SAL measured the differential cross section for elastic photon scattering near the Δ(1232) resonance from ^{1}H, ^{4}He, and ^{12}C. For ^{12}C, it was also possible to measure the inelastic scattering to the first excited state. The carbon results form the core of this thesis.

The measurement was of interest because of the lack of data in this energy range. There have been some calculations attempted for this reaction, notably of the Δ-hole type, but further progress was hampered by lack of data. The experimental problem was, until recently, the lack of an intense high duty factor photon source and detectors of adequate resolution. Now, the Pulse Stretcher Ring at SAL provides the necessary photon beam-coupled with the high resolution spectrometer, BUNI, made the experiment finally technologically feasible.

The results of this experiment, made possible by these innovations, show that the Δ-hole models are not successful in describing photon scattering. The model does not fail in a consistent manner in that the carbon back angle cross sections are lower than the model, whereas previous helium data are higher.

The Schematic model that assumes pure dipole scattering also does not describe the back angle cross sections, the data being consistently higher that the model by orders of magnitude. For carbon, there is some indication of structure that is not evident in helium, though this structure does not correspond to that of the predictions. There must then be additional mechanisms involved. Hopefully, the large database generated by this experiment will stimulate renewed interest in photon scattering calculations in the Δ-resonance region.

For the small angle scattering, there seem to be some discrepancies with the overall normalization of the Schematic model and experimental data in this thesis and helium data [Delli Carpini 90, Delli Carpini 91]. Some improvent in the agreement with the Schematic model might be possible if absorption data for the relevant nuclei were available, instead of relying on extrapolations from beryllium data.

It would be interesting to do elastic photon scattering with a tagged (monochromatic) photon beam. The beam normalization is unambiguous with taggers. A tagged elastic scattering experiment would tie down the absolute normalization of cross sections. Inelastic cross sections may be more easily obtained, since it is easier to resolve peaks rather than the superposition of continua. A tagged experiment would also get an excellent energy dependence for a single angle for both the elastic and inelastic channels. A current analysis at Mainz and a future experiment at SAL will attempt to extract these information in the Δ resonance region.

However, tagged experiments are not well suited for measuring the photon scattering angular distributions. For the back angle data points, where the cross sections are low, current tagging facilities operate with fluxes 100 times lower than high duty cycle bremsstrahlung facilities making the measurement of angular distributions very difficult and time consuming. Since angular distributions are sensitive to the mechanisms in the Δ resonance, a bremsstrahlung experiment is preferred over a tagged one. The high beam intensities allow measurements to be made at many angles in a reasonable time. Such a measurement was accomplished for carbon in the Δ resonance region and is documented in this thesis.

REFERENCES

Ahrens 85 — J. Ahrens, "The Total Absorption of Photons by Nuclei", Nucl. Phys **A446** (1985), 229-240.

Ajzenberg 89 — F. Ajzenberg-Selove, "Energy Levels of Light Nuclei A=11-12", Nucl. Phys. **A506** (1989), 1-158.

Amendt 91 — David Amendt, Differential Cross Sections for Compton Scattering Off the Proton at 185 MeV, M.Sc. Thesis, University of Saskatchewan (1991), SAL Report No.**40**.

Arends 81 — J. Arends, et al, "Measurement of Total Photonuclear Cross Sections in the Δ-Resonance Region", Phys. Lett. **98B** (1981), 423-426.

Arends 82 — J. Arends, et al, "Inclusive Charged Pion Photoproduction on ^{12}C Using Tagged Photons in the Energy Range (200-390) MeV", Z. Phys. **A305** (1982), 205-212.

Arends 82a — J. Arends, et al, "Experimental Investigation of the Reaction $^{12}C(\gamma,\pi^0)X$ in the Photon Energy Range Between Threshold and 450 MeV", Z. Phys. **A311** (1983), 367-374.

Arenhovel 85 — H. Arenhovel, M. Weyrauch, and P.G. Reinhard, "Inelastic Photon Scattering from Complex Nuclei in the Δ-Resonance Region", Phys. Lett. **155B** (1985), 22-26.

Arenhovel 86 — H. Arenhovel, "Subnuclear Degrees of Freedom in Photoabsorption and Scattering", New Vistas in Electro-Nuclear Physics, ed. E.L. Tomusiak, Caplan, H.S., and Dressler, E.T., Plenum Press, 1986, 262.

Austin 86 — E.J. Austin, et al, "Differential Cross Section for Coherent Photon Scattering from ^4He at 180 MeV", Phys. Rev. Lett. **57** (1986), 972-975.

Austin 88a — E.J. Austin, et al, "Cross Sections for the Reaction $^4He(\gamma,\gamma)^4He$ in the Δ(1232)-Resonance Region", Phys. Rev. Lett. **61** (1988), 1922-1925.

Austin 88b — Eric Jon Austin, Elastic Photon Scattering from ^4He in the Δ(1232) Region, Ph.D. Thesis, Boston University (1988).

Baldin 60 — A.M. Baldin, "Polarizability of Nucleons", Nucl. Phys. **18** (1960), 310-317.

Baldin 61 — A.M. Baldin, V.I. Goldanskii, I.L. Rozental, Kinematics of Nuclear Reactions, trans. Ronald F. Peierls, Oxford University Press, 1961.

Baranov 75 — P.S. Baranov et al., "Elastic Scattering of Low-energy Photons by Protons", Sov. J. Nucl. Phys. **21** (1975), 355-359.

Barut 80 — Barut, A.O., Electrodynamics and Classical Theory of Fields and Particles, Dover Publications, Inc., New York,1980, p 19.

Baym 69 — G. Baym, Lectures on Quantum Mechanics, Benjamin, New York, 1969.

Bergstrom 93 — J.C. Bergstrom et al., Phys. Rev. C, submitted for publication.

Bjorken 64 — J.D. Bjorken and S.D. Drell, Relativistic Quantum Mechanics, McGraw-Hill, New York, 1964, 127-132.

Bjorken 65 — J.D. Bjorken and S.D. Drell, Relativistic Quantum Fields, McGraw-Hill, New York, 1965, 211-213.

Booth 90 — E. Booth, private communication, 1990.

Crannell 64 — H.L. Crannell and T.A. Griffy, "Determination of Radiative Transition Widths of Excited States in C^{12}", Phys. Rev. **136** (1964), B1580-B1584.

Crannell 66 — H.L. Crannell, "Elastic and Inelastic Electron Scattering from C^{12} and O^{16}", Phys. Rev. **148** (1966), 1107-1118.

Dallin 90 — L.O. Dallin, High Duty Factor Monochromatic Extractions from EROS, Ph.D. Thesis, University of Saskatchewan (1990), SAL Report No. **38**.

Delli Carpini 90 — D. Delli Carpini, Elastic Photon Differential Cross Sections for Helium Near the Delta Resonance, Ph.D. Thesis, Boston University (1990).

Delli Carpini 91 — D. Delli Carpini, et al, "Coherent Photon Scattering Cross Sections for Helium Near the Delta Resonance", Phys. Rev. **C43** (1991), 1525-1531.

DeWire 61 — J.W. Dewire, M. Feldman, and R. Littauer, "Elastic Scattering of Photons by Protons", Phys. Rev. **124** (1961), 909-912.

Dodge 80 — W.R. Dodge, et al, "E2 Strength in ^{12}C Determined by Elastic Photon Scattering", Phys. Rev. Lett. **44** (1980), 1040-43.

Ehrenberg 59 — H.F. Ehrenberg, et al, "High-Energy Electron Scattering and the Charge Distribution of Carbon-12 and Oxygen-16", Phys. Rev. **113** (1959), 666-674.

Ericson 73 — T.E.O. Ericson and J. Hufner, "Low-Frequency Photon Scattering by Nuclei", Nucl. Phys. **B57** (1973), 604-616.

Friar 75 — J.L. Friar, "Low-Energy Theorems for Nuclear Compton and Raman Scattering and 0+ → 0+ Two-Photon Decays in Nuclei", Ann. of Phys. **95** (1975), 170-201.

Fregeau 55 — J.H. Fregeau and R. Hofstadter, "High-Energy Electron Scattering and Nuclear Structure Determinations. III. Carbon-12 Nucleus", Phys. Rev. **99** (1955), 1503-1509.

Frosch 61 — R.F. Frosch, et al, "Structure of the He^4 Nucleus from Elastic Electron Scattering", Phys. Rev. **160** (1961), 874-879.

Fuller 56 — E.G. Fuller and E. Hayward, "Nuclear Elastic Scattering of Photons", Phys. Rev. **101** (1956), 692-700.

Gell-Mann 54 — M. Gell-Mann, M.L. Goldberger, and W.E. Thirring, "Use of Causality Conditions in Quantum Theory", Phys. Rev. **95** (1954), 1612-1627.

Genzel 76 — H. Genzel et al., "Proton Compton Effect in the Δ(1232) Energy Region", Z. Phys. **A279** (1976), 399-406.

Gerasimov 65 — S.B. Gerasimov and L.D. Soloviev, "Scattering of Light of Low Frequency and the Charged Particle Polarizability", Nucl. Phys **74** (1965), 589-592.

Guiasu 78 — I. Guiasu, C. Pomponiu, and E.E. Radescu, "Elastic γ-Proton Scattering at Low and Intermediate Energies", Ann. Phys. **114** (1978), 296-331.

Hallin 93 — E. Hallin et al., Phys. Rev. C, submitted for publication.

Hayward 57 — E. Hayward and E.G. Fuller, "Photon Self-Absorption and Scattering by the 15.1-MeV Level in C^{12}", Phys. Rev. **106** (1957), 991-995.

Hayward 70 — E. Hayward, Photonuclear Reactions, N.B.S. Monograph 118 (1970).

Hayward 84 — E. Hayward and B. Ziegler, "Photon Scattering from ^{12}C and ^{208}Pb in the Δ-Region", Nucl. Phys. **A414** (1984), 333-346.

Herman 60 — R. Herman and R. Hofstadter, High-Energy Electron Scattering Tables, Stanford University Press, 1960.

Hirata 79 — M. Hirata, "Isobar-Hole Doorway States and π-^{16}O Scattering", Ann. of Phys. **120** (1979), 205-248.

Huber 90 — M.G. Huber, B.Ch. Metsch and H.R. Petry, "Photon and Pion Scattering on the Basis of Quark Models", Lecture Notes in Physics: Perspectives on Photon Interactions with Hadrons and Nuclei, eds. M. Schumacher and G. Tamas, Springer-Verlag, 1990, 145-165.

Jackson 75 — Jackson, J.D., Classical Electrodynamics, 2nd Ed., John Wiley and Sons, New York, 1975, 679-685.

Jackson 75a — ibid., Section 14.7, 679-689.

Jackson 75b — ibid., Section 9.6, 411-418.

Jackson 75c — ibid., Section 9.7, 418-425.

Keuhne 67 — H.W. Keuhne, P. Axel, and D.C. Sutton, "Photon Scattering by the Giant Magnetic Dipole States in ^{12}C, ^{24}Mg, and ^{28}Si", Phys. Rev. **163** (1967), 1278-1291.

Kisslinger 76 — L.S. Kisslinger and W.L. Wang, "The Isobar-Doorway Theory for Pion-Nucleus Interactions", Ann. of Phys. **99** (1976), 374-407.

Koch 83 — J.H. Koch and E.J. Moniz, "Coherent π^0 Photoproduction at Intermediate energy", Phys. Rev. **C27** (1983), 751-764.

Koch 84 — J.H. Koch, E.J. Moniz, and N. Ohtsuka, "Nuclear Photoabsorption and Compton Scattering at Intermediate Energy", Ann. of Phys. **154** (1984), 99-160.

Leicht 81 — R. Leicht et al. "Absorption and Scattering of Photons by ^{208}Pb", Nucl. Phys. **A362** (1981), 111-127.

L'vov 90 — A.I. L'vov and V.A. Petrunkin, "Photon Scattering as a Tool for Study of Nucleon and Nucleus Structure", Perspectives on Photon Interactions with Hadrons and Nuclei, Springer-Verlag, 1990, 124-144.

Lucid 91 — Lucid Data Acquisition and Analysis System User's Guide, (1991).

McCarthy 77 — J.S. McCarthy, I. Sick, and R.R. Whitney, "Electromagnetic Structure of the Helium Isotopes", Phys. Rev. **C15** (1977), 1396-1414.

Mathews 73 — J.L. Matthews and R.O. Owens, "Accurate Formulae for the Calculation of High Energy Electron Bremsstrahlung Spectra", NIM **111** (1973), 157-168.

Miller 88 — J.P. Miller, et al, "Development of a NaI(Tl) Detector with Superior Photon Energy Resolution for Use Above 100 MeV", NIM **A270** (1988), 431-436.

Nathan 86 — A.M. Nathan et al. "Photon Scattering from ^{206}Pb", Phys. Rev. **C34** (1986), 480-488

Nelson 85 — Walter Nelson, Hedeo Hirayama, David Rogers, The EGS4 Code System, SLAC Report **265** (1985).

Oset 81 — E. Oset and Weise, "Photon-Nucleus Scattering and Coherent π^0 Photoproduction in the Δ-hole Model", Nucl. Phys. **A368** (1981), 375-393.

Ottermann 85 — C.R. Otterman et al., "Elastic Electron Scattering from ^{3}He and ^{4}He", Nucl. Phys. **A436** (1985), 688-698.

Penfold 59 — A.S. Penfold and E.L. Garwin, "Gamma Rays from the Nuclear Photoeffect in Carbon, Oxygen, and Copper", Phys. Rev. **116** (1959), 120.

Petrunkin 64 — V.A. Petrunkin, "Scattering of Low-Energy Photons on a Zero-Spin Particle", Nucl. Phys. **55** (1964), 197-206.

Pfeil 74 — W. Pfeil, H. Rollink, and S. Stankowski, "A Partial-Wave Analysis for Proton Compton Scattering in the Δ(1232) Energy Region", Nucl. Phys. **B73** (1974), 166-188.

Pruitt 62 — John S. Pruitt and Steve R. Domen, Determination of Total X-Ray Beam Energy With a Calibrated Ionization Chamber, NBS Monograph **48** (1962).

Pugh 57 — George E. Pugh, et al, "Nuclear Scattering of 50 - 130 MeV γ Rays", Phys. Rev. **105** (1957), 982-995.

Saharia 81 — A.N. Saharia and R.M. Woloshin, "Isobar-doorway Model for Coherent π^0 Photoproduction", Phys. Rev. **C23** (1981), 351-362.

Schelhass 88 — K.P. Schelhaas et al., "Nuclear Photon Scattering by ^{208}Pb", Nucl. Phys. **A489** (1988), 189-224.

Schelhaas 90 — K.P. Schelhaas, "Nuclear Photon Scattering by ^{12}C", Nucl. Phys. **A506** (1990), 307-331.

Schrack 65 — R.A. Schrack, "Nuclear Size Determination by Neutral-Pion Photoproduction", Phys. Rev. **140** (1965), 897-904.

Silbar 68 — R. Silbar, C. Werntz, and H. Uberall, "The Amplitude of Nuclear Photon Scattering and Its Thomson Limit", Nucl. Phys. **A107** (1968), 655-58.

Taylor 82 — Taylor, J.R., An Introduction to Error Analysis, University Science Books, Mill Valley, CA, 1982, (chi2) pp.218-241, (fit) pp.153-173.

Vesper 85 — J. Vesper et al, "Inelastic Photon Scattering in the Delta-Hole Approach", Phys. Lett. **159B** (1985), 233-238.

Wells 90 — D.P. Wells, Ph.D. Thesis, University of Illinois, Urbana, 1990.

Weyrauch 83 — M. Weyrauch, "Exchange Effects in Photon Scattering off the Deuteron", Nucl. Phys. **A480** (1983), 425-460.

Weyrauch 88 — M. Weyrauch, "Compton Scattering off the Deuteron at Low and Intermediate Energies", Phys. Rev. **C38** (1988), 611-624.

Weyrauch 90a — M. Weyrauch, "Deuteron Compton Scattering", Phys. Rev. **C41** (1990), 880-41.

Weyrauch 90b — M. Weyrauch, "Pion Photoproduction and Compton Scattering in Quark Models", Lecture Notes in Physics: Perspectives on Phogon Interactions with Hadrons and Nuclei, eds. M. Schumacher and G. Tamas, Springer-Verlag, 1990, 145-165.

Williams 61 — W.S.C Williams, H.S. Caplan, and D.T. Stewart, "The Nuclear Scattering of High Energy Photons", Proc. Phys. Soc. **78** (1961), 1125-34.

Wilson 57 — Robert R. Wilson, "Precision Quantameter for High Energy X-Rays", NIM **1** (1957), 101-106.

Woloshyn 78 — R.M. Woloshyn, "Neutral Pion Photoproduction in a Phenomenological Isobar Doorway Model", Phys. Rev. **C18** (1978), 1056-1059.

Wright 85 — D.H. Wright et al., "Elastic Photon Scattering from Carbon and Calcium and Its Interpretation", Phys. Rev. **C32** (1985), 1174

Ziegler 86 — B. Ziegler, "Scattering and Absorption of Photons by Nuclei and Nucleons", New Vistas in Electro-Nuclear Physics, ed. E.L. Tomusiak, Caplan, H.S., and Dressler, E.T., Plenum Press, 1986, 293-329.

Ziegler 90 — B. Ziegler, "Observation of Nuclear Giant Resonances in Photon Scattering and Photon Absorption Experiments", Prog. in Part. and Nucl. Phys. **24** (1990), 95-102.

Appendix A. KINEMATICS

A.1 Compton Scattering Kinematics

The kinematics of Compton scattering is quite simple and was easily verified by the endpoint shifts seen in total energy spectra. The kinematics will be derived here.

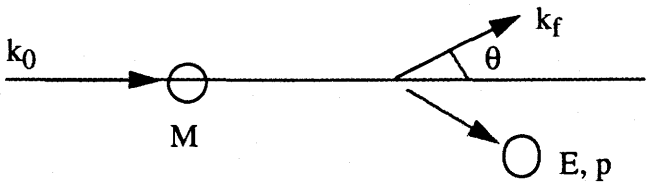

Figure A.1: Elastic Photon Scattering Kinematics

Conservation requires that

$$\begin{aligned} k_0 + M &= k_f + E \\ \vec{k}_0 &= \vec{k}_f + \vec{p} \end{aligned} \tag{A.1}$$

Isolating and squaring the nucleus' variables

$$\begin{aligned} k_0^2 + M^2 + k_f^2 + 2k_0M - 2k_0k_f - 2k_fM &= E^2 \\ k_0^2 + k_f^2 - 2k_0k_f\cos\theta &= p^2 = E^2 - M^2 \end{aligned} \tag{A.2}$$

After subtracting the two equations

$$k_0M + k_0k_f(1 - \cos\theta) - k_fM = 0$$

$$k_f = \frac{k_0}{1 + \frac{k_0}{M}(1 - \cos\theta)} \tag{A.3}$$

This form is least susceptible to "division by zero" errors in the various computer codes used for this experiment. However, by inverting it, the familiar Compton scattering kinematics equation is results.

$$\frac{1}{k_f} = \frac{1}{k_0} + \frac{1}{M}(1 - \cos\theta) \tag{A.4}$$

A.2 Inelastic Photon Scattering Kinematics

In this case, the recoiling nucleus has absorbed some energy. The conservation equations are then

$$\begin{aligned} k_0 + M &= k_f + E + X \\ \vec{k}_0 &= \vec{k}_f + \vec{p} \end{aligned} \tag{A.5}$$

$$k' = \frac{k(1 - \frac{X}{M}) - X(1 - \frac{X}{2M})}{(1 - \frac{X}{M}) + \frac{k}{M}(1 - \cos\theta)} \tag{A.6}$$

As a check, by setting X=0, Eqn. (A.5) reduces to Eqn. (A.3)

A.3 Neutral Photopion Production Kinematics

The kinematics for the decay photons from neutral photopions was important for identifying regions of interest in energy spectra. The photopion endpoint acted as a lower limit for photon scattering. The kinematics is a two step process.

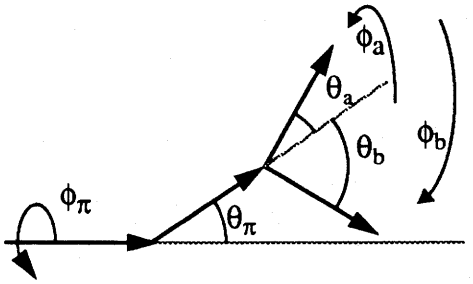

Figure A.2: Neutral Pion Production Kinematics

Conservation requires that

$$\begin{aligned} k + M &= E_\pi + E \\ \vec{k} &= \vec{p}_\pi + \vec{p} \end{aligned} \tag{A.7}$$

Isolating and squaring the nucleus' variables for each expression

$$\begin{aligned} k^2 + M^2 + E_\pi^2 + 2kM - 2E_\pi (k + M) &= E^2 \\ k^2 + p_\pi^2 - 2kp_\pi \cos\theta_\pi &= p^2 \end{aligned} \tag{A.8}$$

After subtracting the two expressions

$$m_\pi^2 + 2kM = 2\,[E_\pi (k + M) - kp_\pi \cos\theta_\pi] \tag{A.9}$$

By dividing through by (k+M) static components can be grouped together and the CM velocity can be substituted

$$\varepsilon_1 = \frac{m_\pi^2 + 2kM}{2(k + M)} \quad \left(= E_\pi - \beta p_\pi \cos\theta_\pi \right) \qquad \beta = \frac{k}{k + M} \tag{A.10}$$

Isolating the angle dependent term, replacing momentum with the energy equivalent, and squaring.

$$\beta^2 (E_\pi^2 - m_\pi^2) \cos\theta_\pi = E_\pi^2 - 2E_\pi \varepsilon_1 + \varepsilon_1^2 \tag{A.11}$$

Finally the quadratic equation can be used to solve for the pion energy

$$E_\pi = \frac{\varepsilon_1 + \beta \cos\theta_\pi \sqrt{\varepsilon_1^2 - m_\pi^2 (1 - \beta^2 (\cos\theta_\pi)^2)}}{(1 - \beta^2 (\cos\theta_\pi)^2)} \tag{A.12}$$

It can be shown that the equivalent expression for pion momentum is

$$p_\pi = \frac{\varepsilon_1 \beta \cos\theta_\pi + \sqrt{\varepsilon_1^2 - m_\pi^2 (1 - \beta^2 (\cos\theta_\pi)^2)}}{(1 - \beta^2 (\cos\theta_\pi)^2)} \tag{A.13}$$

However, it is the decay photons that are detected, such that

$$\begin{aligned} E_\pi &= k_a + k_b \\ \vec{p}_\pi &= \vec{k}_a + \vec{k}_b \end{aligned} \tag{A.14}$$

Isolating the second photon variables, squaring and equating,

$$E_\pi^2 - 2k_a E_\pi + k_a^2 = p^2 + k_a^2 - 2pk_a \cos\theta_a \tag{A.15}$$

Collecting all primary photon terms and pulling k_a out,

$$k_a = \frac{m_\pi^2}{2\,(E_\pi - p_\pi \cos\theta_a)} \tag{A.16}$$

The second photon's energy is

$$k_b = \frac{m_\pi}{2\,(E_\pi - p\cos\,(\theta_a - \theta_b))} \tag{A.17}$$

Note that this is in the frame where the pion direction is the z-axis. The vectors represented by angles θ_a and θ_b must be rotated into the lab frame. Note that because of the extra degree of freedom represented by the second photon, there is not a unique solution for a given detected angle. Also, since the π^0 decays in 10^{-16} seconds, it can be considered to decay instantly. Then the geometry (but not the kinematics) can be treated as if the incoming photon decayed into two photons.

A.4 Electron Scattering Kinematics

$$\begin{aligned} E + M &= E' + E_N \\ \vec{p} &= \vec{p}' + \vec{p}_N \end{aligned} \tag{A.18}$$

Isolating the nucleus' variables, squaring, and subtracting

$$m^2 + EM = E'\,(E + M) - pp'\cos\theta \tag{A.19}$$

$$\varepsilon_1 = \frac{m^2 + EM}{E + M} \qquad \beta = \frac{p}{E + M} \tag{A.20}$$

Just as in the photopion kinematics,

$$E' = \frac{\varepsilon_1 + \beta\cos\theta\sqrt{\varepsilon_1^2 - m^2(1-\beta^2(\cos\theta)^2)}}{1-\beta^2(\cos\theta)^2} \tag{A.21}$$

or for momentum,

$$p' = \frac{\varepsilon_1\beta\cos\theta + \sqrt{\varepsilon_1^2 - m^2(1-\beta^2(\cos\theta)^2)}}{1-\beta^2(\cos\theta)^2} \tag{A.22}$$

A.5 Jacobians

Jacobians are needed to transform Lab differential cross sections to CM. They are also required for photopion production simulations.

Assume that the angular distribution is known and call its corresponding probability function $P(\vec{p})$. The probability that a particle is produced with momentum between $\vec{p}$ and $\vec{p} + d^3\vec{p}$ maps to the center of mass (CM) probability for momentum between $\vec{p}^*$ and $\vec{p}^* + d^3\vec{p}^*$ by

$$P^*(\vec{p}^*)\,d^3\vec{p}^* = P^*(\vec{p}^*)\,p^{*2}dp^*d\Omega^* = P(\vec{p})\,p^2dpd\Omega \tag{A.23}$$

Now define the jacobian for converting lab momenta to CM momenta by

$$dp^*d\Omega^* = J_\pi dpd\Omega \tag{A.24}$$

Then

$$P(\vec{p}) = P^*(\vec{p}^*(\vec{p}))\frac{p^{*2}}{p^2}J \tag{A.25}$$

In this application, the magnitude of the momentum has already been determined by kinematics so that the corresponding component of the probability can be separated:

$$P(\vec{p}) = \delta(p - p_f)\frac{P(\hat{p})}{p^2} \tag{A.26}$$

So that Eqn. (A.25) becomes

$$P(\hat{p})\,\delta(p-p_f) = P^*(\hat{p}^*(\hat{p}))\,J_\pi \sum_m \frac{\delta(p-p_{fm})}{\left|\frac{\partial p^*}{\partial p}\right|_{p=p_{fm}}} \tag{A.27}$$

where the identity

$$\delta(p^*-p_f^*) = \sum_m \frac{\delta(p-p_{fm})}{\left|\frac{\partial p^*}{\partial p}\right|_{p=p_{fm}}} \tag{A.28}$$

was used. For this experiment, there is only one root, p_{fm}, so

$$P(\hat{p}) = \frac{P^*(\hat{p})\,J}{\left|\frac{\partial p^*}{\partial p}\right|} \tag{A.29}$$

Then for angular distributions

$$\frac{d\sigma}{d\Omega_{Lab}} = \frac{J}{\left|\frac{\partial p^*}{\partial p}\right|}\frac{d\sigma}{d\Omega_{CM}} \tag{A.30}$$

This is the transformation of interest. Then call the transformation factor a reduced jacobian defined by

$$\tilde{J} = \frac{J}{\left|\frac{\partial p^*}{\partial p}\right|}. \tag{A.31}$$

Now we address the form of J. There are 3 approaches to this, and the following derivations proceed in various degrees of rigour. The simplest is specifically aimed at relativistic kinematics for cross sections [Baldin]. The number of events in phase space is a relativistic invariant:

$$N\frac{d^3p}{E} = Np^2\frac{dp}{E}d\Omega = N^*\frac{p^{*2}}{E^*}dp^*d\Omega^* \tag{A.32}$$

Making use of Eqn. (A.24), a simple expression

$$J = \frac{p^2}{p^{*2}} \frac{E^*}{E} \tag{A.33}$$

The Lorentz transformations

$$\begin{aligned} E^* &= \gamma(E - \beta p_z) \\ p_z^* &= \gamma(p_z - \beta E) \\ p_{x,y}^* &= p_{x,y} \end{aligned} \tag{A.34}$$

are then substituted into Eqn. (A.33) and evaluated.

Another more cumbersome method is to use the mathematical definition of a jacobian,

$$J = \left\| \frac{\partial p_i^*}{\partial p_j} \right\| \qquad i = 1, 2, 3 \tag{A.35}$$

That is, find the determinant of a matrix populated by the j-th derivative of the i-th momentum element. Generally, this results in a sum of 6 triple products, each product having multiple terms depending on the complexity of the lab to CM kinematic conversions. However, in many cases the coordinate system is chosen with the z-axis parallel to the direction of the motion of the CM. This means there is no ϕ dependence in the lab to CM conversion so the only terms of the determinant are of the form

$$J = \frac{\partial \cos\theta^*}{\partial \cos\theta} \frac{\partial p^*}{\partial p} - \frac{\partial \cos\theta^*}{\partial p} \frac{\partial p^*}{\partial \cos\theta} \tag{A.36}$$

Again the transformations of Eqn. (A.34) are substituted, with the appropriate polar transformations, and the expression evaluated.

The most general form of deriving the Jacobian begins with the general form of the relativistic transformation [Barut 80], instead of using the specific transformation for substitutions at the end.

$$p^* = \underset{\sim}{L} p$$

$$\begin{pmatrix} E^* \\ p_1^* \\ p_2^* \\ p_3^* \end{pmatrix} = \begin{pmatrix} \gamma & -\beta_1\gamma & -\beta_2\gamma & -\beta_3\gamma \\ -\beta_1\gamma & 1+A\beta_1\beta_1 & A\beta_1\beta_2 & A\beta_1\beta_3 \\ -\beta_2\gamma & A\beta_1\beta_2 & 1+A\beta_2\beta_2 & A\beta_2\beta_3 \\ -\beta_3\gamma & A\beta_1\beta_3 & A\beta_2\beta_3 & 1+A\beta_3\beta_3 \end{pmatrix} \begin{pmatrix} E \\ p_1 \\ p_2 \\ p_3 \end{pmatrix} \tag{A.37}$$

where β_i are the vector components of the CM velocity, $\gamma = (1-\beta^2)^{-1}$, and $A = (\gamma-1)/\beta^2$.

This expression is found from rotating the z-parallel boosted transformation

$$\underset{\sim}{L}_3 = \begin{pmatrix} \gamma & 0 & 0 & -\beta_3\gamma \\ 0 & 1 & 0 & 0 \\ 0 & 0 & 1 & 0 \\ -\beta_3\gamma & 0 & 0 & \gamma \end{pmatrix} \tag{A.38}$$

by

$$\underset{\sim}{L} = \underset{\sim}{R}(\theta)\,\underset{\sim}{R}(\phi)\,\underset{\sim}{L}_3 \tag{A.39}$$

where

$$\underset{\sim}{R}(\alpha) = \begin{pmatrix} 1 & 0 & 0 & 0 \\ 0 & R_{11} & R_{12} & R_{13} \\ 0 & R_{21} & R_{22} & R_{23} \\ 0 & R_{31} & R_{32} & R_{33} \end{pmatrix} \tag{A.40}$$

Rewriting L

$$\begin{aligned} \underset{\sim}{L} &= (a_{\alpha\beta}) \\ a_{i0} &= -\beta_i\gamma \\ a_{ij} &= \delta_{ij} + A\beta_i\beta_j \end{aligned} \tag{A.41}$$

so now the momentum can be written

$$p_i^* = a_{i0}E + a_{ij}p_j. \tag{A.42}$$

After differentiating, we get a matrix

$$\left(\frac{\partial p_i^*}{\partial p_k}\right) = (a_{i0}p_k)\frac{1}{E} + (a_{ik}) \; . \tag{A.43}$$

The determinant of this matrix is expanded by using one property of determinants. If one row or column of (a_{ij}) is a binomial of the form $b_{ij} + c_{ij}$, then the determinant is the sum of 2 determinants with the row/column in question substituted by b_{ij} in one and c_{ij} in the other: So by applying this on each row, we obtain a sum of 8 determinants,

$$\left\| \frac{\partial p_i^*}{\partial p_k} \right\| = \frac{1}{E}\|a_{i0}p_k\| + \frac{1}{E}\begin{Vmatrix} a_{11} & a_{12} & a_{13} \\ a_{10}p_2 & a_{20}p_2 & a_{30}p_2 \\ a_{10}p_3 & a_{20}p_3 & a_{30}p_3 \end{Vmatrix} + \ldots$$

$$\ldots + \frac{1}{E}\begin{Vmatrix} a_{10}p_1 & a_{20}p_1 & a_{30}p_1 \\ a_{21} & a_{22} & a_{23} \\ a_{31} & a_{32} & a_{33} \end{Vmatrix} + \|a_{ik}\| \tag{A.44}$$

Next make use of the property

$$\begin{Vmatrix} ka_{11} & ka_{12} & ka_{13} \\ a_{21} & a_{22} & a_{23} \\ a_{31} & a_{32} & a_{33} \end{Vmatrix} = k\|a_{ik}\| . \tag{A.45}$$

All determinants with order in p greater than 1 vanish because there would be at least two identical rows of the form $(a_{10}\ a_{20}\ a_{30})$ which causes determinants to vanish. This leaves

$$\left\| \frac{\partial p_i^*}{\partial p_k} \right\| = \|a_{ik}\| + \frac{p_1}{E}\begin{Vmatrix} a_{10} & a_{20} & a_{30} \\ a_{21} & a_{22} & a_{23} \\ a_{31} & a_{32} & a_{33} \end{Vmatrix} + \frac{p_2}{E}\begin{Vmatrix} a_{1k}\cdots \\ a_{k0}\cdots \\ a_{3k}\ldots \end{Vmatrix} + \frac{p_3}{E}\begin{Vmatrix} a_{1k}\cdots \\ a_{2k}\cdots \\ a_{k0}\cdots \end{Vmatrix} . \tag{A.46}$$

The first term is the cofactor of a_{00}, or the element of the first row and first column, and it can be shown that for L_g to be unitary, the cofactor is the value of a_{00}, or γ. Alternatively, we know that rotation of the coordinate system does not affect the determinant, so that using the z-parallel boosted L we get a cofactor of γ. The second term must be evaluated by brute force, but the result is simple:

$$\left\| \frac{\partial p_i^*}{\partial p_k} \right\| = \gamma - \frac{p_i}{E}\gamma\beta_i = \gamma\left(1 - \frac{\vec{\beta}\cdot\vec{p}}{E}\right) = \frac{E^*}{E} \tag{A.47}$$

Finally, remember that the above determinant was done in cartesian coordinates and the jacobian sought is kinematically normalized by p^2. So finally the jacobian is

$$J = \gamma\left(1 - \frac{\vec{\beta}\cdot\vec{p}}{E}\right)\frac{p^2}{p^{*2}} = \frac{E^*}{E}\frac{p^2}{p^{*2}} \tag{A.48}$$

which is the same as the simple definition, Eqn. (A.33).

A.5.1 Compton Scattering

For photons, momentum $|\vec{k}| = k$ energy, so

$$J = \frac{k}{k^*} \tag{A.49}$$

and

$$k^* = k\gamma(1 - \beta\cos\theta)\,. \tag{A.50}$$

So the reduced jacobian is simply

$$\tilde{J}_\gamma = \frac{1}{\gamma^2(1 - \beta\cos\theta)^2} \tag{A.51}$$

A.5.2 Photopion Production

In order to construct decay photon spectra, the angular distribution of photopion production is needed and series of jacobians derived. This section addresses the latter.

$$J_\pi = \frac{\gamma\varepsilon_1 p_\pi^2}{E_\pi(\gamma^2\varepsilon_1^2 - m_\pi^2)} \frac{1}{\left|\frac{dp_\pi^*}{dp_\pi}\right|} \tag{A.52}$$

$$\frac{\partial p_\pi^*}{\partial p_\pi} = \frac{\partial}{\partial p_\pi}\sqrt{p_{\pi x}^2 + p_{\pi y}^2 + \gamma^2(p_\pi\cos\theta - \beta E)^2} \tag{A.53}$$

$$\frac{\partial p_\pi^*}{\partial p_\pi} = \frac{1}{p_\pi^*}\gamma^2\left(\frac{p}{E} - \beta\cos\theta\right)(E - \beta p\cos\theta) \tag{A.54}$$

$$\tilde{J} = \frac{1}{\sqrt{\gamma^2\varepsilon_1^2 - m^2}} \frac{p^2\pi}{\gamma(p - \beta E\cos\theta)} \tag{A.55}$$

A.5.3 One Decay Photon Detected

The reduced jacobian for detecting one of the decay photons is identical to the elastically scattered photon,

$$\tilde{J}_d = \frac{1}{\gamma^2(1 - \beta\cos\theta)^2} \tag{A.56}$$

Furthermore, the velocity of the center-of-momentum for this jacobian is defined by the π^0. Since the π^0 decays spontaneously with no spectator,

$$\beta_\pi = \frac{p_\pi}{E_\pi} \tag{A.57}$$

so that

$$J_d = \frac{m_\pi^2}{E_\pi^2(1 - \beta\cos\theta)^2} \tag{A.58}$$

Appendix B. FITTING ALGORITHMS

B.1 Basic Principles of Weighted Least Squares Fitting

In many cases, one can assume that the distribution of measured values of an observable is a normal distribution. It can then be shown that the χ^2 test

$$\chi^2 = \frac{1}{n-d-1}\sum_{i=1}^{n}\frac{(f(x_i)-y_i)^2}{\sigma_{yi}^2} \tag{B.1}$$

is a valid means of judging the propriety of using a given model to describe that observable, where x_i , y_i , σ_{yi} are the control variable, measured value, and the uncertainty of the measurement, f(x) is the model, n is the number of measurements, and d is the degrees of freedom inherent to the model. The lower the χ^2, the better the model is at describing the observable.

The basic principle behind weighted least squares fitting is the minimization of χ^2 with respect to variable parameters, a_k, in the model, $f(x; a_0,...a_n)$. This is typically done by taking the derivative of χ^2 with respect to those parameters

$$\frac{\partial}{\partial a_k}\chi^2 = \frac{1}{n-d-1}\sum_{i=1}^{n}\frac{(f(x_i)-y_i)\frac{\partial}{\partial a_0}f(x_i)}{\sigma_{yi}^2} \tag{B.2}$$

and setting the left hand side to zero. Then one either explicitly or numerically solves for the parameters, whose values become the best fit values. For models that are linear functions of parameters a_k, this is a simple exercise in linear algebra. All forms of polynomial functions fall in this category. For non-linear models, except for very simple cases, this is not so easy and usually requires an iterative process of guessing.

B.2 Fitting with Linear Functions

Since the simple n-th order polynomial was the most commonly used linear function, it shall be used to demonstrate the fitting procedure here. The function

$$f(x) = \sum_{k=1}^{m} a_k x^k \tag{B.3}$$

is said to be linear because the parameter a_k is of order 1 for any order of x. Substituting this into Eqn. B.2, for the k-th parameter

$$0 = \sum_{i=1}^{n} \frac{\left(\sum_{j=1}^{m} a_j x_i^j - y_i\right) x_i^k}{\sigma_{yi}^2} \tag{B.4}$$

$$0 = \sum_{i=1}^{n}\sum_{j=1}^{m} \frac{(a_j x_i^{j+k} - y_i x_i^k)}{\sigma_{yi}^2} \tag{B.5}$$

$$0 = \sum_{j=1}^{m}\left(a_j \sum_{i=1}^{n} \frac{x_i^{j+k}}{\sigma_{yi}^2}\right) - \sum_{i=1}^{n} \frac{y_i x_i^k}{\sigma_{yi}^2} \tag{B.6}$$

which are simply m-l+1 linear equations with m-l+1 unknowns. One can use matrix mechanics to solve this system.

B.3 Fitting with Non-Linear Functions

Simple non-linear functions can be handled if they can be linearized. For example, an exponential function can be transformed by

$$\begin{aligned} \ln(f(x)) &= Bx + \ln(A) \\ f(x) &= A\exp(Bx) \end{aligned} \tag{B.7}$$

The fit is made by solving

$$0 = \ln(A)\sum_{i=1}^{n}\frac{1}{\sigma^2_{\ln(y)\,i}} + B\sum_{i=1}^{n}\frac{x_i}{\sigma^2_{\ln(y)\,i}} + \sum_{i=1}^{n}\frac{\ln(y_i)}{\sigma^2_{\ln(y)\,i}}$$

$$0 = \ln(A)\sum_{i=1}^{n}\frac{x_i}{\sigma^2_{\ln(y)\,i}} + B\sum_{i=1}^{n}\frac{x_i^2}{\sigma^2_{\ln(y)\,i}} + \sum_{i=1}^{n}\frac{x_i\ln(y_i)}{\sigma^2_{\ln(y)\,i}} \qquad \text{(B.8)}$$

For anything more complicated, a different prescription must be used.

One must search for the parameters that minimize the derivatives. The simplest way is to sequentially vary all the parameters and then sift through the resulting derivatives until the appropriate values of parameters are found. This can be very laborious, and impossibly time consuming if many parameters are involved. A more efficient method is to estimate how far the parameters are from the optimum, evaluate the derivative and new chi-squared, and repeat the process. Newton's method could be used as is demonstrated in the next section.

B.3.1 Fitting to Energy Spectra

The derivative with respect to the amplitudes is

$$0 = \sum_{i=1}^{n}\frac{\left(\sum_{k=1}^{m} a_k S_k(a_0 x_i) - y_i\right) S_j(a_0 x_i)}{\sigma^2_{yi}} \qquad \text{(B.9)}$$

which is linear. Unfortunately, the derivative with respect to the calibration is

$$0 = \sum_{i=1}^{n}\frac{\left(\sum_{k=1}^{m} a_k S_k(a_0 x_i) - y_i\right)\sum_{k=1}^{m}\left(a_k\frac{\partial}{\partial a_o}S_k(a_0 x_i)\right)}{\sigma^2_{yi}} \qquad \text{(B.10)}$$

which is far from linear.

One way of solving for a_0 is to use Newton's method to find the zero,

$$\frac{d}{da_0}\chi^2 \equiv \chi' = \chi'|_{a_{00}} + \sum_{j=0}^{m}\left(\left.\frac{\partial\chi'}{\partial a_j}\right|_{a_{j0}}(a_j - a_{j0})\right) \tag{B.11}$$

$$\frac{\partial^2}{\partial a_0 a_j}\chi^2 = \{\left(\sum_{k=1}^{m} a_k S_k(a_0 x_i) - y_i\right)\frac{\partial}{\partial a_o}S_j(a_0 x_i) + S_j(a_0 x_i)\sum_{k=1}^{m}\left(a_k\frac{\partial}{\partial a_o}S_k(a_0 x_i)\right)\}\frac{1}{\sigma_{yi}^2} \tag{B.12}$$

$$\frac{\partial^2}{\partial a_0^2}\chi^2 = \sum_{i=1}^{n}\{\left(\sum_{k=1}^{m} a_k S_k(a_0 x_i) - y_i\right)\left(\sum_{k=1}^{m} a_k\frac{\partial^2}{\partial a_0^2}S_k(a_0 x_i)\right) + \left(\sum_{k=1}^{m}\left(a_k\frac{\partial}{\partial a_o}S_k(a_0 x_i)\right)\right)^2\}\frac{1}{\sigma_{yi}^2} \tag{B.13}$$

This is a linear system of equations and can be solved for the respective guesses by matrix mechanics.

B.3.2 With Pileup

This complicates the fitting algorithm by forcing a recomputation of the function at every iteration.

$$g(x, x_i) = \begin{cases} CG(x - x_i) & x_i \neq x \\ 1 - C & x_i = x \end{cases} \tag{B.14}$$

$$f(x_i) = \sum_{j=1}^{n}\left(\sum_{k=1}^{m} a_k S_k(a_0 x_j)\right)g(x_i, x_j) \tag{B.15}$$

The first derivatives are

$$\frac{d}{dC}f(x_i) = \sum_{\substack{j=1 \\ i\neq j}}^{n}\left(\sum_{k=1}^{m} a_k S_k(a_0 x_j)\right)G(a_0(x_i - x_j)) - \sum_{k=1}^{m} a_k S_k(a_0 x_i) \tag{B.16}$$

$$\frac{d}{da_0} f(x_i) = \sum_{j=1}^{n} \left(\sum_{k=1}^{m} a_k \frac{\partial}{\partial a_0} S_k(a_0 x_j) \right) g(a_o(x_i - x_j))$$

$$"" + \sum_{j=1}^{n} \left(\sum_{k=1}^{m} a_k S_k(a_0 x_j) \right) \frac{\partial}{\partial a_0} g(a_0(x_i - x_j)) \qquad \text{(B.17)}$$

$$\frac{\partial}{\partial a_k} f(x_i) = \sum_{j=1}^{n} S_k(a_0 x_j)\, g(a_o(x_i - x_j)) \qquad \text{(B.18)}$$

The second derivatives are

$$\frac{\partial^2}{\partial a_0^2} f(x_i) = \sum_{j=1}^{n} \left(\sum_{k=1}^{m} a_k \frac{\partial^2}{\partial a_0^2} S_k(a_0 x_j) \right) g(a_o(x_i - x_j))$$

$$"" + 2 \sum_{j=1}^{n} \left(\sum_{k=1}^{m} a_k \frac{\partial}{\partial a_o} S_k(a_0 x_j) \right) \frac{\partial}{\partial a_0} g(a_0(x_i - x_j))$$

$$"" + \sum_{j=1}^{n} \left(\sum_{k=1}^{m} a_k S_k(a_0 x_j) \right) \frac{\partial^2}{\partial a_0^2} g(a_0(x_i - x_j)) \qquad \text{(B.19)}$$

$$\frac{\partial^2}{\partial a_0 \partial C} f(x_i) = \sum_{\substack{j=1 \\ i \neq j}}^{n} \left(\sum_{k=1}^{m} a_k \frac{\partial}{\partial a_0} S_k(a_0 x_j) \right) G(a_0(x_i - x_j))$$

$$"" + \sum_{\substack{j=1 \\ i \neq j}}^{n} \left(\sum_{k=1}^{m} a_k S_k(a_0 x_j) \right) \frac{\partial}{\partial a_0} G(a_0(x_i - x_j))$$

$$"" - \sum_{k=1}^{m} a_k \frac{\partial}{\partial a_0} S_k(a_0 x_i) \qquad \text{(B.20)}$$

$$\frac{\partial^2}{\partial a_0 \partial a_k} f(x_i) = \sum_{j=1}^{n} \frac{\partial}{\partial a_0} S_k(a_0 x_j)\, g(a_o(x_i - x_j))$$

$$"" + \sum_{j=1}^{n} \left(\sum_{k=1}^{m} a_k \frac{\partial}{\partial a_0} S_k(a_0 x_j) \right) \frac{\partial}{\partial a_k} g(a_o(x_i - x_j))$$

$$"" + \sum_{j=1}^{n} S_k(a_0 x_j) \frac{\partial}{\partial a_0} g(a_0(x_i - x_j))$$

$$"" + \sum_{j=1}^{n} \left(\sum_{k=1}^{m} a_k S_k(a_0 x_j) \right) \frac{\partial^2}{\partial a_0 \partial a_k} g(a_0(x_i - x_j)) \tag{B.21}$$

$$\frac{\partial^2}{\partial C^2} f(x_i) = 0 \tag{B.22}$$

$$\frac{\partial^2}{\partial C \partial a_k} f(x_i) = \sum_{\substack{j=1 \\ i \neq j}}^{n} \left(S_k(a_0 x_j)\, G(a_0(x_i - x_j)) + \left(\sum_{k=1}^{m} a_k S_k(x_j) \right) \frac{\partial}{\partial a_k} G(x_i - x_j) \right)$$

$$"" - \frac{\partial}{\partial a_k} S_k(a_0 x_i) \tag{B.23}$$

$$\frac{\partial^2}{\partial a_k \partial a_q} f(x_i) = \sum_{j=1}^{n} S_k(a_0 x_j) \frac{\partial}{\partial a_q} g(a_o(x_i - x_j)) \tag{B.24}$$

As can be seen, the task is complicated, with many terms being summed at every iteration. However, a simplification is possible. Eqn. B.14 and Eqn. B.15 can be decomposed into two parts, an unpiled up part and piled up part:

$$f(x_i) = \underbrace{(1 - C) \left(\sum_{k=1}^{m} a_k S_k(a_0 x_i) \right)}_{\text{no pileup}} + \underbrace{C \sum_{\substack{j=1 \\ j \neq i}}^{n} \left(\sum_{k=1}^{m} a_k S_k(a_0 x_j) \right) G(x_i - x_j)}_{\text{pileup}} \tag{B.25}$$

This expression indicates that the effective pileup spectrum can be fitted as if it were another scattering channel with amplitude C. This assumes that the true spectrum is known beforehand. However, it is sufficient for the input spectrum to be approximately correct because of the dispersive nature of pileup. Then the pileup spectrum can be modelled before fitting and used as another scattering spectrum, as outlined in Section B.3.1. To compute the pileup rate, consider the integral of the energy spectrum over the desired ROI and break it down into its component contributions:

$$I = I_S + I_P \tag{B.26}$$

where I_S and I_P are the integrals of scattered (ideal) and piled up events, respectively. Each term can be further broken down into the scaling factors and the integral of the model such that

$$\begin{aligned} I_S &= A(1-C)\, i_S \\ I_P &= BCi_P \\ I &= A(1-C)\, i_S + BCi_P \end{aligned} \tag{B.27}$$

where A and B are the scaling factors of the scattered and piled up spectra if the data experienced 0% and 100% pileup rates, respectively, and do not change with respect to pileup; i_S and i_P are the unscaled ideal and pileup simulation integrals. The factor C then reduces the ideal spectrum, increases the pileup spectrum, and acts as a mixing parameter. The simulated pileup spectrum should be produced with a rate of 100% with a corresponding ideal spectrum so that the ratio of ideal and pileup integrals over some arbitrary ROI can be expressed by

$$\frac{I'_S}{I'_P} = \frac{Ai'_S}{Bi'_P}. \tag{B.28}$$

After fitting, the ratio of the extracted I_S and I_P can be computed and has the following equivalence:

$$\frac{I_S}{I_P} = \frac{A(1-C)i_S}{CBi_P}, \tag{B.29}$$

The pileup rate, C, can then be computed by

$$C = \frac{I_P}{I_S\frac{Bi_P}{Ai_S} + I_P}. \tag{B.30}$$

However, the quantities A and B are not known. The ratio Bi_P/Ai_S is similar to Eqn. B.28 except that the ROI from the pileup simulation and the fit extraction (for cross sections) are most likely different. This ratio could be computed for a specific ROI only if the pileup simulation is run with that ROI. This is too cumbersome in the situation where many ROI are being considered. The Monte Carlo program, **pilesim**, and the yield extraction program, **extract.bunifit**, used a different approach. If a reference ROI is chosen and I_S' and I_P' are recorded, then the ratio can be re-written,

$$\frac{Bi_P}{Ai_S} = \frac{I''_P}{I''_S} = \frac{I''_P\, I'_S}{I'_S\, I''_S}. \tag{B.31}$$

If the pileup model has been normalize by I_S', the simulation sample is normalized out. This has the effect that I_S'' can simply be integrated from the ideal model, rather than the sample population dependent model from the pileup simulation. Then the ratio reduces to an expression which contains values which are all known,

$$\frac{Bi_P}{Ai_S} = I''_P\frac{I'_S}{I''_S}. \tag{B.32}$$

So finally,

$$C = \frac{I_P}{I_S I''_P\frac{I'_S}{I''_S} + I_P} \tag{B.33}$$

where I_S and I_P are integrals from the fit with ROI for cross sections; I'_S and is the integral from the pileup simulation at run time with its inherent ROI (different from the cross

section ROI); I''_S and I''_P are integrals of the models assuming 0% and 100% pileup, respectively, with the ROI for cross sections.

Appendix C. MONTE CARLO PROGRAMS

One of the purposes of Monte Carlo techniques is to simulate a process that consists of one or more well understood phenomena. Generally, these programs are used when these phenomena occur in complicated conditions. In this experiment, Monte Carlo techniques were used to determine:

1. the shape of bremsstrahlung spectra passing through Pb filters during Zero Degree runs;
2. the amount of absorption of photons between the target and BUNI; the response function of BUNI;
3. π^0 decay γ spectra produced at the target;
4. absorption of photons by the target in the beam line.

The 2nd and 4th problems involved a complicated geometry with a finite sized source. The 3rd was a process that had random but highly geometrically dependent probabilities.

C.1 EGS Simulations

In the cases of bremsstrahlung and detector simulations, a software package called Electron-Gamma Shower (EGS version 4) was used. This package reads a user file containing event handling instructions (e.g. what to histogram, when to histogram), geometrical boundary conditions, and any user subroutines. This file is written in MORTRAN which is an EGS macro language for Fortran. It is converted to Fortran, then the physics subroutines and the Monte Carlo code are added. Only electromagnetic interactions are simulated in EGS: bremsstrahlung, pair production, Bhabha scattering, Moller scattering, Rayleigh scattering, photo-electric effect.

Brem and **buni_sim** were the resulting executables used for this experiment. **Brem** was used to simulate the production of bremsstrahlung for this thesis. It contained the radiator, the outrun window, air to the quantameter, a target (with changing angles for carbon), and collimators. Energy deposition spectra could be generated for all regions, but for all but the most important regions a flag was set to suppress output of these histograms. The output file was then read by analysis programs and the relevant information extracted.

It could be run in one of three modes, selected by setting a flag variable in the user file. The more realistic but less efficient mode started with an electron beam which then passed through the radiator. EGS then determined what processes occurred. Since the radiator was about 0.01 radiation lengths, only 1% of the electrons in the simulation produced photons and the remaining 99% were discarded. That is, this mode was 1% efficient. However, this mode was necessary for producing realistic bremsstrahlung spectra for comparison with the Mathews and Owens model [Mathews 73] subsequently used in the analysis, and for collimator size studies.

The second mode bypassed the electron stage of the simulation and used the Mathews and Owen model for the bremsstrahlung spectrum. This mode was used for obtaining beam absorption factors.

The third mode also bypassed the electron stage but used monochromatic photons. This mode was used for absorption of photons in the lead filter for use in zero degree calibrations of BUNI.

Buni_sim was used to simulate the transport of particles from the target after scattering. It contained the target with changing angles, target walls, air between detectors, the thin plastic scintillators, the front cosmic veto scintillators, the lead pre-collimator, the aperture (lead and tungsten components were treated as separate elements), the front

shielding wall, the aluminium walls in BUNI, the core NaI, the annular NaI, and the annular cosmic vetoes. Again, only the important spectra were recorded for subsequent use.

As with **brem**, there were several modes in which **buni_sim** could be run in. These were selectable by a flag in the user code. Every photon mode also had a corresponding electron mode for electron scattering studies with BUNI and a mode with the beryllium plug out of the aperture. The primary mode was to generate response functions for cross section analysis. For this, the photon energy was cycled through a range of 50 MeV in 5 MeV steps. The detected energy was then recorded in the histogram corresponding to the respective initial photon energy, and these histograms were written to a file. The fitting analysis programs, such as **bunifit** and **extract.bunifit**, read the EGS output file to reconstruct a scattered spectrum.

The second mode involved photon energy spectra read from a file, usually a Mathews and Owens bremsstrahlung spectrum. The spectrum was sampled randomly, the energy kinematically shifted, and the event simulated. This produced simulated detected photon spectra directly but was inflexible for situations where fitting to many channels and energy dependences were involved because each program run took 4 to 12 hours. However, these simulations were used for zero degree calibrations because these procedures required only one physical process and no modifications to the incident spectrum. In this case, this mode of simulation provided the confidence in the accuracy of the code to simulate detected spectra and in the use of the response functions.

The third mode was used for studies with monochromatic photons or electrons. Typically, these studies were concerned with the response of the detector with beams off axis and other non-standard experimental conditions.

C.2 Pion Simulation

Neutral pion decay spectra were simulated by a C language Monte Carlo program called **pionsim**. This program used the kinematics and Jacobians derived in Appendix A. The incident photon energy was randomly chosen from the incident photon energy distribution. For a simulation with bremsstrahlung, this distribution was weighted with the neutral pion production total cross section for carbon [Arends 82a]. The pion angle was randomly chosen from a $\sin^2\theta$ distribution that was weighted by the charge form factor [Schrack 65]. Next, the decay angles were randomly chosen in the center of mass, where the angular distribution is a constant, and then transformed to the lab frame (NOT the pion frame). The detected angle was fixed in the lab frame. Since the neutral pion lifetime is 8.4×10^{-17} s, the it does not travel a significant distance before decaying. It can then be assumed that all angles can be measured from the same point. The remaining kinematic variables were solved for, then the Jacobian for the decay process was computed. This Jacobian was the weight for the event because of the restriction placed by the detector angle. All kinematic variables were histogrammed and written to a file from which the decay photon spectrum could be extracted.

C.3 Pileup Simulation

A C language program, **pilegen**, was used to generate piled up total energy spectra. It started by reconstructing the pileup-free, inclusive scattering spectrum from 0 MeV to the elastic endpoint from previous fit results (see Section 3.4). The region below 200 MeV in this reconstructed spectrum was scaled to the equivalent region of the measured pedestal spectrum below 200 MeV. Then the region below 10 MeV in the inclusive spectrum was substituted by the corresponding region in the pedestal spectrum. This became the probability function for the simulation.

The actual simulation used Monte Carlo methods because the second pulse in a pileup event usually arrives at a different time within the ADC gate than the main pulse. The energy of the main pulse and the energy of the pileup pulse are randomly selected

according to the probability function. Since what is required is a 100% piled up energy spectrum, the time of the second pulse is randomly selected between a pulse length in advance of the main pulse to the end of the ADC gate so that some part of second pulse always appears within the gate. The second pulse is superimposed on the main pulse at that time. Then, the new waveform is integrated within the ADC gate and the resulting energy is histogrammed. This histogram is written to a file at the end of the simulation. For normalization purposes, the integral of the true energy spectrum and the integral of the pileup spectrum were recorded at the top of the file.

Appendix D. PROOF: TARGET EMPTY RUN TIMES

A, B are data rates for target full and target empty, respectively (events/time/flux).

R_A, R_B are flux rates for target full and target empty, respectively (flux/time).

N_A , N_B are total counts for target full and target empty, respectively.

t_A , t_B are acquisition times, where the total time is $t = t_A + t_B$.

Q_A , Q_B are total photon flux for target full and target empty, respectively.

$$\begin{aligned} N_A &= R_A A t_A \\ N_B &= R_B B t_B \\ Q_A &= R_A t_A \\ Q_B &= R_B t_B \end{aligned} \tag{D.1}$$

The signal count is eventually calculated from the total and background counts,

$$N_S = N_A - \frac{Q_A}{Q_B} N_B \tag{D.2}$$

with uncertainty of (assuming the quantameter flux has negligible error)

$$\sigma_S^2 = N_A + \left(\frac{Q_A}{Q_B}\right)^2 N_B. \tag{D.3}$$

During the experiment, the rates and the length of time available are usually the given factors.

$$N_S = R_A A t_A - \frac{R_A t_A}{R_B t_B} R_B B t_B = R_A t_A (A - B) \tag{D.4}$$

$$\sigma_A^2 = R_A A t_A + \frac{R_A^2 t_A^2}{R_B t_B} B \tag{D.5}$$

Let $R = B / A$ and $\alpha = R_B / R_A$. Then the fractional uncertainty becomes

$$\%\sigma_S{}^2 = \frac{A}{R_A} \frac{1}{(A-B)^2} \left(\frac{1}{t_A} + \frac{R}{\alpha} \frac{1}{t_B}\right). \tag{D.6}$$

We are looking for the optimum t_B in a fixed time, t, that minimizes σ_S, so

$$\%\sigma_S^2 = \frac{A}{R_A}\frac{1}{(A-B)^2}\left(\frac{1}{(t-t_B)} + \frac{R}{\alpha}\frac{1}{t_B}\right) \tag{D.7}$$

$$\frac{d}{dt_B}\%\sigma_S = \sqrt{\frac{A}{R_A}}\frac{1}{(A-B)}\frac{1}{2}\frac{1}{\sqrt{\frac{1}{(t-t_B)} + \frac{R}{\alpha}\frac{1}{t_B}}}\left\{\frac{1}{(t-t_B)^2} - \frac{R}{\alpha}\frac{1}{t_B^2}\right\} \tag{D.8}$$

$$\frac{d}{dt_B}\%\sigma_S = \sqrt{\frac{A}{R_A}}\frac{1}{(A-B)}\frac{1}{2}\frac{1}{\sqrt{\frac{1}{(t-t_B)} + \frac{R}{\alpha}\frac{1}{t_B}}}\frac{1}{(t-t_B)^2 t_B^2}$$

$$\times \left\{t_B^2 - \frac{R}{\alpha}(t^2 - 2t_B t + t_B^2)\right\} \tag{D.9}$$

The optimum occurs when this is equal to zero.

$$0 = t_B^2\left(1 - \frac{R}{\alpha}\right) + \frac{2Rt_B t}{\alpha} - \frac{R}{\alpha}t^2 \tag{D.10}$$

The only viable solution to this quadratic equation is

$$t_B = \sqrt{\frac{R}{\alpha}}\frac{t}{\left(1 + \sqrt{\frac{R}{\alpha}}\right)} \tag{D.11}$$

Of equal interest was the ratio of target in time versus target out time.

$$t_B = \sqrt{\frac{R}{\alpha}}\frac{t_A + t_B}{\left(1 + \sqrt{\frac{R}{\alpha}}\right)} \tag{D.12}$$

$$t_B = \sqrt{\frac{R}{\alpha}}t_A \tag{D.13}$$

Appendix E. TABLES OF RESULTS

The following tables are the measured differential cross sections for the angular distributions plotted in Chapter 3 and Chapter 4 for carbon.

Table E.1: Differential Cross Sections at 154.0 MeV Average C.M. Energy

C.M. Angle (degree)	dσ/dΩ (b/sr)	error (b/sr)
20.27	4.53e-07	2.36e-07
40.71	4.1e-07	7.45e-08
60.36	2.75e-07	2.69e-08
90.64	1.81e-07	2.08e-08
120.66	1.98e-07	2.01e-08
145.73	1.5e-07	1.91e-08

Table E.2: Differential Cross Sections at 192.7 MeV Average C.M. Energy

C.M. Angle (degree)	dσ/dΩ (b/sr)	error (b/sr)
19.04	2.26e-06	3.94e-07
30.49	1.23e-06	2.07e-07
45.69	8.41e-07	1.2e-07
60.84	3.75e-07	4.66e-08
91.24	6.95e-08	5.35e-09
121.09	2.73e-08	7.54e-09
150.48	5.65e-09	2.96e-09

Table E.3: Differential Cross Sections at 194.7 MeV Average C.M. Energy

C.M. Angle (degree)	dσ/dΩ (b/sr)	error (b/sr)
30.49	1.74e-06	2.08e-07
90.98	1.21e-07	1.40e-08
105.62	3.37e-08	1.38e-08
132.36	2.74e-08	6.37e-09
144.42	1.46e-08	5.28e-09

Table E.4: Differential Cross Sections at 244.7 MeV Average C.M. Energy

C.M. Angle (degree)	dσ/dΩ (b/sr)	error (b/sr)
30.69	5.73e-06	7.26e-07
45.95	3.19e-06	4.74e-07
60.99	8.86e-07	1.23e-07
130.27	4.67e-08	1.66e-08
147.15	4.17e-08	1.53e-08

Table E.5: Pileup Corrected Differential Cross Sections at 244.7 MeV Average C.M. Energy

C.M. Angle (degree)	dσ/dΩ (b/sr)	error (b/sr)
92.25	3.27e-07	4.08e-08

Table E.6: Upper Limits on Differential Cross Sections at 244.7 MeV Average C.M. Energy

C.M. Angle (degree)	dσ/dΩ (b/sr)
105.85	8.65e-08
120.73	7.727e-08
130.27	4.872e-08

Table E.7: Differential Cross Sections at 287.7 MeV Average C.M. Energy

C.M. Angle (degree)	dσ/dΩ (b/sr)	error (b/sr)
20.47	1.56e-05	3.70e-06
30.85	7.89e-06	1.18e-06
46.03	3.29e-06	4.03e-07

Table E.8: Upper Limits Differential Cross Sections at 287.7 MeV Average C.M. Energy

C.M. Angle (degree)	dσ/dΩ (b/sr)
67.07	1.12e-07
91.14	7.40e-08
121.41	3.88e-08
145.41	1.27e-08

The following table is the measured differential cross sections for the angular distributions plotted in Chapter 4 for helium at 145.9 MeV.

Table E.9: Differential Cross Sections at 145.9 MeV Average C.M. Energy

C.M. Angle (degree)	dσ/dΩ (b/sr)	error (b/sr)
20.75	4.21e-08	8.97e-09
41.61	2.82e-08	2.67e-09
62.78	2.15e-08	1.97e-09
92.01	4.35e-08	3.05e-09
121.83	1.12e-07	8.73e-09
146.49	1.74e-07	8.93e-09

The following table contains the cross sections used for the energy dependence study for carbon shown in Chapter 4. A "*" in the error column indicates an upper limit.

Table E.10: Differential Cross Sections at 20 Degrees

E (MeV)	dσ/dΩ (b/sr)	error (b/sr)	E (MeV)	dσ/dΩ (b/sr)	error (b/sr)
134.73	3.16e-07	7.02e-08	225.19	8.43e-06	5.85e-07
139.61	3.40e-07	6.69e-08	229.97	8.56e-06	6.67e-07
144.46	5.33e-07	7.86e-08	234.72	1.09e-05	8.48e-07
149.30	4.64e-07	9.25e-08	239.14	1.39e-05	1.60e-06
153.70	4.00e-07	1.93e-07	271.09	1.42e-05	1.29e-06
175.01	1.03e-06	1.47e-07	275.81	1.72e-05	1.64e-06
179.83	1.73e-06	1.89e-07	280.22	1.71e-05	3.32e-06
184.62	1.93e-06	2.50e-07			
189.08	1.80e-06	3.53e-07			

Table E.11: Differential Cross Sections at 30 Degrees

E (MeV)	dσ/dΩ (b/sr)	error (b/sr)	E (MeV)	dσ/dΩ (b/sr)	error (b/sr)
175.01	1.15e-06	9.72e-08	225.19	4.5e-06	2.73e-07
176.95	1.23e-06	6.85e-08	229.97	5.22e-06	3.09e-07
179.83	1.4e-06	1.13e-07	234.72	5.92e-06	4.04e-07
181.77	1.49e-06	8.19e-08	239.14	6.73e-06	7.15e-07
184.62	1.67e-06	1.42e-07	271.09	7.69e-06	4.6e-07
186.56	1.55e-06	9.92e-08	275.81	8.18e-06	5.1e-07
189.08	1.21e-06	1.9e-07	280.22	7.63e-06	9.59e-07
191.02	1.89e-06	1.89e-07			

Table E.12: Differential Cross Sections at 45 Degrees

E (MeV)	dσ/dΩ (b/sr)	error (b/sr)	E (MeV)	dσ/dΩ (b/sr)	error (b/sr)
134.73	2.79e-07	2.27e-08	225.19	2.10e-06	1.55e-07
139.61	1.95e-07	2.16e-08	229.97	2.09e-06	1.60e-07
144.46	2.75e-07	2.71e-08	234.72	2.34e-06	2.06e-07
149.30	3.22e-07	3.16e-08	239.14	2.76e-06	3.94e-07
153.70	3.82e-07	6.09e-08	271.09	2.33e-06	1.44e-07
175.01	6.45e-07	4.55e-08	275.81	2.09e-06	1.65e-07
179.83	6.72e-07	5.04e-08	280.22	2.85e-06	3.29e-07
184.62	8.63e-07	6.07e-08			
189.08	9.26e-07	1.08e-07			

Table E.13: Differential Cross Sections at 60 Degrees

E (MeV)	dσ/dΩ (b/sr)	error (b/sr)	E (MeV)	dσ/dΩ (b/sr)	error (b/sr)
134.73	1.61e-07	8.29e-09	225.19	6.57e-07	3.9e-08
139.61	1.56e-07	8.63e-09	229.97	5.87e-07	4.07e-08
144.46	1.76e-07	9.36e-09	234.72	5.74e-07	4.63e-08
149.30	1.92e-07	1.14e-08	239.14	6.82e-07	9.53e-08
153.70	2.82e-07	2.38e-08			
175.01	4.39e-07	2.14e-08			
179.83	3.95e-07	2.12e-08			
184.62	4.30e-07	2.60e-08			
189.08	4.12e-07	4.27e-08			

Table E.14: Differential Cross Sections at 70 Degrees

E (MeV)	dσ/dΩ (b/sr)	error (b/sr)
271.09	2.31e-07	2.68e-08
275.81	1.35e-07	1.86e-08
280.22	8.72e-08	5.86e-08

Table E.15: Differential Cross Sections a Back Angles

Angle (deg)	E (MeV)	dσ/dΩ (b/sr)	error (b/sr)
90	153.70	1.57e-07	1.7e-08
	191.02	1.35e-07	1.29e-08
	189.08	7.56e-08	5.03e-09
105	191.02	3.44e-08	1.22e-08
	239.14	2.13e-07	*
120	153.70	2.08e-07	1.88e-08
	189.08	3.29e-08	7.29e-09
	239.14	1.049e-07	*
	280.22	1.072e-07	*
130	191.02	2.31e-08	5.18e-09
	239.14	5.42e-08	1.10e-08
	239.14	4.87e-08	*
150	153.70	1.50e-07	1.68e-08
	189.08	5.73e-09	2.66e-09
	191.02	1.59e-08	4.84e-09
	239.14	4.16e-08	1.34e-08
	280.22	4.74e-08	*

The following table contains the cross sections used for the energy dependence study for helium shown in Chapter 4.

Table E.16: Differential Cross Sections at 20 Degrees

E (MeV)	dσ/dΩ (b/sr)	error (b/sr)	E (MeV)	dσ/dΩ (b/sr)	error (b/sr)
131.64	7.95e-08	1.64e-08	216.80	1e-06	1.35e-07
136.30	5.5e-08	1.56e-08	221.23	1.32e-06	1.66e-07
140.92	1.87e-08	1.4e-08	225.63	1.37e-06	1.93e-07
145.51	3.61e-08	1.48e-08	229.72	2.2e-06	4.21e-07
149.71	7.63e-08	3.73e-08	259.12	2.45e-06	2.39e-07
169.85	1.31e-07	2.43e-08	263.43	2.98e-06	3.16e-07
174.40	2.06e-07	2.50e-08	267.46	3.51e-06	5.96e-07
178.91	2.22e-07	2.94e-08			
183.10	1.8e-07	5.40e-08			

Table E.17: Differential Cross Sections at 30 Degrees

E (MeV)	dσ/dΩ (b/sr)	error (b/sr)	E (MeV)	dσ/dΩ (b/sr)	error (b/sr)
169.85	8.31e-08	1.99e-08	216.80	8.59e-07	6.60e-08
171.68	1.38e-07	1.94e-08	221.23	9.51e-07	7.54e-08
174.40	1.67e-07	2.67e-08	225.63	1.07e-06	9.46e-08
176.22	1.35e-07	2.07e-08	229.72	1.18e-06	1.89e-07
178.91	1.59e-07	3.18e-08	259.12	1.73e-06	1.40e-07
180.73	2.16e-07	2.89e-08	263.43	1.68e-06	1.61e-07
183.10	1.86e-07	5.48e-08	267.46	2.52e-06	3.11e-07
184.91	3.12e-07	5.93e-08			

Table E.18: Differential Cross Sections at 45 Degrees

E (MeV)	dσ/dΩ (b/sr)	error (b/sr)	E (MeV)	dσ/dΩ (b/sr)	error (b/sr)
131.64	2.25e-08	3.8e-09	216.80	4.62e-07	3.58e-08
136.30	2.43e-08	3.92e-09	221.23	6.1e-07	4.4e-08
140.92	2e-08	4.12e-09	225.63	5.81e-07	5.13e-08
145.51	4.16e-08	5.6e-09	229.72	6.58e-07	9.28e-08
149.71	3.14e-08	1.09e-08	259.12	9.16e-07	5.63e-08
169.85	8e-08	1.33e-08	263.43	9.16e-07	6.18e-08
174.40	9.35e-08	1.9e-08	267.46	1.04e-06	1.26e-07
178.91	1.29e-07	2.1e-08			
183.10	1.67e-07	3.65e-08			

Table E.19: Differential Cross Sections at 60 Degrees

E (MeV)	dσ/dΩ (b/sr)	error (b/sr)	E (MeV)	dσ/dΩ (b/sr)	error (b/sr)
131.64	1.57e-08	3.10e-09	216.80	2.80e-07	1.61e-08
136.30	1.95e-08	2.94e-09	221.23	3.40e-07	1.87e-08
140.92	1.93e-08	3.17e-09	225.63	3.25e-07	2.22e-08
145.51	2.26e-08	4.31e-09	229.72	5.42e-07	4.75e-08
149.71	3.28e-08	8.13e-09			
169.85	6.25e-08	9.11e-09			
174.40	7.70e-08	1.20e-08			
178.91	8.54e-08	1.43e-08			
183.10	1.02e-07	2.36e-08			

Table E.20: Differential Cross Sections at 70 Degrees

E (MeV)	dσ/dΩ (b/sr)	error (b/sr)
259.12	3.21e-07	3.19e-08
263.43	3.47e-07	3.95e-08
267.46	3.34e-07	7.03e-08

Table E.21: Differential Cross Sections at 90 Degrees

E (MeV)	dσ/dΩ (b/sr)	error (b/sr)	E (MeV)	dσ/dΩ (b/sr)	error (b/sr)
136.30	3.68e-08	4.63e-09	216.80	1.35e-07	7.91e-09
140.92	4.80e-08	5.29e-09	221.23	1.32e-07	8.51e-09
145.51	4.25e-08	5.63e-09	225.63	1.58e-07	1.09e-08
149.71	5.98e-08	1.10e-08	229.72	2.18e-07	2.21e-08
171.68	6.20e-08	4.97e-09	259.12	1.37e-07	1.12e-08
176.22	5.03e-08	5.52e-09	263.43	1.36e-07	1.31e-08
180.73	7.87e-08	7.43e-09	267.46	1.73e-07	2.79e-08
184.91	9.53e-08	1.22e-08			

Table E.22: Differential Cross Sections at 105 Degrees

E (MeV)	dσ/dΩ (b/sr)	error (b/sr)	E (MeV)	dσ/dΩ (b/sr)	error (b/sr)
171.68	8.80e-08	4.38e-09	216.80	1.11e-07	9.28e-09
176.22	8.02e-08	4.55e-09	221.23	9.74e-08	9.66e-09
180.73	6.96e-08	4.76e-09	225.63	1.17e-07	1.23e-08
184.91	5.21e-08	7.80e-09	229.72	1.61e-07	2.21e-08

Table E.23: Differential Cross Sections at 120 Degrees

E (MeV)	dσ/dΩ (b/sr)	error (b/sr)	E (MeV)	dσ/dΩ (b/sr)	error (b/sr)
136.30	1.08e-07	1.42e-08	216.80	1.13e-07	5.05e-09
140.92	9.9e-08	1.33e-08	221.23	1.18e-07	5.10e-09
145.51	1.15e-07	1.63e-08	225.63	1.17e-07	6.06e-09
149.71	1.22e-07	3.06e-08	229.72	1.56e-07	1.33e-08
169.85	8.95e-08	4.01e-09	259.12	5.66e-08	6.83e-09
174.40	8.68e-08	4.07e-09	263.43	6.87e-08	7.63e-09
178.91	8.28e-08	4.67e-09	267.46	8.37e-08	1.59e-08
183.10	9.72e-08	8.52e-09			

Table E.24: Differential Cross Sections at 130 Degrees

E (MeV)	dσ/dΩ (b/sr)	error (b/sr)
171.68	1.06e-07	6.38e-09
176.22	1.20e-07	7.15e-09
180.73	1.11e-07	7.95e-09
184.91	1.49e-07	1.56e-08
216.80	1.17e-07	6.36e-09
221.23	1.10e-07	6.55e-09
225.63	1.22e-07	7.77e-09
229.72	1.34e-07	1.87e-08

Table E.25: Differential Cross Sections at 150 Degrees

E (MeV)	dσ/dΩ (b/sr)	error (b/sr)	E (MeV)	dσ/dΩ (b/sr)	error (b/sr)
136.30	1.48e-07	1.33e-08	216.80	1.09e-07	8.28e-09
140.92	1.69e-07	1.40e-08	221.23	1.06e-07	8.04e-09
145.51	1.87e-07	1.80e-08	225.63	1.27e-07	1.03e-08
149.71	9.32e-08	3.20e-08	229.72	1.38e-07	2.19e-08
171.68	1.23e-07	5.79e-09	259.12	1.45e-08	1.00e-08
176.22	1.42e-07	6.21e-09	263.43	1.09e-08	1.01e-08
180.73	1.40e-07	7.34e-09	267.46	1.31e-08	1.30e-08
184.91	1.92e-07	1.42e-08			

Appendix F. SCHEMATIC MODEL CALCULATIONS

The zero degree cross sections for use in the Schematic model were calculated[1] using dispersion relations from total absorption cross sections for beryllium measured by Arends [Arends 81]. Since the total absorption cross section scales by A^2, the beryllium cross section was scaled by $(m_A/m_{Be})^2$, where m_A is the mass of the nucleus of interest and m_{Be} is the mass of beryllium. Figure F.1 shows the beryllium cross sections which are also tabulated Table F.1.

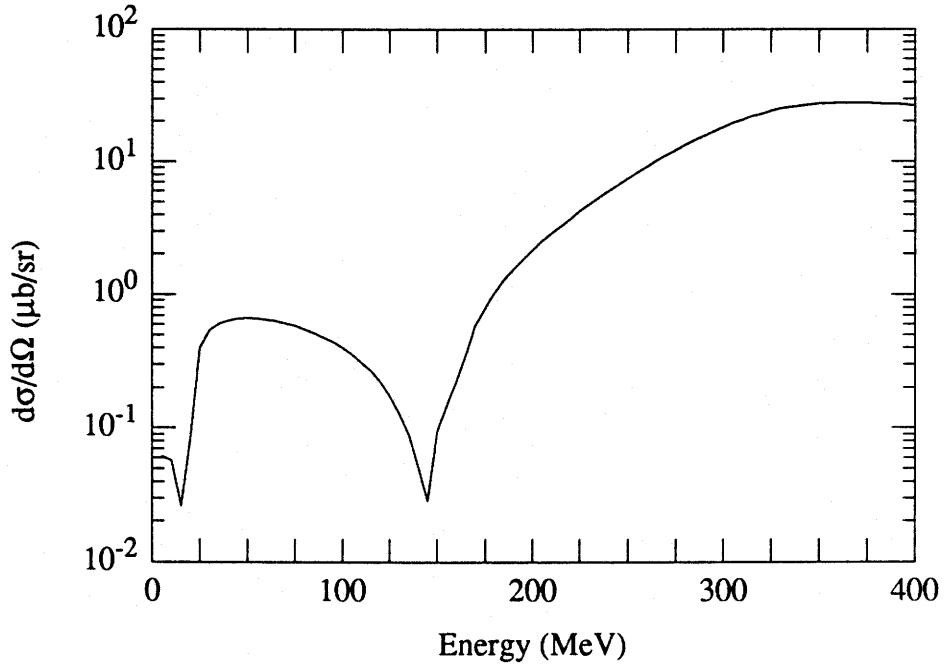

Figure F.1: 0 Degree Differential Cross Section for Beryllium Derived by Dispersion Relations

1. E. Hayward and B. Ziegler, private communication

The carbon form factors were calculated, by a C language program **kine.form**, using the formula for harmonic wells from Herman and Hofstadter [Herman 60],

$$F(q) = \left(1 - \frac{\alpha x^2}{3(2+5\alpha)}\right)\exp(-\frac{x^2}{4k^2}) \qquad \text{(F.1)}$$

where $x = qa$, $a = 2.42$ [Ehrenberg 59, Crannell 66], $\alpha = 4/3$, $k = \sqrt{\frac{3}{2}\frac{(2+5\alpha)}{(2+3\alpha)}}$. This formula agrees well with electron scattering measurements with carbon [Fregeau 55, Ehrenberg 59, Crannell 64, Crannell 66] (see Figure F.2).

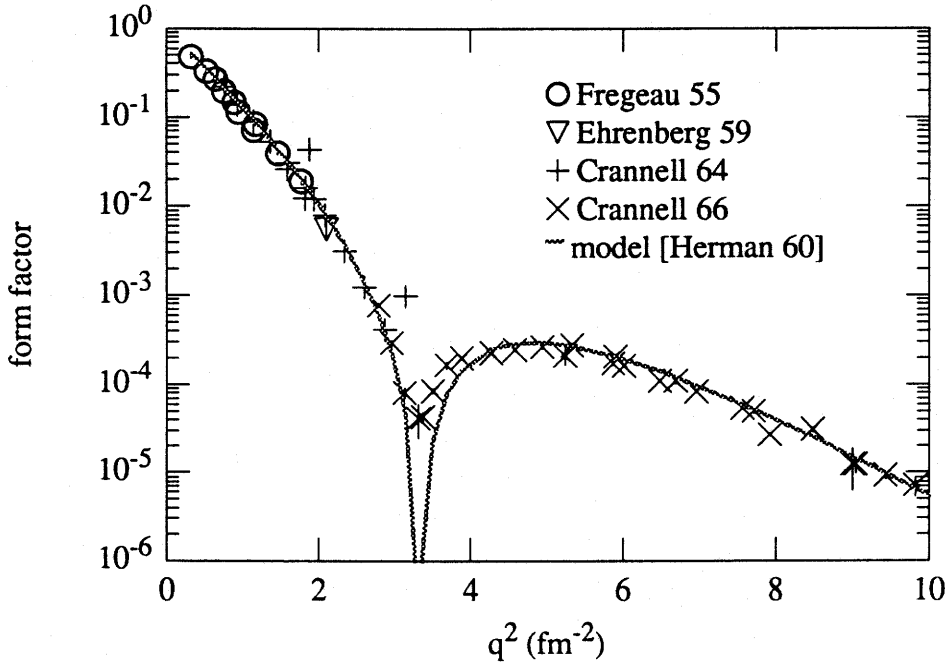

Figure F.2: Form Factors for Carbon

The helium form factors were calculated using a formula from McCarthy [McCarthy 77],

$$F(q) = (1 - (a^2q^2)^6)\exp(-b^2q^2) \qquad \text{(F.2)}$$

where $a = 0.316$ and $b = 0.681$. This formula agrees well with electron scattering measurements with helium [Frosch 61, McCarthy 77, Ottermann 85] (see Figure F.3).

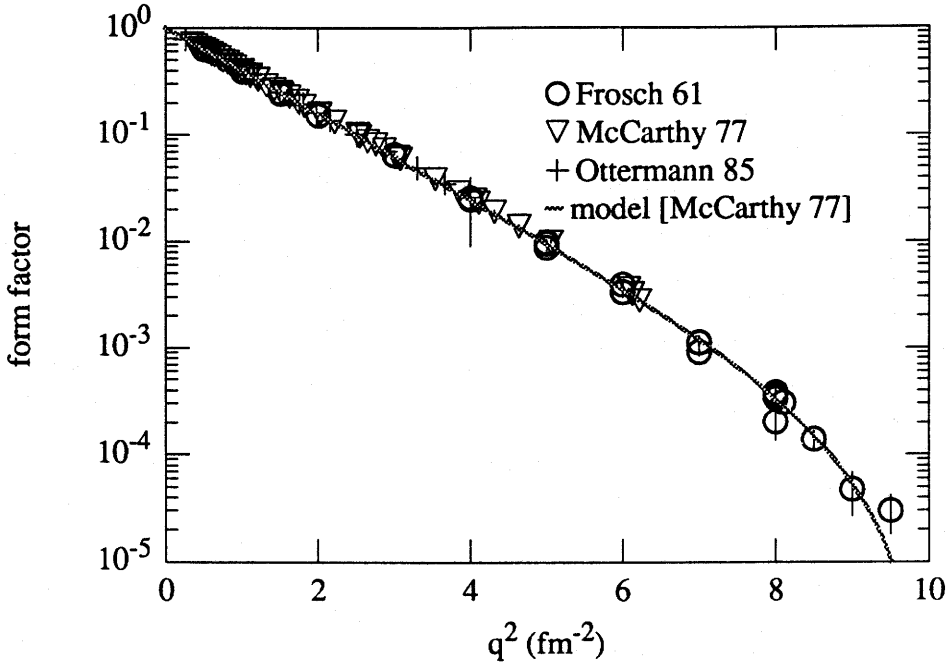

Figure F.3: Form Factors for Helium

For angular distributions, the form factors were first calculated for angles between 0 degrees and 180 degrees at the given energy and saved to a file. The 0 degree cross section was looked up from a table (see Table F.1) for the appropriate lab energy and then scaled by the appropriate jacobian to convert to C.M.. The form factors were then simply scaled by this 0 degree cross section and by $(1 + \cos^2\theta)/2$.

For the energy dependences, a program was written that read the 0 degree cross section, and for each energy looked up the appropriate cross section from the table, calculated the form factor, convolved the latter two, and scaled by $(1 + \cos^2\theta)/2$.

Table F.1: Amplitudes for Total Absorption of Photons from Be

Energy (MeV)	Im(S)	Re(S)	Cross Section (μb/sr)
5	1.65418542541e-02	-.24738735185	0.0614741
10	4.09736365647e-02	-.236409605303	0.0575683
15	3.54646342399e-02	-.157567213122	0.0260852
20	.279152389653	.109736110036	0.0899681
25	.611292520607	-.161146754923	0.399647
30	.622150307606	-.390338267941	0.539435
35	.580356607072	-.52001198122	0.607226
40	.533369475108	-.598449028218	0.642624
45	.489733592888	-.647603956474	0.65923
50	.450976786997	-.678178213034	0.663306
55	.416967989088	-.696002889107	0.658282
60	.387169276427	-.704511621837	0.646237
65	.36098965231	-.705832220892	0.628513
70	.337889171376	-.701325114729	0.606026
75	.31740384484	-.69187132572	0.579431
80	.299144404078	-.678035485212	0.549219
85	.282787154798	-.660161466124	0.515782
90	.268063418485	-.63842907169	0.47945
95	.254749790698	-.612886454235	0.440527
100	.242659840707	-.583465767582	0.399316
105	.231637281	-.549985249475	0.35614
110	.221550434944	-.512137567506	0.311369
115	.212287785162	-.469460293706	0.265459
120	.203754396996	-.421277385602	0.21899
125	.195869041345	-.366584338615	0.172749

Table F.1: Amplitudes for Total Absorption of Photons from Be

Energy (MeV)	Im(S)	Re(S)	Cross Section (μb/sr)
260	2.91514240204	.80573556222	9.14727
265	3.08338949224	.76726552869	10.096
270	3.25520444516	.716524821805	11.1098
275	3.42939886657	.65219168048	12.1861
280	3.60443871741	.573045582204	13.3204
285	3.77843649407	.478055110976	14.5051
290	3.94916687077	.366476944666	15.7302
295	4.11411201829	.237959360748	16.9825
300	4.27054088155	.092640600322	18.2461
305	4.41562330253	-.068770092063	19.5025
310	4.54657505889	-.244942200053	20.7313
315	4.66082414754	-.43391703913	21.9116
320	4.75618306559	-.633153332767	23.0222
325	4.83100767966	-.839628120904	24.0436
330	4.88432214939	-1.049987652004	24.9591
335	4.9158921323	-1.26073430455	25.7554
340	4.92623530619	-1.46842875039	26.4241
345	4.91656774916	-1.66988346428	26.9611
350	4.88869470787	-1.86232529219	27.3676
355	4.84486231918	-2.04351078463	27.6486
360	4.7875909908	-2.21178659987	27.813
365	4.7195109802	-2.366096263	27.8722
370	4.64321681591	-2.5059417641	27.8392
375	4.561151323	-2.63131277304	27.7279
380	4.4755237016	-2.74259737574	27.5522
385	4.38826086136	-2.84048689439	27.3252

Table F.1: Amplitudes for Total Absorption of Photons from Be

Energy (MeV)	Im(S)	Re(S)	Cross Section (μb/sr)
390	4.30098756605	-2.92588455243	27.0593
395	4.21502912102	-2.999824400274	26.7654
400	4.13142994358	-3.06340389117	26.4532